JOURNAL OF RESEARCH

OF THE U.S. GEOLOGICAL SURVEY

MARCH–APRIL 1975
VOLUME 3, NUMBER 2

Scientific notes and summaries of investigations in geology, hydrology, and related fields

U.S. DEPARTMENT OF THE INTERIOR

UNITED STATES DEPARTMENT OF THE INTERIOR
ROGERS C. B. MORTON, Secretary
GEOLOGICAL SURVEY
V. E. McKelvey, Director

For sale by the Superintendent of Documents, U.S. Government Printing Office, Washington, DC 20402. Order by SD Catalog No. JRGS. Annual subscription rate $18.90 (plus $4.75 for foreign mailing). Single copy $3.15. Make checks or money orders payable to the Superintendent of Documents.

Send all subscription inquiries and address changes to the Superintendent of Documents at the above address.

Purchase orders should not be sent to the U.S. Geological Survey library.

Library of Congress Catalog-card No. 72-600241.

The Journal of Research is published every 2 months by the U.S. Geological Survey. It contains papers by members of the Geological Survey and their professional colleagues on geologic, hydrologic, topographic, and other scientific and technical subjects.

Correspondence and inquiries concerning the Journal (other than subscription inquiries and address changes) should be directed to the Journal of Research, Publications Division, U.S. Geological Survey, National Center 321, Reston, VA 22092.

Papers for the Journal should be submitted through regular Division publication channels.

The Secretary of the Interior has determined that the publication of this periodical is necessary in the transaction of the public business required by law of this Department. Use of funds for printing this periodical has been approved by the Director of the Office of Management and Budget through June 30, 1980.

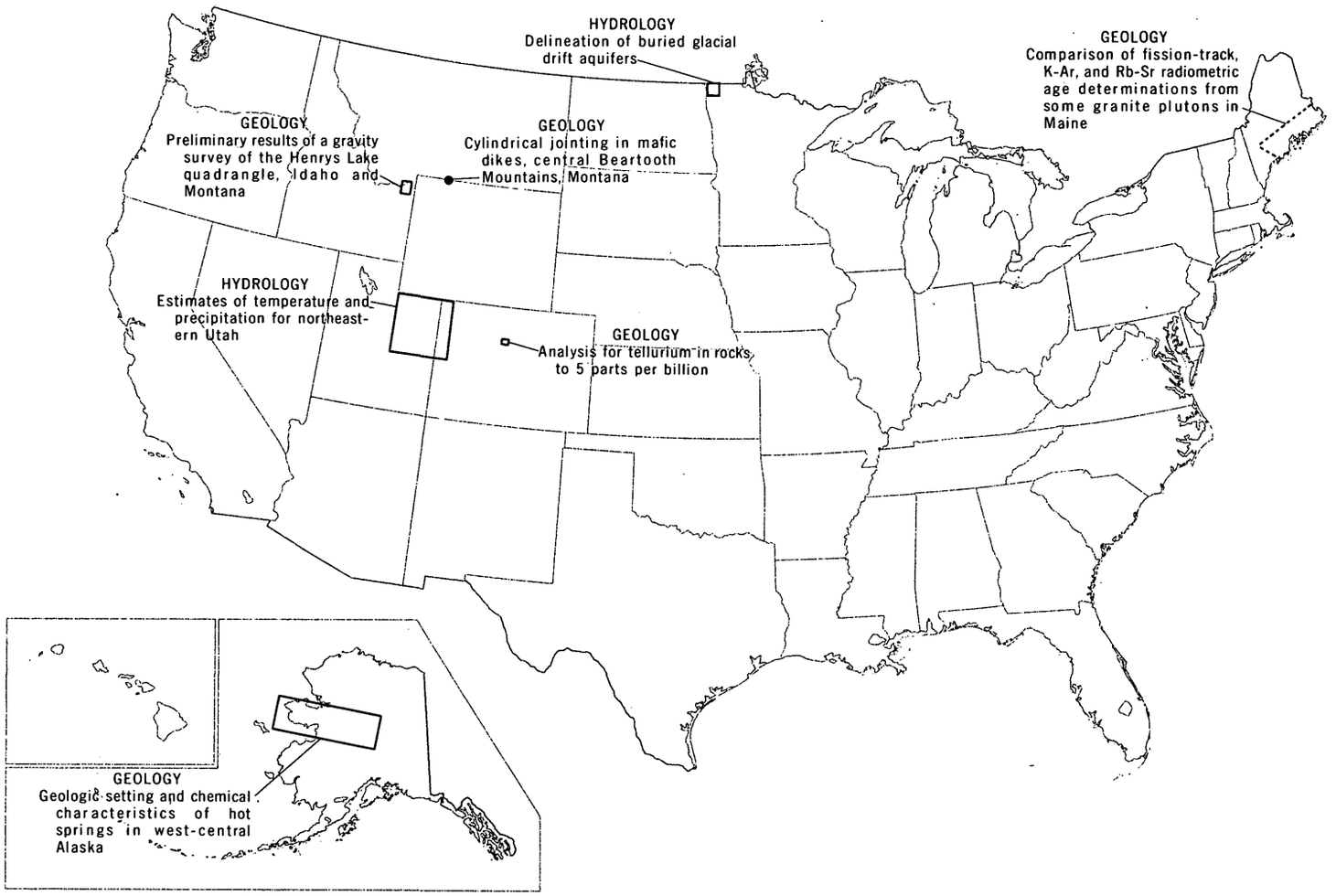

GEOGRAPHIC INDEX TO ARTICLES

See "Contents" for articles concerning areas outside the United States and articles without geographic orientation.

JOURNAL OF RESEARCH

of the

U.S. Geological Survey

Vol. 3 No. 2 Mar.–Apr. 1975

CONTENTS

ABBREVIATIONS

A ---------angstrom
alt -------altitude
avg -------average
B.P. ------before present
cal --------calorie
calc -------calculated
COD ------chemical oxygen demand
concd -----concentrated
cP --------centipoise
D ---------debye unit
d ---------day
d.f. -------degree of freedom
diam ------diameter
DO -------dissolved oxygen
Eh --------oxidation-reduction potential
eq --------equation
ERTS -----Earth Resources Technology Satellite (now Landsat)
ft-c -------foot-candle
h ---------hour
J ---------joule
K ---------kelvin
kg --------kilogram
kV --------kilovolt
kWh ------kilowatt-hour
lat --------latitude
LDMW ---locally derived meteoric water
lm --------lumen
log --------logarithm (common)
long ------longitude
M --------molarity, molar (concentration)
m ---------molality; molal (concentration)
mA -------milliampere
MBAS ----methylene blue active substance
MeV ------megaelectronvolt
mg -------milligram
mGal -----milligal
MIBK ----methyl isobutyl ketone
min -------minute
Ml --------million litres
ml --------millilitre
mo --------month
mol -------mole
mV -------millivolt
m.y. ------million years
μcal -------microcalorie
μg ---------microgram
μm --------micrometre
μmho -----micromho
N ---------normality
n ---------neutron
NASA ----National Aeronautics and Space Administration
nm -------nanometre
P.d.t. -----Pacific daylight time
pH -------measure of hydrogen ion activity
ppb -------part per billion
ppm ------part per million
r/min -----revolutions per minute
s ---------second
(s) -------solid
SMOW ----standard mean ocean water
std -------standard
σ ---------population standard deviation
W ---------watt
w/v -------weight per volume
yd --------yard
yr --------year

METRIC-ENGLISH EQUIVALENTS

Metric unit		English equivalent	
Length			
millimetre (mm)	=	0.03937	inch (in)
metre (m)	=	3.28	feet (ft)
kilometre (km)	=	.62	mile (mi)
Area			
square metre (m^2)	=	10.76	square feet (ft^2)
square kilometre (km^2)	=	.386	square mile (mi^2)
hectare (ha)	=	2.47	acres
Volume			
cubic centimetre (cm^3)	=	0.061	cubic inch (in^3)
litre (l)	=	61.03	cubic inches
cubic metre (m^3)	=	35.31	cubic feet (ft^3)
cubic metre	=	.00081	acre-foot (acre-ft)
cubic hectometre (hm^3)	=	810.7	acre-feet
litre	=	2.113	pints (pt)
litre	=	1.06	quarts (qt)
litre	=	.26	gallon (gal)
cubic metre	=	.00026	million gallons (Mgal or 10^6 gal)
cubic metre	=	6.290	barrels (bbl) (1 bbl=42 gal)
Weight			
gram (g)	=	0.035	ounce, avoirdupois (oz avdp)
gram	=	.0022	pound, avoirdupois (lb avdp)
tonne (t)	=	1.1	tons, short (2,000 lb)
tonne	=	.98	ton, long (2,240 lb)
Specific combinations			
kilogram per square centimetre (kg/cm^2)	=	0.96	atmosphere (atm)
kilogram per square centimetre	=	.98	bar (0.9869 atm)
cubic metre per second (m^3/s)	=	35.3	cubic feet per second (ft^3/s)

Metric unit		English equivalent	
Specific combinations—Continued			
litre per second (l/s)	=	.0353	cubic foot per second
cubic metre per second per square kilometre [$(m^3/s)/km^2$]	=	91.47	cubic feet per second per square mile [$(ft^3/s)/mi^2$]
metre per day (m/d)	=	3.28	feet per day (hydraulic conductivity) (ft/d)
metre per kilometre (m/km)	=	5.28	feet per mile (ft/mi)
kilometre per hour (km/h)	=	.9113	foot per second (ft/s)
metre per second (m/s)	=	3.28	feet per second
metre squared per day (m^2/d)	=	10.764	feet squared per day (ft^2/d) (transmissivity)
cubic metre per second (m^3/s)	=	22.826	million gallons per day (Mgal/d)
cubic metre per minute (m^3/min)	=	264.2	gallons per minute (gal/min)
litre per second (l/s)	=	15.85	gallons per minute
litre per second per metre [(l/s)/m]	=	4.83	gallons per minute per foot [(gal/min)/ft]
kilometre per hour (km/h)	=	.62	mile per hour (mi/h)
metre per second (m/s)	=	2.237	miles per hour
gram per cubic centimetre (g/cm^3)	=	62.43	pounds per cubic foot (lb/ft^3)
gram per square centimetre (g/cm^2)	=	2.048	pounds per square foot (lb/ft^2)
gram per square centimetre	=	.0142	pound per square inch (lb/in^2)
Temperature			
degree Celsius (°C)	=	1.8	degrees Fahrenheit (°F)
degrees Celsius (temperature)	=	[(1.8×°C)+32]	degrees Fahrenheit

Jour. Research U.S. Geol. Survey
Vol. 3, No. 2, Mar.–Apr. 1975, p. 127–129

INFORMATION THROUGH COLOR IMAGERY

By ALDEN P. COLVOCORESSES, Reston, Va.

Abstract.—The color-sensing capability of the human eye is a powerful tool. In remote sensing we should use color to display data more meaningfully, not to re-create the scene. Color disappears with distance, and features change color with viewing angle. Color infrared film lets us apply color with additional meaning even though we introduce a false color response. Although the marginal gray scale on an ERTS (Earth Resources Technology Satellite) image may indicate balance between the green, red, and infrared bands, and although each band may be printed in a primary color, tests show that we are not fully applying the three primary colors. Therefore, contrast in the green band should be raised. For true three-color remote sensing of the Earth, we must find two generally meaningful signatures in the visible spectrum, or perhaps extend our spectral range. Before turning to costly digital processing we should explore analog processing. Most ERTS users deal with relative spectral radiance; the few concerned with absolute radiance could use the computer-compatible tapes or special annotations. NASA (National Aeronautics and Space Administration), which assigns the range and contrast to the ERTS image, controls processing and could adjust the density range for maximum contrast in any ERTS scene. NASA cannot alter processing for local changes in reflective characteristics of the Earth but could adjust for Sun elevation and optimize the contrast in a given band.

In spite of the complexity and the current proliferation of computers, decisions are still largely made by the human being and are based principally on what one sees. What one sees may be a natural scene, or it may be information in the form of alphanumerics or graphics. Graphics may be an artificial presentation, or they may be an image of the natural scene as recorded by a remote sensor. Remotely sensed imagery is the subject of immediate concern.

The human eye, through a system of fine cones, senses three distinct groups of wavelengths (colors) which make up the visible spectrum. If the image is portrayed in all three colors, it should impart far more information than if in monochromatic form, such as a black-and-white photograph. On the basis of information theory according to Arch Park of Earthsat Corp. (oral commun., 1974), the relative value of color is 1!, 2!, or 3! (1, 2, 6) depending on the number of colors that are fully and meaningfully used. I'm not going to try to prove or disprove these numbers, but there is no doubt that color, as compared with the monochromatic presentation, can greatly increase the information content of a given image. Information, however, must be meaningful if it is to really help the decisionmaking process, and two basic questions arise: Should colored imagery approximate the tones and hues of the real scene, or should color be treated as a tool for adding information regardless of the true color of the scene itself? Except for a few special cases, I feel we are making a big mistake in trying to re-create true tone and hue of a remotely sensed scene in a colored image. The time has come to treat color as an independent parameter and apply it to imagery with the same force that we now apply color to maps, graphs, and other artificial graphics. Let us look at the evolution, current use, and future potential of color as it applies to remotely sensed imagery.

HISTORY AND CURRENT STATUS

Since color photography was first developed, there have been repeated efforts to apply it in the aerial mode. Recently the Apollo and Skylab programs have carried color photography into space. About 1940, camouflage-detection (color infrared) film was developed, and it also has been applied in both the aerial and the space modes. But what has all this meant in relation to general use and practical applications? As of today more than 90 percent of all aerial photographs are still exposed on black-and-white films, which raises the question of just how useful color photography really is.

We all know that at reasonably close range color film can record hues and tones with a high degree of reliability. But what happens when we move up in the atmosphere? For one thing, color differences (hues) quickly disappear, and except over dry desert areas the Earth takes on a fairly uniform response. Thus the parameter of color as seen in the visible spectrum tends to be lost, even at reasonably low altitudes. Another problem is that the same features change color with the viewing angle. Now if we record the Earth from space with conventional color film, in most areas practically everything in the photographed area tends to turn blue. We can get basically the same response on black-and-white film, and if we

like the blue color, we can print it in blue.

But what about color infrared film? Here we have a response that extends well beyond what the eye sees. Now the parameter of color can be applied with additional meaning even though we introduce a false color response in the process. For example, an ERTS image, at low resolution but in the color infrared mode, may carry a marginal gray scale indicating a balance involving bands 4 (green), 5 (red), and 7 (infrared). If each band is assigned a primary color for printing, we can say we are applying the three primary colors. We can say it, but it isn't really true. Remember that color photographs from space are generally monochromatic. How can we, therefore, get two meaningful colors out of a monochromatic response? We can't, and I suspect our whole approach to color and color infrared photography is suffering because of this.

ERTS offers us a unique and widespread opportunity to look at the color problem since we start with four separate waveband records which register perfectly when properly handled. We have taken ERTS images of New Jersey, Florida, and Arizona and tested our concepts by combining only bands 5 and 7 (red and IR) and comparing them with the conventional three-color combinations of bands 4, 5, and 7. In each of our experiments the two-color approach resulted in a colored image of equal or better informational content than the three-color approach. To maintain color balance, band 5 was used to activate two of the subtractive colors (yellow and magenta) while band 7 activated cyan. These results would seem to imply that band 4 is of little or no value, but such an implication is obviously not true. On band 4, water tones, though subtle, are real and are not found on the other bands. Then why can't water tones—or other tones unique to band 4—be meaningfully combined in a color composite? The answer apparently lies in the small density range currently assigned to band 4 images by NASA. We can raise the contrast of band 4 and thus accentuate the subtle water ones, but when we do, we tend to saturate (overexpose) the beaches, roads, and other areas of high response. We have to find out if two generally meaningful signatures in the visible spectrum can be obtained from space, and it may be that we will have to use a completely different portion of the spectrum, such as the thermal wavelengths, before we can fully apply three colors to an image of the Earth that has been sensed through the atmosphere. One simple answer to this problem is to forget photographic processing and turn to the digital domain; however, we must remember that digital data, regardless of how well processed, must still be transmitted to the human brain, which again involves the color-sensitive human eye. Moreover, digital processing is both complex and costly, and before we all go digital, let's see if we have properly explored analog processing. Because of its characteristics and availability, I've chosen ERTS for this discussion, but it applies to high-altitude aerial photographs or Skylab imagery as well.

ERTS IMAGE PROCESSING

ERTS imagery serves two principal groups of users who depend upon spectral response. The first group consists of those who are concerned with the absolute radiance of an object or area. These are generally scientifically oriented and probably constitute a fairly small percentage of NASA investigators. The second group, which includes the vast majority of ERTS users, are those looking for information which is based on relative spectral radiance. This is a matter of difference (contrast) in tone and hue.

Photographic film has an information-storing capability far beyond that which the human eye can directly detect. However, conventional photographic products, such as photopaper, have limited dynamic range, and the Earth's varied response, as sensed by ERTS, must be compressed if it is to be recorded on a print in absolute terms. If each ERTS scene carried the full response (darkest to brightest), there would be little choice except to print the full response. Actually, in any one given ERTS scene, the response in any one band is quite limited. Occasionally a scene may be half snow and half dark woods, thus creating a sizable range of response, but ordinarily the density range of an ERTS scene is only a small fraction of that encountered throughout a complete cycle of Earth coverage. This means that the contrast of any one ERTS image could be much greater if its density range were aimed at maximizing the scene rather than dealing in absolute terms. In theory, specialized photoprocessing can bring out and print in visible form any information available on film. However, a photoprint or lithographed photocopy will normally display no more than what is shown at reasonable contrast on the film. Therefore the range and contrast assigned by NASA to the original ERTS image as printed by the Electron Beam Recorder (EBR) control the entire chain of photographic processing, except for those few agencies that can afford the time and cost of sophisticated (custom) image processing.

The problem of reproducing ERTS imagery is basically the same as for aerial photographs used in photomaps or orthophotoquads. In aerial photographs, all possible effort is made to properly record the entire

response of the project on the aerial film. On the developed film the density (D) range is determined (D_{min} and D_{max}), from which a proper processing gamma is determined which will just fit the dynamic range of the photographic product. This procedure merely extends the recorded density range over the straight-line portion of the characteristic curve of the photographic product and thus achieves maximum contrast without overexposure or underexposure of any project element. The key to this procedure is restricting the project to one of generally uniform response. If a bright desert and a dark timbered area are included on the same project for which the overall response is set, the contrast on any one image must be much lower than if the project were all wooded or all desert; the overall density range would then be smaller and the gamma (contrast) on the final product would be higher. Why not look at an ERTS image the same way we look at an aerial-photography project?

ERTS must record a tremendous density range due to the difference in the Earth's reflective characteristics as well as the Sun's altitude, which varies from 0° near the poles to more than 60° where the satellite crosses the ecliptic. NASA cannot alter processing for local changes in reflective characteristics of the Earth but could modulate the basic process according to Sun elevation to maximize the normal Earth scene. On ERTS–1 four MSS (multispectral scanner) bands are involved. Bands 6 and 7 (near infrared) as imaged by the EBR now show a high contrast; band 5 (red), fair contrast; but band 4 (green), generally poor contrast. As a result, band 4 as now processed contributes little to color composites when combined with bands 5 and 7.

Changing the processing range according to Sun elevation or increasing the gamma on band 4 is obviously going to hamper the work of those few scientific investigators who are looking for absolute radiance. Those investigators should use the computer-compatible tapes, which do record absolute radiance (as it reaches the sensor), and leave the images to those looking for relative radiance. However, when ERTS imagery is modulated to maximize the response, there is no reason why the density ranges and gamma used (or some indication thereof) could not be annotated by the EBR which produces the original image. Likewise, when further processing is done, marginal indications of the processing parameters could be added.

Altering absolute to relative radiance values and maximizing image contrast is often referred to by such terms as "haze removal" or "image enhancement," but to me it is nothing more than proper photographic processing. Every time a photographer alters his lens settings, film type, or processing procedure, he is doing exactly the same thing. Where would photography be today if we always attempted to record absolute radiance? I suggest we would be back in the pinhole era.

ACTION TO BE TAKEN

With regard to ERTS, the U.S. Geological Survey has recently been selected by NASA to carry out image processing experiments based on providing optimum final products—both in color and in black-and-white. The concepts and procedures discussed in this paper will be tested in our laboratories with the goal of improving the quality of ERTS image products. However, the most important action that should be taken is perhaps philosophical. We must accept the color-sensing capability of the human eye as the powerful tool that it is for transmitting information to the brain; therefore, we should attempt to display remotely sensed data in a full three-color meaningful form. By such action the value of an image should increase materially and thus aid the decisionmaking process in which the human eye is the key.

Just as speed-reading techniques help us to absorb the information of the written word, the proper use of color can increase our ability to absorb the information now available through imagery of the Earth.

Jour. Research U.S. Geol. Survey
Vol. 3, No. 2, Mar.–Apr. 1975, p. 131–136

ESTIMATES OF TEMPERATURE AND PRECIPITATION FOR NORTHEASTERN UTAH

By F. K. FIELDS and D. B. ADAMS, Salt Lake City, Utah

Work done in cooperation with the Utah Department of Natural Resources

Abstract.—Estimates of temperature and precipitation were made for northeastern Utah from information that was collected at 67 locations. The variable-length records were converted to the common-time base of 1941–70; then general relations were developed to extend the converted point values to unsampled sites. Regression techniques were used to fill voids in the temperature-data base. Incomplete precipitation records were adjusted to the 1941–70 average on the assumption that the ratio of concurrent data is directly proportional to the ratio of the respective 1941–70 average annual values at nearby sites. Equations were then developed through a computer program to express the relationship of temperature and precipitation with altitude and location and to extend the information to unsampled sites. Two-thirds of the observed and estimated average annual temperature and precipitation values are within ±1.5°F (1.0°C) and 2.08 in (53 mm), respectively, of the calculated averages. Schematic diagrams, plotted by computer, were prepared to show variations of altitude, temperature, and precipitation; and maps, also plotted by computer, show lines of equal altitude, precipitation, and temperature.

Most numbers are given in this report in English units followed by metric units in parentheses. The conversion factors used are:

English units	*Multiply by*	*To obtain metric units*
Feet (ft)	0.3048	Metres (m)
Inches (in.)	25.4	Millimetres (mm)
Square miles (mi^2)	2.59	Square kilometres (km^2)

Air temperature is given in degrees Fahrenheit. Degrees Celsius on a thermometer scale equals (°F − 32)/1.8. Difference in degrees Fahrenheit can be converted to difference in degrees Celsius by multiplying the value in degrees Fahrenheit by 0.55.

As part of a detailed hydrologic appraisal in northeastern Utah climatic records of variable length were converted to a common-time base, point-sample information was extended to unsampled sites, and estimates of lines of equal precipitation and temperature were expressed through computer graphics.

The conversion of data samples of variable length to a common-time base eliminates many of the subjective considerations that would otherwise be required. For instance, one 5-yr average for a given point can be quite different from another, and neither may express a long-term average. After conversion, reliable and simple means are available to transfer the point-sample information to unsampled sites and to illustrate the data by computer graphics. The methods that were used to carry out these procedures are briefly explained in this article.

Monthly averages of air temperature for 44 sites and precipitation for 58 sites were compiled from summaries published by the National Weather Service. The sites extend into Colorado and Wyoming for an enlarged sampling and greater diversification of parameter values.

CONVERTING THE DATA TO A COMMON-TIME BASE

Two methods, regression and ratio, were used to convert the climatic data to the common-time base of 1941–70. Both methods require a period of concurrent data at two sites. After an estimating equation has been defined from concurrent records, the regression method only requires data at the independent site during the record voids of the dependent site. One site must have a complete record, however, if the ratio method is to be used.

Changes in average monthly temperatures at a single site reflect a general change of air temperature within the area. Because of the high correlation of temperature data, therefore, regression techniques were used to fill all data voids in the temperature-sample base. The concurrent monthly average temperatures for each incomplete-record site and several nearby complete-record sites were regressed to obtain estimating equations. The equations with the smallest standard error of estimate and largest correlation coefficients were used to estimate the data voids.

The site-to-site comparisons of precipitation records revealed an extreme variability for month-to-month and year-to-year comparisons. This irregular distribution eliminates the use of regression techniques. The

incomplete record sites (PST) were adjusted to the 1941–70 average ($PST_{(E)}$) on the assumption that the ratio of concurrent annual averages ($PST_{(K)}/PLT_{(K)}$) is directly proportional to the ratio of the respective 1941–70 average annual values ($PST_{(E)}/PLT_{(I)}$). Only complete calendar-year values were used in the ratios, which are expressed as

$$\frac{PST_{(K)}}{PLT_{(K)}} = \frac{PST_{(E)}}{PLT_{(I)}},$$

and the estimated average precipitation for 1941–70 is

$$PST_{(E)} = \frac{PLT_{(I)} \times PST_{(K)}}{PLT_{(K)}},$$

where PST = short-term site,
PLT = complete-record site,
K = average annual precipitation for the concurrent period of record,
I = observed average annual precipitation during 1941–70, and
E = estimated average annual precipitation during 1941–70.

Accuracy of site estimates

The average standard error of estimate of the monthly temperature values is about 2°F (1.0°C). This is equal to an error of about 10 percent for the average January temperature (20°F or −6.5°C) and about 3 percent for the average June temperature (61°F or 16.0°C). On the average, the standard error of estimate for the monthly values is about 5 percent.

The accuracy of an estimate made by a ratio calculation is more difficult to appraise. The accuracy level is primarily dependent upon the length of the concurrent records; the longer the period, the more reliable the estimate. This relation is shown in figure 1 and is generated from the comparison of over 300 estimates with actual values for 8 complete-record sites. These estimates are calculated for periods of 1, 2, 5, 10, and 20 yr for about 40 different time intervals within 1941–70. The median timespan of the individual precipitation records is 14 yr.

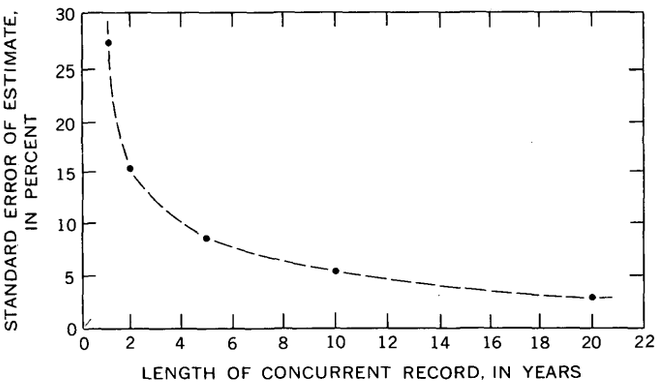

FIGURE 1.—The relation of the standard error of precipitation estimate, made by the ratio method, to the length of concurrent record.

Each long-term average ($PST_{(E)}$) that was calculated for an incomplete-record site (PST) is the average value of four computations obtained from four complete-record sites ($PLT_{(I)}$). The estimates for each site were consistent. The standard deviation of the estimate residuals for the entire collection of ratio estimates was 0.42 in (11 mm) for a mean of the estimated annual precipitation value of 16.2 in (411 mm).

EXTENSION OF POINT-SAMPLE INFORMATION TO UNSAMPLED SITES

The individual site averages for the 1941–70 period are point samples or estimates. Optimum use of these data requires an objective method to distribute or transfer the information to ungaged sites within the study area. Through the computer program KWIKR8 (Esler and others, 1968), equations were developed that accounted for the variance of temperature and precipitation with the parameters of location (A and B) and altitude (C). All locations are referenced to 38° lat and 108° long. These parameters are expressed as follows: A is minutes north of the latitude reference point (latitude, in degrees, minus 38°) times 60 min per degree; B is minutes west of the longitude reference point (longitude, in degrees, minus 108°) times 60 min per degree; and C is altitude, in thousands of feet.

The equations include a series of coefficients that are expressed in scientific notation when followed by the letter E. Each coefficient is multiplied by 10 raised to the exponent shown after the letter E; for example, $4E-02$ is 4×10^{-2}, or 0.04. These equations are used to transfer the existing data-base values and estimates to ungaged sites, but no rational explanation for the variance, relative to location, has been explored. The equations are as follows:

Average annual temperature for the period 1941–70 =
$$24.61 - 18.59E-02(A) + 16.38E-02(B) + 10.99(C) + 24.63E-05(A)^2 + 32.62E-05(A)(B) - 41.05E-06(B)^2 + 41.80E-04(A)(C) - 36.88E-03(B)(C) - 68.30E-02(C)^2,$$
where the correlation coefficient is 0.95, standard error of estimate is 1.5°F (1.0°C), and sample mean is 45.2°F (7.5°C).

Average annual precipitation for the period 1941–70 =
$$33.04 - 17.53E-02(A) + 10.13E-01(B) + 23.26E-01(C) + 28.36E-04(A)^2 - 49.70E-04(A)(B) - 45.16E-04(B)^2 + 42.06E-03(A)(C) - 85.19E-03(B)(C) + 22.13E-02(C)^2 + 12.03E-07(A)^3 +$$

$$12.42E-06(A)^2(B)-81.54E-05(A)^2(C)+34.19E-07(A)(B)^2+25.01E-07(B)^3+58.50E-05(B)^2(C)+11.52E-03(A)(C)^2-60.76E-04(B)(C)^2-35.73E-03(C)^3+20.41E-05(A)(B)(C),$$

where the correlation coefficient is 0.96, standard error of estimate is 2.08 in (53 mm), and sample mean is 14.9 in (378 mm).

Two-thirds of the observed and estimated average annual temperatures are within ±1.5°F (1.0°C) of the defined relation, whereas two-thirds of the precipitation values and estimates are within ±2.08 in (53 mm) of the expression.

Graphical methods of expressing the climatic equations

The empirical equations are difficult to use; therefore, the distributions of the climatic variables were expressed in graphical form. A grid with a 6-min latitude and longitude interval was superimposed upon a topographic map of the area. The altitude was determined at each grid intersection or node point, and a computer solution of the value of temperature and precipitation for each node was made by means of the previously developed equations. These values provided parameter estimates for more than 800 unsampled points. Then, using the measured altitudes and the estimated climatic values, figures 2, 3, and 4 were plotted on a drum plotter using the computer program THREE-D (California Computer Products, Inc., 1969).

Figures 2–4 effectively portray the distributions of altitude, temperature, and precipitation. It is not practicable, however, to obtain quantitative values from these figures. For this reason, the parameter values were converted to contours, lines of equal temperature,

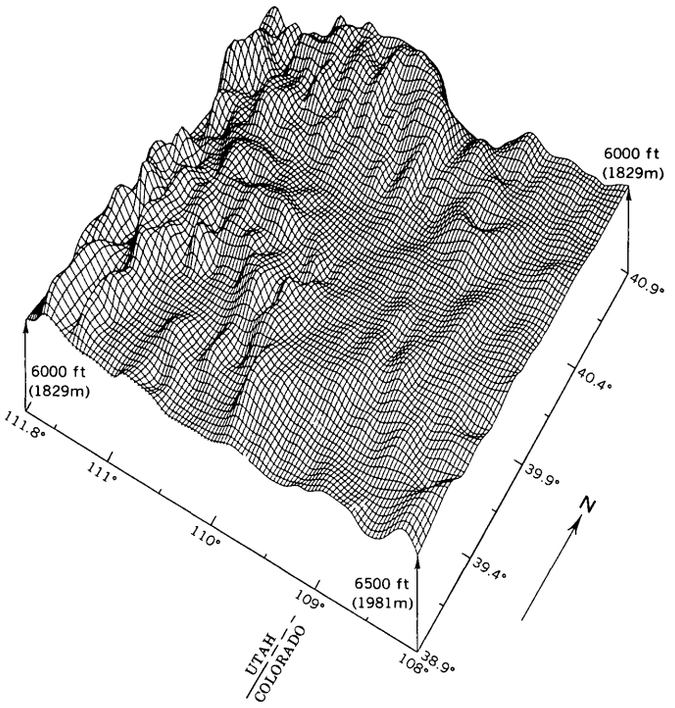

FIGURE 2.—Distribution of land-surface altitude.

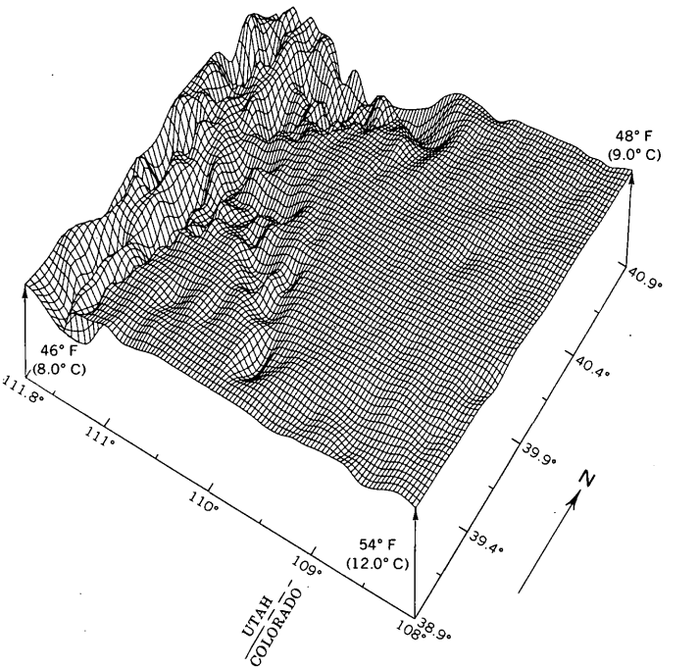

FIGURE 3.—Distribution of average annual temperature, 1941–70.

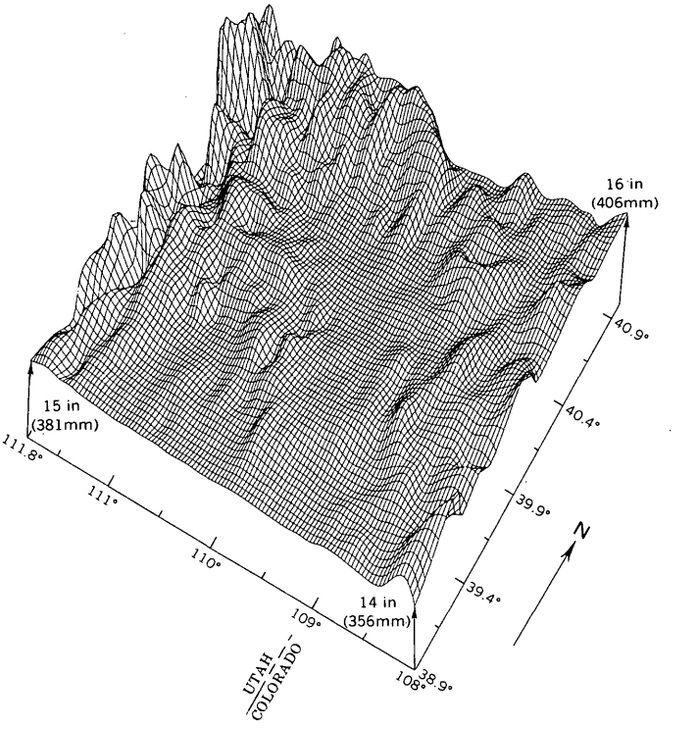

FIGURE 4.—Distribution of average annual precipitation, 1941–70. Each vector base is equal to 9 in (229 mm).

and lines of equal precipitation in figures 5, 6, and 7, which were plotted on a drum plotter by means of the computer program GPCP (California Computer Products, Inc., 1971).

The distributions in figures 2–4 are shown for an area within a range of 2° lat and 3.8° long. However, the east and west boundary values are poorly defined. Figures 5–7 show the lines of equal value within a range of 1.9° lat and 2.7° long, after the removal of the poorly defined fringe areas.

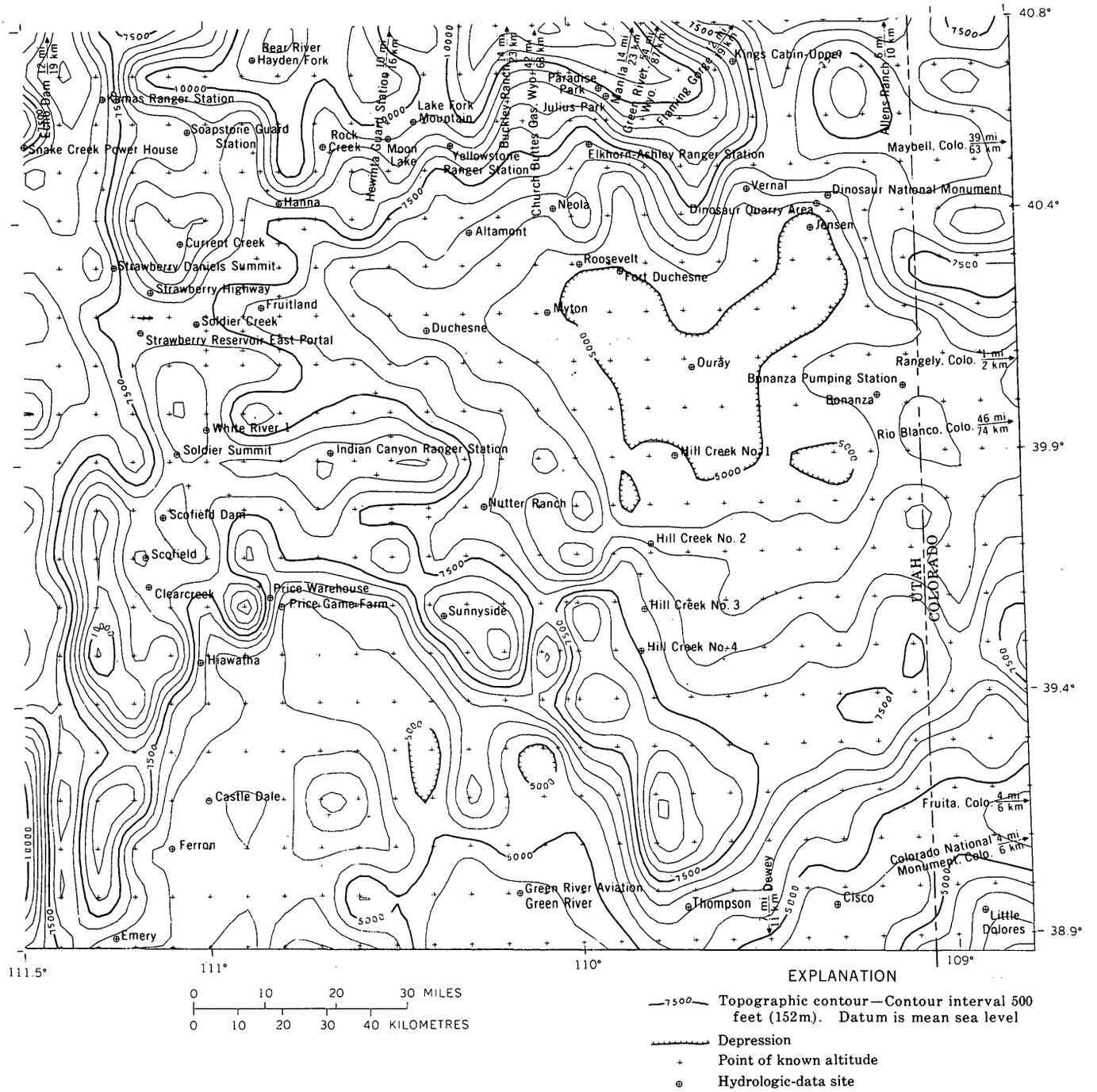

FIGURE 5.—Topographic map.

The lines of equal value in figures 5–7 were plotted on the basis of an analysis of eight neighboring values surrounding each grid intersection. The effect of the neighboring points is inversely related to the square of their distances from the node point, and the smoothness of the contours is directly related to the number of neighboring points considered (a user's option) in the grid analysis.

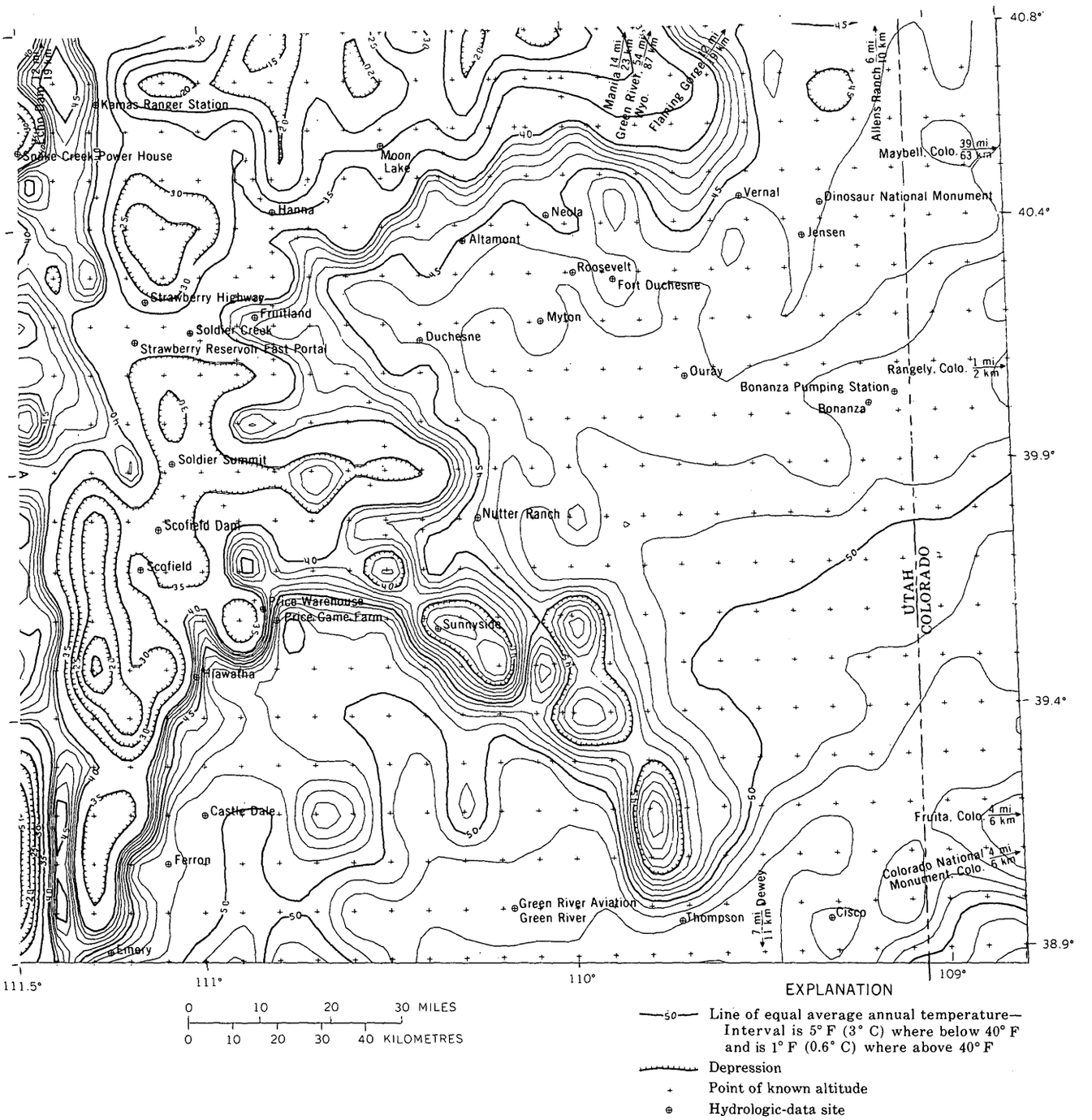

FIGURE 6.—Lines of equal average annual temperature, 1941–70.

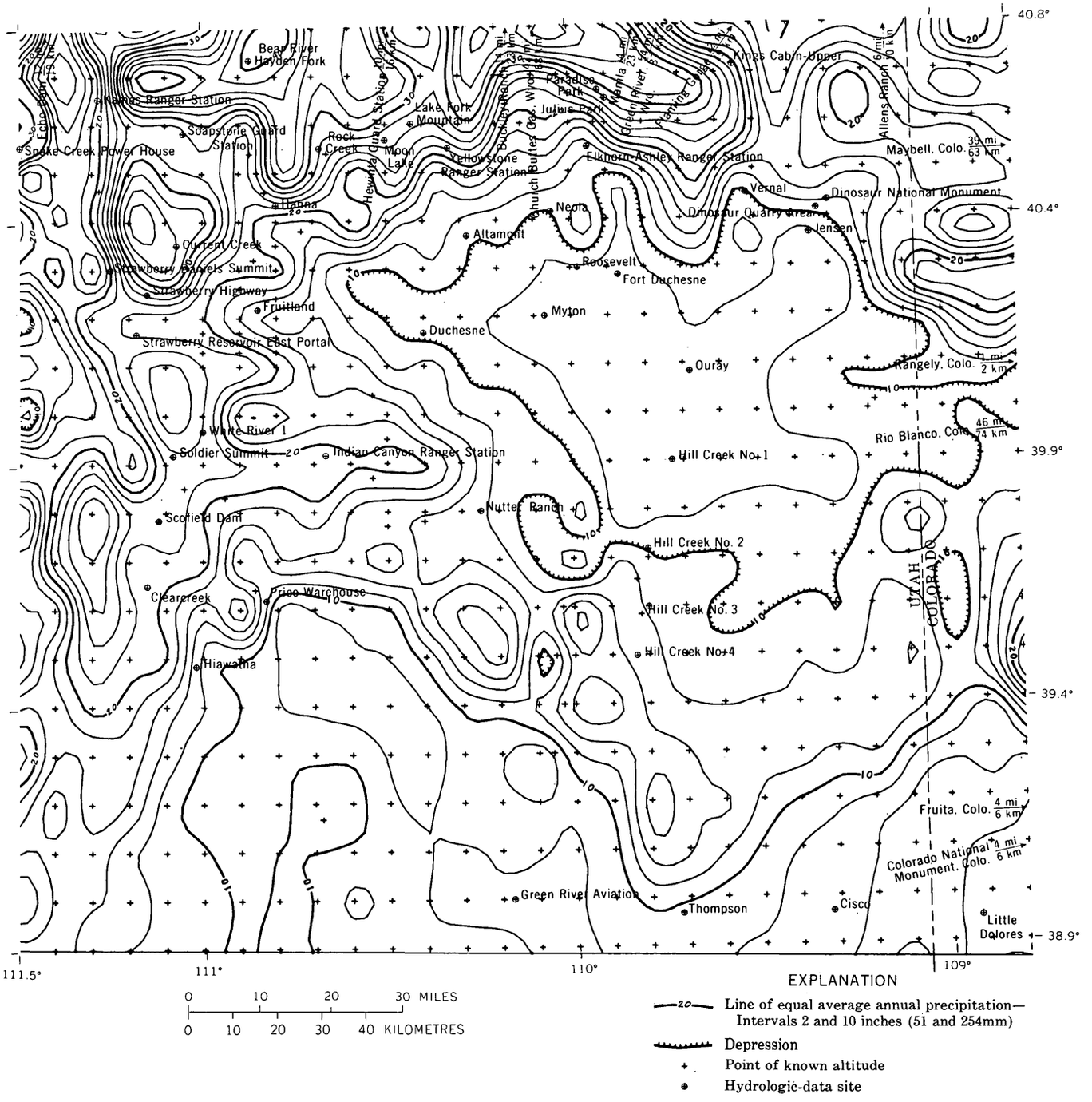

FIGURE 7.—Lines of equal average annual precipitation, 1941–70.

REFERENCES CITED

California Computer Products, Inc., 1969, THREE-D, A prospective drawing software system: Anaheim, Calif., California Computer Products, Inc., 45 p.

——— 1971, GPCP, A general purpose contouring program: Anaheim, Calif., California Computer Products, Inc., 129 p.

Esler, J. E., Smith, P. F., and Davis, J. C., 1968, KWIKR8, A Fortran IV program for multiple regression and geologic trend analysis: Kansas State Geol. Survey, 31 p.

Jour. Research U.S. Geol. Survey
Vol. 3, No. 2, Mar.–Apr. 1975, p. 137–148

DELINEATION OF BURIED GLACIAL-DRIFT AQUIFERS

By THOMAS C. WINTER, Denver, Colo.

Abstract.—Locating and delineating buried glacial-drift aquifers poses one of the major problems to hydrogeologists working in glacial terrain. To show the vertical and horizontal boundaries of aquifers, most techniques require a multiple set of maps, a fence diagram, or a combination of maps and sections. Calculations of the first two moments, mean and standard deviation, of a discontinuous distribution result in values that represent the center of gravity (mean position) and spread (standard deviation) of all the sand units in a drill hole. Data for the moment method consist of depth to center point and thickness of each sand unit. A 2,600 mi^2 (6,730 km^2) area in northwestern Minnesota that contained 71 test holes drilled to bedrock was used to test the usefulness of the moment method in glacial terrain. Plots of relative position of center of gravity and relative spread (calculated as percentage of total drift thickness) showed three groupings for relative center of gravity (shallow, 0–26 percent, medium, 30–55, and deep 58–72) and three for spread of sand units (narrow, 1–5 percent, medium, 8–19, and wide, 22–38). The resulting vertical-variability pattern map shows the areas of each of the nine combinations of these two factors. Because the vertical-variability map does not show quantity of sand, the map is most informative if the total thickness of sand, or percent sand of total drift thickness, is recorded by each hole location on the map. The center of gravity is useful for describing the vertical position of the principal sand in a drill hole because it lies within the principal sand unit in 34 of the 63 holes that contained sand, and it is within 15 percent (based on total drift thickness) of the principal sand unit in 22 of the remaining 29 holes.

Locating and delineating buried glacial-drift aquifers poses one of the major problems to hydrogeologists working in glacial terrain. Because of deposition unique to glacial processes, standard geologic-mapping methods developed for stratified rocks have often been inadequate.

Drift consists largely of till (an unsorted mixture of clay through boulder-size material) and stratified material which is generally clay through gravel size. Till is deposited (1) at the base of a glacier as it moves over an area, (2) at the terminus of a glacier where bodies of till, incorporated into the ice, slough off the melting glacier and pile up at its edge, or (3) as ablation till, which is supraglacial till that settles as the underlying ice melts. Stratified deposits, usually as outwash or ice-contact forms, are water-laid and, therefore, well sorted. The sediment-laden melt waters issuing from the glacier either drop their load immediately adjacent to the ice (ice contact) or carry the material beyond the ice where the diminishing competence of the flowing water results in deposition. The constantly changing water budget of glaciers results in greater or lesser quantities of melt-water flow and thus causes wide variations in sediment deposition. In addition, the courses of the streams shift continually, resulting in highly irregular shapes and thicknesses of stratified deposits, particularly of ice-contact deposits. Immediate burial of ice-contact stratified drift can take place by the sloughing bodies of till.

When a glacier melts, the resulting moraines usually contain a high percentage of buried sand and gravel, but in a highly irregular pattern of distribution. Thus, for practical purposes, the sand is considered to be randomly distributed both areally and vertically. In spite of this randomness in location, the environments of deposition suggest that correlation is justified over small distances, usually not more than several miles, or as much as 10 mi (16 km). The exception to this, of course, is the presence of large widespread outwash plains that are generally associated with interglacial or interstadial periods.

In areas of multiple glaciation, the deposits just described are covered by succeeding glaciers, which often completely destroy any surface expression of the older deposits. This concealment makes it extremely difficult to map drift aquifers as is demonstrated by the many techniques used by hydrogeologists working in glacial terrain. It is evident from the methods used that these techniques were originally used to map large, widespread sand bodies, buried outwash plains, or to map the distribution of all sands in a drift section. Successive glacial deposits, however, are shown effectively only by maps with accompanying sections, by fence diagrams, or by a number of maps.

The purpose of this paper is to review a number of the mapping techniques that have been developed and to compare their advantages and disadvantages. In addition, this paper presents a statistical approach to mapping, which objectively considers the distribution of all sands in a drift section. This method results in a

single map which depicts the areal and vertical distribution of sand within the entire volume of drift studied.

This report does not discuss methods of initially locating buried stratified drift. Usually, this is done directly only by test drilling and indirectly by geophysical prospecting methods such as earth resistivity. Even if geophysical methods are employed, test drilling is usually needed to prove the existence of an aquifer. Although a great many aquifers are found by chance, a basic requirement for locating an aquifer is an understanding of the glacial history of the area. This understanding leads to selection of target areas for prospecting that enhance the possibility of locating buried aquifers.

Acknowledgment.—Critical discussion of this paper by H. O. Pfannkuch, University of Minnesota, is greatly appreciated.

TECHNIQUES OF DELINEATING BURIED DRIFT AQUIFERS

Hydrologists have tried a number of methods of delineating (mapping) buried drift aquifers, including use of well-completion altitudes, well depths, correlation of glacial units, lithic percentage, and aquifer index maps. Other techniques that are used for delineation but also for quantitative description of aquifers include lithofacies clastic-ratio maps and transmissivity maps. There is considerable overlap between some of these techniques whether they are used for delineation or for description (largely concerning particle-size variation) of an aquifer. Undoubtedly, methods other than those discussed below have been developed. Those included here, however, give some idea of the variety of approaches.

Well-Completion-Altitude Method

Well-completion-altitude maps show areas where wells are completed at a common altitude. The completion altitudes are plotted on a map and groups of wells that have similar completion altitudes are delineated. The basic assumption for this type is that the wells are completed in a single aquifer zone. The technique is useful only for delineating extensive sand units, those most likely to be buried outwash plains. The smaller local sand units, those that are considered to be randomly distributed, are essentially ignored. Where the technique was used fairly extensively in parts of Minnesota (Winter, Maclay and Pike, 1967), an area was not delineated unless sand and gravel occurred at the given altitude in at least one well log in the area. To be illustrated effectively, results must be shown on a map with accompanying sections (fig. 1).

Advantages of the well-completion-altitude method are that the maps can be constructed rather quickly after a well inventory of an area and that reconnaissance-type well scheduling provides most of the basic data—few well logs are needed. Anderson (1968) used a similar technique to discuss the concentration of aquifer zones in Island County, Wash., but he did not delineate the aquifer zones on a map.

Well-Depth Method

The well-depth method is similar to that of well-completion altitudes. Again, after a well inventory, the depths of wells are plotted on a map and areas where wells are completed at a common depth range

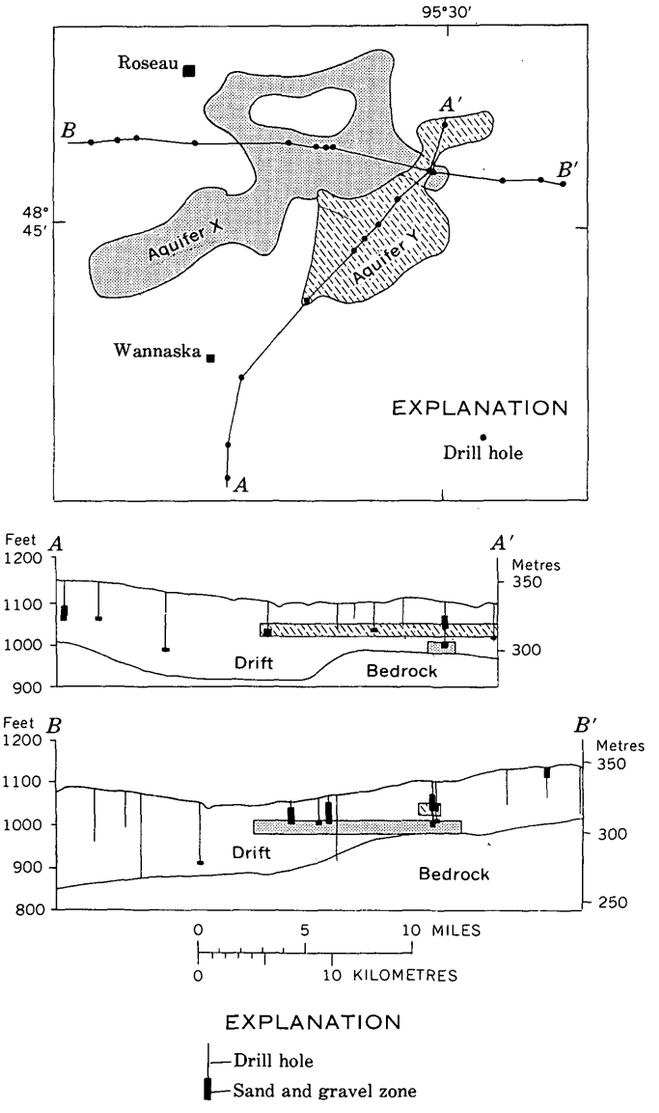

FIGURE 1.—Aquifers delineated by well-bottom altitudes and drill logs in the Roseau River watershed, Minnesota. Modified from Winter, Maclay, and Pike (1967).

are delineated. If the land surface is flat, the well-depth map is essentially a well-completion-altitude map. Where the terrain is hummocky, as in an end moraine or an ice-collapse topography, the well depths usually indicate only that within a certain depth sufficient sand occurs in the drift in which a well can be completed for domestic use. This type of mapping is especially useful in reconnaissance studies because only well-inventory data are needed—logs are not essential. Well-depth maps should not be considered aquifer maps as specific aquifers are not delineated, except by chance. The well-depth maps are useful, however, because they give some idea of the range one must drill in order to intercept a sand and gravel unit adequate for a domestic water supply. The technique has been used extensively in reconnaissance studies in Minnesota (fig. 2).

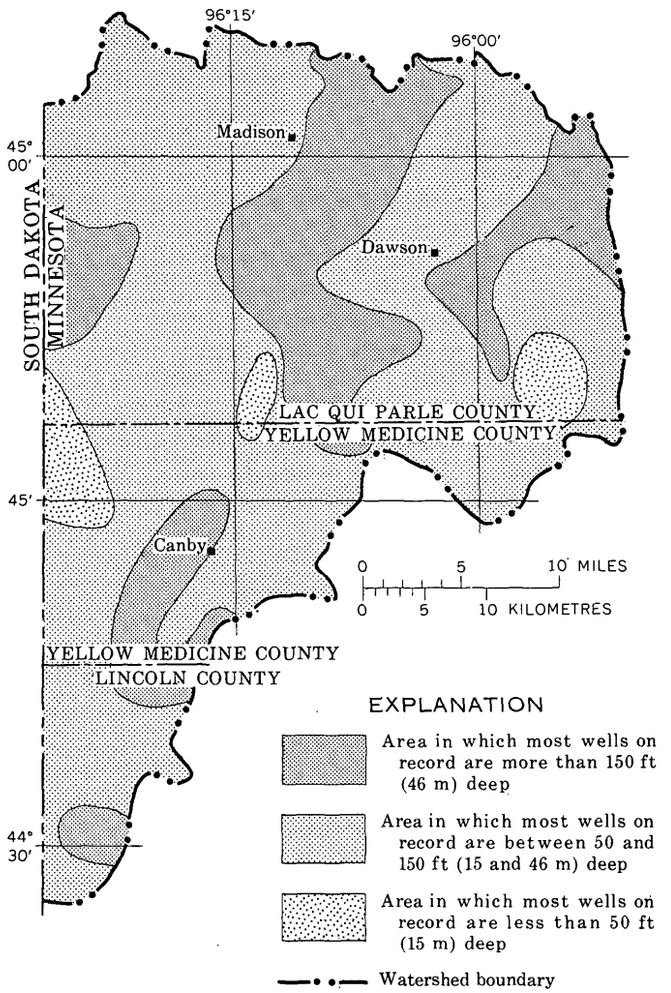

FIGURE 2.—Depth of wells in the Lac Qui Parle River watershed, Minnesota. From Cotter and Bidwell (1968).

Correlation Method

Because tills generally have readily observed diagnostic characteristics, they usually can be correlated more easily than sand and gravel. Moreover, if enough data exist on the physical and chemical characteristics of the till, such as color, particle-size distribution, particle shape, pebble lithology, clay-mineral and heavy-mineral content, and soluble material, these characteristics can be correlated over rather large distances. Unlike the previously discussed techniques, a considerable quantity of geologic data is necessary in order to attempt this type of mapping. In the Mesabi Iron Range area of Minnesota (Winter, Cotter, and Young, 1973) tills were mapped and samples were collected from the open-pit mines. After the tills were characterized, they were correlated throughout the area of the mines and then identified in numerous drill holes south of the open-pit mine area. By correlating and mapping the tills, the interlayered sand and gravel bodies were then delineated and isopach maps were drawn to show the volume of aquifer that exists at various stratigraphic intervals (Winter, 1973). (See figure 3.) As in the well-completion-altitude method, only the large, interglacial outwash units are of interest. Information on the small, randomly distributed sands is ignored. To illustrate the results of a correlation-method study effectively, a set of maps, a fence diagram, or a map with accompanying sections must be constructed.

Rosenshein (1962) also correlated drift units over rather large distances and thus was able to show widespread distribution of sand in northwestern Indiana. Although his report contains a number of sections, it does not include a map showing areal configuration of the aquifers.

Delineation by correlation, a standard geologic-mapping approach to delineating specific stratigraphic units, is often illustrated by fence diagrams. The advantage of fence diagrams is that they effectively portray a three-dimensional view of a volume of material. Being simply a number of connected sections, however, they have the disadvantage of showing only what is present along the lines of section and the shape of the unit of interest in the intervening volumes must be inferred. Fence diagrams are useful when mapping rather simply shaped units, such as channel sands or linear units (Winter, 1967), but are difficult to interpret when they are used to illustrate highly irregular complex sand units (Thompson, 1965).

Lithic-Percentage Method

Maps showing the areal variability of the percentage of sand in drift are common. In areas of relatively thin

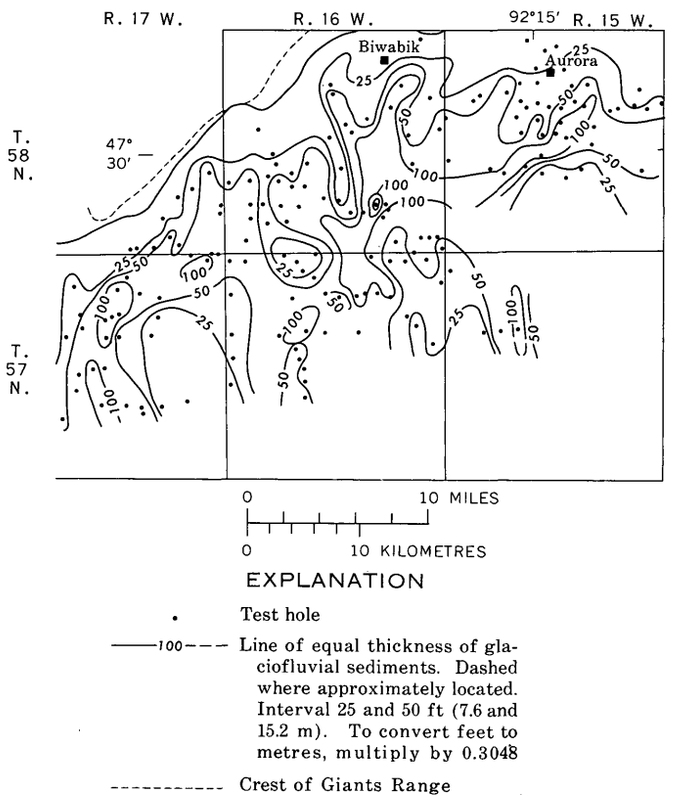

FIGURE 3.—Thickness of glaciofluvial sediments between bouldery and surficial tills in the eastern Mesabi Iron Range area, Minnesota. From Winter (1973).

drift, drill holes generally penetrate the entire section. In such areas, the percentage of sand in the section is calculated and the data are plotted on a map and contoured. Because few wells penetrate the entire section in areas of thick drift, the percentage of sand for the unpenetrated part of the drift section is a major unknown and some arbitrary thickness, such as the upper 200 ft (61 m) of drift, must be defined in order to use this method. The difficulty with such an approach is that it does not delineate specific aquifers or show the vertical stratigraphic position of the sand and gravel units. For example, a given amount of sand could be scattered as many individual units throughout the entire drift section, or it could be concentrated in one unit somewhere within the drift section. The lithic-percentage method also requires that log information be available.

Aquifer-Index Method

Twenter and Knutilla (1972) developed an "aquifer index" to differentiate the drift in Oakland County, Mich. The index is a composite of numbers assigned to rock types and modifiers: for example, sand (rock type), gravelly (modifier), and coarse grained (modifier). The resulting number is a reflection of the percentage of aquifer-like material in a drill hole and, therefore, is an indication of the water-yielding ability of the drift.

Twenter and Knutilla illustrated their results by a series of slice maps (fig. 4), each representing successive 50-ft (15.2-m) depth intervals of the drift. The slice maps provide insight into the vertical dimensions of the various units. Although individual aquifers are not delineated, the aquifer-index map gives a good picture of the variation in drift texture. By using data from all the units, the small randomly distributed sands are considered as well as the large extensive units. Good descriptive drill logs are necessary in order to use this method effectively.

Lithofacies, Clastic-Ratio Method

Pettyjohn and Randich (1966) classified particle-size data using lithofacies and clastic-ratio trilinear

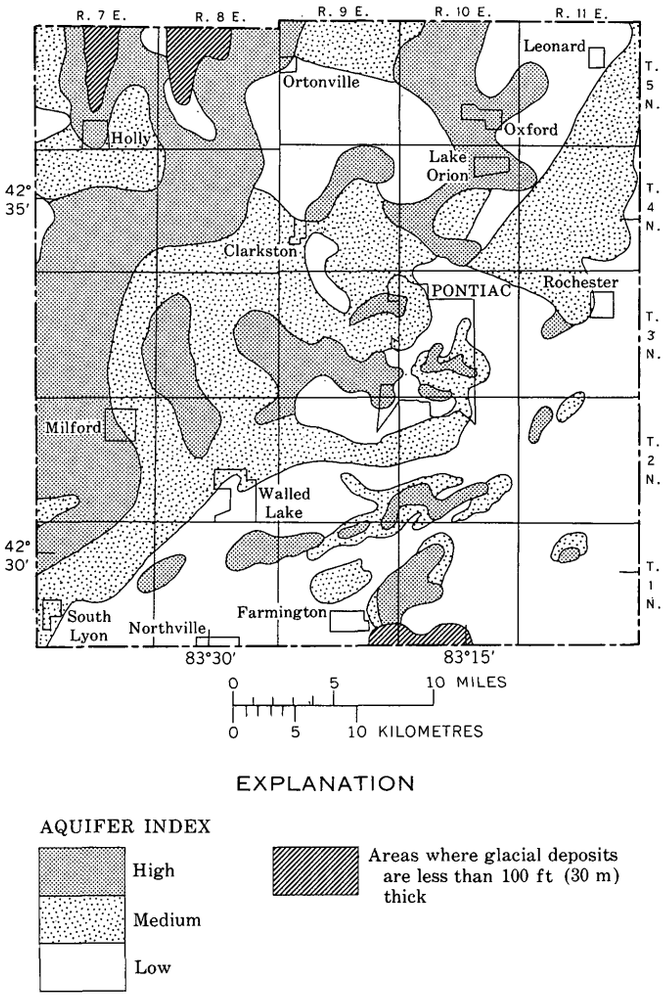

FIGURE 4.—Aquifer index of material from 50 to 100 ft (15–30 m) below land surface in Oakland County, Mich. From Twenter and Knutilla (1972).

graphs. Nine lithofacies categories and six coarse-fine ratio lines were taken from the graphs and displayed in the form of slice maps (fig. 5). This figure shows that the aquifer material is clearly delineated and that the delineation can be dependent upon any specified textural type. That is, if sand is defined as the aquifer, the line delineating the sand can be used as the boundary. If silty sand is defined as the aquifer, the line delineating silty sand can be considered the delineation or the boundary of the aquifer. By using successive slice maps, the vertical dimension of the aquifers can be shown to a certain degree. An advantage of this method is that textural variation within the aquifer can be shown as well as the boundary. The lithofacies, clastic-ratio method requires laboratory data on particle sizes of drill-hole samples; however, such data are often unavailable.

Transmissivity Method

Delineation of buried drift aquifers by the transmissivity method is similar to the lithofacies clastic-ratio method, but it is less precise. Instead of classifying the material by trilinear graphs, hydraulic conductivity (permeability) values are assigned to various grain sizes in a section or drill hole. This value is then multiplied by the thickness of the various units. The total transmissivity of the section is the sum of the transmissivities of the individual units. This value is recorded by the hole location on a map and the transmissivity values are delineated by lines of equal value (fig. 6). The boundary of an aquifer depends on the transmissivity line chosen for a particular study. As transmissivity maps are basic for ground-water flow modeling, this method has been used widely. (See Lindholm, 1970; Helgesen, 1973; and Winter, 1973.) Most transmissivity maps do not show the vertical position of the sand units. An advantage of both the lithofacies clastic-ratio and the transmissivity methods is that they give information on areal variation in texture in addition to the delineation of the boundary of the aquifer. As transmissivity is a function of both hydraulic conductivity and thickness, however, a thickness map is needed if information on areal variation of texture is to be obtained.

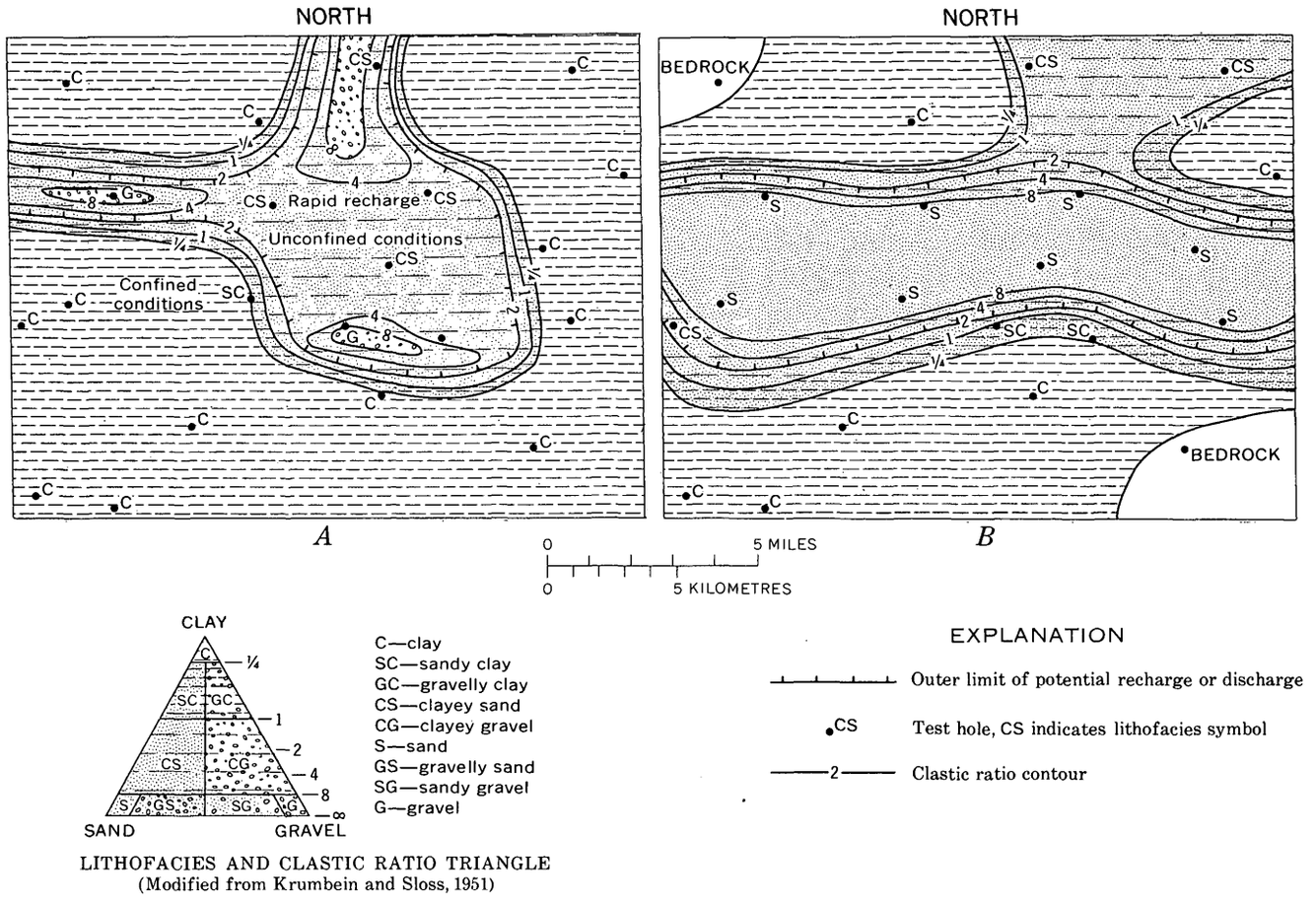

LITHOFACIES AND CLASTIC RATIO TRIANGLE
(Modified from Krumbein and Sloss, 1951)

FIGURE 5.—Variation in composition of drift with depth below land surface near Minot, N. Dak. *A*, Interval, 0 to 50 ft (15 m). *B*, Interval, 50 to 100 ft (15–30 m). From Pettyjohn and Randich (1966).

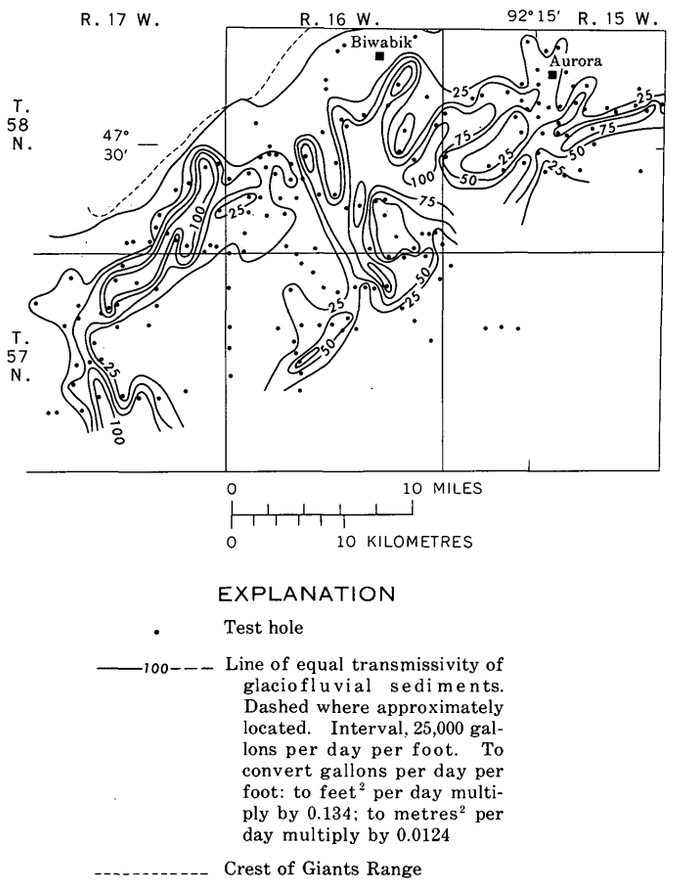

FIGURE 6.—Transmissivity of glaciofluvial sediments between bouldery and surficial tills in the eastern Mesabi Iron Range area, Minnesota. From Winter (1973).

Generally, transmissivity maps are constructed for individual aquifers of known extent. For some studies, however, a transmissivity map is constructed for the entire drift section; in these maps individual aquifers are not delineated, but data from all sand units are used.

A STATISTICAL APPROACH TO MAPPING THE DISTRIBUTION OF AQUIFERS IN DRIFT

Forgotson (1960) classified quantitative stratigraphic maps into the following five categories: (1) structure and topographic maps, (2) thickness maps, (3) facies maps, (4) vertical-variability maps, and (5) maps based on either a statistical analysis or other kind of mathematical treatment of a contour map. It is evident from the preceeding discussion that hydrogeologists have preferred some variation of his type-3 maps which describe the composition of a stratigraphic unit. Percentage and transmissivity maps are included with facies maps in this category. Each of the techniques for delineating buried drift aquifers has its particular advantages and disadvantages. A disadvantage common to all is that a three-dimensional picture of the subsurface cannot be presented without a series of maps or a map and accompanying vertical sections. A technique is needed that shows the vertical variability of sand and gravel units within a section allowing a three-dimensional picture to be presented on a single two-dimensional map. A statistical technique that satisfies this need was developed by Krumbein and Libby (1957); it involves computation of the weighted mean position (vertically) and of the spread of all the sand units in a drill hole. They constructed a map of the areal and vertical distribution of Cretaceous sands in north-central Wyoming to illustrate the method. The vertical-variability map that they developed was based on statistical moments that express the position of the sand units as a continuous variable. The first moment is the weighted mean position of all the sand units and is termed the center of gravity. The second moment is the average dispersion, or the standard deviation, of the sand units within the section. The third moment is skewness, a measure of the deviation from the normal distribution of the sand distribution. A composite map of center of gravity and dispersion shows, for example, areas where sands occur high in the section with small spread, low in the section with small spread, and in any number of combinations of center of gravity and spread.

Because of the random distribution of sand units within glacial drift, a statistical method of mapping those units seems most appropriate. An area in northwestern Minnesota that had been mapped geologically by conventional correlation methods (Maclay, Winter, and Bidwell, 1972) was selected to test the usefulness of the vertical-variability method.

Application of the Vertical-Variability Method in Northwestern Minnesota

The northwest corner of Minnesota was chosen to test the vertical-variability method because an extensive drilling program there resulted in 71 test holes being drilled to bedrock. These holes were spaced rather uniformly over about 2,600 mi² (6,730 km²). In this area, glacial drift overlies stratified sedimentary rock, chiefly Cambrian to Ordovician sandstones and limestones in the western part and Precambrian crystalline rock in the eastern part. Drift thickness in the area (fig. 7) is generally between 200 and 400 ft (61 and 122 m). The composition of the drift is largely silty, clayey, calcareous till that contains numerous limestone, dolomite, and shale pebbles in addition to large quantities of Precambrian crystalline rocks, such as granite and metasedimentary rocks. The till

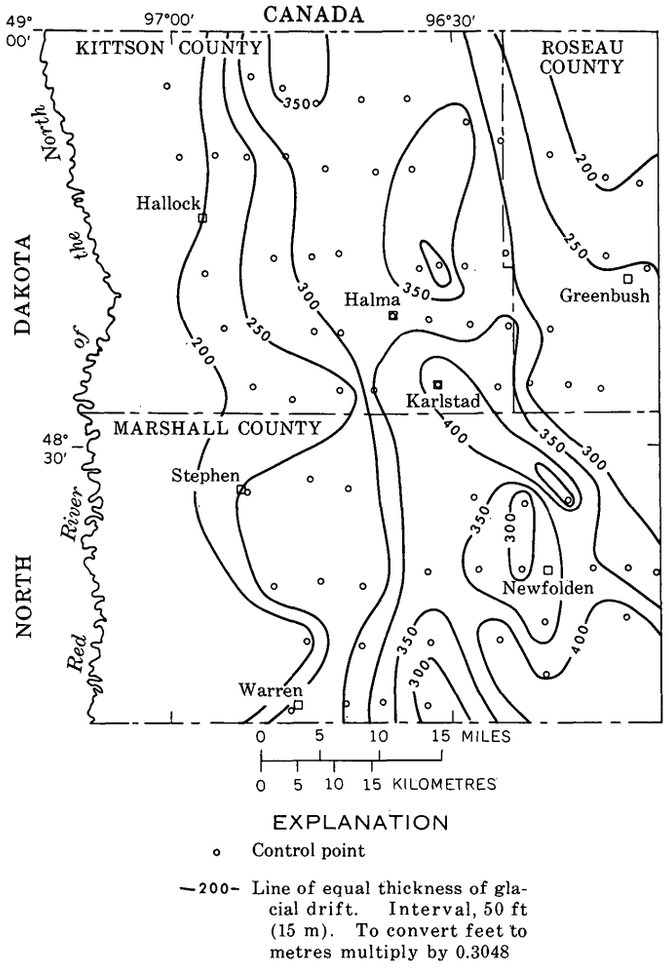

FIGURE 7.—Thickness of drift in northwestern Minnesota.

is interlayered with glacial lake deposits and in the western part is overlain by deposits of glacial Lake Agassiz.

Data collection and calculations

The test holes were logged descriptively and geophysically. Samples were collected at 5-ft (1.5 m) intervals by a geologist at the drill site. The samples were sieved and pebble counts were made of the tills. Basic data for calculation of the statistical measures are: (1) the distance from the top of the hole to the center point of a sand unit, and (2) the thickness of that sand unit. For this study, only units greater than 2 ft (0.6 m) thick consisting of sands of fine sizes and greater were used. Silty fine sands were not considered aquifer material. Calculations were made according to the following equations (Krumbein and Libby, 1957):

$$CG = \frac{\Sigma x_i t_i}{\Sigma t_i},$$

$$SD = \frac{\Sigma x_i^2 t_i - \frac{(\Sigma x_i t_i)^2}{\Sigma t_i}}{\Sigma t_i} + \frac{\Sigma t_i^3}{12\Sigma t_i},$$

and

$$SK = \frac{\Sigma x_i^3 t_i + \frac{\Sigma x_i t_i^3}{4}}{\Sigma t_i},$$

where CG = center of gravity,
SD = standard deviation,
SK = skewness,
x_i = distance from land surface to the center point of the sand unit, and
t_i = thickness of the sand unit.

Krumbein and Libby cautioned about the use of skewness because they said it would be very sensitive to operator effects, depending on the omission or inclusion of the sands near the top or bottom of the stratigraphic unit. Because of this, they did not show skewness for the Wyoming data. Skewness was calculated for northwestern Minnesota data, however, to determine what values could be expected as typical of various sand distributions. The sign of the skewness value indicates on which side of the mean (above or below in this case) the bulk of the sand units are located.

Discussion

A plot of relative center of gravity (the center of gravity divided by total drift thickness) of sand in the drift of northwestern Minnesota (fig. 8) shows several possible groupings, but for convenience three are considered reasonable: shallow (0–26 percent of the total drift thickness), medium (30–55 percent), and deep (58–72 percent). A plot of relative standard deviation of the sand units (fig. 8) shows three clearly defined groups: narrow (1–5 percent of the total drift thickness), moderate (8–19 percent), and wide (22–38 percent. Maps were constructed of each of the two parameters and were overlaid to develop the composite vertical-variability map (fig. 9). Areas were not delineated in figure 9 unless at least two adjacent locations showed the same pattern; that is, they had the same combination of center of gravity and dispersion. This limitation assures some justification for depicting an areal extent for a given aquifer zone. It must be emphasized that the patterns in a vertical-variability map do not necessarily represent specific aquifers; in a strict sense, the patterns represent a quantitative statement that the sands in an area exhibit a similar vertical statistical distribution.

Because a vertical-variability map shows the distribution of aquifers nearly everywhere within an area, it is a useful guide for further prospecting. For example, prime target areas for potential groundwater supplies are areas where the center of gravity

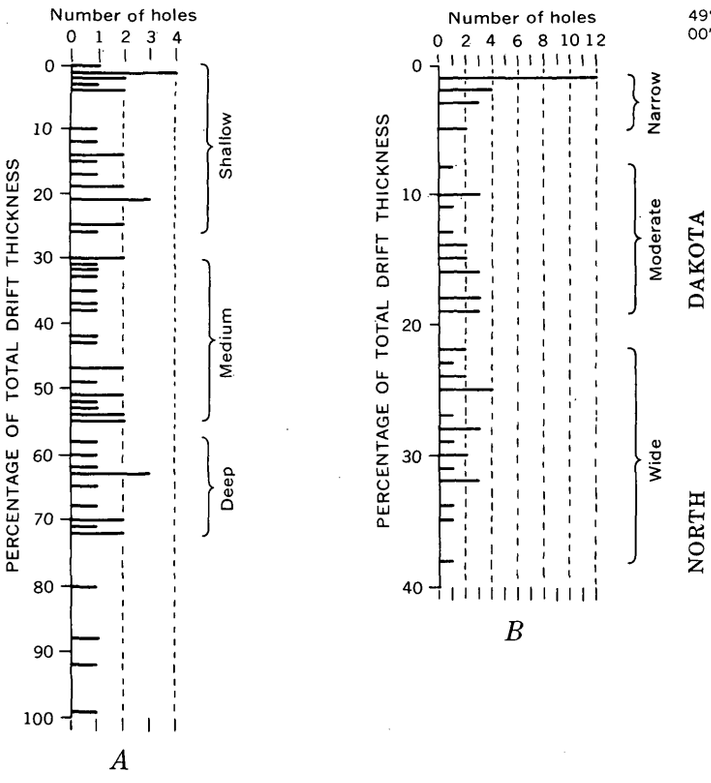

FIGURE 8.—Relative center of gravity (*A*) and relative standard deviation (*B*) of sand units in the drift of northwestern Minnesota. The percentage value is obtained by dividing the value of the center of gravity or the standard deviation by total drift thickness for each hole.

is shallow and the standard deviation is narrow. These conditions indicate, of course, that the majority of the sands are clustered within a fairly narrow zone near the land surface. If the relative center of gravity is too shallow, however, a degree of caution is warranted because in northwestern Minnesota these are usually beach-ridge aquifers that are partly unsaturated. Therefore, areas of closely grouped deeper sands might be better prospects for water supplies. An area of clustered, moderate-depth sands occurs in the central part of Kittson County from the Hallock area to about 10 mi (16 km) east of Hallock. A deep zone of sands, clustered closely together, occurs in west-central Roseau County and east-central Kittson County.

One of the drawbacks of a vertical-variability map is that it does not indicate the total thickness of sand or the number of sand units that occur in the drill hole. Therefore, it is useful to supplement or combine a vertical-variability map with another map, such as a number-of-sand-units map or a relative-thickness-of-sands map. A comparison of the number-of-sands map (fig. 10) with the vertical-variability map shows that the areas of narrow spread are esssentially the areas

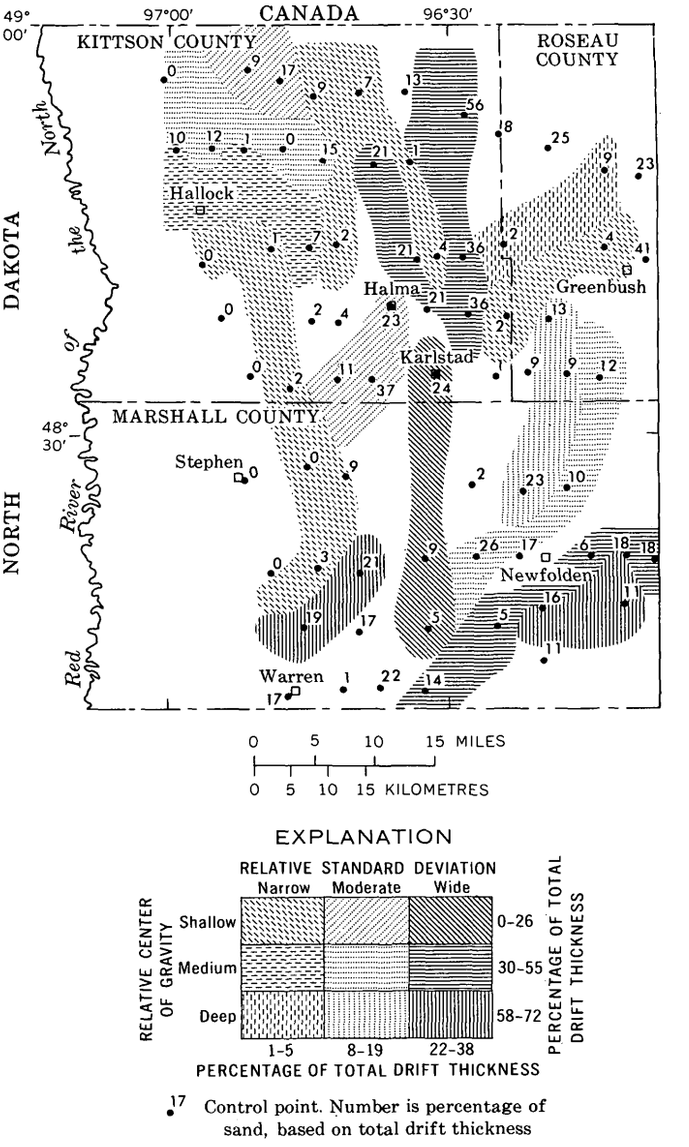

FIGURE 9.—Distribution of sand units in the drift of northwestern Minnesota.

where only one sand occurs in the drill hole. In the areas of medium to wide standard deviation, the number of sand units generally ranges from 2 to 5. Perhaps the most useful combination of maps is the vertical-variability map and a map showing the percentage of sand in the total drift section. Together these two maps show the most probable areas for penetrating an aquifer—those where percentage of sand is great, center of gravity is high, and standard deviation is narrow. Such an area occurs in the southern part of Kittson County from Halma southward to west of Karlstad. In this area, the sands are shallow and have a moderate relative standard deviation, and the percentage of sand ranges from 11 to 37. In

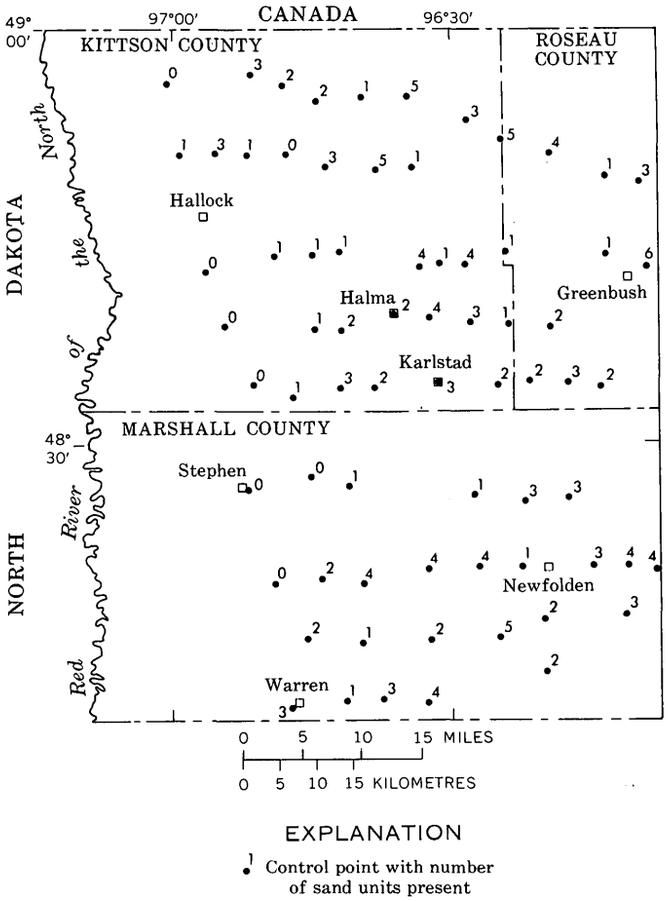

FIGURE 10.—Number of sand units in the drift of northwestern Minnesota.

two other areas, adjacent to each other, in southwestern Roseau and north-central Marshall Counties, the sands occur at a medium and at a deep relative center of gravity, have moderate disperson, and have percentages of sand ranging from 9 to 26.

Comparing the map of northwestern Minnesota developed by statistical methods with that developed by conventional correlation methods, it is of interest that the Halma area mentioned above does overlie a major aquifer. A drilling program undertaken after the one on which the data for this paper is based resulted in delineation and testing of perhaps the most prolific aquifer in northwestern Minnesota (Schiner, 1963; Maclay and others, 1972). An area of note and also of some economic importance is the area in eastern Kittson County that shows medium relative depth of sands with a wide standard deviation. This area also contains a relatively large percentage of sand (21–57 percent). The western arm of this area is part of the Halma–Lake Bronson aquifer.

The vertical-variability-map approach was used by Domenico and Stephenson (1964) to describe the distribution of sand in the alluvial basin at Las Vegas, Nev. They also noted the need to combine the vertical-variability map with a lithic-percentage map or lithic-ratio map to provide maximum information.

One of the difficulties of using the vertical-variability mapping method for aquifer prospecting is that the calculated center of gravity does not necessarily fall within a significant sand unit. For example, if sands of equal thickness occur at the top and bottom of a section, the center of gravity falls halfway between the sands and could possibly be hundreds of feet away from either sand. Although calculating the center-of-gravity is not intended as a method of locating specific aquifers, it is of interest to see how well it does this. The numerator of the values listed in figure 11 is the distance from the center of gravity to the nearest boundary of the thickest sand in each drill hole and the denominator is the percentage of hole depth (based on total drift thickness) represented by that distance. The center of gravity is within the principal sand unit in 34 of the 63 holes that penetrated sand units (figure 11). Nineteen of these holes have only one sand unit and, of course, the center of gravity is a perfect predictor. In 15 of the remaining 29 holes, the center of gravity is within 10 percent (based on total drift thickness) of the principal sand unit. In 22 of the 29 holes, the center of gravity is within 15 percent of the total drift thickness and in 28 of the 29, it is within 25 percent.

When dealing with interpretations based on parameters such as statistical moments, Sharp (1973) points out that additional knowledge about the physical distribution of units can be extracted by an additional calculation. The parameter, based on information theory (Shannon and Weaver, 1963), is a measure of the information content of any message and is calculated as follows:

$$D(n) = \sum_{i=1}^{n} f_i \log_a f_i$$

where $\sum_{i=1}^{n} f_i = 1$

and D = dispersion, entropy, or information content,
f_i = fraction of the total distribution found in the ith interval,
a = base of logarithms used, and
n = number of equally spaced intervals the distribution has been divided into.

For this paper, the equally spaced interval used is 10 and the data is the amount of sand in each 10 percent of total thickness interval. Logarithms to the base 10 are then used for the calculations. The in-

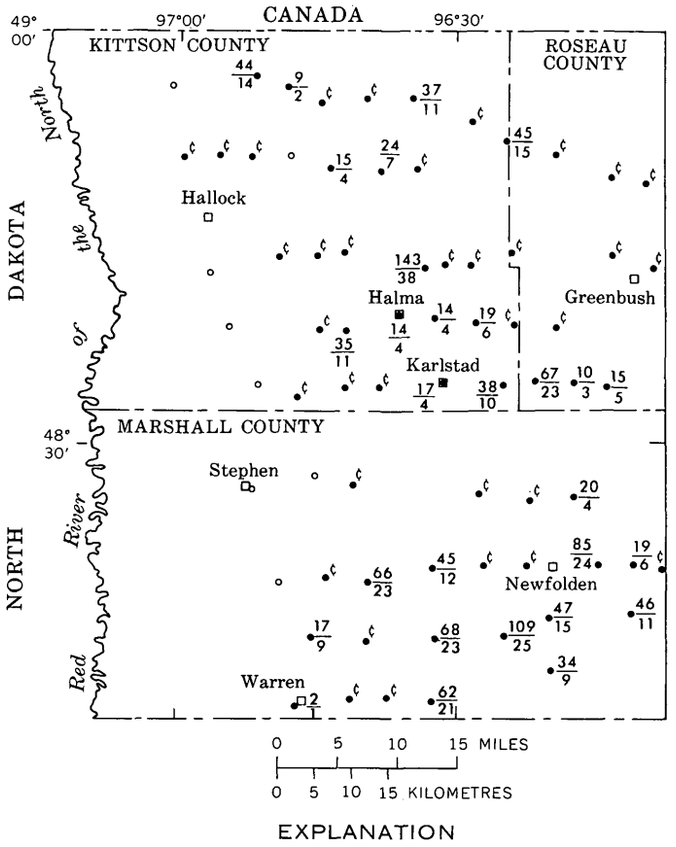

FIGURE 11.—Amount of error in predicting position of principal sand unit from center of gravity, northwestern Minnesota.

formation content (D) of Shannon and Weaver (1963) is essentially a measure of how consistent to the normal distribution are the positions of the sand units in a section. As discussed previously, for sands of equal thickness at the top and bottom of a section, the statistical moments are a poor descriptor of the sand unit distribution. Calculation of the D value would clearly show a low value, about 0.3, and a better picture of the distribution of sand units is thus obtained. By contrast, a D value of 1 indicates that the distribution of sand units is very close to the normal distribution. A D value of 0 is obtained if there is only a single sand in the drill hole.

In northwestern Minnesota, the D value of sand distribution in drift ranges from a low (excluding the zeroes) of 18 to a high of 77 (fig. 12). A comparison of the vertical-variability map with the D value, shows that the areas of wide standard deviation generally have the highest values; it is particularly interesting to note that the area of medium center of gravity and wide standard deviation in eastern Kittson County has the highest average D value, from 60 to 77.

Another attempt to describe the statistical distribution of certain types of data was made by Sharp and Fan (1963). This index, termed the sorting index, is virtually the reciprocal of Shannon and Weaver's information content (D value).

COMPARISON OF TECHNIQUES USED TO DELINEATE BURIED GLACIAL-DRIFT AQUIFERS

The advantages and disadvantages of the various techniques of delineating buried glacial-drift aquifers are summarized in table 1. All the techniques require a considerable amount of work in constructing maps or cross sections. The principal advantage of the well-completion-altitude and well-depth methods is that they can be prepared from minimal field data after a quick reconnaissance. Basic data are largely well depths and a few driller's logs. The aquifer-index, lithofacies and clastic-ratio, and transmissivity meth-

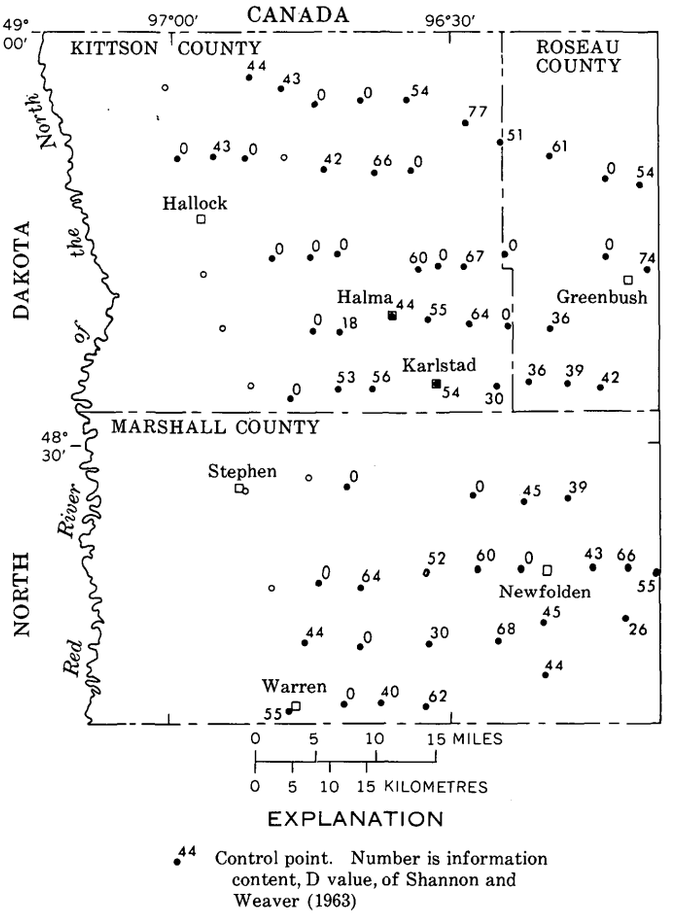

FIGURE 12.—Information content, D value, of sand-unit distribution, northwestern Minnesota.

ods are useful if areal variation in grain size (texture) is to be mapped. This, of course, requires a large amount of reliable information on grain size either in the form of sieve data or descriptive well logs. In all these methods the vertical dimension of sand units can be depicted only by multiple illustrations.

The major advantages to the statistical approach, none of which are confined to this approach, are that (1) it objectively considers all pieces of data; that is, it takes into consideration every sand unit penetrated, and (2) the results show, on a single map, both the depth distribution and the areal distribution of sand units. An additional advantage is that such a map can be constructed rapidly. One merely needs the drill logs to obtain the data and, once coded, the computer calculates all the information that is needed, resulting in a very quick evaluation of drill-log data. The statistical method, as viewed by this writer, is not a substitute for other mapping methods but is a useful reconnaissance tool to be used during the course of a project to guide further prospecting and aquifer delineation.

TABLE 1.—*Comparison of methods of delineating drift aquifers*

Method	Advantages	Disadvantages
1. Well-completion altitude	Can be constructed from well-depth data from an inventory—few logs are needed.	Delineation of an aquifer is somewhat nebulous—is based on the assumption that wells completed at similar altitudes are in the same aquifer.
	Results in an attempt to delineate specific aquifer zones.	To show boundaries of aquifer, needs a series of maps or a map and sections.
		Does not consider texture.
2. Well depth	Can be constructed from well depth data from an inventory—few logs are needed.	Does not result in delineation of individual aquifers—simply states approximate depth range at which an adequate supply of water can be obtained.
		To show boundaries of aquifer, needs a series of maps or a map and sections.
		Does not consider texture.
3. Correlation	Results in fairly detailed delineation of specific aquifer zones.	Needs a large amount of good geologic data; drill logs, mineralogy, particle size.
		To show boundaries of aquifer, needs a series of maps or a map and sections.
		Does not consider texture.
4. Lithic percentage	Gives good general knowledge of areal variability of sand distribution. Considers all data.	Needs a fair number of well logs.
		Does not show vertical distribution of sand.
		Does not consider texture.
5. Aquifer index	Provides information on the variation of textural composition of drift.	Needs good descriptive drill logs.
		To show boundaries of aquifer, needs a series of maps or a map and sections.
	Considers all data.	Does not result in delineation of individual aquifers.
6. Lithofacies clastic-ratio	Shows areal variation in lithology in addition to delineation of aquifer.	Needs a large amount of particle-size data.
	Considers all data.	To show boundaries of aquifer, needs a series of maps or a map and sections.
7. Transmissivity	Shows areal variation in lithology (if thickness map is presented) in addition to delineation of aquifer.	Needs good descriptive drill logs or geophysical logs if estimates of hydraulic conductivity are to be reasonable.
	Considers all data.	To show boundaries of aquifer, needs a series of maps or a map and sections.
8. Vertical-variability map	Considers all sand-location data	Does not precisely delineate individual aquifers.
	Can show vertical distribution of sand in addition to areal dimensions.	Needs good drill logs.
		Does not consider texture.

REFERENCES CITED

Anderson, H. W., Jr., 1968, Ground-water resources of Island County, Washington: Washington Dept. Water Resources Water Supply Bull. 25, pt. 2, p. 35–317.

Cotter, R. D., and Bidwell, L. E., 1968, Water resources of the Lac Qui Parle River watershed, southwestern Minnesota: U.S. Geol. Survey Hydrol. Inv. Atlas, HA–269.

Domenico, P. A., and Stephenson, D. A., 1964, Application of quantitative mapping techniques to aid in hydrologic systems analysis of alluvial aquifers: Jour. Hydrology, v. 2, p. 164–181.

Forgotson, J. M., Jr., 1960, Review and classification of quantitative mapping techniques: Am. Assoc. Petroleum Geologists Bull., v. 44, no. 1, p. 83–100.

Helgesen, J. O., 1973, Appraisal of ground water for irrigation in the Little Falls area, Morrison County, Minnesota: U.S. Geol. Survey Water-Supply Paper 2009–D, 40 p.

Krumbein, W. C., and Libby, W. G., 1957, Application of moments to vertical variability maps of stratigraphic units: Am. Assoc. Petroleum Geologists Bull., v. 41, no. 2, p. 197–211.

Krumbein, W. C., and Sloss, L. L., 1951, Stratigraphy and sedimentation: San Francisco, Freeman and Co., 497 p.

Lindholm, G. F., 1970, An appraisal of ground water for irrigation in the Wadena area, central Minnesota: U.S. Geol. Survey Water-Supply Paper 1983, 56 p.

Maclay, R. W., Winter, T. C., and Bidwell, L. E., 1972, Water Resources of the Red River of the North drainage basin

in Minnesota: U.S. Geol. Survey Water-Resources Inv., WRI 1–72, 129 p.

Pettyjohn, W. A., and Randich, P. G., 1966, Geohydrologic use of lithofacies maps in glaciated areas: Water Resources Research, v. 2, p. 679–689.

Rosenshein, J. S., 1962, Geology of Pleistocene deposits of Lake County, Indiana *in* Geological Survey research 1962: U.S. Geol. Survey Prof. Paper 450–D, p. D127–D129.

Schiner, G. R., 1963, Ground-water exploration and test pumping in the Halma–Lake Bronson area, Kittson County, Minnesota: U.S. Geol. Survey Water-Supply Paper 1619–BB, 38 p.

Shannon, C. E., and Weaver, Warren, 1963, The mathematical theory of communication: Urbana, Univ. of Illinois Press, 125 p.

Sharp, W. E., 1973, Entropy as a parity check: Earth Research, v. 1, p. 27–30.

Sharp, W. E., and Fan, Pow-Foong, 1963, A sorting index: Jour. Geology, v. 71, no. 1, p. 76–84.

Thompson, G. L., 1965, Hydrology of melt-water channels in southwestern Minnesota: U.S. Geol. Survey Water-Supply Paper 1809–K, 11 p.

Twenter, F. R., and Knutilla, R. L., 1972, Water for a rapidly growing urban community—Oakland County, Michigan: U.S. Geol. Survey Water-Supply Paper 2000, 150 p.

Winter, T. C., 1967, Linear sand and gravel deposits in the subsurface of Glacial Lake Agassiz, *in* Mayer-Oakes, W. J., ed., Life, land, and water—Environmental studies of the Glacial Lake Agassiz Region Conf., 1966: Winnipeg, Manitoba Univ. Press, Proc., p. 141–154.

——— 1973, Hydrogeology of glacial drift, Mesabi Iron Range, northeastern Minnesota: U.S. Geol. Survey Water-Supply Paper 2029–A, 23 p.

Winter, T. C., Cotter, R. D., and Young, H. L., 1973, Petrography and stratigraphy of glacial drift, Mesabi-Vermilion Iron Range area, northeastern Minnesota: U.S. Geol. Survey Bull. 1331–C, 41 p.

Winter, T. C., Maclay, R. W., and Pike, G. M., 1967, Water resources of the Roseau River watershed, northwestern Minnesota: U.S. Geol. Survey Hydrol. Inv. Atlas, HA–241.

Jour. Research U.S. Geol. Survey
Vol. 3, No. 2, Mar.–Apr. 1975, p. 149–162

GEOLOGIC SETTING AND CHEMICAL CHARACTERISTICS OF HOT SPRINGS IN WEST-CENTRAL ALASKA

By THOMAS P. MILLER; IVAN BARNES, and WILLIAM W. PATTON, Jr.

Anchorage, Alaska; Menlo Park, Calif.

Abstract.—Numerous hot springs occur in a variety of geologic provinces in west-central Alaska. Granitic plutons are common to all the provinces, and the hot springs are spatially associated with the contacts of these plutons. Of 23 hot springs whose bedrock geology is known, all are within 4.8 km (3 mi) of a granitic pluton. The occurrence of hot springs, however, appears to be independent of the age, composition, or magmatic history of the pluton. Most of the analyzed hot springs appear to have chemical and isotopic compositions indicating that they were derived from deeply circulating meteoric water. About 25 percent of the analyzed hot springs show a distinct saline character with high concentrations of chloride, sodium, potassium, and calcium indicating either much more complex water-rock reactions than in the other hot springs or the addition of another type of water. Chemical geothermometers suggest subsurface temperatures in the general range of 70° to 160°C. If the hot spring waters have derived their heat solely from deep circulation, they must have reached depths of 2 to 5 km (6,000–15,000 ft), assuming geothermal gradients of 30° to 50°C/km. If a shallow igneous heat source exists in the area or if dilution or mixing has occurred, these depths may be shallower. The geologic and chemical data, although preliminary, suggest that most of the hot springs of west-central Alaska have relatively low subsurface temperatures and limited reservoir capacities in comparison with geothermal areas presently being utilized for electrical power generation. The springs may, however, have some potential for limited power generation locally, if and when heat-exchange technology becomes available, as well as for space heating and agricultural uses.

Hot springs have long been known to occur in west-central Alaska but have received little study since they were discussed by Waring (1917) who visited 6 of the 15 hot springs known in 1915. At least 27 hot springs are now known in this area (fig. 1), and these springs constitute about 30 percent of the presently known hot springs in Alaska (Miller, 1973). Because the occur-

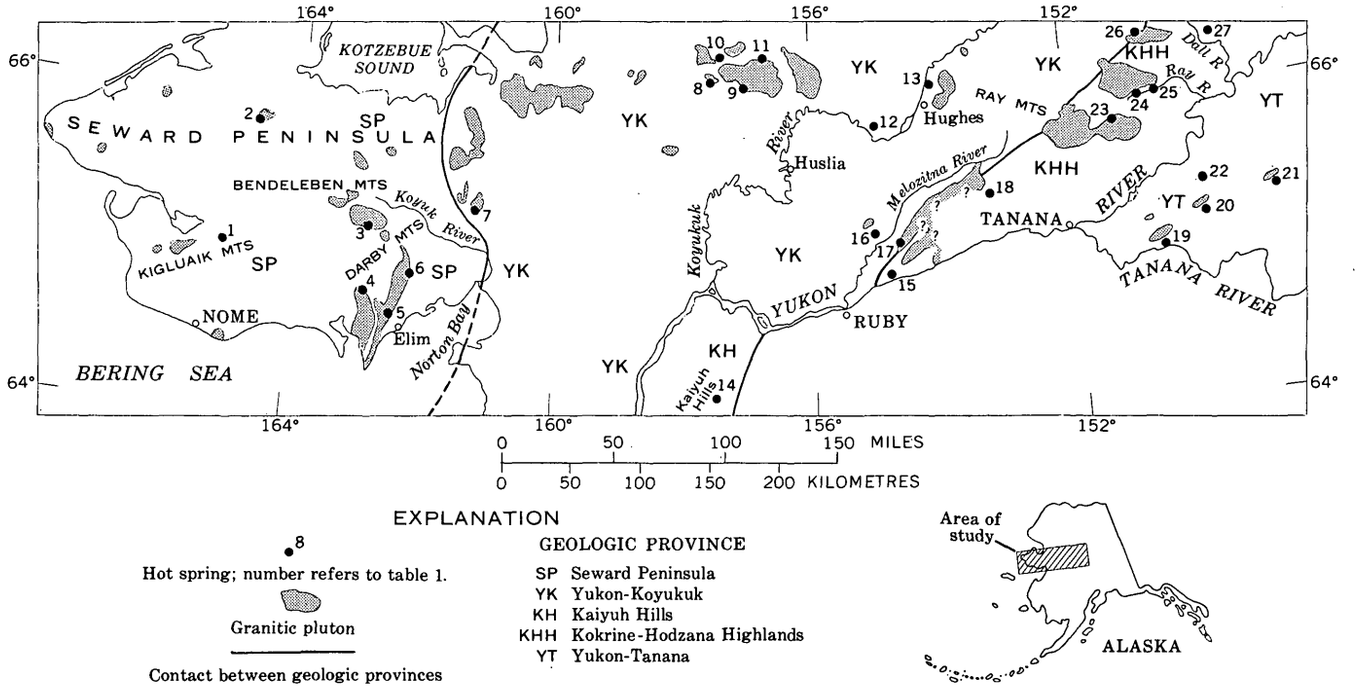

FIGURE 1.—Distribution of known hot springs and major granitic plutons in west-central Alaska.

rence of hot springs suggests possible geothermal resources and because interest in such resources as sources of energy is increasing, an updated report on these springs is warranted. Recent studies (Muffler, 1973; Combs and Muffler, 1973; White, 1973; Mahon, 1966; Fournier and Rowe, 1966; Fournier and Truesdell, 1973) have shown that knowledge of the geologic setting of hot springs and the composition of their waters can give clues to conditions at depth such as subsurface temperatures, source of heat, and type of hot-spring system. This report, therefore, discusses the geologic setting and chemical composition of known hot springs in west-central Alaska with regard to their potential as a geothermal resource.

This study should be regarded as preliminary since only 19 of 27 presently known hot springs within the study area have been visited by us and chemical data are available for only 16; indeed, fairly complete analyses are available from only 5 springs. Measured temperatures are available on 13 hot springs, and no information of temperatures is available from 5 of the remaining 14. In a few places, geologic mapping of the general spring site is not complete, and none of the hot springs has been studied in detail. Additional hot springs probably occur in the area but are unreported because it is sparsely populated and geologic mapping has been chiefly small-scale reconnaissance.

White (1957a) has classified springs as hot, or thermal, if their temperature is more than 6°C (15°F) above the mean annual temperature of the area. Problems arise in applying White's definition to this part of Alaska because the mean annual temperature for much of the region is −4° to −7°C (Johnson and Hartman, 1969), which means that springs with temperatures barely above freezing would be considered thermal. We have therefore restricted this report to springs with temperatures of at least 15°C (59°F).[1]

Acknowledgments.—We are indebted to our Geological Survey colleagues R. L. Elliott, D. G. Grybeck, and H. L. Heyward who assisted us in the sampling of hot springs and J. B. O'Neil for oxygen and hydrogen isotopic analysis. R. B. Barnes, J. B. Rapp, T. S. Presser, and L. M. Willey provided chemical analyses of water samples. T. B. Hudson provided water samples and temperatures from Serpentine Hot Springs, and M. L. Olson of Golovin, Alaska, supplied information on the location of several hot springs in southeastern Seward Peninsula. R. M. Chapman provided data on several hot springs in the Yukon-Tanana Upland and Kokrine-Hodzana Highlands in the eastern part of the area.

GENERAL DESCRIPTION

The part of Alaska considered in this report includes the area between lat 64° and 66° N. and from the Bering Straits east almost to Fairbanks (fig. 1). This area is part of the Intermontane Plateaus physiographic division (Wahrhaftig, 1965) and includes parts of the Northern Plateaus, Western Alaska, and Seward Peninsula physiographic provinces. It consists of low mountain ranges, uplands, and alluvium-filled lowlands; altitudes of the mountains and uplands range from over 1,500 m (5,000 ft) in the east to generally less than 1,200 m (4,000 ft) in the west. Much of the region lies within the zone of continuous permafrost (Ferrians, 1965).

The hot springs of west-central Alaska generally are found along valley margins and at low altitudes on mountain and hill slopes. Only Pilgrim Hot Springs (No. 1, fig. 1) in the Seward Peninsula is in the middle of a large alluvium-filled valley more than 2 km wide; all others are either in smaller valleys or along the fronts of mountain ranges. A few localities show considerable differences in altitudes of individual springs; at Clear Creek (fig. 1, No. 6), for example, there is as much as 62 m (200 ft) difference in altitude between hot springs 400 m (¼ mi) apart.

Most of the hot springs are in forested areas; the exceptions are Pilgrim, Serpentine, Lava Creek, and Granite Mountain hot springs (Nos. 1, 2, 3, and 7, fig. 1) on the Seward Peninsula, which are beyond tree line. Although the immediate area around the springs is commonly marked by open grass-covered meadows and bare ground, the margins of hot-spring areas support a variety of lush vegetation. The lush vegetation aids in locating hot springs, particularly in late spring or fall when the green coloring is most conspicuous against the gray and brown of the surrounding area. On cooler days in the summer, low clouds of vapor commonly form over many springs.

Thick growths of algae including red, white, and green varieties are common on the bottom of hot springs and their runoff channels, as are long streamers of white bacteria (Brock and Brock, 1971).

Measured temperatures are available from 12 hot springs and range from 17° to 77°C with only one spring below 40°C; estimated temperatures are available from another 7 localities and range from 15° to 60°C. Data on the daily temperature fluctuation are almost nonexistent. T. B. Hudson (written commun.,

[1] Waring (1917) mentioned a possible warm spring on the headwaters of the Inmachuk River in the north-central Seward Peninsula; from a later inspection, Gordon Herreid (oral commun., 1973) stated that the waters of the spring were not noticeably warm to the touch. The spring has not been included in this report.

1969) kept daily temperature records over a 6-week period in the summer of 1969 at Serpentine Hot Springs and reported a range of only 3°C from 74° to 77°C. Seasonal data are not available. Temperatures measured in recent years are generally similar to those reported by Waring (1917) over 50 yr ago from the same springs.

The amount of warm ground (insofar as indicated by vegetation patterns) at individual hot springs ranges from a few tens of square metres to as much as tens of thousands of square metres at Division hot springs (No. 11, table 1, fig. 1). Judging from the lack of change in vegetation patterns, the area of high heat flow at individual hot springs appears to be relatively stable.

Information regarding discharge rates is also sparse. Waring (1917) reported discharges ranging from a few gallons per minute to as much as a few hundred. Estimates made by us at springs not visited by Waring are in the same range. These are minimum estimates since it is not known how much hot water seeps undetected into the unconsolidated material overlying bedrock at many of the springs.

Current and historical use of hot-spring waters in west-central Alaska has been for bathing and limited agricultural purposes; cultivated areas have not exceeded 0.24 km² (60 acres) at any hot-spring locality.

REGIONAL GEOLOGIC SETTING

About 80 percent of the area discussed in this report is covered by modern geologic mapping at a scale 1:250,000 or larger. Topical studies on many of the plutonic rocks and mineral deposits of the region have been carried out in recent years. Regional aeromagnetic surveys have been made of parts of the area but at flightpath spacings too large (greater than 1 km) to provide much information on the relatively small hot-spring areas. Gravity maps are not available at a scale larger than 1:1,000,000.

The hot springs of west-central Alaska occur in several geologic provinces (table 1, fig. 1). From west to east, these are the Seward Peninsula, the Yukon–Koyukuk, the Kokrine–Hodzana Highlands, the Yukon–Tanana Upland, and the Kaiyuh Hills.

The Seward Peninsula is underlain chiefly by a thrust-faulted sequence of regionally metamorphosed pelitic and carbonate rocks of probable Precambrian age and by lesser amounts of Paleozoic carbonate rocks. Numerous stocks and plutons of granitic rocks of Cretaceous and possibly Tertiary age intruded this assemblage, particularly along the arcuate trend defined by the Kigluaik, Bendeleben, and Darby Mountains (fig. 1). Basalt of Quaternary age covers large parts of the north-central part of the peninsula.

East of the Seward Peninsula is the Yukon-Koyukuk province, a large wedge-shaped tract of volcanogenic sedimentary and andesitic volcanic rocks of Early and late Early Cretaceous age (Patton, 1973). Locally this assemblage is overlain by Late Cretaceous and Tertiary subaerial volcanic rocks and intruded by Cretaceous granitic rocks along the east-west Hogatza plutonic belt. Quaternary basalt covers several hundred square kilometres in the western part of the province. The province is bounded by narrow belts of mafic volcanic and intrusive rocks that probably belong to an ophiolite sequence.

The igneous and metamorphic complex of the Kokrine–Hodzana Highlands lies east of the Yukon–Koyukuk province and consists of a thick sequence of pelitic schists, quartzites, and carbonate rocks of Paleozoic and perhaps Precambrian age intruded by late Mesozoic granitic plutons. The metamorphic grade is chiefly greenschist facies with high-temperature thermal aureoles around the plutons.

The Yukon-Tanana Upland and Kaiyuh Hills areas consist chiefly of sedimentary and low-grade metamorphic rocks ranging in age from Precambrian(?) to Mississippian and overlain by Cretaceous and Tertiary sedimentary rocks (Foster and others, 1970; Mertie, 1937a,b). Ultramafic and mafic volcanic rocks of probable Devonian age and Permian-Triassic age are also present, and the entire sequence is intruded by granitic plutons of Cretaceous and Tertiary age.

Within this large area of about 155,000 km² (60,000 mi²), a variety of geologic features and structural trends is found; some are confined to a single province, whereas others are in two or more provinces. A feature that is common to all the provinces, however, regardless of geologic or structural setting, is the occurrence of granitic plutons of late Mesozoic and early Cenozoic age, and it is with these plutons that the hot springs are spatially associated (fig. 1). This association, first noted by Waring (1917), is a close one; all 23 hot-spring localities where the bedrock geology is known are within 4.8 km (3 mi) of the contact of a granitic pluton. Of these 23 hot springs, 11 are inside the pluton within 2.5 km (1.5 mi) of the contact, 2 are approximately on the contact, and 10 are outside the pluton within 4.8 km (3 mi) of the contact. The local geologic setting of each hot spring, insofar as it is known, is given in table 1.

There appears to be no relation between the absolute age or composition of the plutonic rocks and the occurrence of hot springs. Plutons with associated hot

TABLE 1.—*Description and geologic setting*

Locality No. and name	Location	General description
1. Pilgrim (formerly Kruzgamepa).	Bendeleben A–6 quadrangle; 65°06′ N., 164°55′ W.; 65 km (40 mi) north of Nome, 0.8 km (0.5 mi) south of Pilgrim River.	Several springs are found within a distance of a few hundred feet in middle of 8-km(5-mi)-wide alluvium-filled valley of Pilgrim River. An area 100 by 800 m appears to be underlain by warm ground. Discharge is small, less than 0.6 l/s (10 gal/min) according to Waring (1917). Recorded temperatures range from 69° (1915) to 60°C (1972). Chemical analysis available. Classified as "Known Geothermal Resource Area" (Godwin and others, 1971).
2. Serpentine (Arctic)	65°51′ N., 164°42′ W.; Bendeleben D–6 quadrangle; 150 km (95 mi) north of Nome on Hot Springs Creek.	Springs in two main areas about 800 m (0.5 mi) apart on Hot Springs Creek. Discharge at eastern spring estimated at about 2.2 l/s (35 gal/min) and temperature measured as 77°C. (T. B. Hudson, written commun., 1970). Chemical analysis available.
3. Lava Creek	65°13′ N., 162°54′ W.; Bendeleben A–2 quadrangle; 80 km (50 mi) north of Golovin on south side of Bendeleben Mountains.	One principal spring on east side of Lava Creek about 30 m (100 ft) above valley floor. Strong flow; temperature estimated at 60°–65°C. Noticeable H_2S odor. Chemical analysis available.
4. Battleship Mountain	64°48′ N., 162°55′ W.; Solomon D–2 quadrangle; 30 km (20 mi) north of Golovin.	One spring on east side of east fork of Cliff Creek on small bedrock terrace about 25 m (75 ft) above creek. H_2S odor; temperature of 17°C. measured in 1970. Chemical analysis available.
5. Kwiniuk	64°42′ N., 162°28′ W.; Solomon C–1 quadrangle; 14 km (9 mi) northwest of Elim.	One principal spring about 100 m (100 yd) north of Kwiniuk River. Temperature estimated at 40°–50°C in 1971. Chemical analysis available.
6. Clear Creek	64°51′ N., 162°18′ W.; Solomon D–1 quadrangle; 26 km (16 mi) north of Elim.	Hot springs are on both sides of east-flowing tributary of Clear Creek. Spring south of tributary has large flow estimated at several tens of litres per second and is about 120 m (400 ft) above Clear Creek valley floor. Temperature of 63°C measured in 1970. Two hot springs occur north of tributary. The upper spring is inaccessible by helicopter; the lower one has a smaller flow than the spring to the south and a temperature of 67°C. Chemical analysis available.
7. Granite Mountain (Sweepstakes).	65°22′ N., 161°15′ W.; Candle B–5 quadrangle; 65 km (40 mi) southeast of Candle on south side of Granite Mountain.	Several hot springs are found within a distance of about 30 m (100 ft) on the west side of Spring Creek about 15 m (50 ft) above valley bottom. Temperature: 49°C (1972). Chemical analysis available.
8. Hawk River	66°14′ N., 157°35′ W.; Shungnak 1:250,000 quadrangle; 80 km (50 mi) south-southwest of Kobuk.	At least one hot spring is in east bank of Hawk River on south side of Purcell Mountains. Spring is at south end of clearing 25 m by 60 m (75 ft by 200 ft) in tall timber and flows directly into Hawk River. Temperature estimated at +50°C. No chemical analysis available.
9. South	66°09′ N., 157°07′ W.; Shungnak 1:250,000 quadrangle; 84 km (52 mi) south of Kobuk on south side of Purcell Mountains.	Several hot springs scattered about a west-facing timbered slope 60 to 120 m (200–400 ft) above south-flowing tributary to Hawk River. Only one hot spring visited. Temperatures estimated at +50°C. Chemical analysis available.
10. Purcell Mountain	66°23′ N., 157°32′ W.; Shungnak 1:250,000 quadrangle; 71 km (44 mi) south-southwest of Kobuk.	Spring is on north bank of unnamed north-flowing tributary to Shinilikrok Creek about 8 km (5 mi) northeast of Purcell Mountain. Small flow, temperature estimated at 15°–20°C. No chemical analysis available.
11. Division	66°22′ N., 156°44′ W.; Shungnak 1:250,000 quadrangle; 61 km (38 mi) south of Kobuk on north side of Purcell Mountain.	Numerous springs on both sides of a headwater stream of Selawik River. Large open meadows as much as 900 m (1,000 yd) long by 180 m (200 yd) wide; largest area of apparent thawed ground of any hot spring in western Alaska. Temperature estimated at 50°–60°C. No chemical analysis available.
12. Deniktow Ridge	65°54′ N., 155°00′ W.; Melozitna D–4 quadrangle	Melozitna D–4 topographic map (1:63,000 scale) shows hot-spring symbol on north side of Hot Springs Creek 8 km (5 mi) from Koyukuk River. Not visited by us and no information regarding temperature, flow, number of springs, or chemistry is available.
13. Tunalkten Lake	66°11′ N., 154°01′ W.; Hughes A–3 quadrangle; 19 km (12 mi) northeast of Hughes 2.4 km (1.5 mi) from Koyukuk River.	Hot-spring symbol shown on Hughes 1:250,000-scale quadrangle.
14. Reported hot spring	General location: east side of Kaiyuh Hills	Waring (1917) quotes prospector as reporting a hot spring on tributary of upper Innoko River. No other information available.
15. Horner	64°55′ N., 154°47′ W.; Ruby D–4 quadrangle; 40 km (25 mi) northeast of Ruby on north side of Yukon River.	Hot springs issue from several points along small spring on west side of creek (Waring, 1917). Temperatures range from 30°C to 49°C. Chemical analysis available. Not visited by us.
16. Dulbi	65°16′ N.. 155°16′ W.; Melozitna B–5 quadrangle; 31 km (19.5 mi) N. 61° W. of Melozi Springs.	Several hot springs are found within a distance of about 100 m (100 yd) in small clearing along west side of south-flowing tributary to Dulbi River. Temperatures estimated at 50°–60°C. No chemical analysis available.
17. Melozi Hot Springs (Melozitna).	65°08′ N., 154°40′ W.; Melozitna B–1 quadrangle; on Hot Springs Creek 48 km (30 mi) northeast of Ruby.	From Waring (1917): One main hot spring flowing over 5-m (17-ft) bank into Hot Springs Creek. Temperature measured at 55°C. Total flow of 8.3 l/s (130 gal/min). H_2S odor. Chemical analysis available.
18. Little Melozitna Hot Springs.	65°28′ N., 153°20′ W.; Melozitna B–1 quadrangle; 64 km (40 mi) west of Tanana.	Hot springs on west bank of Hot Springs Creek. Temperature of 38°C (Waring, 1917). H_2S odor. Partial chemical analysis available.
19. Manley Hot Springs (Baker Hot Springs).	65°00′ N., 150°38′ W.; Tanana A–2 quadrangle; at north edge of Manley Hot Springs.	Principal hot springs are in valley of Karshner Creek, a tributary to Hot Springs Slough. Temperature of 50°C measured. In 1915 area had 0.25 km^2 (60 acres) under cultivation (Waring, 1917). Chemical analysis available.
20. Hutlinana	65°13′ N., 149°59′ W.; Livengood A–6 quadrangle; about 110 km (70 mi) west of Fairbanks.	Several hot springs are found within a distance of about 10 m (30 ft) on west side of Hutlinana Creek. Faint H_2S odor. Temperature of 43°C; discharge estimated at about 3 l/s (50 gal/min) (Waring, 1917). Chemical analysis available.
21. Tolovana	65°16′ N., 148°50 W.; Livengood B–4 quadrangle	From R. M. Chapman, written commun., 1972: Several hot springs are found along west side of creek draining east side of Hot Springs Dome. Temperatures of 60°C measured. Chemical analysis available.

of hot springs in west-central Alaska

Geologic setting		
Geologic province	Host rock	Remarks
Seward Peninsula	Concealed	Bedrock concealed; springs are 4 km (2.5 mi) north of plutonic and high-grade metamorphic rocks of Kigluaik Mountains and 4 km (2.5 mi) south of low-grade metamorphic rocks of Hen-and-Chicken Mountain. Springs are 2½ km (1.5 mi) west of inferred fault (Sainsbury and others, 1969). Aeromagnetic survey (State of Alaska aeromagnetic survey, 1972, Bendeleben A–4, A–5, A–6 quadrangles) suggests springs may lie along possible east-west fault that may be an extension, or branch, of range-front fault bounding south side of central and eastern Bendeleben Mountains (Miller and others, 1972).
do	Biotite granite	Springs occur in Serpentine Hot Springs pluton about 1.6 km (1.0 mi) from faulted contact. Pluton composed of biotite granite of Cretaceous or Tertiary age; country rock is Precambrian metasiltite and related rocks. (Sainsbury and others, 1969).
do	Quartz monzonite	Spring almost on contact between Late Cretaceous quartz monzonite of Bendeleben pluton and migmatite zone of Precambrian age. Biotite sample from Bendeleben pluton has yielded K:Ar age of 79.8±2.4 m.y. (Miller and others, 1972). Parts of floor of Lava Creek underlain by basalt of Quaternary age.
do	Granodiorite	Spring is in granodiorite of Kachauik pluton near contact with Precambrian schistose marble. Granodiorite is of probable Cretaceous age (Miller and others, 1972).
do	Quartz monzonite	Spring is in Darby pluton about 3.2 km (2 mi) from country rock and on or near conspicuous lineaments in pluton contacts. Darby pluton is Late Cretaceous in age (Miller and others, 1972).
do	do	Springs are in quartz monzonite of Darby pluton less than 400 m (0.25 mi) from contact with Devonian limestone. Pluton and limestone contact is inferred to be major fault (Miller and others, 1972) trending N. 18° E.
Yukon-Koyukuk	Nepheline syenite	Springs are in small satellitic stock of mafic nepheline syenite about 1.5 km (1 mi) south of Granite Mountain pluton of mid-Cretaceous age (Miller, 1972). Country rock is Lower Cretaceous andesite (Patton, 1967).
do	Concealed	Spring is in alluvial valley of Hawk River, and bedrock is concealed. On basis of map position (Patton and others, 1698), bedrock is probably hornfelsic andesite of Early Cretaceous age. Spring lies about 400 m (0.25 mi) south of mid-Cretaceous monzonite of Hawk River pluton and very close to east-west fault that cuts pluton (Miller, 1970).
do	Quartz monzonite	Springs are in Late Cretaceous quartz monzonite of Wheeler Creek pluton within 400 m (0.25 mi) of contact with Lower Cretaceous andesite (Miller, 1970). Springs are approximately on conspicuous lineament trending N. 80° W. (Patton and others, 1968).
do	Quartz latite	Spring is in Late Cretaceous hypabyssal volcanic complex composed of tuffs, flows, and intrusive rocks (Patton and others, 1968). Spring is about 400 m (0.25 mi) from contact with Lower Cretaceous andesite and near contact with granitic pluton (Miller, 1970).
do	Andesite	Springs are in Lower Cretaceous andesite near conspicuous N. 70° W.-trending lineament and about 2.5 km (1.5 mi) north of quartz monzonite of Wheeler Creek pluton (Patton and others, 1968; Miller, 1970).
do	Andesite(?)	Spring locality is in area of generally hornfelsic andesite cut by numerous quartz latite porphyry dikes. The numerous dikes and widespread thermal metamorphism suggests an unexposed pluton at shallow depth (Miller and Ferrians, 1968).
do	Graywacke-mudstone	Hot springs is in alluvial deposits but probably underlain by Cretaceous graywacke and mudstone. Spring locality about 4 km (2.5 mi) west of granodiorite of Indian Mountain pluton near inferred synclinal axis (Patton and Miller, 1966).
Kaiyuh Hills	Unknown	Unknown.
Kokrine-Hodzana Highlands.	Granite	According to Waring (1917), springs are in fractured granite of small pluton. Country rock is probably schist of Precambrian(?) to Paleozoic age. Springs are near Kaltag fault (Patton and Hoare, 1968).
Yukon-Koyukuk	Graywacke-mudstone	This report: spring is in hornfelsic graywacke and mudstone of Cretaceous age about 3.2 km (2 mi) from a possible pluton inferred from aerial photographs.
Kokrine-Hodzana Highlands.	Quartz monzonite	This report: spring is in quartz monzonite pluton about 3.2 km (2 mi) from contact with hornfelsic mafic and ultramafic rocks and 2.5 km (1.5 mi) from pelitic schist.
do	Granite	From Waring (1917); Springs are in small granitic pluton intruded into schist.
Yukon-Tanana Upland.	Concealed	Bedrock at springs locality is concealed; black hornfels crops out 800 km (0.5 mi) up Karshner Creek from hot springs and presence of abundant large blocks of biotite granite float suggests contact is very close. Hornfels probably represents metamorphosed sedimentary rocks of Jurassic and (or) Cretaceous age; biotite granite is of Cretaceous and (or) Tertiary age (Mertie. 1937; Chapman and others, 1971).
do	Quartzite-hornfelsic graywacke.	Spring is at base of sheared quartzite of Jurassic and(or) Cretaceous age (Chapman and others, 1971) about 5 km (3 mi) east of granitic pluton of Cretaceous and(or) Tertiary age.
do	Mudstone	Springs are in mudstone of Jurassic and(or) Cretaceous age about 1.5 km from granitic rocks of Cretaceous and(or) Tertiary age exposed in the Tolovana Hot Springs Dome (R. M. Chapman, written commun., 1972).

TABLE 1.—*Description and geologic setting of*

Locality No. and name	Location	General description
22. Reported hot spring near little Minook Creek.	General location: 66°25′ N., 150°00′ W.; Livengood B–6 or Tanana B–1 quadrangles.	Waring (1917) gives prospectors report of a hot spring near divide between Little Minook Creek and a tributary of Hess (Hoosier?) Creek. No other information available.
23. Kilo Hot Springs	65°49′ N., 151°12 W.; Tanana D–3 quadrangle; 177 km (110 mi) northwest of Fairbanks on Kanuti Kilolitna River.	From R. M. Chapman, written comm., 1973: Several hot springs are in an open grassy area of about 100 m² (1,000 ft²). Temperature estimated at 50°C. No chemical analysis available.
24. Ray Hot Springs	65°58′ N., 150°55′ W.; Tanana D–2 quadrangle; about 170 km (105 mi) northwest of Fairbanks on north side of Ray River.	Hot spring is at base of hill in flood plain on north side of Ray River. Slight H_2S odor. Temperature measured at 47°C. Chemical analysis available.
25. Lower Ray River	65°59′ N., 150°35′ W.; Tanana D–2 quadrangle	Several hot springs are found within a distance of 60 m (200 ft) in gravel bar on north side of Ray River. H_2S odor. Temperature measured at 61°C. Chemical analysis available.
26. Kanuti	66°20′ N., 150°48′ W.; Bettles 1:250,000 quadrangle; 8 km (5 mi) southwest of Caribou Mountain.	Several hot springs are on east side of Kanuti River in large open grassy area 100 m (100 yd) in diameter underlain by alluvium. Strong H_2S odor. Temperature measured at 66°C. Chemical analysis available.
27. Dall Creek	General location near Dall River in southwest Beaver 1:250,000 quadrangle.	Brosgé, Brabb, and King (1970) show a possible hot spring near Dall River.

springs have yielded potassium-argon age dates ranging from 106 m.y. (Early Cretaceous) for the Granite Mountain pluton in the western Yukon-Koyukuk province (Miller, 1972) to 63 m.y. (early Tertiary) for the Hot Springs Dome pluton in the Yukon-Tanana Upland area (Chapman and others, 1971), a range of over 40 m.y. These plutons are composed of such rock types as biotite granite, quartz monzonite, granodiorite, monzonite, syenite, nephelene syenite, and quartz latite; thus calc-alkaline, subalkaline, and alkaline rocks are included. Preliminary analysis (C. M. Bunker, written commun., 1971) suggests that the plutons with which the hot springs are associated have a considerable range in radioactivity and in radiogenic heat production. Uranium and thorium content and the heat production range from 2–4 ppm, 17–22 ppm, and 5.7–8.1 μcal/(g yr), respectively, in the Bendeleben pluton with which the Lava Creek hot springs (No. 3, fig. 1) is associated, to 9–15 ppm, 49–65 ppm, and 17.4–22.3 μcal/(g yr) for the Darby pluton with which the Kwiniuk and Clear Creek hot springs (Nos. 5 and 6, fig. 1) are associated. The radioactivity and radiogenic heat of the Bendeleben pluton are similar to granitic rocks elsewhere (Rodgers and Adams, 1969; Wollenberg and Smith, 1968), but the Darby pluton is anomalously high.

Plutons with hot springs are composed of rocks that are typically massive and well jointed with little or no foliation or lineation. The jointing may increase the fracture permeability sufficiently to promote deep circulation of meteoric water (local snowmelt and rainwater). Plutons composed of rocks with a well-developed foliation, such as the large Selawik Hills pluton (Miller, 1970) in the western Yukon-Koyukuk province, do not appear to have hot springs, possibly owing to a low fracture permeability.

The occurrence of hot springs also appears to be independent of the size of the pluton because plutons with associated hot springs range from 39 km² (15 mi²) to over 780 km² (300 mi²) in outcrop area.

The strong correlation that exists between the distribution of Cretaceous and early Tertiary plutons and hot springs in western and central Alaska is present in nearby areas in Alaska, for example at Circle and Chena hot springs in east-central Alaska (Waring, 1917). It is also found in the adjacent eastern Chukotka Peninsula, U.S.S.R. where most of the reported hot springs are spatially associated with granitic rocks (Golovachev, 1937; Nikolski, 1937, Rabkin, 1937). The association of hot springs with the pluton contacts and in some places with known faults and lineaments suggests that well-developed open fracture systems exist near the pluton margins and allow hot water to rise to the surface. A necessary prerequisite for the occurrence of a hot spring in this part of Alaska appears to be the presence of a mass of competent, well-fractured rock such as the massive granitic plutons. Significantly all 10 hot springs that lie near but outside a pluton occur in rocks such as graywacke, mudstone, basalt, and andesite that may have been affected to some extent by thermal metamorphism but not by regional metamorphism. Apparently fracture systems were not developed or are not sufficiently open in well-foliated regionally metamorphosed rocks to allow deeply circulating hot water to gain access to the surface. Massive contact metamorphic rocks on the other hand may have a higher fracture permeability resulting in a more favorable setting for hot springs.

Some of the hot springs are near mapped or inferred faults and lineaments; for example, Pilgrim, Serpentine, Kwiniuk, Clear Creek, Hawk River, South, Division, and Horner hot springs (Nos. 1, 2, 5, 6, 8, 9, 11, and 15, fig. 1). These faults and lineaments range in length from a few km to over 440 km (275 mi) for the Kaltag fault (Patton and Hoare, 1968). Hot springs, however, occur only where the faults and

hot springs in west-central Alaska—Continued

Geologic setting		
Geologic province	Host rock	Remarks
Yukon-Tanana Upland.	Unknown	General area is underlain by Paleozoic conglomerate and shale and Jurassic and (or) Cretaceous mudstone intruded by small granitic stocks of Cretaceous and(or) Tertiary age (Waring, 1917; Chapman and others, 1971).
Kokrine-Hodzana Highlands.	Quartz monzonite	Springs issue from pluton of porphyritic quartz monzonite of tentative Cretaceous age on, or very close to, contact with schist and hornfels of Precambrian(?) and Paleozoic age (R. M. Chapman, written commun., 1973).
do	Concealed	Bedrock concealed but spring probably occurs on contact between Early Cretaceous quartz monzonite of the Sithylemenkat pluton (Patton and Miller, 1973) and pelitic schist of Precambrian(?) and Paleozoic age. (Chapman and Yeend, 1972).
do	do	Bedrock concealed but springs are approximately on contact between quartz monzonite of probable Cretaceous age and pelitic schist of Precambrian(?) and Paleozoic age (Chapman and Yeend, 1972).
do	do	Bedrock concealed but springs are in area underlain by mafic volcanic rocks of Permian, Triassic, and Jurassic age within 400 m (0.25 mi) of contact with Cretaceous granitic rocks of Hot Springs pluton (Patton and Miller, 1973).
do	Unknown	General area is underlain by pelitic schist of Precambrian or Paleozoic age intruded by granitic pluton of probable Cretaceous age.

lineaments are near the plutons; that is, those parts of the faults away from plutons seemingly have no hot springs associated with them. The hot springs as a group are not spatially associated with faults along which recent movement has taken place, although a few do occur near such faults (for example, Horner and Little Minook Creek hot springs, Nos. 15 and 22).

A local structural control is suggested at several localities where hot springs are not in the bottoms of valleys but issue from different altitudes (Clear Creek, South, Nos. 6 and 9, fig. 1). White (1968) has suggested that differences in altitude of individual hot springs from the same locality may indicate that no single structure is permeable enough to discharge all the water in the system.

Hot springs elsewhere in the world are commonly related to recent volcanic activity. Late Cenozoic basalts are found in several areas of west-central Alaska, particularly in the western part where they cover about 9,100 km^2 (3,500 mi^2). Potassium-argon age dates on these basalts and correlative basalts on the islands of the Bering Sea (Hoare and others, 1968) range from about 6 m.y. to 30,000 yr. Hopkins (1963) stated that Lost Jim lava flow near Imuruk Lake in the central Seward Peninsula, which appears to be one of the youngest flows in western Alaska, is at least several hundred and possibly several thousand years old. The existence of volcanic rocks ranging in age from 6 m.y. to 30,000 yr or younger certainly suggests that parts of western Alaska may still be a volcanically active region. No hot springs, fumaroles, or other manifestations of current volcanic activity, however, occur within areas underlain by these basalt flows, and the known hot springs show no spatial association with these young basalts. The closest hot spring to basalt is the Lava Creek spring (No. 3, fig. 1), which is about 4.8 km (3 mi) from the probable source area for basalt that flowed down Lava Creek in the Bendeleben Mountains (Miller and others, 1972).

The late Cenozoic volcanic rocks described above are all basalts or basaltic andesite (Hopkins, 1963; Miller and others, 1972); no Pliocene or younger volcanic rocks of intermediate or silicic composition are known within the area described in this report. A discontinuous belt of felsic volcanic rocks of Late Cretaceous and Tertiary age are found near the east margin of the Yukon-Koyukuk province (Patton and Miller, 1970). Although only a single potassium-argon age of 58 ± 1.7 m.y. (Eocene) has been obtained from these rocks (Patton and Miller, 1973), it is unlikely that they are younger than mid-Tertiary in age, and no hot springs, fumaroles, or other signs of recent volcanic activity have been found associated with these rocks.

The distribution of hot springs is independent of the age and lithology of country rock around the pluton because the country rock ranges from Precambrian to Late Cretaceous and includes limestone, graywacke, andesite, mafic volcanic rocks, and regionally metamorphosed rocks of low and high grade.

GEOCHEMISTRY

Chemical analyses of water samples from west-central Alaska are given in table 2. All the analyses listed as being from the U.S. Geological Survey files were done by the methods described in Brown, Skougstad, and Fishman (1970). The analytical results given under L. M. Willey and T. S. Presser, analysts, are the most reliable because the samples were filtered in the field through a 0.2-μm-effective filter paper. In addition, samples for calcium, magnesium, aluminum and iron analyses were acidified in the field to a pH $\leqq 2$ with sulfuric acid. Bicarbonate and pH were also determined in the field using methods described by Barnes (1964). The analyses reported from analysts other than Willey and Presser were on unfiltered samples with no treatment in the field. Also given in table 2 are the highest values of constituents found in

TABLE 2.—*Chemical analyses of water from thermal springs in west-central Alaska*

[All data in milligrams per litre except temperature (in degrees Celsius) and pH]

Name	Pilgrim		Serpentine			Lava Creek	Battleship Mountain	Kwiniuk	Creek Clear	Granite Mountain		South
Locality No. (fig. 1, table 1)	1	1	2	2	2	3	4	5	6	7	7	9
Analyst	L.M. Willey, T.S. Presser [1]	[2]	L.M. Willey, T.S. Presser [1]	J.B. Rapp [1]	J.B. Rapp [1]	L.M. Willey, T.S. Presser [1]	L.M. Willey, T.S. Presser [1]	L.M. Willey [1]	L.M. Willey, T.S. Presser [1]	L.M. Willey, T.S. Presser [1]	J.B. Rapp [1]	R.B. Barnes [1]
SiO_2	100	87	100	90	89	84	56	45	83	75	69	65
Al	0.044	4.1	0.083	0.06	0.06	----	----	----	----	0.094	0.2	0.1
Fe	----	.7	----	<.01	<.01	----	----	----	----	----	<.01	<.01
Ca	530	545	47	75	78	2.0	4.8	130	2.0	2	1.8	5.9
Mg	1.4	7.4	.48	.35	.34	<0.1	<0.1	.1	<0.1	.04	.05	.01
Na	1,450	1,587	730	800	800	79	120	500	55	51	67	83
K	61	61	40	41	41	1.8	1.2	9	1.6	1.3	1.9	2.1
Li	4.0	----	4.7	----	----	0.13	0.2	----	0.05	.04	----	----
NH_3	----	----	----	----	----	<1	<1	----	<1	----	----	----
HCO_3	30.1	21	64.5	57	56.8	120.9	53.8	10.2	95	45.7	90	----
CO_3	----	----	----	1.3	.7	5	----	----	8	----	----	----
SO_4	24	25	29	1	1	53	16	----	27	62	50.3	122
Cl	3,346	3,450	1,480	1,450	1,420	5.9	120	912	4.2	9.3	6.4	6
F	4.7	----	6.4	6	6	10	9	5.8	3.9	8.2	----	----
Br	----	----	----	4.9	4.8	----	----	4	----	----	----	----
B	2.4	----	3.4	2.9	2.8	0.08	0.66	1	0.16	.13	.22	----
pH	6.75	----	7.91	----	7.94	8.6	9.20	7.3	8.33	10.14	9.55	
Temperature	55	69	60	77	71	50	17	[3]+50	60	49	49	[3]+50

Name	Horner	Melozi	Manley			Hutlinana		Tolovana	Ray River	Lower Ray River	Kanuti	Maximum value found in surface waters of Alaska [5]
Locality No. (fig. 1, table 1)	15	17	19	19	19	20	20	21	24	25	26	
Analyst	[2]	[2]	L.M. Willey, T.S. Presser [1]	L.M. Willey, T.S. Presser [1]	[2]	L.M. Willey, T.S. Presser [1]	[2]	[4]	R.B. Barnes [1]	R.B. Barnes [1]	R.B. Barnes [1]	
SiO_2	29	78	65	65	59	40	44	75	----	----	----	41
Al	.2	----	.016	.046	.8	.014	----	----	----	----	----	----
Fe	2.7	.75	----	----		----	.09	.02	----	----	----	89
Ca	10	11	4	6.8	9.1	20.2	22	82	5.6	11	2.7	280
Mg	3	2.8	1	.29	.9	6.6	6.0	1.2	.7	.1	.3	74
Na	58	107	130	130	121	180	208	321	71	95	111	67
K			4.5	4.8	8.2	7.9		23	1.4	2.0	3.7	9.5
Li	----	----	.28	.28	----	.16	----	----	----	----	----	----
NH_3	----	----	4.9	.5	----	.4	----	----	----	----	----	----
HCO_3	22	32	89.6	90.7	86	488	494	49	74	93	169	1,040
CO_3	32	31	----	----	0.0	----	0.0	----	22	21	----	----
SO_4	45	61	54	51	48	55	67	40	19	23	21	184
Cl	39	92	134	132	120	40	38	615	9.1	25	28	100
F	----	----	8.5	8.2	----	.8	----	.2	----	----	----	1
Br	----	----	----	----	----	----	----	----	----	----	----	----
B	----	----	1.3	1.2	----	.3	----	----	.6	1.6	1.3	----
pH	----	----	7.7	7.72	----	7.66	----	7.7	9.16	9.04	8.01	----
Temperature	47	56	59	56	52	43	45	52	45	66	66	----

[1] Analysis from U.S. Geological Survey files. [2] Analysis from Waring (1917). [3] Estimated. [4] Analysis from Anderson (1970).
[5] Analysis from U.S. Geological Survey (1959).

analyses of surface waters of Alaska unaffected by seawater (U.S. Geol. Survey, 1969); most of the recorded values are far below the analyses of hot-springs maxima reported in west-central Alaska.

Chemical composition

General agreement (White and others, 1963) is that most of the water discharged at the surface in thermal areas is meteoric in origin but that a small part might be magmatic, metamorphic, or connate. When the composition of hot springs in west-central Alaska is compared with the composition of hot springs that are probably entirely meteoric in origin (White and others, 1963, table 25; Feth and others, 1964) and with the known composition of surface waters in Alaska (table 2), most of the Alaska springs do indeed appear to be derived from local meteoric water. Their composition can be explained by deeply circulated meteoric water whose increased solvent action due to the increase in

temperature and long flow path brought about leaching of the country rock (White and others, 1963). The high discharge rates and the generally high chloride content relative to nearby ground water indicate that the hot springs of west-central Alaska belong to the hot-water type of geothermal system and not to the vapor-dominated type (White, 1970).

Four of the 16 hot springs for which chemical analyses are available are saline in nature, however, and are characterized by concentrations of chloride, sodium, calcium, potassium and perhaps lithium, bromide, and boron that are considerably greater than the other 12 analyzed springs. These four springs are Pilgrim (No. 1, table 2), Serpentine (No. 2, table 2), Kwiniuk (No. 5, table 2), and Tolovana (No. 21, table 2); the first three are in the Seward Peninsula, and Tolovana is over 480 km (300 mi) to the east (fig. 1).

The composition of these springs compared with that of the more dilute springs appears to demand either increased leaching or the addition of another type of water. If the anomalous composition of these springs is the result of an increased amount of leaching, then this leaching differed in some ways from the water-rock reactions typically seen elsewhere in granitic rocks. The composition of meteoric waters issuing from granitic rocks has been published by Feth, Roberson, and Polzer (1964) and Miller (1961); the Na^+/Cl^- ratios calculated from their data all exceed a value of 1 as do similar ratios for 11 of the other 12 analyzed hot springs in western and central Alaska. The Na^+/Cl^- ratios for the four saline springs, however (table 3),

TABLE 3.—Na^+/Cl^- *and* Cl^-/Br^- *ratios from available data on the hot-spring waters*

Locality No. and name (fig. 1, table 2)	Na^{+1}/Cl^{-1}	Cl^{-1}/Br^{-1}	Locality No. and name (fig. 1, table 2)	Na^{+1}/Cl^{-1}	Cl^{-1}/Br^{-1}
1. Pilgrim -----	.46	---	15. Horner ----	1.5	---
2. Serpentine --	.55	296	17. Melozi -----	1.2	---
3. Lava Creek --	13.3	---	19. Manley ----	1.0	---
4. Battleship Mountain.	1.0	---	20. Hutlinana --	4.5	---
			21. Tolovana ---	.52	---
5. Kwiniuk ----	.55	228	24. Ray River --	7.8	---
6. Clear Creek -	13.1	---	25. Lower Ray River.	3.8	---
7. Granite Mountain.	10	---			
			26. Kanuti -----	4.0	---
9. South -------	14	---	Seawater ------	.55	292

are all less than 1 and indeed are similar to seawater, 0.55.

Although the composition of these four saline springs may be due to the addition of magmatic, metamorphic, or connate waters to local meteoric water, the interpretation of the histories of mineralized thermal waters from their chemical composition is difficult (White, 1957a, b, 1969, 1973). Of the constituents given in the analyses in table 2, few may be used to determine unequivocally the origin of the solutions. Silica may reflect only the solution of quartz in the thermal waters (Fournier and Rowe, 1966; Mahon, 1966), and aluminum may be involved in reactions of too many aluminosilicates to reflect the earlier history of the solution. Iron is largely controlled by the local oxidation potential (Barnes and Back, 1964; Barnes and others, 1964). Calcium data may only reflect local solution and deposition of calcite; thus the bicarbonate and calcium data may give information on present processes rather than the earlier history of the water. Magnesium concentrations may be controlled by reactions of not only magnesian carbonates but also chlorite in geothermal systems (Muffler and White, 1969). Potassium and lithium are both sufficiently low in concentration that additions or subtractions of small amounts would obscure the earlier history. Sodium alone of the cations is present in sufficient concentrations and sufficiently nonreactive that small additions or losses would not obscure the earlier sodium concentrations.

As far as the anions are concerned, sulfate may be affected to a large extent by reduction of sulfide or oxidation of sulfide minerals to sulfate. Fluoride may be partly controlled by the solubility of fluorite (CaF_2), and boron, although leached from some rocks at moderate temperatures (White, 1957b), is difficult to use since its mineralogic source is not always known. The chloride and bromide concentrations, in contrast to the other anions, may be more significant in interpreting the history of the water. Although the chloride, in most rocks is easily leached by water at high temperatures (Ellis and Mahon, 1964), host rocks of the hot springs in the study area are not likely to be rich in chloride, judging from their known composition. No obvious mineralogic source or sink for either chloride or bromide has been found in the rocks of the study area.

The high chloride and sodium content suggests that magmatic water may have been added because hot-spring waters found in areas of active volcanism often contain large amounts of these elements (White and others, 1963). Such springs, however, commonly contain larger amounts of bicarbonate, sulfate, and silica than the saline hot springs of west-central Alaska. Furthermore, the saline hot springs are unrelated geographically to the most direct evidence of young magma, the Quaternary volcanic rocks.

Metamorphic waters are defined by White (1957b) as water that is or has been associated with rocks during their metamorphism and is probably derived from the reconstitution of hydrous minerals to anhydrous minerals. Such waters are thought to be high in sodium, bicarbonate, and boron (Barnes, 1970) in contrast to the saline hot springs of this report that do not have large concentrations of bicarbonate and boron.

The saline nature of the hot springs suggests the mixture of connate seawater or of present-day seawater.[2] The Na^+/Cl^- and Cl^-/Br^- ratios from available data on the hot-spring waters are given in table 3. The Na^+/Cl^- data fall in two groups—a group with the ratio 1 or greater, similar to the results of Feth, Roberson, and Polzer (1964) and Miller (1961), and a group with the ratio near the 0.55 ratio of seawater. The Cl^-/Br^- seems to give the same result, a separation of locally derived meteoric water from the more saline waters with a more complex history; the data, however, are too few to warrant extensive interpretation. If leaching is to account for the Cl^-/Br^- ratios, the leaching fortuitously results in ratios the same as present-day seawater.

An objection to the mixture of either old or present seawater is the geologic and geographic distribution of the saline hot springs. Although the Na^+/Cl^- and Cl^-/Br^- ratios may be interpreted as dilution of seawater, the geologic evidence is against submergence of the rocks of the region probably since the Cretaceous. Also, three of the four saline springs occur in a region of igneous and regionally metamorphosed rocks where connate water is unlikely. While two of the saline springs (Pilgrim and Kwiniuk) occur relatively near seawater and along structural trends that may directly connect with the ocean, the other two are either far removed from the ocean (Tolovana) or do not lie on such structures (Serpentine). The four saline springs show no geologic pattern to their distribution. Other hot springs in the Seward Peninsula, where three of the four saline springs occur, are nonsaline; this is particularly striking in regard to Kwiniuk (saline) and Clear Creek (nonsaline) hot springs, which are only 7.5 km (12 mi) apart and in the same pluton (fig. 1).

The isotopic data (table 4) available from 10 of the hot springs in the study area, 2 saline and 8 nonsaline, give some indication of the source of the constituents in the saline springs. These data show that in terms of deuterium (D), the saline springs, Pilgrim and Serpentine, are almost identical to Serpentine LDMW (locally derived meteoric water) indicating that all are derived from the same source, namely local snowmelt and rainwater. The salts in these saline springs would

TABLE 4.—*Oxygen and hydrogen isotopic compositions, in parts per thousand, of hot-spring waters and locally derived meteoric waters*

[SMOW, standard mean ocean water; LDMW, locally derived meteoric water. Analyses kindly supplied by J. R. O'Neil]

Source of samples (locality No. and name refer to fig. 1 and table 2)	δD (SMOW)	δO^{18} (SMOW)	O^{18} (calc)
Seward Peninsula:			
1. Pilgrim	−122	−14.9	−16.6
2. Serpentine	−123	−15.2	−16.7
Serpentine LDMW	−124	−16.4	−16.7
4. Battleship Mountain	−106	−13.8	−14.5
6. Clear Creek	−119	−15.6	−16.2
LDMW for samples 4 and 6	-----	−14.2	-----
7. Granite Mountain	−116	−15.7	−15.8
Granite Mountain LDMW	−118	−16.0	−16.0
Interior Alaska:			
19. Manley	−142	−18.1	−19.0
Manley LDMW	−130.3	−15.7	−17.5
20. Hutlinana	−144.9	−19.2	−19.3
Hutlinana LMDW	−148.5	−19.7	−19.8
24. Ray River	−150	−19.1	−20.0
25. Lower Ray River	−157	−19.2	−20.8
26. Kanuti	−146	−18.0	−19.5
LDMW for samples 24–26	−159	−19.9	−21.1

therefore appear to be derived from the leaching of rocks, and the proportions of ions are indeed only fortuitously identical to those of seawater. The two saline springs also show an enrichment in O^{18}, as indicated by the difference in δO^{18} and δO^{18} calculated,[3] and thus suggest more extensive water-rock reactions than found in the nonsaline springs of which only three of eight springs show a similar enrichment in O^{18}. Of these three exceptions, at Manley Hot Spring (No. 19; table 4), either the LDMW sample is not representative or the recharge takes place at a higher altitude with greater depletion in D; at Lower Ray River and Kanuti springs (Nos. 25, 26; table 4) the LDMW shows a similar enrichment in O^{18}, suggesting perhaps that the relation between δD and δO^{18} is not linear in this area.

The differences in δD and δO^{18} between the hot springs from the Seward Peninsula (Nos. 1, 2, 4, 6, and 7; table 4) and the hot springs from the interior (Nos. 19, 20, 24, 25, and 26; table 4) are probably the result of increasing distance from the ocean; the interior waters are isotopically lighter (lower in δD and δO^{18}), similar to trends noted elsewhere (White and others, 1973).

These preliminary chemical and isotopic data thus suggest that both the saline and nonsaline springs are derived from deeply circulating meteoric water. The difference in chemistry between the two types of springs appears to result from a difference in the extent

[2] Waring (1917) recognized the saline character of Pilgrim Hot Springs and, although noting that the spring was not far above the tide level, suggested that the high salinity was not due to admixture of seawater because the ratios of SO_4:Cl and Ca:Na were not similar to those of seawater. In view of the possible water-wallrock reactions involving calcium and sulfate, Waring's objection may not be valid.

[3] δO^{18} may be estimated by the following equation from Craig (1961): $\delta O^{18}\ (\text{calc}) = \frac{\delta D - 10}{8}$, assuming a linear relation between δO^{18} and δD.

of leaching, or water-rock reactions. It may be that the nonsaline springs have been subjected to a greater amount of leaching in the past, or for a longer period of time, than the saline springs, resulting in a smaller supply of solutes now available for leaching. Such a suggestion would be compatible with the oxygen isotope data in that the more extensive the oxygen isotope exchange has been between water and rock, the more depleted the rock is in O^{18} and the less the effect in the water (owing to isotopic exchange) with resulting lower δO^{18} at present for the nonsaline springs.

Chemical geothermometers

Water chemistry has proved valuable in estimating subsurface temperatures, and the various techniques and approaches are described by Mahon (1970), Fournier and Rowe (1966), White (1970), and Fournier and Truesdell (1973). The most quantitative temperature indicators have been shown to be (1) the variation in solubility of quartz as a function of temperature and (2) the temperature dependence of base exchange or partitioning of alkalies between solutions and solid phases with a correction applied for the calcium content of the water (the Na-K-Ca geothermometer). There is some ambiguity and uncertainty in both methods, and in any particular region, subsurface information may be necessary to calibrate adequately, or choose between, the methods. Silica, for example, may be precipitated rapidly enough from waters hotter than 180°C to give erroneously low values (White, 1970). The calculated subsurface temperatures (table 5), using the quartz conductive-cooling geothermometer, are

TABLE 5.—*Hot-spring subsurface temperatures, in degrees Celsius, calculated from quartz conductive-cooling geothermometer and appropriate* Na-K-Ca *geothermometer determinations*

Locality No. and name of hot spring (fig. 1, table 2)	Quartz	Na-K-Ca
1. Pilgrim	137	146
2. Serpentine	137	167
3. Lava Creek	128	91
4. Battleship Mountain	107	63
5. Kwiniuk	97	72
6. Clear Creek	127	83
7. Granite Mountain	122	75
9. South	115	72
17. Melozi	124	---
19. Manley	115	137
20. Hutlinana	92	98
21. Tolovana	122	162
24. Ray River	---	60
25. Lower Ray River	---	60
26. Kanuti	---	136

137°C as a maximum; therefore, silica precipitation may not affect the validity of the results. The Na-K-Ca geothermometer may be in error either because of continued reaction of the water with the rocks at temperatures below the highest subsurface temperature calculated or because of calcite precipitation. Continued reaction may yield low calculated temperatures owing to increases in calcium content (Fournier and Truesdell, 1973). Calcite precipitation may yield erroneously high subsurface temperatures because of decreases in calcium content of the water (Fournier and Truesdell, 1970).

Lacking knowledge of subsurface reactions, we have calculated subsurface temperatures using both the quartz solubility (assuming conductive cooling) and Na-K-Ca geothermometers. For the quartz solubility geothermometer (Fournier and Rowe, 1966), the equation is (Fournier, oral commun., 1973):

$$-\log_{10} C_{SiO_{2(aq)}} = (1.309 \times 10^3/T) - 5.19,$$

where T = temperature in kelvins, and

C_{SiO_2} = concentration of silica in milligrams per litre.

For calculations of subsurface temperatures from Na-K-Ca concentrations (from Fournier and Truesdell, 1973), the equation for temperatures above 100°C is

$$\log_{10}(m_{Na^+}/m_{K^+}) + \tfrac{1}{3}\log_{10}(\sqrt{m_{Ca^{+2}}}/m_{Na^+}) = 1647/T - 2.240$$

where T = temperature in kelvins, and

m_{Na^+} = molality of sodium ion,

m_{K^+} = molality of potassium ion, and

$m_{Ca^{+2}}$ = molality of calcium ion.

For temperatures below 100°C the equation is

$$\log_{10}(m_{Na^+}/m_{K^+}) + \tfrac{4}{3}\log_{10}(\sqrt{m_{Ca^{+2}}}/m_{Na^+}) = 1647/T - 2.240.$$

The results of these calculations for individual hot springs are given in table 5. The quartz conductive-cooling geothermometer shows a range of 92° to 137°C for the 12 springs for which it could be calculated. The Na-K-Ca geothermometer shows a range (on the basis of 14 springs) of 63° to 167°C. The difference between temperatures measured by the two geothermometers for any one spring ranges from 6° to 47°C. Perhaps the most important point that can be determined from these data is the relatively low subsurface temperature suggested for the hot springs of west-central Alaska. The maximum temperatures recorded are 137°C for the quartz conductive method and 167°C for the Na-K-Ca method. These suggested subsurface temperatures are low compared with subsurface temperatures of geothermal fields presently being exploited. Both of these maximum temperatures, for example, are below the minimum temperature (180°C) currently thought necessary to drive steam-turbine generators (Muffler, 1973).

The lack of siliceous sinter and the common occurrence of travertine in the hot-springs deposits also imply low subsurface temperatures (White, 1970).

DISCUSSION

A study of the geologic setting of hot springs in west-central Alaska shows a close correlation between the occurrence of hot springs and the contact zones of granitic plutons. Where the bedrock geology of the hot-spring area is known, the hot springs are almost without exception within 4.8 km (3 mi) of the contact of a pluton. Where the country rock is strongly foliated metamorphic rocks, the hot springs are restricted to the pluton proper; where sedimentary or volcanic rocks form the country rock, the hot springs occur both within and outside the pluton. The occurrence of hot springs also appears to be related to fracture and fault zones near the margins of the pluton. The distribution of hot springs is, however, independent of the age, composition, and magmatic events that formed the pluton.

The chemical and isotopic compositions of analyzed hot springs within the region suggest that most of them are composed of locally derived meteoric water. Four of the 16 analyzed hot springs however, have very saline compositions that appear to require either increased leaching of country rock at the present time or addition of another type of water. The present data suggest that the leaching is more likely.

The tentative model suggested by the available information on the geologic setting and geochemistry of the hot springs in west-central Alaska is as follows. Most of the hot springs are the result of deeply circulating, locally derived meteoric water that has percolated through the fractured granitic plutons and the surrounding wallrock to depths of several thousand feet, become heated owing to the geothermal gradient, and found access to the surface along the fractured and faulted margins of the pluton. If no addition of magmatic water or heat is considered, the subsurface temperatures indicated by the chemical geothermometers suggest that the water must have reached depths of 3.3 to 5.3 km (9,000–15,000 ft) on the basis of assumed geothermal gradients of 30°C/km and 50°C/km and a maximum subsurface temperature of 167°C. If heat from an underlying magma has been added to the system, the water may have reached a shallower depth than that calculated from the above geothermal gradients.

The hot springs appear to occur along fractured zones near the margins of granitic plutons, and the reservoir of such a system may not be large. According to White (1965), the yield of stored heat may drop relatively quickly in crystalline rocks with low permeability where circulation of water is localized in faults and fractures. The total surface area of rocks in direct contact with migrating fluids is relatively small, and the recoverable stored heat is transferred to the circulating fluids by conduction over long distances. These fault and fracture zones in the crystalline plutonic rocks are likely to be narrow or widely spaced and less numerous at greater depths.

Although the data available on the geologic setting and chemistry of the hot springs of west-central Alaska are preliminary in nature, they suggest that most, if not all, of the hot springs are characterized by reservoirs of limited extent and relatively low temperatures in comparison with temperatures of geothermal systems presently being exploited for power generation. Muffler (1973) gave 180°C as the lowest reservoir temperature that can presently be utilized for the generation of electricity by steam-turbine generators. The subsurface temperatures suggested by the present study are lower than 180°C but are within ranges suggested for proposed turbines using a heat-exchange system involving such working fluids as Freon and isobutane. An experimental plant of this type, for example, operating at Paratunka, Kamchatka (USSR), since 1970 utilizes 81.5°C water (Facca, 1970). These springs may therefore have potential for limited power generation locally, if and when heat-exchange technology becomes available, as well as for space heating and agricultural uses.

REFERENCES CITED

Anderson, G. S., 1970 Hydrologic reconnaissance of the Tanana basin, central Alaska: U.S. Geol. Survey Hydrol. Inv. Atlas, HA–319.

Barnes, Ivan, 1964, Field measurement of alkalinity and pH: U.S. Geol. Survey Water-Supply Paper 1535–H, 17 p.

Barnes, Ivan, 1970, A brief hydrologic and geologic reconnaissance in the Cordova area, Alaska: U.S. Geol. Survey open-file rept., 6 p.

Barnes, Ivan, and Back, William, 1964, Geochemistry of iron-rich ground water of southern Maryland: Jour. Geology, v. 72, p. 435–447.

Barnes, Ivan, Stuart, W. T., and Fisher, D. W., 1964, Field investigations of mine waters in the northern anthracite field, Pennsylvania: U.S. Geol. Survey Prof. Paper 473–B, 8 p.

Brosgé, W. P., Brabb, E. E., and King, E. R., 1970, Geologic interpretation of reconnaissance aeromagnetic survey of northeastern Alaska: U.S. Geol. Survey Bull. 1271–F, p. 1–14.

Brock, T. D., and Brock, M. L., 1971, Life in the geyser basins: Bloomington, Indiana, Yellowstone Library and Museum Association, 32 p.

Brown, Eugene, Skougstad, M. W., and Fishman, M. J., 1970, Methods for collection and analysis of water samples for dissolved minerals and gases: U.S. Geol. Survey Techniques Water-Resources Inv., book 5, chap. A1, 160 p.

Chapman, R. M., Weber, F. R., and Taber, Bond, 1971, Preliminary geologic map of the Livengood quadrangle, Alaska: U.S. Geol. Survey open-file rept., scale 1:250,000.

Chapman, R. M., and Yeend, W. E., 1972, Preliminary geologic map of the northeastern part of the Tanana quadrangle, Alaska: U.S. Geol. Survey Misc. Field Studies Map, MF–342, scale 1:250,000.

Combs, Jim, and Muffler, L. J. P., 1973, Exploration for geothermal resources, *in* Kruger, Paul, Otte, Carel, eds., Geothermal energy—resources, production, stimulation: Palo Alto, Calif., Stanford Univ. Press, 360 p.

Craig, Harmon, 1961, Isotopic variations in meteoric waters: Science, v. 133, p. 1702–1703.

Ellis, A. J., and Mahon, W. A. J., 1964, Natural hydrothermal systems and experimental hot-water/rock interactions: Geochim. et Cosmochim. Acta., v. 28, p. 1323–1357.

Facca, G., 1970, General report of the status of world geothermal development, *in* United Nations Symposium on Development and Utilization of Geothermal Resources, Pisa, Italy: Rapporteur's Report, 47 p. of proof.

Ferrians, O. J., Jr., compiler, 1965, Permafrost map of Alaska: U.S. Geol. Survey Misc. Geol. Inv. Map I–445, scale 1:2,500,000.

Feth, J. H., Roberson, C. E., and Polzer, W. L., 1964, Sources of mineral constituents in water from granitic rocks, Sierra Nevada, California and Nevada: U.S. Geol. Survey Water-Supply Paper 1535–I, 70 p.

Foster, H. L., Brabb, E. E., Weber, F. R., and Forbes, R. B., 1970, Regional geology of Yukon-Tanana Upland, Alaska [abs.]: Am. Assoc. Petroleum Geologists Bull., v. 54, no. 12, p. 2481.

Fournier, R. O., and Rowe, J. J., 1966, Estimation of underground temperatures from the silica content of water from hot springs and steam wells: Am. Jour. Sci., v. 264, p. 685–697.

Fournier, R. O., and Truesdell, A. H., 1970, Chemical indicators of subsurface temperature applied to hot spring waters of Yellowstone National Park, Wyoming U.S.A., *in* United Nations Symposium on Development and Utilization of Geothermal Resources, Pisa 1970, Proc., v. 2, pt. 1, Geothermics, Spec. Issue 2: p. 529–535.

Fournier, R. O., and Truesdell, A. H., 1973, Empirical Na-K-Ca geothermometer for natural waters: Geochim. et Cosmochim. Acta., v. 37, p. 1255–1276.

Godwin, L. H., Haigler, L. B., Rioux, R. L., White, D. E., Muffler, L. J. P., and Wayland, R. G., 1971, Classification of public lands valuable for geothermal steam and associated geothermal resources: U.S. Geol. Survey Circ. 647, 18 p.

Golovachev, F. A., 1937, The mineral springs of the southeastern extremity of the Chukchee Peninsula [Russian; English summary]: Arctica, v. 5, no. 5, p. 57–80.

Hoare, J. M., Condon, W. H., Cox, Allan, and Dalrymple, G. B. 1968, Geology, paleomagnetism and potassium-argon ages of basalts from Nunivak Island, Alaska, *in* Coats, R. R., Hay, R. L., and Anderson, C. A., eds., Studies in volcanology: Geol. Soc. America Mem. 116, p. 377–414.

Hopkins, D. M., 1963, Geology of the Imuruk Lake area, Seward Peninsula, Alaska: U.S. Geol. Survey Bull. 1141–C, 101 p.

Johnson, P. R., and Hartman, C. W., 1969, Environmental atlas of Alaska: Alaska Univ. Inst. Arctic Environmental Eng., 111 p.

Mahon, W. A. J., 1966, Silica in hot water discharged from drill holes at Wairakei, New Zealand: New Zealand Jour. Sci., v. 9, p. 135–144.

——— 1970, Chemistry in the exploration and exploitation of hydrothermal systems, *in* United Nations Symposium on Development and Utilization of Geothermal Resources, Pisa 1970, Proc., v. 2, pt. 2, Geothermics, Spec. Issue 2: p.1310–1322.

Mertie, J. B., Jr., 1937a, The Yukon-Tanana region, Alaska: U.S. Geol. Survey Bull. 872, 276 p.

——— 1937b, The Kaiyuh Hills, Alaska: U.S. Geol. Survey Bull. 868–D, p. 145–178.

Miller, J. P., 1961, Solutes in small streams draining single rock types, Sangre de Cristo Range, New Mexico: U.S. Geol. Survey Water-Supply Paper 1535–F, 23 p.

Miller, T. P., 1970, Preliminary correlation of Mesozoic plutonic rocks in Bering Sea region [abs.]: Am. Assoc. Petroleum Geologists Bull., v. 54, no. 12, p. 2496.

——— 1972, Potassium-rich alkaline intrusive rocks of western Alaska: Geol. Soc. America Bull., v. 83, p. 2111–2128.

——— compiler, 1973, Distribution and chemical analyses of thermal springs in Alaska: U.S. Geol. Survey open-file rept., 5 p.

Miller, T. P., and Ferrians, O. J., Jr., 1968, Suggested areas for prospecting in the central Koyukuk River region, Alaska: U.S. Geol. Survey Circ. 570, 12 p.

Miller, T. P., Grybeck, D. G., Elliott, R. L., and Hudson, T., 1972, Preliminary geologic map of the eastern Solomon and southeastern Bendeleben quadrangles, eastern Seward Peninsula, Alaska: U.S. Geol. Survey open-file rept., scale 1:250,000.

Muffler, L. J. P., 1973, Geothermal resources, *in* Brobst, D. A., and Pratt, W. P., eds., United States Mineral Resources: U.S. Geol. Survey Prof. Paper 820, p. 251–261.

Muffler, L. J. P., and White, D. E, 1969, Active metamorphism of Upper Cenozoic sediments in the Salton Sea geothermal field and the Salton Trough, southeastern California: Geol. Soc. America Bull., v. 80, p. 157–182.

Nikolski, A. P., 1937, The hot springs in the district of the Gulf of Lavrenty and the Mechigmensk Bay [Russian; English summary]: Arctica, v. 5, no. 5, p. 81–92.

Patton, W. W., Jr., 1967, Regional geologic map of the Candle quadrangle, Alaska: U.S. Geol. Survey Misc. Geol. Inv. Map I–492, scale 1:250,000.

——— 1973, Reconnaissance geology of the northern Yukon-Koyukuk province, Alaska: U.S. Geol. Survey Prof. Paper 774–A, 17 p.

Patton, W. W., Jr., and Hoare, J. M., 1968, The Kaltag fault, west-central Alaska, *in* Geological Survey research 1968: U.S. Geol. Survey Prof. Paper 600–D, p. D147–D153.

Patton, W. W., Jr., and Miller, T. P, 1966, Regional geologic map of the Hughes quadrangle, Alaska: U.S. Geol. Survey Misc. Geol. Inv. Map I–459, scale 1:250,000.

——— 1970, A possible bedrock source for obsidian found in archeological sites in northwestern Alaska: Science, v. 169, p. 760–761.

——— 1973, Bedrock geologic map of Bettles and southern part of Wiseman quadrangles, Alaska: U.S. Geol. Survey Misc. Field Studies Map, MF–492, scale 1:250,000.

Patton, W. W., Jr., Miller, T. P., and Tailleur, I. L., 1968, Regional geologic map of the Shungnak and southern part of the Ambler River quadrangles, Alaska: U.S. Geol. Survey Misc. Geol. Inv. Map I–554, scale 1:250,000.

Rabkin, M. I., 1937, The hot springs of Neshkin [Russian; English summary]: Arctica, v. 5, no. 5, p. 93–101.

Rodgers, J. J. W., and Adams, J. A. S., 1969, Uranium, *in* Wedepohl, K H., ed., Handbook of geochemistry, Springer-Verlag, Pub., v. II/3, chap. 92, p. 92–I.

Sainsbury, C. L., Hudson, Travis, Kachadoorian, Reuben, and Richards, T. R., and Todd, W. E., Reconnaissance geologic maps and sample data, Teller A–1, A–2, A–3, B–1, B–2, B–3, C–1 and Bendeleben A–6, B–6, C–6, D–5, D–6 quadrangles, Seward Peninsula, Alaska: U.S. Geol. Survey open-file rept., 49 p.

Waring, G. A., 1917, Mineral springs of Alaska: U.S. Geol. Survey Water-Supply Paper 418, 114 p.

Wahrhaftig, Clyde, 1965, Physiographic divisions of Alaska: U.S. Geol. Survey Prof. Paper 482, 51 p.

White, D. E., 1957a, Thermal waters of volcanic origin: Geol. Soc. America Bull., v. 68, p. 1637–1658.

——— 1957b, Magmatic, connate, and metamorphic waters: Geol. Soc. America Bull., v. 68, p. 1659–1682.

——— 1965, Geothermal energy: U.S. Geol. Survey Circ. 519, 17 p.

——— 1968, Hydrology, activity, and heat flow of the Steamboat Springs thermal system, Washoe County, Nevada: U.S. Geol. Survey Prof. Paper 458–C, 109 p.

——— 1969, Thermal and mineral waters of the United States—Brief review of possible origins: Internat. Geol. Cong. 23d, Prague 1968, Comptes rendus, v. 19, p. 269–286.

——— 1970, Geochemistry applied to the discovery, evaluation, and exploitation of geothermal resources, *in* United Nations Symposium on Development and Utilization of Geothermal Resources, Pisa, Italy: Rapporteur's Report, 47 p. of proof.

——— 1973, Geothermal resources, *in* Kruger, Paul, and Otte, Carel, eds., Geothermal energy—resources, production, stimulation: Palo Alta, Calif. Stanford Univ. Press, 360 p.

White, D. E., Barnes, Ivan, and O'Neil, J. R., 1973, Thermal and mineral waters of non-meteoric origin, California Coast Range: Geol. Soc. America Bull., v. 84, p. 547–560.

White, D. E., Hem, J. D., and Waring, G. A., 1963, Chemical composition of subsurface waters: U.S. Geol. Survey Prof. Paper 440–F, 67 p

Wollenberg, H. A., and Smith, A. R., 1968, Radiogeologic studies in the central part of the Sierra Nevada batholith, California: Jour. Geophys. Research, v. 73, no. 4, p. 1481–1495.

Jour. Research U.S. Geol. Survey
Vol. 3, No. 2, Mar.–Apr. 1975, p. 163–167

RELATIVE EFFICIENCIES OF SQUARE AND TRIANGULAR GRIDS IN THE SEARCH FOR ELLIPTICALLY SHAPED RESOURCE TARGETS

By DONALD A. SINGER, Reston, Va.

Abstract.—The relative efficiencies of equivalent-density, square and equilateral triangular (hexagonal) grids used in the search for elliptical targets are determined for ellipses having relative semimajor axes ranging from 0.50 to 1.00 of the square grid spacing and having shapes (minor axes/major axes) ranging from 0.2 to 1.0. Using the probability of one or more hits, the grid types are equally efficient for targets having semimajor axes less than or equal to one-half of the grid spacing. The triangular grid is as much as 6 percent more efficient for targets having relative sizes greater than 0.50. The square grid is less than 1 percent more efficient in a small region centered on a relative size of 0.80 and a shape of 0.45. Both grids are equally efficient for targets that are hit with certainty and tend toward equal efficiency as the ellipses become more needlelike in shape. A random search is more efficient than both grid types when the relative size is less than 0.50 and the probability of two or more hits is used to define relative efficiency. For two or more hits and targets having relative sizes larger than 0.50, the triangular grid is as much as 91 percent less efficient than the square grid; however, the probabilities are small. In a region centered on a relative size of 0.80, the triangular grid is slightly more efficient if the criterion is two or more hits. The probability of two or more hits is inversely related to the probability of one or more hits for many target sizes and shapes.

Many mineral science problems involve the search for elliptical targets using various grids; grid drilling is most commonly used in the search for uranium, lead, and zinc, and less commonly, in the search for other mineral resources. Selection of the proper grid spacing can have a significant impact upon the efficiency of the search, regardless of whether efficiency is measured in terms of reduced costs, increased chance of success, or increased return on the investment; the selection of the proper grid type may also improve the efficiency of the search. In this paper, the relative efficiencies of square and equilateral triangular (hexagonal) grids used in the search for elliptical targets are examined. For this evaluation, the probabilities for square and triangular grids obtained by the method of Singer and Wickman (1969) are utilized.

Because the problems of the selection of the proper grid type and of the selection of the proper grid spacing are closely related, much of the work on grid spacing has included at least a mention of the grid-type selection problem. Slichter (1955) found that for a circular target of a certain size the triangular grid is more efficient than the square grid. Celasun (1964) stated that for elliptical targets the triangular grid is more efficient than the square grid if the probability of detection is greater than 0.785. Drew (1966) concluded that the triangular grid is more efficient than the square grid if the major axis of an elliptical target is greater than the grid spacing of the triangular grid, whereas the two grids are equally efficient if the major axis is less than the grid spacing. Research has also been published emphasizing optimal grid spacing (Drew, 1967; Ellis and Blackwell, 1959; Griffiths, 1966; Griffiths and Drew, 1966; and Griffiths and Singer, 1973).

The determination of the probability of detection of elliptical targets by the use of a grid is a prerequisite for determining the optimal grid spacing or grid type. Drew (1966) used a combination of analytic and simulation techniques to determine the probabilities for a square grid. Savinskii (1965) used simulation to obtain the probabilities for rectangular and square grids. Exact probabilities for square, hexagonal, and rectangular grids are provided by the method derived and explained by Singer and Wickman (1969); probabilities calculated by this method are used in this paper to compare the efficiencies of square and triangular grids.

MEASURES OF RELATIVE EFFICIENCY

Use of probabilities to compare efficiencies requires that the following four assumptions are fulfilled:

1. In plan view, the shape of the targets of interest can be represented reasonably well by ellipses.
2. There is no preferred orientation of the targets.
3. In plan view, there is no regular pattern of the distribution of the targets.
4. If a target is hit with a grid point, the event can be recognized with certainty.

The probabilities used in this study are calculated by means of the program Elipgrid (Singer, 1972). The variables needed to determine the probabilities

are as follows: The size of the semimajor axis of the target relative to the size of the grid, the breadth-to-length ratio or shape of the ellipse, the orientation of the ellipse with respect to the grid, and the grid type. For both the square and triangular grids, probabilities are calculated for 11 different sizes and 9 different shapes for each size of ellipse. The size of the semimajor axis varies from 0.50 to 1.00 of the square grid size. Shape varies from 1.0 to 0.2; that is, from a circle to a rather elongate ellipse. The orientation of the ellipses with respect to the grid was varied from 0° to 90° in steps of one-tenth of a degree. The range 0° to 90° was chosen because an axis of symmetry of the probabilities common to both grids is 90°. Probabilities were calculated for each orientation, and the average of the probabilities, which represents the probability for a randomly oriented ellipse, was calculated.

Given the same grid spacing (distance between vertices), the triangular grid would require more drill holes than the square grid. For the comparison of the relative efficiencies of the grid types, the grid spacings are adjusted so that the same number of holes is required for each given unit of area. The grid spacing for the triangular grid should be 1.07457 (that is, $\sqrt{2}/\sqrt[4]{3}$) times that of a square grid. This procedure gives equivalent density grids.

The relative efficiencies of the grid types for various sizes and shapes of ellipses are defined in terms of the percentage change in the probabilities of detection for equivalent density grids. The following equation was used to estimate the relative efficiencies:

$$\text{Relative efficiency} = 100\ (P_{TRI} - P_{SQ})/P_{SQ}$$

where P_{TRI} = probability of hitting with the triangular grid, and

P_{SQ} = probability of hitting with the square grid.

The chance of hitting a target can be defined in several different ways; however, only two are considered here. The probability of hitting a target one or more times is an appropriate criterion for use in most problems. The probability of hitting a target two or more times might be of use when the event of hitting the target with a grid is not recognized with certainty. The probability of two or more hits upon targets of various sizes and shapes also provides insight into the nature of the efficiency of hitting a target one or more times. The relative efficiencies of the square and triangular grids are therefore defined first in terms of the probability of one or more hits, then in terms of the probability of two or more hits.

COMPARISON OF EFFICIENCIES FOR ONE OR MORE HITS

The probability of one or more hits when a square grid is used for each size and shape combination considered is presented in table 1. The probabilities increase as the targets become larger and as they approach a circular shape. In table 2, the percentage relative efficiency of the triangular grid over the square grid for one or more hits is presented.

For targets in which the semimajor axis is less than or equal to one-half of the grid spacing, the triangular and square grids are equally efficient. In the upper right region of table 2, the triangular and square grids are equally efficient because both types of grids discover targets with these characteristics with certainty. There is also a trend toward equally efficient grids as the ellipses become more needlelike in shape; that is, as shape tends to zero. The most striking aspect shown in table 2, however, is the superiority of the triangular grid over the square grid (as much as 6 percent more efficient for a circle having a relative size of 0.55), except for a small region centered on a shape of 0.45 and a relative size of 0.80, where the square grid is more efficient. This anomalous region was not anticipated and is difficult to explain without an understanding of the relative efficiencies of the grids when the probability of two or more hits is considered.

TABLE 1.—*Probability of one or more hits with square grid*

	Size of semimajor axis relative to square grid										
Shape	0.50	0.55	0.60	0.65	0.70	0.75	0.80	0.85	0.90	0.95	1.00
1.0	0.785	0.888	0.951	0.987	1.000	1.000	1.000	1.000	1.000	1.000	1.000
.9	.707	.834	.916	.967	.994	1.000	1.000	1.000	1.000	1.000	1.000
.8	.628	.749	.854	.931	.978	.998	1.000	1.000	1.000	1.000	1.000
.7	.550	.658	.760	.853	.932	.980	.997	1.000	1.000	1.000	1.000
.6	.471	.565	.658	.748	.833	.907	.960	.988	.998	1.000	1.000
.5	.393	.472	.553	.633	.713	.788	.854	.908	.948	.975	.993
.4	.314	.378	.445	.513	.582	.650	.715	.774	.827	.874	.912
.3	.236	.284	.335	.388	.444	.500	.555	.610	.662	.713	.760
.2	.157	.190	.224	.261	.300	.340	.382	.423	.466	.508	.550

TABLE 2.—*Percentage relative efficiency of the triangular grid over the square grid for one or more hits*

Shape	Size of semimajor axis relative to square grid										
	0.50	0.55	0.60	0.65	0.70	0.75	0.80	0.85	0.90	0.95	1.00
1.0	0.0	6.0	5.2	1.4	0.0	0.0	0.0	0.0	0.0	0.0	0.0
.9	.0	2.4	5.6	3.4	.6	.0	.0	.0	.0	.0	.0
.8	.0	1.4	2.7	3.5	2.2	.2	.0	.0	.0	.0	.0
.7	.0	1.0	1.8	1.8	1.2	1.1	.4	.0	.0	.0	.0
.6	.0	.8	1.3	1.3	.7	.0	.0	.4	.2	.0	.0
.5	.0	.6	1.0	.9	.4	−.1	−.2	.0	.5	.9	.6
.4	.0	.4	.8	.7	.3	−.1	−.2	−.1	.3	.8	1.0
.3	.0	.3	.5	.5	.2	−.1	−.2	−.1	.2	.5	.6
.2	.0	.2	.3	.3	.1	−.1	−.1	.0	.1	.3	.4

COMPARISON OF EFFICIENCIES FOR TWO OR MORE HITS

Table 3 contains the probability of two or more hits for each size and shape combination for the square grid. The probability of two or more hits is, of course, zero for all targets with relative sizes less than or equal to one half of the grid spacing as it is impossible to hit such a target twice; therefore, a random search is more efficient under these conditions. Targets shown in the upper right part of table 3 are blank because the program used to calculate the probabilities will not calculate the probability of two or more hits when the targets will be hit with certainty at some orientation.

If the relative efficiency is measured in terms of the probability of one or more hits, the triangular grid is more efficient for most sizes and shapes, the square grid being more efficient in a region centered on a shape of 0.45 and a size of 0.80 (table 2). If the relative efficiency is measured in terms of the probability of two or more hits, the pattern is the same, but the more efficient type is now the square grid except for an anomalous region where the triangular grid is more efficient (table 4). Although the probabilities are small, the triangular grid is as much as 91 percent less efficient than the square grid for two or more hits. The

TABLE 3.—*Probability of two or more hits with square grid*

Shape	Size of semimajor axis relative to square grid										
	0.50	0.55	0.60	0.65	0.70	0.75	0.80	0.85	0.90	0.95	1.00
1.0	0.000	0.062	0.180	0.341	0.540						
.9	.000	.022	.102	.228	.391						
.8	.000	.012	.051	.131	.254						
.7	.000	.007	.031	.076	.145	0.257					
.6	.000	.005	.020	.048	.091	.153	0.246				
.5	.000	.003	.013	.030	.057	.095	.151	0.227			
.4	.000	.002	.008	.018	.034	.057	.090	.134	0.190	0.260	0.346
.3	.000	.001	.004	.010	.018	.030	.048	.071	.101	.138	.182
.2	.000	.000	.002	.004	.008	.013	.021	.031	.043	.059	.078

TABLE 4.—*Percentage relative efficiency of triangular grid over the square grid for two or more hits*

Shape	Size of semimajor axis relative to square grid										
	0.50	0.55	0.60	0.65	0.70	0.75	0.80	0.85	0.90	0.95	1.00
1.0	0.0	−87.0	−49.9								
.9	.0	−91.4	−49.9	−14.5							
.8	.0	−90.9	−45.5	−25.1	−8.6						
.7	.0	−90.8	−44.3	−20.5	−8.0	−4.2					
.6	.0	−90.8	−43.8	−19.6	−6.1	−.1	0.2				
.5	.0	−90.7	−43.6	−19.2	−5.5	.8	1.3	0.1			
.4	.0	−90.7	−43.5	−19.0	−5.1	1.2	1.7	.5	−1.2	−2.6	
.3	.0	−90.7	−43.5	−18.9	−5.0	1.4	1.9	.6	−1.1	−2.5	−2.6
.2	.0	−90.8	−43.5	−18.9	−5.0	1.4	1.9	.7	−1.0	−2.5	−2.6

anomalous region where the triangular grid is more efficient is centered on a relative size of 0.80 and a shape of 0.2. This pattern suggests that the two measures of efficiency are approximately inversely related.

If the orientations of the target are plotted against the probabilities, it can be seen that the probability of one or more hits is inversely related to the probability of two or more hits (fig. 1). For both the square and triangular grids, the probability of one or more hits reaches a maximum when the orientation is such that the probability of two or more hits is zero. The displacement from the maximum is exactly equal to the increase in the probability of two or more hits. This relationship obviously does not hold when the probability of one or more hits is equal to one.

The anomalous regions in tables 2 and 4 thus represent particular size and shape ranges where the triangular grid is more likely to hit the target twice and, thus by the inverse relationship, less likely to hit the target once. This reduction in the probability of hitting the target once is reflected in the relative efficiencies.

SUMMARY AND CONCLUSIONS

The relative efficiencies of square and triangular grids used in the search for elliptical targets are calculated in terms of the probabilities of hitting such targets. Equivalent density grids are used to calculate the relative efficiencies of the grid types for various sizes and shapes of ellipses, where relative efficiencies are defined in terms of the percentage change in the probabilities of detection. The probabilities are defined in terms of the chance of hitting an ellipse one or more times and in terms of hitting the target two or more times, and relative efficiencies are calculated for each group.

When the probability of one or more hits is used, the grid types are equally efficient for targets with semimajor axes less than or equal to one-half of the grid spacing. For targets with relative sizes greater than 0.50, the triangular grid is as much as 6 percent more efficient than the square grid, except for a small region centered on a shape of 0.45 and a relative size of 0.80 where the square grid is more efficient. There is a trend toward equally efficient grids as the ellipses become more needlelike in shape. The grids are also equally efficient when the targets become so large that they cannot be missed.

A different situation occurs when the probability of two or more hits is used to define the relative efficiency. A random search is more efficient than both grid types

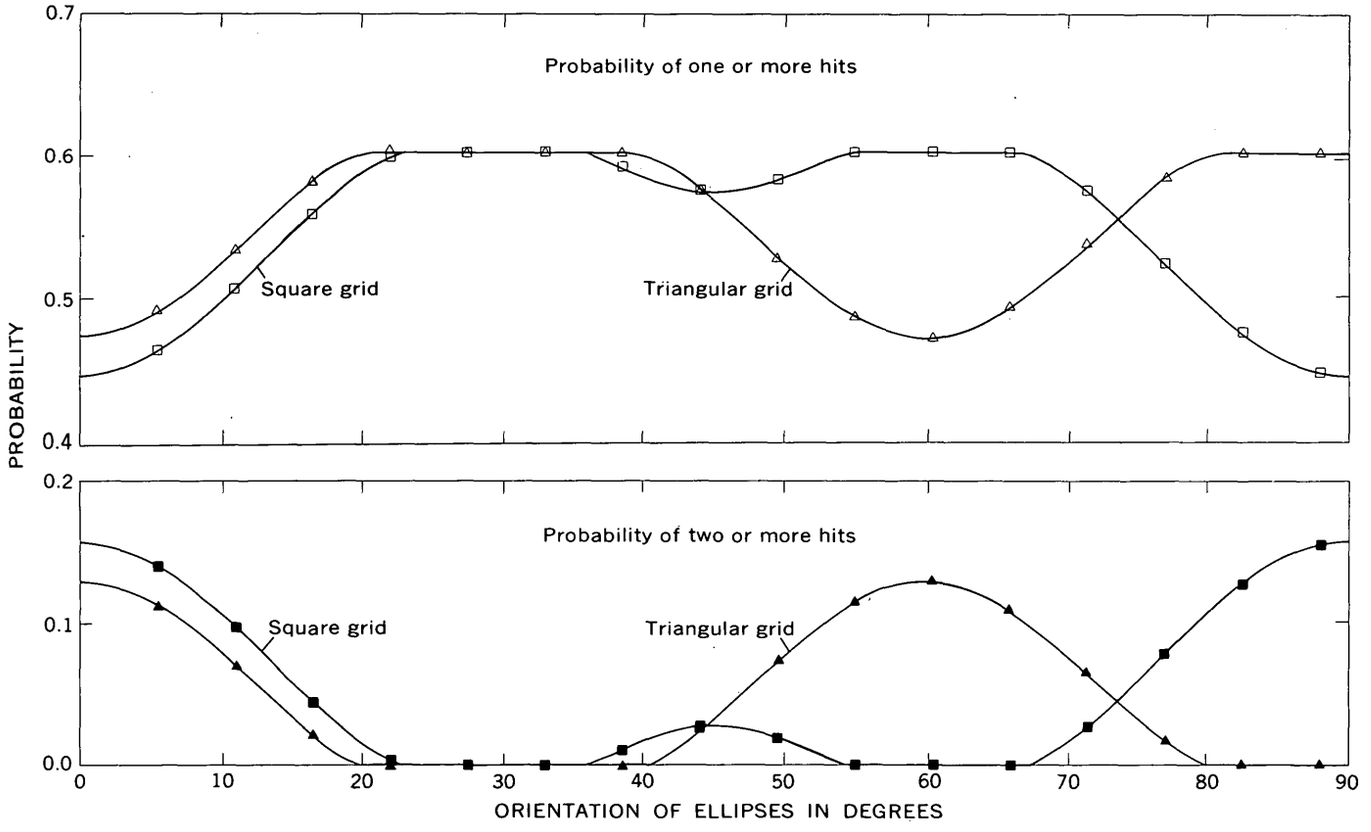

FIGURE 1.—Probability of one or more hits and of two or more hits for square and triangular grids at various orientations of ellipses to the grids. Semimajor axis equals 0.80 of square grid size; shape equals 0.3.

when the semimajor axis is less than or equal to one-half of the grid spacing because such a target cannot be hit twice with the grid but can be hit twice in a random search. For two or more hits, the triangular grid is as much as 91 percent less efficient than the square grid, except for an anomalous region centered on a relative size of 0.80 where the triangular grid is more efficient than the square grid. The probabilities are small, however.

The probability of one or more hits is inversely related to the probability of two or more hits for many target sizes and shapes. The anomalous region mentioned above represents particular size and shape ranges where the triangular grid is more likely to hit the target twice and, by the inverse relationship, less likely to hit the target once. The relative efficiencies reflect this inverse relationship.

If the criterion of success used is the probability of one or more hits, the triangular grid is recommended because it is as much as 6 percent more efficient and, at the worst, less than one-half of 1 percent less efficient in the small anomalous region. If the criterion of success is measured in terms of the probability of two or more hits, the square grid is recommended for those targets with semimajor axis greater than one-half of the grid spacing because the square grid is as much as 91 percent more efficient and, at worst, 4 percent less efficient than the triangular grid. It is important to note, however, that the probabilities of detection are rather small for two or more hits.

REFERENCES CITED

Celasun, Merih, 1964. The allocation of funds to reconnaissance projects: Colorado School Mines Quart., v. 59, no. 4, p. 169–186.

Drew, L. J., 1966, Grid drilling exploration and its application to the search for petroleum: University Park, Pennsylvania State Univ., unpub. Ph. D. thesis, 141 p.

———1967, Grid-drilling exploration and its application to the search for petroleum: Econ. Geology, v. 62, no. 5, p. 698–710.

Ellis, R. M., and Blackwell, J. H., 1959, Optimum prospecting plans in mineral exploration: Geophysics, v. 24, no. 2, p. 344–358.

Griffiths, J. C., 1966, Exploration for natural resources: Operations Research, v. 14, no. 2, p. 189–209.

Griffiths, J. C., and Drew, L. J., 1966, Grid spacing and success ratios in exploration for natural resources, *in* Internat. Symposium on Computers and Operations Research, 6th Ann., 1966: Pennsylvania State Univ., Mineral Industries Expt. Sta. Spec. Pub. 2–65, v. 1, p. Q1–Q24.

Griffiths, J. C., and Singer, D. A., 1973, Size, shape, and arrangement of some uranium ore bodies: Internat. Symposium Computer Applications in Mineral Industry, 11th, Tucson, Ariz., 1973, Proc., p. B82–B112.

Savinskii, I. D., 1965, Probability tables for locating elliptical underground masses with a rectangular grid: New York, Consultants Bur., 110 p.

Singer, D. A., 1972, Elipgrid, a Fortran IV program for calculating the probability of success in locating elliptical targets with square, rectangular, and hexagonal grids: Geocom Programs, no. 4, p. 1–16; also published in Geocom Bull. 5, no. 5–6.

Singer, D. A., and Wickman, F. E., 1969, Probability tables for locating elliptical targets with square, rectangular, and hexagonal point-nets: Pennsylvania State Univ., Mineral Sci. Expt. Sta. Spec. Pub. 1–69, 100 p.

Slichter, L. B., 1955, Geophysics applied to prospecting for ores, *in* Pt. 2 *of* Bateman, A. M., ed., Economic geology, 50th anniversary volume, 1905–1955: Urbana, Ill., Econ. Geology Pub. Co., p. 885–969.

Jour. Research U.S. Geol. Survey
Vol. 3, No. 2, Mar.–Apr. 1975, p. 169–179

LINKAGE EFFECTS BETWEEN DEPOSIT DISCOVERY AND POSTDISCOVERY EXPLORATORY DRILLING

By LAWRENCE J. DREW, Reston, Va.

Abstract.—For the 1950–71 period of petroleum exploration in the Powder River Basin, northeastern Wyoming and southeastern Montana, three specific topics were investigated. First, the wildcat wells drilled during the ambient phases of exploration are estimated to have discovered 2.80 times as much petroleum per well as the wildcat wells drilled during the cyclical phases of exploration, periods when exploration plays were active. Second, the hypothesis was tested and verified that during ambient phases of exploration the discovery of deposits could be anticipated by a small but statistically significant rise in the ambient drilling rate during the year prior to the year of discovery. Closer examination of the data suggests that this anticipation effect decreases through time. Third, a regression model utilizing the two independent variables of (1) the volume of petroleum contained in each deposit discovered in a cell and the directly adjacent cells and (2) the respective depths of these deposits was constructed to predict the expected yearly cyclical wildcat drilling rate in four 30 by 30 min (approximately 860 mi^2) sized cells. In two of these cells relatively large volumes of petroleum were discovered, whereas in the other two cells smaller volumes were discovered. The predicted and actual rates of wildcat drilling which occurred in each cell agreed rather closely.

The total level of wildcat drilling consists of two components, ambient (long-term regional exploration) and cyclical (exploration play [1]) wildcat drilling. The primary objective of this investigation is to estimate the efficiencies of these two types of wildcat drilling.

The ambient wildcat drilling component is characterized by the drilling of a few wells per year per cell according to long-range regional geological and geophysical studies.

The cyclical component of wildcat drilling is characterized by a rapid rise in the rate of wildcat drilling above the mean ambient rate followed by a more gradual return to the ambient rate. These cyclical surges in the wildcat drilling rate are usually initiated ("kicked off") by the discovery of a large deposit and, although the duration of exploration plays ranges widely, they usually continue 3 to 5 years. During the 1950–71 period, two major exploration plays occurred in the Powder River Basin, northeastern Wyoming and southeastern Montana: The Minnelusa Sandstone play, during the late 1950's and early 1960's, and the Muddy Sandstone play in the late 1960's and early 1970's. Several minor plays involving exploration for deposits in the Dakota and Parkman Sandstones occurred during the middle 1950's.

A second objective of the study is to determine the existence of a discovery-anticipation factor for deposits discovered during periods when only ambient wildcat drilling occurred. The specific hypothesis tested was that during ambient phases of exploration the discovery of a deposit could be anticipated by a small but significant rise in the ambient drilling rate in the discovery cell during the year prior to the year of discovery; the discovery of a deposit in a cell is often strongly suggested by the identification of anomalies in the analysis of regional geologic information. In other words, the enthusiasm generated by assembling and interpreting such data results in a small but significant surge in the ambient drilling rate during a short period prior to the actual discovery of a deposit.

A third objective is to test whether a regression model based upon data isolated from the ambient exploration record could be used successfully to predict the expected yearly cyclical wildcat drilling rate as a result of the multiple discoveries which occur during the relatively short duration of an exploration play. The validity of this model was tested in four cells, on the eastern flank of the basin, in which 10 to 60 discoveries occurred within relatively short periods of time (3–10 years).

Acknowledgments.—The input data were collected while the author was a research geologist with Cities Service Oil Co., Tulsa, Okla. I wish to gratefully acknowledge the support I received from Cities Service. Particular acknowledgment goes to Joseph Huffstetler who prepared several of the basic documents for this study. Sincere thanks also go to D. P. Harris of the Mineral Economics Department of the Pennsyl-

[1] Exploration play is the descriptive term given to the magnitude and time sequence of exploratory drilling and other exploration activities triggered by the discovery of an unexpectedly large deposit in a stratigraphic unit in a region not previously thought to have high-discovery potential.

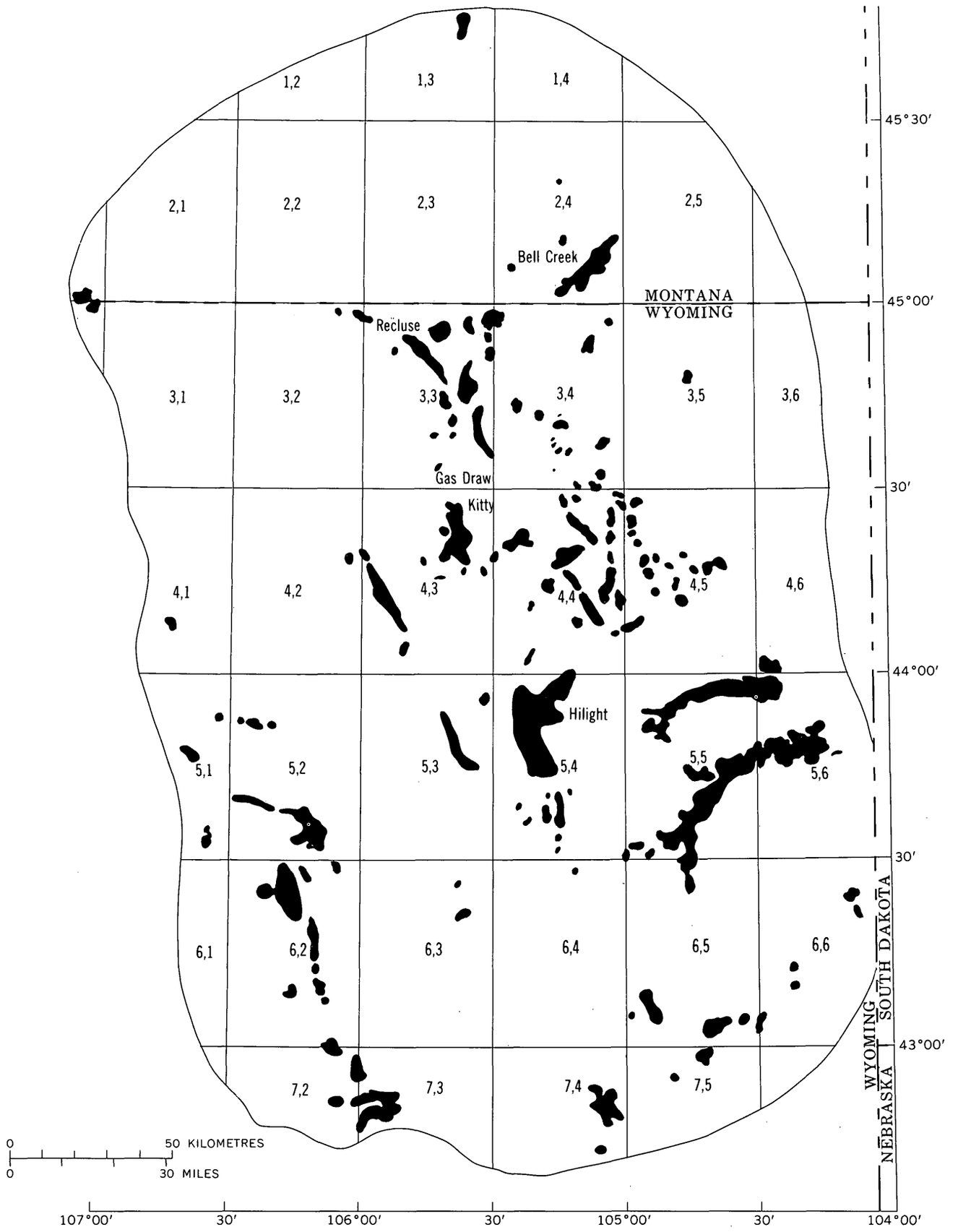

FIGURE 1.—Location of petroleum deposits and cells in the Powder River Basin.

vania State University for a thorough and very useful review.

SOURCES OF DATA AND DATA-GATHERING PROCEDURE

Wildcat drilling data were obtained from the Well History Control File (Petroleum Information, Inc.). Only those wells that had a wildcat predrilling intent designation (Lahee's classification[1]) were considered. These data were divided into subsets by individual years and plotted on 1:32,000-scale maps. A 30′ by 30′ grid was superimposed on each map and the number of wildcat wells drilled each year in each cell was tabulated (fig. 1 and 2). The volume of petroleum discovered in each cell each year is shown in figure 3. The number of deposits discovered each year and the average of their depths are shown in figures 4 and 5, respectively.

Estimates of the total productible petroleum contained in each deposit were obtained from confidential sources and also from The Oil and Gas Journal and Wyoming Geologic Survey publications.

[1] Lahee, F. H., 1944, Classification of exploration drilling and statistics for 1943: Am. Assoc. Petroleum Geologists Bull., v. 28, no. 6, p. 701–721.

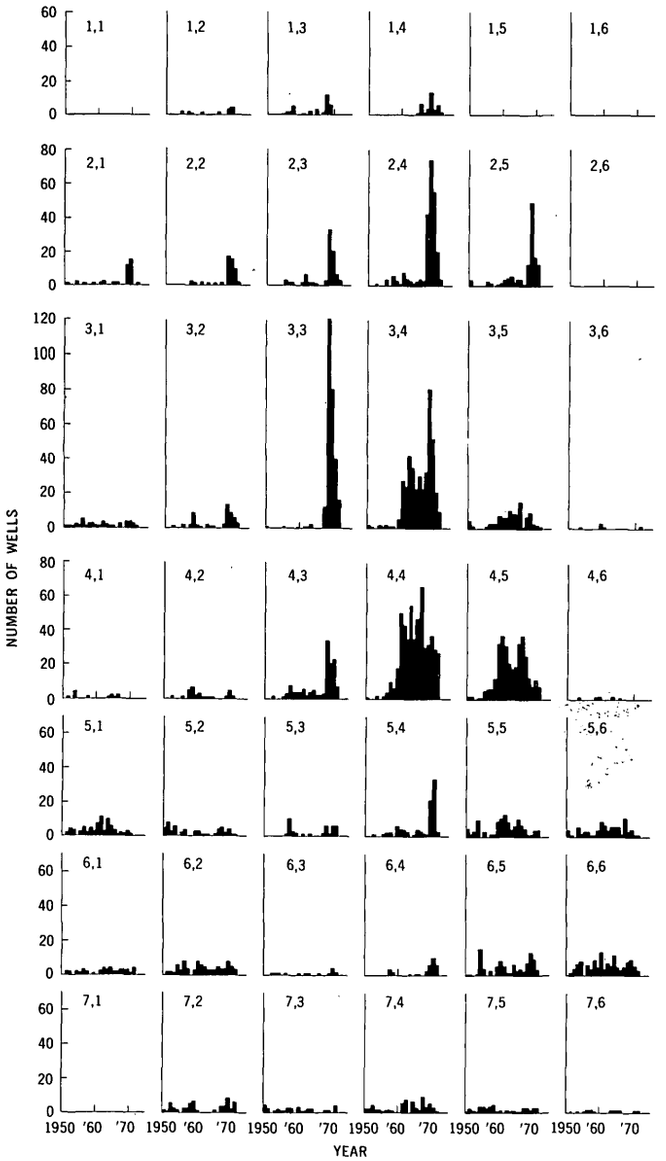

FIGURE 2.—Number of wildcat wells drilled each year.

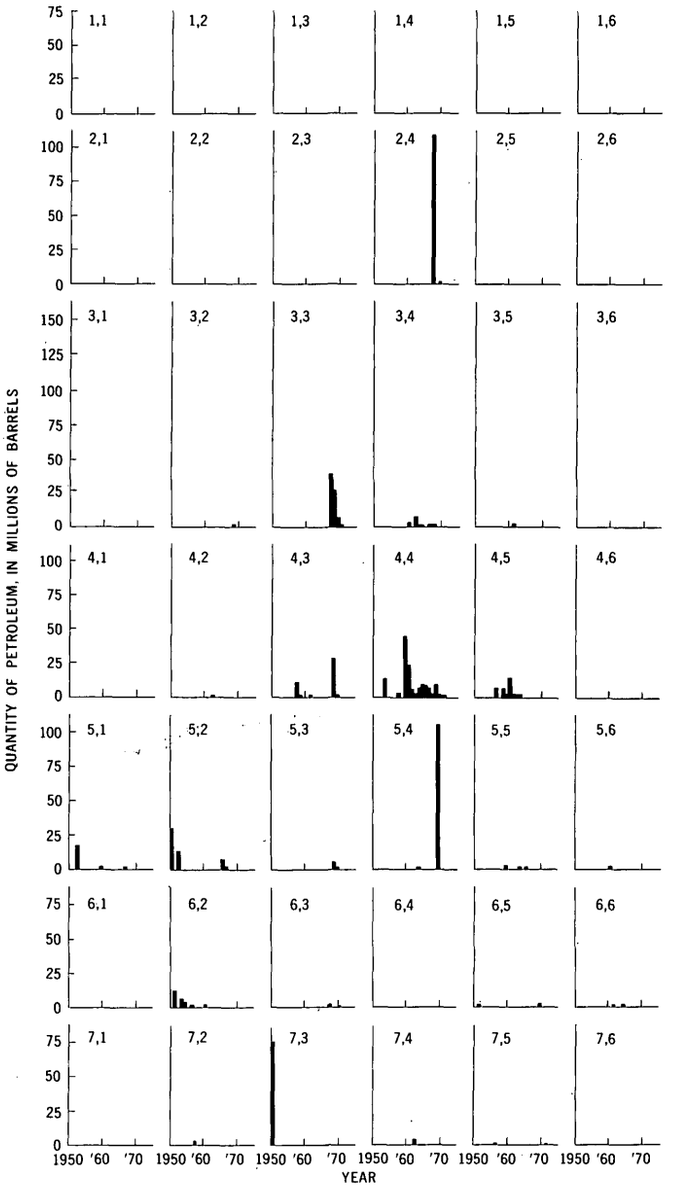

FIGURE 3.—Quantity of petroleum discovered each year.

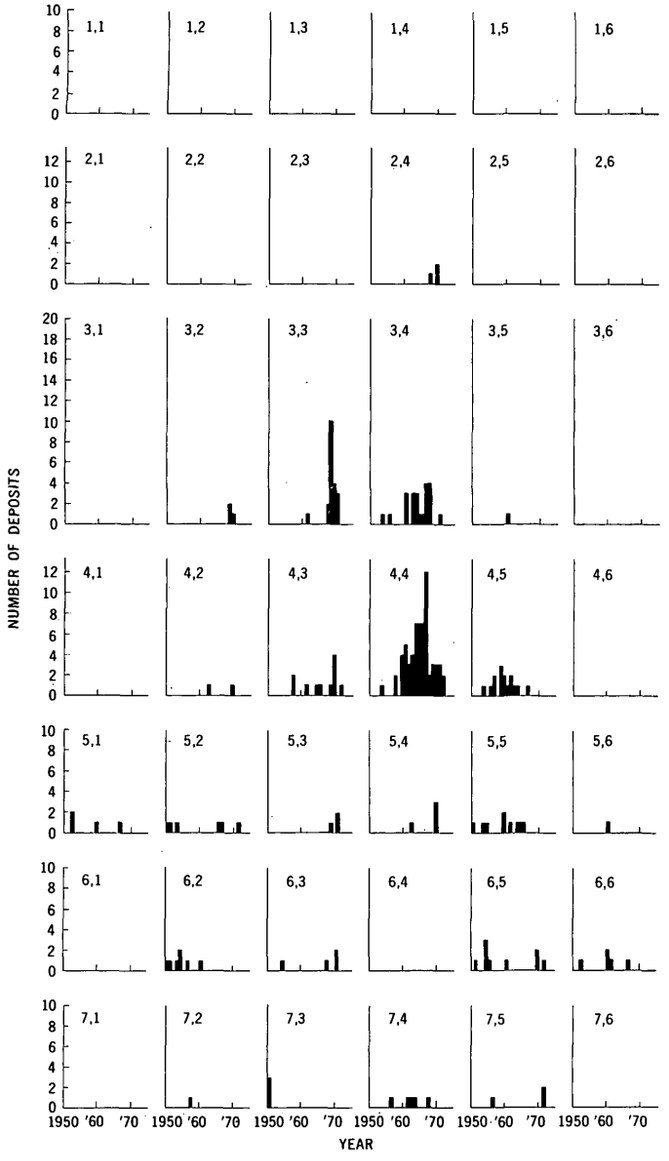

FIGURE 4.—Number of deposits discovered each year.

ANALYSIS

Efficiency of ambient versus cyclical wildcat drilling

The rate of ambient wildcat drilling in each cell was estimated by using the following rule: The observed intensity of wildcat drilling occurring in each cell in a given year is classified as ambient if no significant (greater than 500,000 barrels of producible petroleum) discoveries were made in the cell or any of the adjacent cells during that year or any of the three preceding years. For those years when the observed wildcat drilling rate in a cell was part of the surge attributable to an exploration play, the ambient wildcat drilling rate was estimated by using the mean ambient wildcat drilling rate for the cell. For example, the mean ambient wildcat drilling rate in cell 2,4 (fig. 2) per year for the years 1950–66 is 2.47 wells. In 1967, the discovery of the Bell Creek deposit "kicked off" the Muddy Sandstone play and resulted in a massive surge of wildcat drilling in cell 2,4 from 1967 to 1970. The author assumed that in this period, however, some operators remained insensitive to this play and drilled,

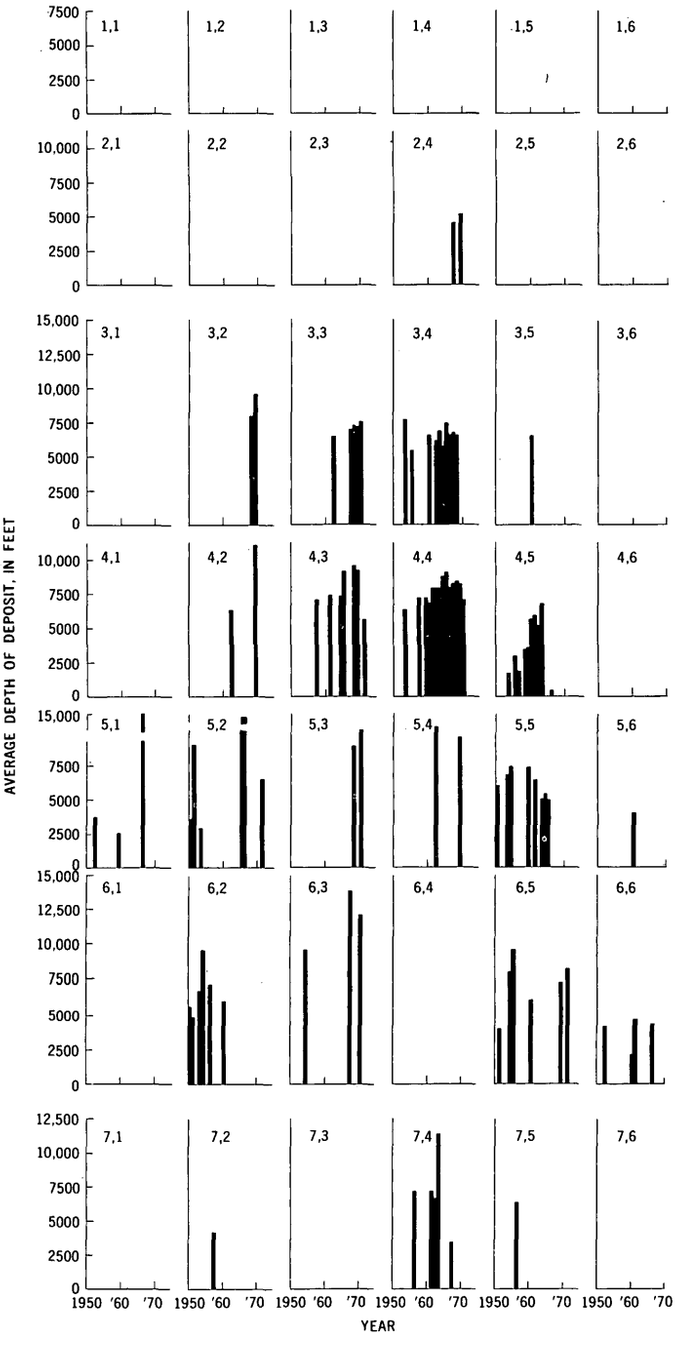

FIGURE 5.—Average depth of petroleum deposits discovered each year.

on the basis of the long-range regional geological and geophysical studies, an average of 2.47 wildcat wells each year.

The same rule was used to estimate the rate of ambient wildcat drilling in a cell affected by an exploration play even though no discoveries occurred within that cell itself. For example, the rate of wildcat drilling in cell 2,5 was strongly affected by the discovery of the Bell Creek deposit in cell 2,4.

The total number of ambient wildcat wells drilled during the 1950–71 period is estimated, on the basis of the data-processing methods just described, to be 1,146 wells, or 31.05 percent of the total 3,691 wildcat wells drilled in the basin during this period. By subtraction it follows that the total number of cyclical wildcat wells drilled is 2,545 wells, or 68.95 percent of the total number of wildcat wells drilled during the period.

The volume of petroleum discovered by each of the two components of wildcat drilling was determined by assigning deposits that were discovered during periods of cyclical wildcat drilling to the cyclical component and those discovered during periods of ambient wildcat drilling to the ambient component. During the 1950–71 period the total volume of petroleum discovered in the Powder River Basin is conservatively estimated to be the equivalent of 665,494,000 bbl. This estimate of reserves is not to be interpreted rigorously, because reserve estimates were available for only 38 of the larger 160 discoveries of this period. For the other 122 deposits, cumulative production figures through February 29, 1972, were used as estimates of the total producible petroleum. Of the total volume of petroleum discovered, 371,131,000 bbl (55.80 percent) were from the ambient component of wildcat drilling. Inasmuch as 31.05 percent of the total wildcat drilling resulted in discovery of 55.80 percent of the reserves, the ambient component is 2.80 times as effective as the cyclical component. In terms of the mean quantities of petroleum discovered per well, the mean ambient wildcat well discovered 323,734 bbl and the average wildcat well drilled during the cyclical phases of exploration discovered 115,520 bbl.

Although the mean quantity of petroleum discovered per wildcat well was nearly three times smaller during periods when exploration plays were active, the practice of following exploration plays rather than drilling regional prospects was not without its reward. The risk of failure was found to be substantially higher during the ambient phase, with only three and one half chances of success per hundred wildcat wells drilled. During the cyclical periods the chance of success rose to five wildcat wells per hundred being successful. Accepting a nearly three-to-one reduction in expected returns in order to increase the proportion of successful wells by 43 percent shows that the average operator in the basin had a strong aversion to risk. This aversion is so strong that it forced the average operator to accept and drill during exploration plays those prospects which returned on the average about 36 percent of that which was gained by drilling prospects based upon long-range regional evaluations.

The nearly three-to-one inefficiency of the cyclical wildcat drilling component over the ambient component could, perhaps, be significantly reduced through exploration lease-unitization procedures in which the rate of exploratory drilling in a region is restrained during the more active period of a play, thereby releasing substantial amounts of exploration capital for use in the more efficient ambient component of exploration.

The estimate of the 2.80 greater discovery efficiency of the ambient component of wildcat drilling may be considered conservative for two reasons. First, 372 ambient wildcat wells were estimated to have been drilled in cells during periods when exploration plays were active, but no estimate could be made of the volume of petroleum discovered by these wells. Only the deposit discovered at the start of the play was considered to be discovered by the ambient component. Second, it can be argued that once an exploration play begins in an area, ambient exploratory drilling stops immediately, attributing no wells to the ambient phase, thus implying that the above mentioned 372 wells assigned to the ambient component should be assigned to the cyclical component. The author reasons that this should not be done because some operators will be insensitive to the general enthusiasm generated by a play, particularly if targets in different stratigraphic units are being sought. However, if ambient wildcat drilling in a region does cease immediately once any exploration play gains momentum, the efficiency of ambient wildcat drilling would increase to 4.75 times that of cyclical drilling for the 1950–71 period of exploration in the Powder River Basin. In terms of mean quantities of petroleum per well, the mean ambient wildcat well would discover 479,497 bbl and the average well drilled during the cyclical phases of exploratory drilling would discover 100,913 bbl.

The frequency distributions of the volume of petroleum contained in the deposits discovered during both phases of exploration are shown in figure 6. Both of these distributions are bimodal in form. This bimodality is a consequence of the difference in the sizes of the deposits discovered in the two major productive

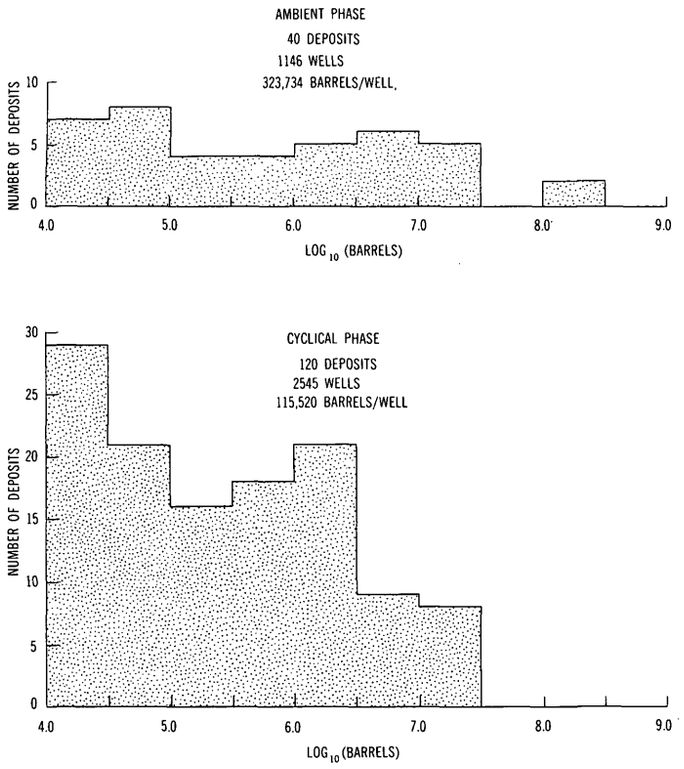

FIGURE 6.—Frequency distributions of the volume of petroleum discovered in the ambient and cyclical phases of exploration.

units in the study area. The deposits forming the peaks in the 6.0 to 7.0 logarithmic-units range are predominantly in the Minnelusa Sandstone, whereas the peaks in the 4.0 to 5.0 logarithmic-units range are predominantly small, single- or double-well deposits in the Muddy Sandstone Member. The general form of these two distributions, however, is somewhat different. The distribution describing the pattern of discovery of deposits during ambient phases of exploration is nearly uniform in shape, whereas that of the cyclical periods of exploration declined rather steeply with increasing deposit size. Therefore, the volume of petroleum contained in the deposit discovered during the ambient phases of exploration occurred with nearly equal probability across the entire range. In contrast, during the cyclical phases of exploration of the basin, smaller deposits are discovered more frequently than larger deposits.

Discovery-anticipation factor during ambient phases of exploratory drilling

Within the total record of ambient wildcat drilling a pattern appears which is characterized by the frequent occurrence of a small surge in the wildcat drilling rate in the year prior to the discovery of a deposit in a cell. This effect is hypothesized to be caused by the identification of anomalies in the analysis of regional geologic and (or) geophysical information; it is assumed that shortly after anomalies are identified, they are tested by drilling.

The existence of such an anticipation effect was tested using data from 13 discovery events isolated from the total record of ambient wildcat drilling. The structure of the statistical test was developed as follows: Compute the mean and standard deviation of the number of wildcat wells drilling during the 5-year period of ambient drilling ending 1 year prior to each of the 13 discoveries (fig. 7). For example, if a deposit was discovered during the year 1956, (the first discovery event plotted in fig. 7), the statistics were based upon the levels of ambient drilling which occurred during the 5-year period 1950–54. If the discovery of a deposit was anticipated, the rate of wildcat drilling during 1955, the year prior to discovery, should fall above an upper confidence limit determined from the statistics. Of the 13 discovery events which could be isolated for study, 6 were anticipated by such a rise.

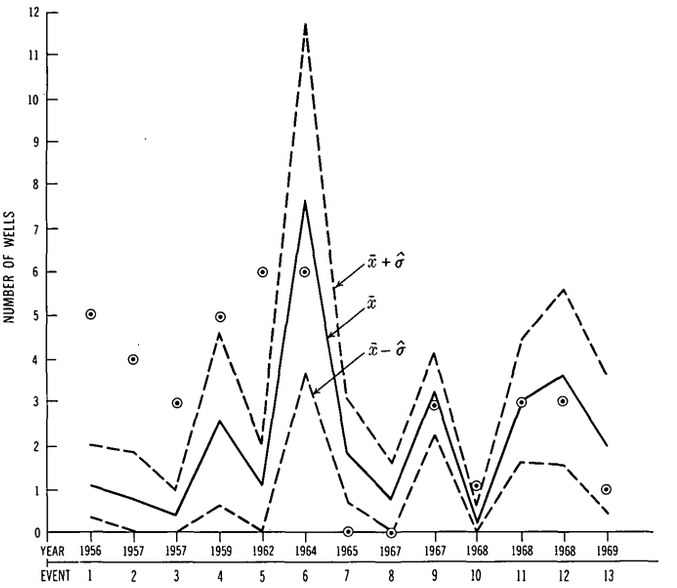

FIGURE 7.—Confidence interval for anticipation of discovery study. $\bar{x}$, mean number of wells; $\hat{\sigma}$, standard deviation of number of wells.

Using an upper confidence limit of one standard deviation and assuming that the normal law of errors describes the variability of the ambient drilling rate, the probability (P) that a discovery anticipation effect does not exist is less than one in a hundred:

$$P(r \geqq 6) = \sum_{r=6}^{13} \binom{13}{r} \cdot p^r \cdot (1-p)^{13-r} = 0.00997,$$

where $p = 0.1587$, the probability that the ambient rate of wildcat drilling will exceed the upper confidence level of one standard deviation in a single year (assuming the normal law of errors).

Thus, based upon the limited number of single discovery events which could be isolated from the total record, there is strong evidence that the discovery of deposits was anticipated by an increase in the ambient drilling rate during the year prior to discovery. Examination of figure 6 suggests, however, that this anticipation effect was not stable through time; all the significant positive deviations, with one exception, occurred during the first half of the time period. A plausible explanation for this phenomenon is that the deposits discovered during this earlier period occurred for the most part in structural traps, whereas the deposits discovered during the later half of the period occurred principally in stratigraphic traps. During the first half of the time period, local small-scale exploration targets were probably isolated by techniques which defined local structural closure in which deposits were subsequently discovered; the ability to define such targets thus caused the anticipation of discovering a deposit to rise significantly in a local area (cell). During the second half of the period, when stratigraphically trapped deposits were the principle objectives being sought, no techniques were available which could be used to define local small-scale exploration targets, the result being a much more spatially diffuse pattern of ambient wildcat drilling.

Prediction of the cyclical drilling rate with a regression model

Two regression equations were developed, tested, and found to be particularly useful in predicting the expected yearly rates of cyclical wildcat drilling in a cell where a large number of discoveries occurred within that cell and (or) in adjacent cells during periods when an exploration play was active. This model is based only on data from discovery events occurring during ambient phases of wildcat drilling in the basin. The first equation accounts for the contribution to the cyclical wildcat drilling rate caused by the discovery of deposits within the target cell in a given year or in either of the two previous years; this effect is called the "within-cell discovery effect." The second equation developed in the model accounts for that subcomponent of the cyclical wildcat drilling rate which is caused by a discovery in any of the four directly adjacent cells in a given year or either of the two previous years; this effect is called the "adjacent-cell discovery effect."

Eighteen discovery events (table 1) were isolated from the total record of ambient wildcat drilling and used to calculate the within-cell discovery effect equation:

$$E = 7.475 + 0.267 \cdot v - 0.000633 \cdot d + 1.178 \cdot t_1 - 1.225 \cdot t_2,$$

with $R^2 = 0.567$, $F = 16.01$, d.f. $= 49$, (significant at the 0.001 level),

where E = expected number of cyclical wildcat wells drilled in a cell as a result of the discovery of a deposit in that cell containing v million barrels of reserves at a depth of d feet,

t_1 = dummy variable for the second time period,

t_2 = dummy variable for the third time period,

$t_1 = 0$ and $t_2 = 0$ for the first time period,

$t_1 = 1$ and $t_2 = 0$ for the second time,

$t_1 = 0$ and $t_2 = 1$ for the third time period.

TABLE 1.—*Discovery events used to compute the "within-cell discovery effect"*

[Size of deposit in millions of barrels of reserves; F_A, area correction factor for boundary cells; R_A, mean ambient drilling rate for 5-year period prior to discovery, corrected for F_A; number of wildcat wells corrected for F_A; and YOD, year of discovery]

Discovery	Year	Cell	Size of deposit	Depth (feet)	F_A	R_A	Number of wildcat wells		
							YOD	YOD+1	YOD+2
Bell Creek	1967	2,4	110.000	4,532	1.00	2.6	42	74	55
Dead Horse Creek	1957	4,3	11.000	6,968	1.00	0.4	9	4	4
Mitchell Creek	1953	3,4	0.080	7,040	1.00	2.4	2	1	2
Barber Creek West	1962	4,2	0.400	6,868	1.00	1.0	1	1	0
Tisdale East	1959	5,1	2.200	2,244	1.72	3.1	5	12	19
Pheasant	1966	5,1	5.200	14,990	1.72	10.2	2	4	2
Reno	1965	5,2	6.200	14,942	1.00	1.2	1	4	5
Kitty	1965	4,3	30.000	9,089	1.00	3.2	34	21	23
Hilight	1969	5,4	135.000	9,575	1.00	1.0	21	34	4
Twenty Mile	1960	6,2	0.600	6,013	1.00	3.6	8	6	5
Powell	1954	6,2	0.001	9,480	1.00	1.2	1	0	1
Kaye	1969	6,5	3.000	5,467	1.00	4.8	13	10	4
House Creek	1968	5,3	4.500	8,257	1.00	0.4	6	2	6
North Fork	1952	5,1	16.000	6,486	1.72	1.4	4	9	8
Red Bird	1964	6,5	0.300	3,106	1.09	6.5	13	8	5
Moorcroft	1956	4,5	7.000	3,400	1.00	1.8	6	6	5
Slattary	1957	4,4	4.000	8,064	1.00	1.6	10	6	2
Donkey Creek	1953	4,4	13.000	6,400	1.00	0.4	2	0	2

Eleven discovery events (table 2) were isolated from the total record of ambient wildcat drilling and used to calculate the adjacent-cell discovery effect equation:

$$E = 10.899 + 0.0857 \cdot v - 0.000862 \cdot d_1 - 0.000765 \cdot d_2 + 8.309 \cdot t_1 - 0.709 \cdot t_2,$$

with $R_2 = 0.542$, $F = 6.52$, d.f. $= 27$ (significant at the 0.001 level),

where E = expected number of cyclical wildcat wells drilled in a target cell as a result of the discovery of a deposit in an adjacent cell containing v million barrels of reserves at a depth of d_1 feet; d_2 denotes the depth of the equivalent stratigraphic unit in the target cell,

t_1 = dummy variable for the second time period,

t_2 = dummy variable for the third time period.

The effectiveness of this model in predicting the aggregate behavior of cyclical wildcat drilling was tested using four cells (3,3, 3,4, 4,4, and 4,5), each of which experienced a large volume of wildcat drilling during various periods (see fig. 2).

Prediction of cyclical wildcat drilling in cell 3,3.—This cell experienced the greatest single yearly surge in wildcat drilling of any of the cells studied; in 1968 the rate rose to 121 wells from a rate of only 13 wells the previous year (fig. 2). With the exception of a single minor discovery in 1962, all the discoveries made in this cell through 1971 occurred during the 4-year period 1967–70. The tremendous exploration enthusiasm developed during this 4-year period is attributable to the Muddy Sandstone play which started in 1967 with the discovery of the large Bell Creek deposit in cell 2,4.

Figure 8 shows the actual rates of wildcat drilling in cell 3,3 and the rates predicted by the model. The predicted curve is based upon the petroleum reserves and depths of the 12 deposits discovered within cell 3,3 and on the 11 deposits discovered within three of the four directly adjacent cells (3,2, 3,4, and 4,3; no deposits were discovered during the period in cell 2,3, the cell directly adjacent to the north). An arbitrary cutoff for including deposits in the predictions was set at a minimum of 500,000 bbl.

Of the 234.48 cyclical wildcat wells predicted for cell 3,3 during the total time period, 159.18 wells (67.03 percent) are attributed to the within-cell discovery effect. During the period 1967–71, when the Muddy Sandstone exploration play was active in this cell, the cyclical rate of wildcat drilling is practically the total wildcat drilling rate because the mean rate of ambient wildcat drilling is estimated to be only 0.41 well per year. The agreement between the actual rate of cyclical drilling and that predicted by the model is close, with the exception of the year 1968. During this year, 121 wells were drilled in the cell as compared to 61.2 predicted by the model. This discrepancy would be substantially reduced if the effects of discoveries in diagonally adjacent cells had been considered in the model; in this particular example a large deposit (the Bell Creek deposit) was discovered in cell 2,4 during the previous year (1967), which seemingly influenced in part the tremendous rise in exploration enthusiasm in cell 3,3 during the following year. A regression equation characterizing such a "diagonal-cell discovery effect" could not be computed from the current data set because only four diagonal-cell discovery events could be isolated from the total record of ambient wildcat drilling. This is only about one-fourth the number of data points required to compute a "reliable" equation characterizing this effect.

Prediction of cyclical wildcat drilling in cell 3,4.—The variation in the intensity of wildcat drilling

TABLE 2.—*Discovery events used to compute the "adjacent-cell discovery effect"*

[Size of deposit in millions of barrels of reserves; depth in adjacent cell is that of equivalent stratum; F_A, area correction factor for boundary cells; R_A, mean ambient drilling rate for 5-year period prior to discovery in adjacent cell, corrected for F_A; number of wildcat wells drilled in adjacent cell, corrected for F_A; and YOD, year of discovery]

Discovery	Year	Size of deposit	Discovery cell	Adjacent cell	Depth in discovery cell (feet)	Depth in adjacent cell (feet)	F_A	R_A	Number of wildcat wells drilled in adjacent cell		
									YOD	YOD+1	YOD+2
Bell Creek	1967	110.0	2,4	2,5	4,532	3,200	1.00	3.4	13	48	17
	1967	110.0	2,4	1,4	4,532	5,280	2.00	1.8	8	26	6
	1967	110.0	2,4	2,3	4,532	6,928	1.00	1.0	3	33	7
Dead Horse Creek	1957	11.0	4,3	4,2	6,968	7,266	1.00	1.0	5	7	2
	1957	11.0	4,3	5,3	6,968	6,931	1.00	0.2	10	5	2
Twenty Mile	1960	0.6	6,2	6,3	6,013	12,400	1.00	0.2	1	0	1
Kitty	1965	30.0	4,3	4,2	9,089	10,907	1.00	0.4	1	5	2
Hilight	1969	135.0	5,4	6,4	9,575	10,258	1.00	1.0	6	10	6
North Fork	1952	16.0	5,1	4,1	6,486	7,185	1.25	0.2	1	5	1
Kaye	1969	3.0	6,5	7,5	5,467	6,978	2.04	2.0	4	6	6
	1969	3.0	6,5	6,6	5,467	5,127	1.09	7.2	10	7	4

in this cell is far more complex than that in cell 3,3 (see fig. 2). During the period 1960–71 only nine deposits were discovered in this cell, none of which contained more than 6 million barrels of producible petroleum (see fig. 3). However, 425 wildcat wells were drilled in the cell during this 12-year period, and it should, therefore, be expected that the predominant force causing the high rate of wildcat drilling in this cell is the discovery of numerous deposits in the adjacent cells. Indeed, the fact is that 45 deposits, each containing more than 500,000 bbl of producible petroleum, were discovered in the four adjacent cells. The surge in the wildcat drilling rate during the earlier part of this period (1960–66) is attributable to the Minnelusa Sandstone play which was concentrated in cell 4,4, the cell directly adjacent to the south. During this 7-year period some 40 deposits were discovered in this cell in the Minnelusa Sandstone (fig. 4). The variation in the wildcat drilling rate during the period 1967–70 is attributed predominantly to the Muddy Sandstone play which was located principally in the cell adjacent to the north (cell 2,4), and also in a cell directly adjacent to the west (cell 3,3).

The predicted and actual rates of wildcat drilling for the 1950–71 period for this cell are shown in figure 9. The form and magnitude of the two curves are in reasonably close agreement. The predicted magnitude of the cyclical wildcat drilling component for the total period 1950–71 is 460.55 wells. Of this total only 72.00 wells (15.63 percent) are attributed to the within-cell discovery effect. The remaining 385.55 wells (84.37 percent) are predicted to have been drilled as a result of a surge in the expectation of discovering deposits in this cell similar to the 45 deposits discovered in the four directly adjacent cells. Thus, the cyclical wildcat drilling component in this cell is almost wholly attributable to the adjacent-cell discovery effect, which contrasts with drilling behavior observed in cell 3,3 which is predominantly attributable to the within-cell discovery effect.

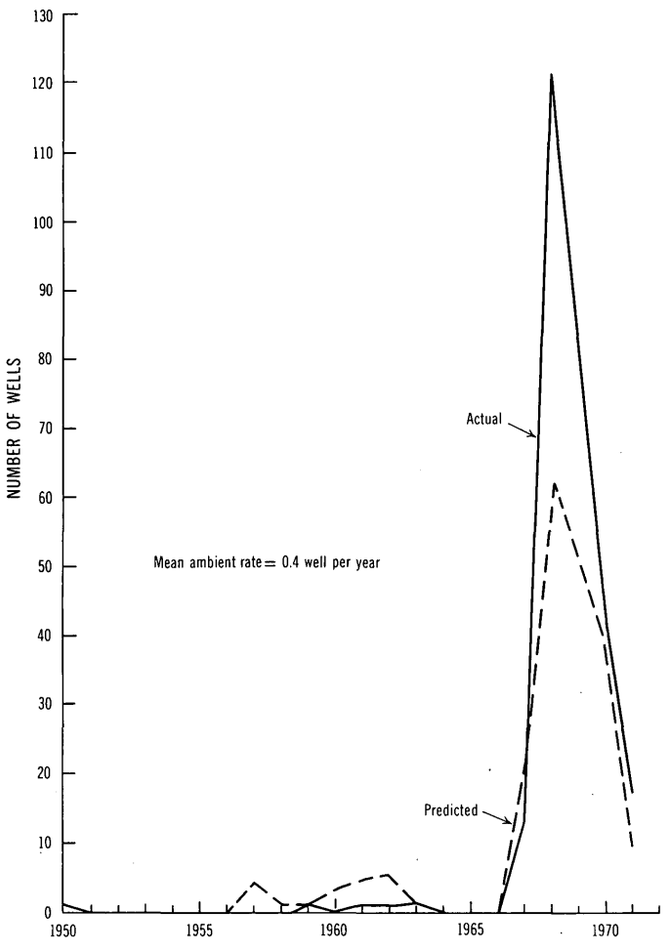

FIGURE 8.—Actual and predicted rates of wildcat drilling in cell 3,3 (cyclical only).

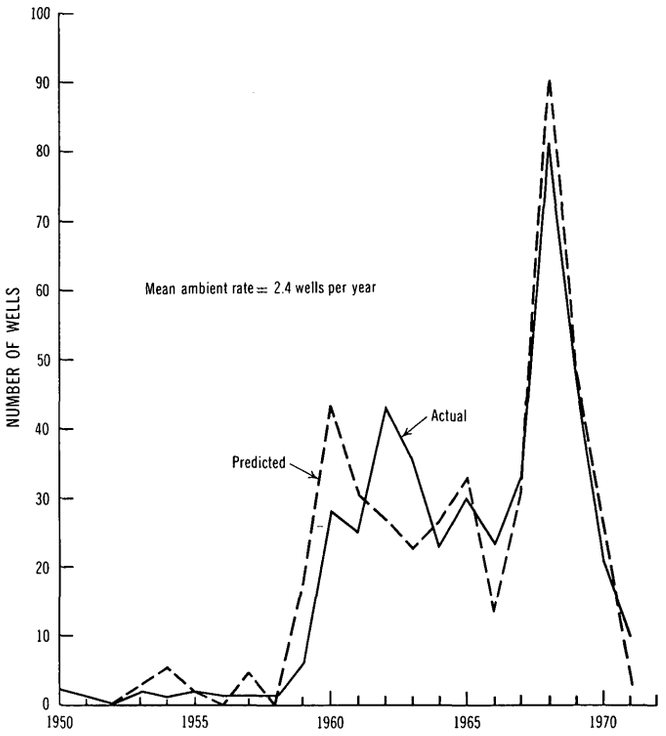

FIGURE 9.—Actual and predicted rates of wildcat drilling in cell 3,4 (cyclical only).

Prediction of cyclical wildcat drilling in cell 4,4.— In this cell 62 deposits were discovered during the 1950–71 period (fig. 4). Most of these deposits were discovered in Minnelusa Sandstone and collectively contained at least 125 million barrels of producible petroleum (fig. 3). Half of these deposits, however, individually contained less than 500,000 bbl of pro-

ducible petroleum. In the four directly adjacent cells, 19 deposits, each containing at least 500,000 bbl of producible petroleum, were discovered during this period. During the period in which both the Minnelusa Sandstone and Muddy Sandstone plays were active (1957–71), 522 wildcat wells were drilled in the cell (fig. 2). On the basis of the 31 deposits containing at least 500,000 bbl of producible petroleum discovered in the cell and the 19 deposits discovered in the four directly adjacent cells, the model predicts a total of 499.63 wildcat wells to be subsequently drilled in the cell. Of this total, 324.81 wells (65.01 percent) are attributed to the within-cell discovery effect and 174.81 wells (34.99 percent) to the adjacent-cell discovery effect.

Figure 10 shows the predicted and actual rates of wildcat drilling in the cell. The correspondence between the form and magnitude of the two curves is, again, judged to be good; a surprisingly close agreement exists between the total number of wildcat wells drilled during the 1957–71 period (522 wells) and the sum of the predicted number of cyclical and ambient wildcat wells (499.63 + 22.0 = 521.63 wells).

Prediction of the cyclical wildcat drilling in cell 4,5.—The behavior of the cyclical component of wildcat drilling in this cell is attributable principally to the adjacent-cell discovery effect, as was also the situation for cell 3,4. Only six deposits, each containing a minimum of 500,000 bbl of producible petroleum, were discovered within this cell. In contrast, 35 such deposits were discovered in the four directly adjacent cells during the 1950–71 period. Figure 11 shows the actual and

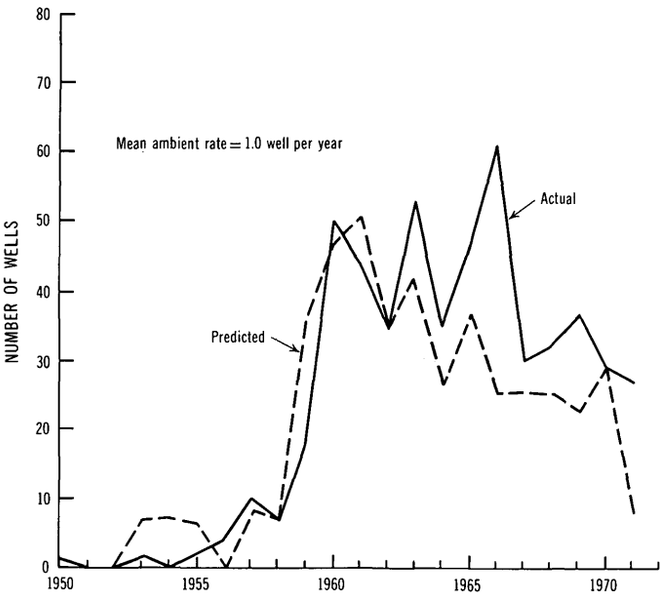

FIGURE 10.—Actual and predicted rates of wildcat drilling in cell 4,4 (cyclical only).

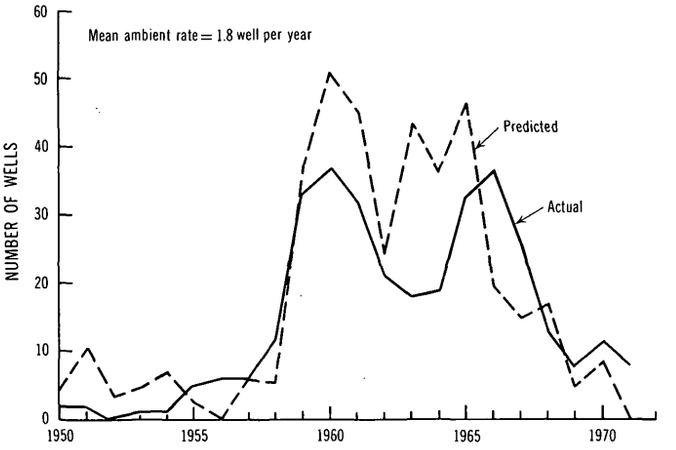

FIGURE 11.—Actual and predicted rates of wildcat drilling in 4,5 (cyclical only).

predicted rates of wildcat drilling in the cell. Although only about 15 million barrels of petroleum were discovered in this cell during the 1950–71 period, a total of 312 wildcat wells were drilled during the period when both the Minnelusa Sandstone and Muddy Sandstone plays (1957–71) were active. The model predicts that during this period only 91.87 (24.95 percent) of the predicted total of 368.27 cyclical wildcat wells were drilled as a result of the discovery of deposits within the cell and the remaining 276.40 wildcat wells (75.05 percent) are attributable to the discovery of deposits in the four adjacent cells.

CONCLUSIONS

For the 1950–71 period of exploration for petroleum deposits in the Powder River Basin, the efficiency factor for ambient versus cyclical wildcat drilling is estimated to be 2.80. In terms of the average quantity of petroleum discovered per well, the average ambient wildcat well discovered 323,734 barrels per well versus 115,520 barrels per well for the average wildcat well drilled during the cyclical phases of exploration.

Although the mean quantity of petroleum discovered per wildcat well was nearly three times lower during periods when exploration plays were active, the practice of following exploration plays rather than drilling regional prospects was not without its reward. The risk of failure was found to be substantially higher during the ambient phase, with only three and one half chances of success per hundred wildcat wells drilled. During the cyclical periods the chance of success rose to five wildcat wells per hundred being successful. Accepting a nearly three-to-one reduction in expected returns in order to increase the proportion of successful wells by 43 percent shows the average operator in the basin had a strong aversion to risk. This aversion

is so strong that it forced the average operator to accept and drill during exploration plays prospects which returned on the average only about 36 percent of that which was gained by drilling prospects based upon long-range regional evaluations.

This nearly three-to-one inefficiency in the cyclical versus ambient wildcat drilling components could possibly be significantly reduced by using exploration lease unitization procedures.

Statistical evidence exists to support the hypothesis that the discovery of deposits during ambient phases of exploration is anticipated by a small, but statistically significant rise in the ambient wildcat drilling rate during the year prior to the year in which a deposit is discovered. This anticipation phenomenon, however, is not stable through time. During the first half of the 1950–71 period, when the principle exploration targets being sought were located in structural traps, the anticipation of deposit discovery is clearly evident. In contrast, during the later half of the period, when stratigraphic traps were the principal targets being sought, no evidence exists to support the hypothesis.

A regression model was used to predict the expected rates of cyclical wildcat drilling in four cells in which large amounts of wildcat drilling occurred. The surge of exploration enthusiasm generated by the exploration play phenomenon affected the rates of cyclical wildcat drilling differently in each of the four cells studied. For example, in one cell the exploration play phenomenon influenced the rates of wildcat drilling during only a single 4-year period (1967–70). During this period, however, the most extreme variation in the yearly wildcat drilling rate occurred; 121 wildcat wells were drilled in 1968, whereas only 13 wells were drilled in 1967. This massive increase in the cyclical wildcat drilling rate was predicted by the model to be predominantly (67.03 percent) caused by the discovery of deposits within the cell. By contrast, the cyclical wildcat drilling occurring in another cell studied was attributed almost wholly (84.37 percent) to the discovery of deposits in the four directly adjacent cells.

Jour. Research U.S. Geol. Survey
Vol. 3, No. 2, Mar.–Apr. 1975, p. 181–185

AN INTEGRATED-INTENSITY METHOD FOR EMISSION SPECTROGRAPHIC COMPUTER ANALYSIS

By CATHARINE P. THOMAS, Reston, Va.

Abstract.—An integrated-intensity method has been devised to improve the computer analysis of data by emission spectrography. The area of the intensity profile of a spectral line is approximated by a rectangle whose height is related to the intensity difference between the peak and background of the line and whose width is measured at a fixed transmittance below the apex of the line. The method is illustrated by the determination of strontium in the presence of greater than 10 percent calcium. The Sr 3380.711-A line, which is unaffected by calcium and which has a linear analytical curve extending from 100–3,000 ppm, has been used to determine strontium in 18 standard reference rocks covering a wide range of geologic materials. Both the accuracy and the precision of the determinations were well within the accepted range for a semiquantitative procedure.

Visual semiquantitative analysis by emission spectrography is not only tedious but is also subject to the personal bias of the analyst. To circumvent these problems, data by such semiquantitative analyses are now processed by the computer to determine the concentrations of 68 elements in silicate rocks. The samples are arced in an argon-oxygen atmosphere under carefully controlled conditions. The spectra are recorded on a 102- by 508-mm (4- by 20-in) photographic plate. Dorrzapf (1973) has described conditions for the arcing and for the plate development. Transmittance readings, taken every 5 μm along each spectrum, are recorded on magnetic tape. Helz (1973) has described the magnetic tape system used to record transmittances from the plate. The data on the magnetic tape are processed by a computer master program, written in Fortran IV, described in detail by Walthall (1974). This paper describes a method for determining elemental concentrations, based on the integrated intensities of spectral lines, which is implemented by a subprogram of the master program.

THE COMPUTER PROGRAM

The master program examines the data and searches for a maximum of 500 preselected spectral lines over the wavelength region 2332–4750 A. It also calibrates the plate emulsion for every 250-A interval and uses this information to convert transmittances to intensities. Concentrations of 68 elements are calculated, on the basis of the coefficients of the analytical curves, which are internally stored in the computer, and on the peak and background intensities of each spectral line. The program also corrects for spectral interferences and selects the best concentration from among the concentrations computed from all lines available for each element. The selection is based on the optimal concentration range of each line and a scheme that instructs the computer to examine analytical lines in a preselected order of priority. The maximum priority is given to lines with high sensitivity and freedom from interference. If the transmittance of a spectral line is less than 2 percent, a very small change in transmittance corresponds to a very large change in intensity. This results in an increased relative error in determining intensities at the extremes of the calibration curve for the plate emulsion. To avoid this error, the computer program defines peaks having less than 2 percent transmittance as too dark for analysis. When a peak is too dark, the computer is programed to report "greater than the upper concentration limit of this line" and to consider the next line in the ordered priority. Some elements have only a few analytical lines, and all may be too dark because of the concentration of the element or because of interferences. It was therefore desirable to develop an alternate computational procedure, amenable to computer usage, to be applied when such problems occur.

DETERMINATION OF LINE INTENSITIES IN SPECTROGRAPHIC ANALYSIS

Chaney (1967) has shown that there are distinct advantages to relating integrated intensities, rather than the more frequently used peak intensities, to concentrations on calibration lines. Such lines based on integrated intensities are more linear, and, being unaffected by self-absorption, extend over longer concentration ranges. Winefordner (1963) has emphasized that one should clearly indicate whether one measured the peak intensity at the line center, the integrated intensity, or some intermediate thereof, when reporting spectro-

chemical data. Our recorded transmittance readings are made on the darkest part of the line, which is converted to the peak line intensity. The integrated intensity I of a spectral line is proportional to the instantaneous intensity i, the exposure time t, and the spectral wavelength λ. It can be represented by the integral equation:

$$\int (I)\, d\lambda = k \int_{\lambda_1}^{\lambda_2} \int_0^t i\, dt\, d\lambda \qquad (1)$$

where k is a constant. The photographic emulsion performs the integration for the exposure time, leaving the integration for the wavelength to be done by other means. DeGalen and Winefordner (1968) have discussed the modification of the intensity profile of a line by the slit function of the spectrometer, $S\ (\Delta\lambda)$. This spectral distribution, or the irradiance, $E\ (\lambda)$, is responsible for the darkening of the photographic plate:

$$E\ (\lambda) = \int_{\alpha}^{\alpha} S\ (\Delta\lambda)\ I\ (\lambda - \Delta\lambda)\ d\Delta\lambda. \qquad (2)$$

They have examined the Gaussian and Lorentzian intensity profiles of spectral lines modified by triangular, Gaussian, and Lorentzian slit functions and have shown that:

$$\int E\ (\lambda)\ d\lambda = I_0\, b\, s\, k \qquad (3)$$

where: I_0 = peak intensity,
b = line width parameter of the spectral line intensity profile,
s = width of the slit function, and
k = constant related to the geometry of the optics and shapes of the line profile and slit function.

If the slit width and spectrometer optics remain constant between analyses, then for any given spectral line the spectral distribution can be approximated by a rectangle of height I_0 and width b. The width of the line remains constant until the concentration of the element becomes so great that self-absorption occurs. At this point, the peak intensity of the line remains relatively constant as the line broadens. The integrated intensity (the area of the rectangle, $I_0 b$), however, remains directly proportional to the concentration of the element (Chaney, 1967).

We have used this relation between the peak intensity, the line width, and the concentration of the element to devise an integrated-intensity method which has improved our spectrochemical computer analyses. The intensity profile of the spectral line is studied under different concentration and matrix conditions to determine how it may best be approximated by a rectangle. The transmittance, at which to measure the width of the rectangle, is chosen to discriminate against interferences from neighboring spectral lines and simultaneously to minimize the effect, on the area of the rectangle, of a variation of ± 1 reading, in the width, inherent in any digital representation of a continuous function such as a line profile. To minimize the relative error in converting from transmittance to intensity at the extremes of the plate-emulsion calibration curve, a fixed transmittance, determined by the shape and behavior of the particular spectral line in use, is added to all peak transmittances. This procedure enhances the reproducibility of computations based on very dark peaks and has little deleterious effect on the light peaks. This integrated-intensity method has been applied to the determination of high concentrations of strontium in a calcium matrix. Previously, such a determination would have required a special spectrochemical treatment and a separate plate exposure, because in this matrix under routine arcing conditions, the strontium lines are too dark for a determination based solely on peak intensities. Special determination conditions are incompatible with computer spectrographic analysis which produces semiquantitative analyses for many elements in a suite of samples, on the basis of one exposure per sample.

SPECTROGRAPHIC DETERMINATION OF STRONTIUM IN GEOCHEMICAL SAMPLES

Strontium is the fifteenth most abundant trace element in the Earth's crust (Mason, 1966, p. 45–46). Chemically, it is similar to calcium, the fifth most abundant element. Both calcium and strontium are concentrated primarily in the feldspar mineral group of silicate rocks. Both elements form large divalent cations. According to Taylor (1966), Sr^{+2} with a radius of 1.18 A tends to replace Ca^{+2} with a radius of 0.99 A in the lattice of plagioclase. In spite of the tendency for strontium to concentrate in calcium-rich minerals, Turekian and Kulp (1956) found no coherence between strontium and calcium in most rock types on a worldwide basis. They suggested that the distribution of strontium in basaltic rocks is primarily governed by regional differences in the strontium content of the source magma and magmatic differentiation, rather than simple coherence with calcium. However, Turekian and Kulp reported positive correlations between strontium and calcium in granitic rocks and deep-sea sediments.

The partial geochemical coherence between strontium and calcium and the high calcium content of most rocks make it desirable to be able to measure strontium in the presence of large amounts (>10 percent) of calcium. Strontium emits intense lines between 2332 A and 4750 A that are suitable for spectrochemical computer analysis. Turekian, Gast, and Kulp (1957) reported that the intensity of the Sr 4607.3-A line is

greatly affected by rock matrices, especially by those high in alkali metals and calcium. They proposed a procedure for spectrochemical analysis, based on dilution of the sample with strontium-free calcium carbonate to buffer the sample and to minimize the effect of variation of calcium from sample to sample, and used the Ca 4578.56-A line as an internal standard for Sr 4607.3 A. This method is unsuitable for the simultaneous determination of calcium and strontium. It is also unsuitable for spectrochemical computer analysis, because, even with the 47-percent neutral density filter routinely used, the peak transmittances of these lines are normally less than 2 percent. Therefore, the lines are too intense to use when calculating concentrations from peak intensities alone. Furthermore, Sr 4607.3 A is a resonance line and is therefore particularly subject to self-absorption at high strontium concentrations.

The spectrochemical computer analysis scheme at the U.S. Geological Survey reports the concentration of strontium as one of the concentrations computed from the peak intensities of the strontium lines listed in table 1. The spectral line used in the analysis is that line with the lowest priority number, which reports an answer within its concentration range. Auxiliary lines, denoted by priority numbers greater than 19, are used for comparison because they duplicate concentration ranges already covered by other lines in the priority scheme. The analytical curves for lines with priority numbers in the 20's are based on peak intensities, whereas those for lines with priority numbers in the 30's are based on integrated intensities. Auxiliary lines are used for analysis only when lines of greater priority are affected by interference. For example, when the concentration of strontium in a geological sample is greater than 464 ppm but less than 1 percent, the program chooses the concentration reported by either priority line 4 or 5. A problem arises if the sample also contains greater than 10 percent calcium, because Ca 4161.806 A interferes with Sr 4161.795 A. If the sample contains more than 1 percent iron, the concentration from Sr 2931.830 A must be corrected for Fe 2931.81 A.

TABLE 1.—*Strontium lines used in analysis*

Priority No.	*Wavelength (A)*	*Concentration range (percent)*
1	4077.715	0.000046– 0.000215
2	4607.31	0.000100– 0.00316
3	3464.457	0.00147 – 0.0464
4	4161.796	0.00464 – 0.1470
5	2931.830	0.0681 – 6.81
6	2569.469	1.00 –46.4
7	2428.095	2.15 –46.4
21	3307.534	0.1470 – 6.81
22	3380.711	0.00100 – 0.0681
31	3380.711	0.0100 – 0.300

When these analytical problems arise, they are now circumvented by skipping to the priority 31 line which applies the integrated-intensity method to the Sr 3380.711-A line. For this particular spectral line, the width of the rectangle is defined as the number of transmittance readings within 1 percent of the peak transmittance. The height of the rectangle is defined as the difference between the intensities corresponding to the background transmittance and the peak transmittance plus 0.5 percent. The calibration curve for this line, based on the integrated intensity, extends from 100 ppm to 3,000 ppm (fig. 1). No major constituents of rocks pose interference problems. However, the lines Ni 3380.885 A and Ni 3380.574 A bracket the Sr 3380.711-A line and are of similar intensity. Therefore, if the nickel and strontium concentrations are of the same order of magnitude, the nickel will cause interference and the computer will print "H," for interference, instead of a strontium concentration on the report form. Fortunately, such interferences are seldom found in most rocks high in strontium.

The strontium concentrations of 18 standard reference rocks representing a variety of geologic materials are given in table 2. Concentrations, computed by the integrated-intensity method, are compared with accepted strontium concentrations. The accuracy and precision of the analyses are both well within the expected range of +50 and −33⅓ percent of the accepted value for the regular semiquantitative spectro-

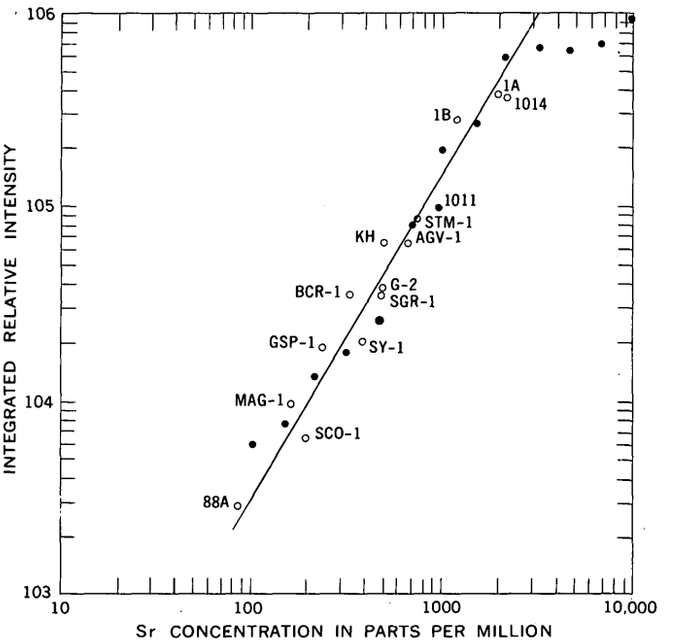

FIGURE 1.—Analytical curve for Sr 3380.711 A. Solid circles indicate intensities at various Sr concentrations. Rocks analyzed, indicated by open circles and symbols, are identified in table 2.

graphic method used in this laboratory. Table 3 illustrates the need for an alternate method of strontium concentration computation in the presence of a calcium interference. The strontium concentrations reported in table 3 are based on the unmodified priority scheme shown in table 1 and on peak-intensity calculations. Now when the computer detects a calcium concentration greater than 7 percent, it is programed to select the strontium concentration reported by the priority 31 line, resulting from the integrated-intensity method as applied to Sr 3380.711 A, in preference to a concentration resulting from the peak-intensity method as applied to Sr 4161.796 A or Sr 2931.830 A, the priority 4 and 5 lines.

TABLE 2.—*Comparison of* Sr *concentrations, computed using the integrated-intensity method on* Sr *3380.711–A line, with accepted* Sr *concentrations in a variety of geochemical reference samples*

Rock identification	Rock type	Number of analyses	Sr accepted (ppm)	Sr reported (ppm)	Accuracy (percent)	Standard deviation (percent)
NBS–88A	Dolomitic limestone	2	[1] 84.6	96	13	----
99	Soda feldspar	6	[2] 150	130	−13	16
USGS–SCO–1	Cody Shale	6	[3] 192	180	−6.3	27
MAG–1	Marine mud	6	[3] 168	190	13	25
GSP–1	Granodiorite	6	[4] 233	300	29	4.0
SSC–SY–1	Syenite	1	[5] 286	300	4.9	----
NBS–98	Plastic clay	6	[2] 300	390	30	15
USGS–QLO–1	Quartz latite	6	[4] 329	330	−.30	15
BCR–1	Basalt	6	[4] 330	420	27	9.7
SGR–1	Green River Formation	5	[3] 445	390	−12	----
G–2	Granite	6	[4] 479	440	−8.1	6.7
ZGI–KH	Limestone	2	[4] 490	600	22	----
USGS–AGV–1	Andesite	6	[4] 657	740	13	17
STM–1	Nepheline syenite	6	[4] 710	690	−2.8	4.8
NBS–1011	Portland cement	1	[1] 960	780	−19	----
1B	Limestone	3	[1] 1,200	1,200	0	----
1A	Limestone	2	[6] 1,900	1,700	−11	----
1014	Portland cement	1	[1] 2,200	1,700	−23	----

[1] National Bureau of Standards recommended value.
[2] U.S. Geological Survey, Reston, Va., visual emission spectroscopy.
[3] U.S. Geological Survey, Reston, Va., X-ray fluorescense.
[4] Flanagan (1973).
[5] Sine, Taylor. Webber, and Lewis (1969).
[6] U.S. Geological Survey, Reston, Va., atomic absorption.

TABLE 3.—*Comparison of* Sr *concentrations computed using the peak-intensity method with accepted* Sr *concentrations in a variety of geochemical reference samples*

Rock identification	Ca accepted (percent)	Sr accepted (ppm)	Sr reported (ppm)	Accuracy (percent)	Relative standard deviation (percent)	Sr line used for analysis (A)
NBS–88A	[1] 21.5	[1] 84.6	38	−56	--	4161.796
99	[1] .16	[2] 150	120	−20	7.3	3464.457
USGS–SCO–1	[3] 1.83	[3] 192	220	+15	3.5	3464.457
MAG–1	[3] 1.01	[3] 168	190	+13	2.0	3464.457
GSP–1	[4] 1.44	[4] 233	320	+37	4.1	3464.457
SSC–SY–1	[5] 7.29	[6] 286	420	+47	--	4161.796
NBS–98	[1] .15	[2] 300	330	+10	2.7	3464.457
USGS–QLO–1	[4] 2.29	[4] 329	440	+34	12	3464.457
BCR–1	[4] 4.97	[4] 330	430	+30	2.9	3464.457
SGR–1	[3] 6.34	[3] 445	560	+26	6.8	4161.796
G–2	[4] 1.39	[4] 479	600	+25	4.2	4161.796
ZGI–KH	[4] 34.1	[4] 490	940	+92	--	4161.796
USGS–AGV–1	[4] 3.56	[4] 657	910	+38	7.8	4161.796
STM–1	[4] .829	[4] 710	840	+18	4.9	4161.796
NBS–1011	[1] 47.1	[1] 960	<681	----	--	2931.830
1B	[1] 36.4	[1] 1,200	<681	----	--	2931.830
1A	[1] 29.5	[6] 1,900	850	−55	--	2931.830
1014	[1] 45.1	[1] 2,200	870	−60	--	2931.830

[1] National Bureau of Standards recommended value.
[2] U.S. Geological Survey, Reston, Va., visual emission spectroscopy.
[3] U.S. Geological Survey, Reston, Va., X-ray fluorescence.
[4] Flanagan (1973).
[5] Sine, Taylor, Webber, and Lewis (1969).
[6] U.S. Geological Survey, Reston, Va., atomic absorption.

REFERENCES CITED

Chaney, C. L., 1967, Integrated spectral-line intensities: Spectrochim. Acta, v. 23A, no. 1, p. 1–14.

DeGalen, L., and Winefordner, J. D., 1968, Slit function effects in atomic spectroscopy: Spectrochim. Acta, v. 23B, no. 4, p. 277–289.

Dorrzapf, A. F., Jr., 1973, Spectrochemical computer analysis —argon-oxygen d-c arc method for silicate rocks: U.S. Geol. Survey Jour. Research, v. 1, no. 5, p. 559–562.

Flanagan, F. J., 1973, 1972 values for international geochemical reference samples: Geochim. et Cosmochim. Acta, v. 37, no. 5, p. 1189–1200.

Helz, A. W., 1973, Spectrochemical computer analysis—instrumentation: U.S. Geol. Survey Jour. Research, v. 1, no. 4, p. 475–482.

Mason, Brian, 1966, Principles of geochemistry [3d ed.]: New York, John Wiley and Sons, 329 p.

Sine, N. M., Taylor, W. O., Webber, G. R., and Lewis, C. L., 1969, Third report of analytical data for CAAS sulfide ore and syenite rock standards: Geochim. et Cosmochim. Acta, v. 33, no. 1, p. 121–131.

Taylor, S. R., 1966, The application of trace element data to problems in petrology, *in* Ahrens, L. H., and others, eds., Physics and chemistry of the earth, [v.] 6: Oxford, Pergamon Press, p. 133–213.

Turekian, K. K., Gast, P. W., and Kulp, J. L., 1957, Emission-spectrographic method for the determination of strontium in silicate materials: Spectrochim. Acta, v. 9, no. 1, p. 40–46.

Turekian, K. K., and Kulp., J. L., 1956, The geochemistry of strontium: Geochim. et Cosmochim. Acta, v. 10, nos. 5–6, p. 245–296.

Walthall, F. G., 1974, Spectrochemical computer analysis—Program description: U.S. Geol. Survey Jour. Research, v. 2, no. 1, 61–71.

Winefordner, J. D., 1963, The effect of spectrometer slit width on intensity of atomic emission lines in emission flame photometry and the effect of source line width on absorbance of atomic absorption lines in absorption flame photometry: Applied Spectroscopy, v. 17, no. 5, p. 109–111.

Jour. Research U.S. Geol. Survey
Vol. 3, No. 2, Mar.–Apr. 1975, p. 187–190

SPECTROPHOTOMETRIC–ISOTOPE DILUTION DETERMINATION OF ARSENIC IN SOILS AND ROCKS

By FLOYD W. BROWN, FREDERICK O. SIMON, and L. PAUL GREENLAND,
Reston, Va.

Abstract.—Arsenic in soil and rock samples may be determined in part-per-million concentrations using a radiochemical-isotope dilution method. Arsenic in the sample plus added As^{76} tracer is separated as arsine and determined spectrophotometrically as a molybdenum blue complex. The As^{76} activity in the absorbing solution allows corrections for chemical losses. A lower limit of 1 ppm is determinable in a 0.5-g sample.

The silver diethyldithiocarbamate (AgDDC) method in conjunction with the separation of arsenic as arsine by the action of zinc in hydrochloric or sulfuric acid media (Vašák) and Šedivec, 1952) is widely used for determining arsenic. The most serious concern when evolving arsine is the generally accepted fact that certain metals tend to alter the rate of or restrict the evolution of arsine. Others cause rapid and violent evolution of hydrogen, leading to difficulties in the absorption of arsine. Whitnack and Martens (1971) recognized that the formation of molybdenum and vanadium arsenite complexes would suppress the evolution of arsine. Heavy metals are especially likely to interfere and Sandell (1959) suggested that this method be used only when they are absent. There are conflicting reports as to the amounts that can be tolerated and the particular metals which interfere with the evolution. Sandell (1959) states that chromium and molybdenum may be present in reasonably large amounts without interference, whereas Brown, Skougstad, and Fishman (1970) state that chromium and molybdenum interfere with the evolution of arsine.

Another concern when evolving arsine is the inherent possibility of losing arsenic if the joints of the apparatus are not immediately and properly connected to form a tight seal when zinc is added to the flask.

Approximately 5,000 soil and rock samples were analyzed to determine part-per-million concentrations of arsenic; a fast and accurate procedure was necessary. Initially it was decided that the commonly used silver diethyldithiocarbamate (Dubois and others, 1969) method be used for the analysis. During the investigation of the AgDDC method for suitability, several splits of the USGS standard diabase W–1 were analyzed for arsenic. The results from several analysts showed that the arsenic values consistently ranged from 1.4 to 1.6 ppm. The generally accepted neutron activation values for arsenic ranged from 2.2 to 2.79 ppm. The low results obtained by the AgDDC method showed the need to develop a more reliable method for the determination of arsenic. An AgDDC–isotope dilution method was attempted on W–1 standards; the results showed arsenic values ranging from 1.6 to 2.9 ppm.

The authors feel that a suitable AgDDC–isotope dilution method can be developed, but the disadvantage of the unpleasant odor of pyridine calls for the development of an alternative method, especially if large numbers of samples are to be analyzed.

Another problem which exists is the instability of the AgDDC reagent. We have found on occasion that some commercially available AgDDC reagents were not acceptable; there appears to be a tendency during preparation of the reagent for the silver to be reduced, leading to a subsequent breakdown of the complex and to a poorer sensitivity for the detection of arsenic.

The problems associated with the evolution of arsine are of no concern once yields are determined, thus suggesting the development of a radiochemical-isotope dilution method. In the procedure described in this report, arsenic is separated as arsine and determined as a molybdenum blue. Arsenic losses are corrected by determining the As^{76} activity.

The sample is fused with sodium peroxide and sodium hydroxide in the presence of As^{76} tracer. After cooling, the melt is transfererd with water to the generation flask and acidified with hydrochloric acid. Quinquevalent arsenic is reduced to the trivalent state by the addition of stannous chloride and potassium iodide solutions. Arsine is generated by the addition of zinc shot and the evolving gas absorbed and oxidized

to arsenic acid in iodine-potassium iodide-sodium bicarbonate solution. The arsenic yield is determined by counting the 0.56 MeV γ-ray photopeak of As^{76} with a single-channel analyzer. The solution is heated with the ammonium molybdate-hydrazine sulfate reagent to develop the blue color, and the absorbance is measured at 840 nm in a 1-cm cuvette using the reagent solution alone as the reference. Standards ranging from 1 to 10 μg As are carried through the procedure, corrected for yield, and the amount of arsenic is determined from the standard curve.

The proper choice of apparatus and instrumentation can save considerable time for the analyst. The use of an automatic micropipet is ideally suited for introducing the arsenic tracer. A spectrophotometer equipped with a "micro flow-thru system" provides a rapid method for reading a series of samples by eliminating the use of cells and by reading the color solution directly from the 4-dram vials. Three people working together can complete 200 samples a week.

EXPERIMENTAL METHOD

Reagents and Apparatus

Stannous chloride solution: Dissolve 40 g of $SnCl_2 \cdot 2H_2O$ in 100 ml concentrated HCl.

Potassium iodide solution: Dissolve 15 g of KI in 100 ml of water.

Zinc shot: Arsenic free.

Iodine-potassium iodide solutions: Dissolve 0.25 g of iodine in a small volume of water containing 0.5 g of potassium iodide and dilute to 100 ml.

Sodium bicarbonate solution: Dissolve 4.2 g of $NaHCO_3$ in 100 ml of H_2O.

Sodium metabisulfite: Dissolve 0.5 g of $Na_2S_2O_5$ in 10 ml of water.

Ammonium molybdate-hydrazine sulfate solution: Prepare just before use by mixing 10.0 ml each of solutions 1 and 2 and by diluting the mixture to 100 ml with water. Solution 1: Dissolve 1.0 g of $(NH_4)_6Mo_7O_{24} \cdot 4H_2O$ in 10 ml of water and add 90 ml of 5 *N* H_2SO_4. Solution 2: Dissolve 0.15 g of $H_2NNH_2 \cdot H_2SO_4$ in 100 ml of water.

Cotton pads: Approximately 0.5 in.^{2}; soak in 10 percent lead acetate solution. Squeeze out excess liquid and dry overnight at 60°C.

As^{76} tracer: Irradiate 1.5 mg of As_2O_3 for 4 h in a neutron flux of 5×10^{13} n·cm^{-2}·s^{-1}, dissolve in 10 ml of 2 percent NaOH, add 5 g of NaOH, and dilute to 1 litre. If arsenic tracers are purchased, the radiochemical purity should be determined prior to use.

Counting equipment: A 3- by 3-in. NaI(Tl) detector coupled with a single-channel analyzer. The window of the analyzer is set to encompass the 0.56 MeV γ-ray of As^{76}.

Arsine generator: The apparatus described in Fisher Catalog 70 was used.

Procedure

1. Pipet 0.100 ml of arsenic tracer into zirconium crucibles, add 1 pellet NaOH, and evaporate to dryness on a steam bath.
2. Weigh 0.500 g of sample and 2.5 g of sodium peroxide into the crucible, cover, and heat to dull redness for 15–20 min or until decomposition is complete.
3. Cool, leach the melt with approximately 8 ml of water, transfer to the generation flask, and wash the crucible with approximately 3 *N* HCl, adding the washings to the generation flask. Dilute to approximately 25 ml.
4. Slowly add 10 ml of concentrated hydrochloric acid with swirling motion.
5. Add 1 ml of potassium iodide solution and 2 ml of stannous chloride solution to reduce As^{+5} to As^{+3}. Allow to stand at room temperature for 15 min. If solution does not turn colorless, heat on a steam bath for 10 min and add additional stannous chloride solution until it does.
6. Pipet 1.0 ml of iodine-potassium iodide solution and 0.2 ml of sodium bicarbonate solution into the absorption tube.
7. Add 8.0 g of zinc shot to the generation flask and quickly insert the absorber. Allow the arsine to bubble through the absorbing solution for 15 min.
8. Transfer iodine–potassium iodide–sodium bicarbonate solution into 4-dram screwcap vials.
9. Determine the yield of arsenic by counting the As^{76} with a single-channel analyzer.
10. Add 5.0 ml of ammonium molybdate-hydrazine sulfate solution, one drop of sodium metabisulfite solution, and mix (the iodine color disappears).
11. Cover the vial with a watchglass and heat on a steam bath for 15 min. Cool to room temperature.
12. Measure the absorbance at 840 nm in a 1-cm cuvette using the ammonium molybdate-hydrazine sulfate solution as the reference.

Standard Curve

Standards are prepared by pipetting 1 to 10 μg As into zirconium crucibles and by proceeding with steps 1–12 above.

A counting standard is prepared by pipetting 0.1 ml of arsenic tracer into a 4-dram vial.

Calculations: Correct the amount of As taken for the standard curve and the sample weights for the yield determined with As^{76}. From the corrected standard curve, determine the amount of arsenic in each sample and divide by the corrected sample weight to obtain the arsenic concentration of the samples. A lower limit of 1 ppm can be determined on a 0.50 sample. Greater sensitivity can be obtained by using a longer cell path and by taking a larger sample weight. Typical data and calculations are given in table 1.

TABLE 1.—*Typical data and calculations for determining amount of arsenic in parts per million in samples*

[Rs, counting rate of processed standards and sample; R_B, counting rate of background, 344 counts/20 s; Rc, counting rate of unprocessed standard, 22,384 counts/20 s]

Standards and sample	Rs (counts/20 s)	Yield $\left(\frac{Rs-R_B}{Rc-R_B}\right)$	Standard curve	
			Absorbance	μg As (μg in std × yield)
1-μg std	16,582	0.737	0.050	0.737
5-μg std	16,028	.711	.199	3.56
8-μg std	16,450	.731	.318	5.85
10-μg std	11,236	.494	.268	4.94
0.5-g sample	16,536	.735	.183	----

CALCULATIONS.—
Sample absorbance=0.183
μg As from standard curve=3.2

$$\text{ppm As in sample}=\frac{\mu g\ As}{\text{sample weight} \times \text{yield}}=\frac{3.2}{0.5 \times 0.735}=8.7$$

Results and Discussion

This procedure has been designed for the rapid determination of arsenic using normal care in analytical techniques. Two steps, however, are critical for maintaining precision and accuracy. The addition of the tracer is obviously an important step and must be administered carefully so as to transfer the same amount to each sample and standard. The second critical step is the molybdenum blue color formation. Reagents must be added precisely, but the time of the heating is not critical as long as the color has fully developed. The blue complex which is formed is stable for 5–6 h.

The use of zinc shot rather than granular zinc is preferred to limit the rate of evolution of hydrogen. If the hydrogen gas is evolved too vigorously, incomplete absorption of arsine may result or a portion of the absorbing solution may be lost by bubbling over the neck of the absorption tube.

The arsenic yields varied from 40 to 90 percent, depending on the analyst and the types of samples analyzed. However, whether the yield was high or low, the duplicate checks of samples showed good agreement, lending credence to the method. The variation in yields observed here emphasizes the need for tracer corrections in routine analysis.

Almost 300 soil samples containing 2 to 100 ppm As were analyzed in duplicate by various analysts over a period of a year. The standard deviation calculated from the duplicates is given in table 2 for several

TABLE 2.—*Analytical precision*

Range of As content (ppm)	Number of samples	Standard deviation (ppm)
2.0– 5.0	34	0.47
5.1– 15	176	1.1
16 – 50	81	1.8
50 –100	6	2.1

ranges of As content. These data indicate an analytical precision of ±10 to 20 percent for the lowest As content (<5 ppm), decreasing to better than ±5 percent for arsenic contents exceeding 50 ppm. We also analyzed 32 samples of the USGS standard rock W–1 over a period of several months; these results yielded a mean of 2.2 ppm and a relative deviation of 11 percent. It is apparent that the analytical precision is entirely adequate for routine analysis.

Table 3 compares our analysis of a USGS standard rock with values obtained by neutron activation techniques. Neutron activation is an entirely independent method generally regarded to be of high accuracy; therefore, the good agreement of our value with the activation results confirms the accuracy of this procedure. It should be noted that the slightly lower "recommended" value of Flanagan (1973) incorporates several results by the AgDDC method which, as discussed above, tends to give low values, and it is probable, then, that the actual As content of W–1 is higher than the "recommended" value.

TABLE 3.—*Comparison of* As *determinations in USGS standard rock W–1*

[All values obtained by neutron activation method except as indicated]

As (ppm)	Reference
2.79	Fleischer, 1969.
2.24	Fleischer, 1965.
2.2	Fleischer and Stevens, 1962.
2.53	Do.
2.19	U.S. Geological Survey, unpub. data, 1973.
[1]1.9	Flanagan, 1973.
[2]2.2±0.25	This report.

[1] A "recommended" value which incorporates several results by the AgDDC method.
[2] Value obtained by spectrophotometric–isotope dilution method described in this report.

REFERENCES CITED

Brown, Eugene, Skougstad, M. W., and Fishman, M. J., 1970, Methods for collection and analysis of water samples for dissolved minerals and gases: U.S. Geol. Survey Techniques Water Resources Inv., book 5, chap. A1, 160 p.

Dubois, L., Teichman, T., Baker, C. J., Zdrojewski, A., and Monkman, J. L., 1969, Interferences in the measurement of arsenic by the method of Vašák and Šedivec: Mikrochim. Acta, p. 185–192.

Flanagan, F. J., 1973, 1972 values for international geochemical reference samples: Geochim. et Cosmochim. Acta, v. 37, p. 1189–1200.

Fleischer, Michael, 1965, Summary of new data on rock samples G–1 and W–1, 1962–1965: Geochim. et Cosmochim. Acta, v. 29, p. 1263–1283.

——— 1969, U.S. Geological Survey standards–I. Additional data on rocks G–1 and W–1, 1965–1967: Geochim. et Cosmochim. Acta, v. 33, p. 65–79.

Fleischer, Michael, and Stevens, R. E., 1962, Summary of new data on rock samples G–1 and W–1: Geochim. et Cosmochim. Acta, v. 26, p. 525–543.

Sandell, E. B., 1959, Colorimetric determination of traces of metals [3d ed.], volume 3 *of* Colorimetric metal analysis: New York, Interscience Publishers, Inc., 1,032 p.

Vašák, V., and Šedivec, V., 1952, Colorimetric determination of arsenic: Chem. Listy [Prague], v. 46, p. 341.

Whitnack, G. C., and Martens, H. H., 1971, Arsenic in potable desert ground water—an analysis problem: Science, v. 171, p. 383–385.

Jour. Research U.S. Geol. Survey
Vol. 3, No. 2, Mar.–Apr. 1975, p. 191–195

ANALYSIS FOR TELLURIUM IN ROCKS TO 5 PARTS PER BILLION

By JOHN R. WATTERSON and GEORGE J. NEUERBURG, Denver, Colo.

Abstract.—In the proposed method, a 12.5-g sample is digested with nitric acid and evaporated to dryness; the excess nitric acid is removed by reaction with formic acid. Tellurium is extracted from the dried residue into hydrobromic acid and is then coprecipitated with arsenic, using hypophosphorous acid as the reducing agent. The precipitate is dissolved in a solution of hydrobromic acid and bromine, from which the tellurium is extracted into 0.6 ml of methyl isobutyl ketone. Tellurium content is estimated by atomic absorption spectrophotometry. Recovery of tellurium from nitric acid solutions carried through the procedure approached 100 percent through the analytical range 5–200 ppb. The relative standard deviation of five consecutive analyses of USGS standard rock GSP–1 was 5.26 percent at a mean concentration of 20.8 ppb. Under optimum conditions an average of 20 samples may be analyzed per man-day.

In a previous U.S. Geological Survey study (Gott and Botbol, 1972), 12,000 samples of soils and rocks from the Coeur d'Alene district, Idaho, were analyzed for tellurium by a method sensitive to 100 ppb (Nakagawa and Thompson, 1968). Although only 10 percent of these samples contained tellurium above the limit of detection, they defined a deep mineralized zone and stimulated further interest in the geochemistry of this element. The 5-ppb method presented here roughly reverses the percentages of rock samples falling above and below the limit of detection of the previous atomic absorption method.

Tellurium in soil above the Montezuma stock, central Colorado, shows a pattern only partly attributable to known mineralization (Neuerburg, 1971; fig. 1, this report). Nearly all of 500 rock samples had tellurium contents below 100 ppb, and most of these contained between 5 and 50 ppb tellurium. While the low tellurium content of these rocks seemingly excludes them as a source of the soil tellurium, a tellurium pattern in the rocks that is analogous to that in the soils would suggest some type of genetic relationship. Data produced by the more sensitive (5 ppb) method indicate a possible rock source (fig. 1*D*), as well as a vein source (fig. 1*C*), for soil tellurium in the southeast quarter of the stock. High tellurium content in the soils of the northeast quarter must have some more obscure origin.

Acknowledgments.—We appreciate the suggestion by A. E. Hubert of the U.S. Geological Survey that arsenic be used as the collector. We are grateful to H. W. Lakin for his encouragement.

REAGENTS AND APPARATUS

Standard tellurium solution (1,000 μg/ml): Dissolve 1.2508 g primary standard quality TeO_2 in 10 ml HBr; dilute to 1 litre with 3 *N* HBr.

Dilute tellurium solution (100 μg/ml): Dilute 10 ml of 1,000-μg/ml solution to 100 ml with 3 *N* HBr.

Dilute tellurium solution (10 μg/ml): Dilute 10 ml of 100-μg/ml solution to 100 ml with 3 *N* HBr.

Atomic absorption standards: Pipet 0.0, 0.5, 1.0, 2.5, 5.0, 10 and 20 ml of 10-μg/ml standard solution, respectively, into seven 100-ml volumetric flasks. Add 52 ml MIBK (methyl isobutyl ketone) to each flask; 2 ml dissolves. Bring to the mark with 3 *N* HBr, stopper, and shake the flasks 1 min to mix. The flasks contain, respectively, 0.0, 0.1, 0.2, 0.5, 1.0, 2.0, and 4.0 μg Te per ml MIBK over 3 *N* HBr; MIBK-saturated 3 *N* HBr should be added to the flasks as the MIBK is used up by aspiration.

Nitric acid, reagent grade.

Bromine, reagent grade.

Hydrobromic acid, reagent grade.

Hydrobromic acid, 3 *N*: Dilute 342 ml HBr to 1 litre with water.

Hydrobromic acid–bromine solution (100:0.5): Dissolve 5 ml Br_2 in 1 litre HBr.

Hydrobromic acid–bromine solution (1:1): Dissolve 20 ml Br_2 in 20 ml HBr. Keep in stoppered bottle in a refrigerator.

Methyl isobutyl ketone (MIBK), reagent grade. Properly named 4–methyl–2–pentanone.

Arsenic solution: Dissolve 5 g reagent grade As_2O_3 in 1 litre HBr.

Formic acid, approximately 60 percent: Dilute 700 ml reagent grade (88–91 percent) formic acid to 1 litre with water.

Hypophosphorous acid, 50 percent, reagent grade.

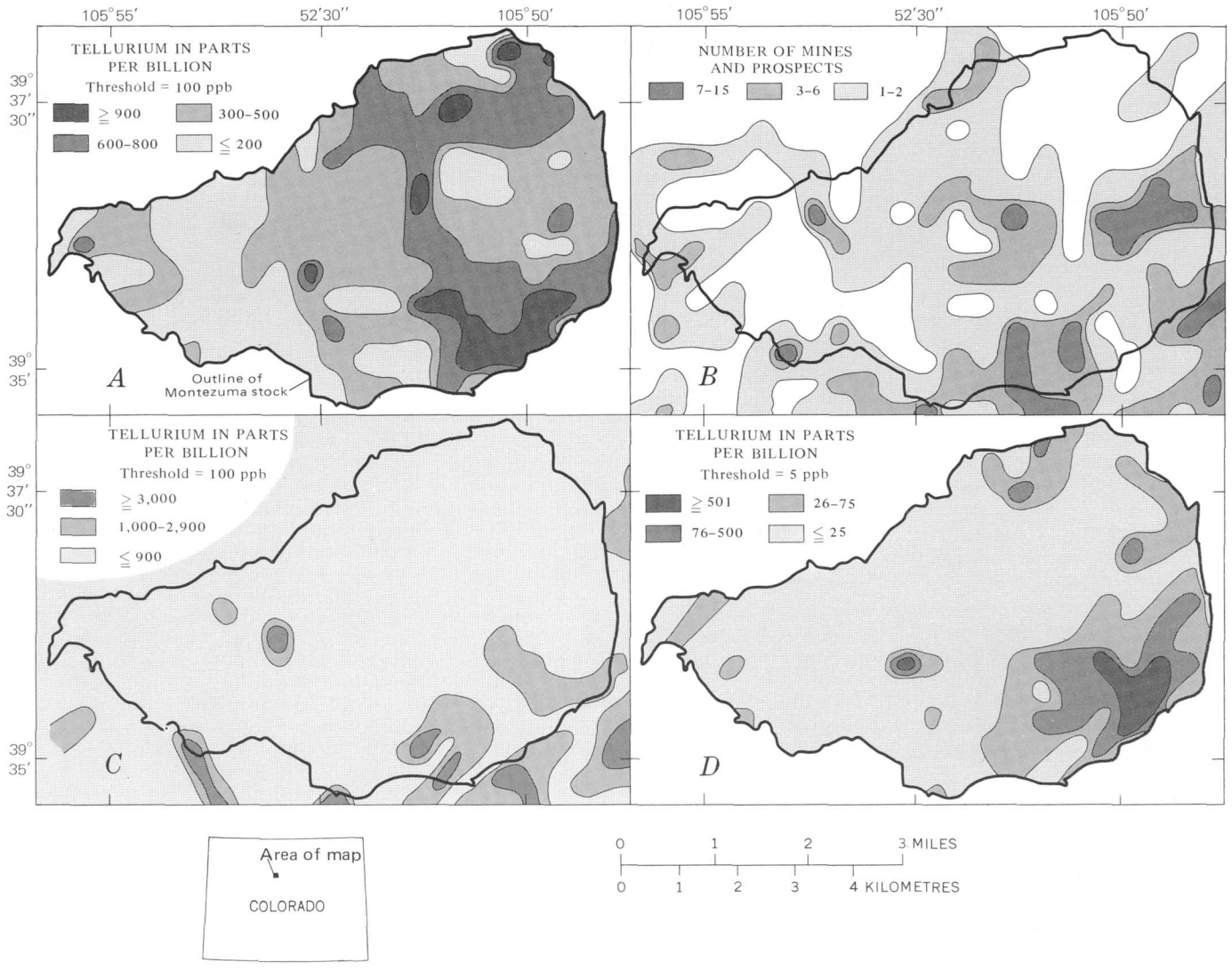

FIGURE 1.—Distribution of tellurium content of soils over the Montezuma stock (*A*), in comparison with the areal density of mines and prospects (*B*), the tellurium content of the altered wallrocks of vein deposits (*C*), and the tellurium content of rocks from outcrops adjacent to each soil-sample site (*D*). Contouring is on centers of grid squares 480 m on a side and is based on the maximum value from among the samples in each square.

Pyrex petri dishes or their cover lids, approximately 10 by 100 mm.

Culture tubes, screwcap, 25 by 200 mm and 16 by 150 mm.

Volumetric flasks, 10 ml.

Scraping blade, approximately 1 by 10 by 150 mm.

Atomic absorption measurements were made with a Perkin-Elmer Model 303 atomic absorption spectrophotometer equipped with a Beckman Model 1005, 10-in. recorder. A Perkin-Elmer tellurium hollow-cathode lamp was used.

Tellurium absorption was measured at 214.3 nm. The recorder was set to run at 1 in./min, on linear function, and in the 10 mV range. A slit setting of 4 with a 1 × scale expansion setting and a noise-suppression setting of 1 were used in all runs. A three-slot burner head with air and acetylene flow rates of about 9 and 12, respectively, seemed to give the best results.

PROCEDURE

1. Weigh 12.5 g of minus-80-mesh rock sample into a 10-cm Pyrex petri dish.
2. Add 15 ml HNO_3. After a few minutes swirl the petri dish gently to assure contact between sample and acid and to form an even-depth layer of sample over the bottom of the petri dish. Allow the acid to evaporate to dryness overnight on a steamtable in a hood.
3. Remove the petri dish and allow to cool. Add 10 ml 60-percent formic acid to wet the sample,

allow 5 min for the reaction, and evaporate to dryness on the steamtable. This process requires approximately 4 h.

4. Transfer the dry sample to a 25- by 200-mm screwcap culture tube with a scraping tool and brush.
5. Add 10 ml HBr-Br_2 solution (100:0.5); cap and shake for 15 s. Centrifuge at 2,000 r/min for approximately 10 min. Decant into another clean 25- by 200-mm screwcap culture tube.
6. Repeat step 5 twice on the residue, using 5 ml portions of HBr and adding the supernatant HBr to that previously decanted.
7. The HBr-Br_2 solution from steps 5 and 6 is heated in a hot water bath in a hood for 1–2 h to expel excess Br_2.
8. Add 1 ml arsenic solution; mix by swirling. Add 9 ml 50-percent H_3PO_2, swirl to mix, replace cap, and allow the precipitate to mature in the hot water bath for 6–8 h or until the liquid is colorless or nearly so.
9. While still hot, centrifuge the culture tube for 25 min at 2,000 r/min. Carefully pour off and discard the liquid. Without delay, transfer the precipitate to a clean 16- by 150-mm screwcap culture tube with a fine stream of water. Cap.
10. Centrifuge for 25 min at 2,000 r/min. Carefully decant and discard the liquid immediately after centrifuging.
11. Add 3 ml of HBr-Br_2 solution (100:0.5) and cap. The tube is then agitated at room temperature until the precipitate dissolves. If the solution turns gray—indicating insufficient oxidant—add a small drop of HBr-Br_2 solution (1:1) and continue to agitate. Avoid an excess of Br_2.
12. Transfer the solution to a 10-ml volumetric flask. Rinse the culture tube twice with 2-ml portions of water. Add the rinses to the volumetric flask and swirl the flask to mix.
13. Pipet 0.95 ml MIBK into the flask, stopper, and shake 40 times. Bring the aqueous sublayer to the mark and shake the flask 20 times.
14. Centrifuge the volumetric flask at 800 r/min for approximately 2 min. Estimate the tellurium content of the MIBK layer by atomic absorption within a few hours.

Notes on procedural steps

Step 4.—Coprecipitation occurs more rapidly and completely in a concentrated solution of HBr than in one that has been diluted. To transfer the sample in a dry state was thus found more convenient than to rinse the residue from the petri dish with portions of HBr-Br_2 solution and water.

Step 9.—Centrifuging while hot has the advantage that condensation forming on the sides of the tube as it cools tends to rinse down any particles adhering to the glass above the waterline. The centrifuge should be allowed to come to a stop slowly to avoid disturbing the precipitate.

Steps 9 and 10.—Decanting over a well-lighted surface assists in avoiding loss of any precipitate.

Step 11.—Dissolution seems to occur more quickly if the HBr-Br_2 solution is added while the precipitate is still wet. A small amount of Br_2 is conveniently added as 1:1 HBr-Br_2 with the tip of a capillary tube. We found it preferable to use the minimum 0.5-percent concentration of Br_2 in step 11 and then to add any additional Br_2 required to dissolve individual precipitates because a lacrimator is formed by any excess Br_2 with the ketone.

Step 13.—MIBK is partially soluble in 3 *N* HBr. The portion of the MIBK that is solvated, however, does not retain tellurium. By experimentation we found that approximately 0.6 ml of MIBK separates after shaking 0.95 ml of MIBK with 10 ml of 3 *N* HBr.

Step 14.—If samples were not estimated within a few hours, evaporation of MIBK became a problem. Evaporation was prevented by melting a drop of paraffin over the flask stoppers when delay was unavoidable. The optimum wavelength for tellurium absorption does not coincide exactly with a maximum on the energy meter. Thus, after other parameters are optimized in the ordinary way, the wavelength should be reset by aspirating a tellurium standard alternately with a blank and maximizing the signal difference. During estimation by atomic absorption, the 0.6-ml ketone layer only allows several seconds of aspiration. This aspiration time should be noted with a stopwatch for several unknown samples. The standards should then be aspirated for the same length of time as the unknowns.

DISCUSSION

The initial requirements for this tellurium method were that it be applicable to rocks containing pyrite and that it be sensitive enough to produce above-threshold data on the tellurium content of most granitic rocks of the Montezuma stock. Because a number of the Montezuma samples contained pyrite, nitric acid appeared to be the acid of choice. Also, of the 39 tellurium minerals listed by Sindeeva (1964), only ferrotellurite, $FeTeO_4$, was listed as being insoluble in nitric acid; it, however, is soluble in hydrochloric acid.

Of several oxidants and combinations of oxidants tested on 1- and 2-g samples of pyrite, nitric acid proved to be the most satisfactory. Nitric acid, how-

ever, interferes with the precipitation step and must be removed. Excess nitric acid was removed by several methods: (1) Drying the sample on a hotplate, (2) boiling to fumes of sulfuric acid, (3) boiling to fumes of perchloric acid, (4) drying on a steamtable, and (5) drying on a steamtable with a subsequent addition of formic acid (Beaty, 1973), and redrying. Drying the samples on a hotplate, even at low temperatures, tended to cause some loss of tellurium. The addition of sulfuric acid produced a gummy sulfur precipitate. Perchloric acid also precipitated sulfur and appeared to prevent the complete precipitation of arsenic. The use of formic acid appeared to be unnecessary if the samples were thoroughly dried, but because a vigorous reaction takes place between hypophosphorous acid and the least amount of nitric acid, formic acid was added as a routine safety measure.

Three reducing agents were tried in precipitating tellurium with arsenic (Luke, 1959) : stannous chloride, hypophosphorous acid, and sodium hypophosphite monohydrate. In all trials the precipitation was more efficient if carried out hot. Stannous chloride solutions precipitated more sulfur than could be tolerated. Both sodium hypophosphite and hypophosphorous acid produced a satisfactory precipitation of arsenic and tellurium with a minimum of sulfur from hot concentrated hydrobromic acid. The precipitate produced by hypophosphorous acid, however, was coarser than that produced by sodium hypophosphite and thus more suitable for separation by centrifuging and decanting.

INTERFERENCE

Iron, the only element that appeared to cause interference in this test series, was almost always eliminated during the precipitation step. By doing a blank series containing incremental iron additions, it was found that iron begins to carry through the precipitation step, under the conditions specified, at a level corresponding to 8 percent iron or about 17 percent pyrite in the sample. Where iron was present in an amount that interfered with the precipitation step, a smaller sample was taken. Iron is known to cause interference with tellurium estimation by atomic absorption.

The reaction between nitric acid and samples containing more than about 15 percent pyrite is too vigorous to be contained in a 10-cm petri dish; in practice, this indicates those samples that have a troublesome iron content.

Nakagawa and Thompson (1968) determined that, of the elements that absorb light in wavelengths near that of the favored tellurium line, none interferes in concentration ratios of element to tellurium up to 2,000.

RECOVERY, PRECISION, AND ACCURACY

A 1,000-μg/ml standard solution of Te was made from Matthey Specpure TeO_2 by dissolving 1.2508 g TeO_2 in a minimum volume of HNO_3 and making the final 1-litre solution 10 percent in HNO_3 and 1.5 percent in HCl. Substandards were made from this. Amounts appropriate to test recovery of tellurium over the range 5–200 ppb were added to clean petri dishes. The results of these tests (table 1) indicate that recovery is satisfactory.

TABLE 1.—*Recovery of tellurium from duplicate nitric acid solutions using the proposed procedure*

Total tellurium per petri dish (nanograms)	Average total tellurium found (nanograms)	Average tellurium recovery (percent)
0	[1] <60	--
84	78	93
120	120	100
240	280	117
480	400	83
960	940	98
1,200	1,150	96
1,920	1,880	98
2,400	2,220	93

[1] Based on instrument detection limit of 0.1μg/ml.

Precision was estimated by making eight replicate determinations of a "typical" granite from the Montezuma stock, sample B552–3RV, and by making five replicate determinations of USGS standard rock GSP–1, a granodiorite. The first eight determinations resulted in a relative standard deviation of 10.2 percent at an arithmetic mean concentration of 71 ppb (table 2). The last five determinations resulted in a relative standard deviation of 5.26 percent at an arithmetic mean concentration of 20.8 ppb (table 2). Beaty and Manuel (1973) have reported that GSP–1 contains 20±3 ppb Te.

TABLE 2.—*Replicate tellurium analyses*

Sample	Material	Replicate tellurium determinations (ppb)	Arithmetic mean (ppb)	Relative standard deviation (percent)
B552–3RV	Greisen	60, 63, 69, 73, 76, 82, 76, 69	71	10.2
GSP–1	Granodiorite	20, 20, 20, 22, 22	20.8	5.6

The results of the recovery, precision, and accuracy tests indicate that the method is adequate for geochemical exploration purposes.

REFERENCES CITED

Beaty, R. D., 1973, Atomic absorption determination of nanogram quantities of tellurium using the sampling boat technique: Anal. Chemistry, v. 45, no. 2, p. 234–238.

Beaty, R. D., and Manuel, O. K., 1973, Tellurium in rocks: Chem. Geology, v. 12, no. 2, p. 155–159.

Gott, G. B., and Botbol, J. M., 1972, Zoning of major and minor metals in the Coeur d'Alene mining district, Idaho, U.S.A.: Internat. Geochem. Explor. Symposium, 4th, London 1972, Proc., p. 1–12.

Luke, C. L., 1959, Photometric determination of traces of selenium or tellurium in lead or copper: Anal. Chemistry, v. 31, no. 4, p. 572–574.

Nakagawa, H. M., and Thompson, C. E., 1969, Atomic absorption determination of tellurium, *in* Geological Survey research 1968: U.S. Geol. Survey Prof. Paper 600–B, p. B123–B125.

Neuerburg, G. J., 1971, Maps showing soil analyses of interest for prospecting the Montezuma stock, Summit County, Colorado: U.S. Geol. Survey Misc. Geol. Inv. Map I–634.

Sindeeva, N. D., 1964, Mineralogy and types of deposits of selenium and tellurium [translation from original Russian]: New York, Interscience Publishers, 363 p.

Jour. Research U.S. Geol. Survey
Vol. 3, No. 2, Mar.–Apr. 1975, p. 197–202

PERCHED SILICA MINERALS ON MORDENITE FIBERS

By ROBERT B. FINKELMAN, Reston, Va.

Abstract.—Ellipsoidal quartz grains and spherulitic chalcedony are perched on mordenite fibers in geodes from Chihuahua, Mexico. Examination of samples of fibrous mordenite from six additional localities indicated that most mordenites have perched quartz crystals. A linear relationship exists between the Si:Al ratios and the refractive indices of the mordenites. The pH of the mineralizing solutions appears to be the primary factor controlling the presence of perched silica minerals (the lower the pH, the higher the Si:Al ratios and the lower the probability of precipitating quartz). Other factors that may affect the presence of perched silica minerals are (1) the compactness of the mordenite fibers, (2) the morphology of the fibers, and (3) the concentration of Al, Ca, Na, and K in the mineralizing solutions.

An interesting association of quartz, chalcedony, and mordenite [$(Ca,Na_2K_2)Al_2Si_{10}O_{24}\cdot 7H_2O$] was observed in two geodes from a Tertiary rhyolite in Chihuahua, Mexico. The first geode, only a fragment of which was available, contains tufts of fibrous mordenite that grew from a chalcedony base. Milky white spheroidal and randomly oriented ellipsoidal grains are perched on many of the mordenite fibers. In one area the ellipsoids are packed so densely that they nearly obscure the fine mordenite fibers. Less commonly, the spheroids are perched on chalcedony mounds that project from the chalcedony base. The spheres are 150–200 μm in diameter, and the ellipsoidal grains are 20–200 μm in length, the diameter being approximately one-half to one-fourth of the length.

Examination of these grains with a scanning electron microscope (SEM) revealed that the surfaces of the spheres are covered by overlapping ellipsoidal grains (fig. 1) which seem identical to the isolated ellipsoidal grains on the mordenite fibers (fig. 2). Polished thin sections of these grains indicate that the spheroids consist mainly of radiating fibers. The ellipsoidal grains, however, are generally single crystals, although several appeared to be composites of two or three crystals. X-ray diffraction analysis of the spheroids and ellipsoids indicated the presence of α-quartz only. Thus, the spheroidal grains are chalcedony spherulites covered by a layer of ellipsoidal quartz crystals.

In the other geode, mordenite formed a 1-cm-thick fibrous white mat over the entire quartz-lined inner surface. The remainder of the cavity was filled by a large single crystal of calcite. These mordenite fibers are much finer than the mordenite fibers in the first geode, ($\approx$ 0.3 μm vs. 25 μm) and are more densely packed. Rare, irregular silica-rich clusters (5–10 μm) are present; some have a hexagonal outline, and all seem to be covered by mordenite fibers (fig. 3). An X-ray powder pattern of a cluster of these mordenite fibers had several lines corresponding to α-quartz. The quartz lines were spotty, suggesting that individual crystals were dispersed in the mordenite cluster,

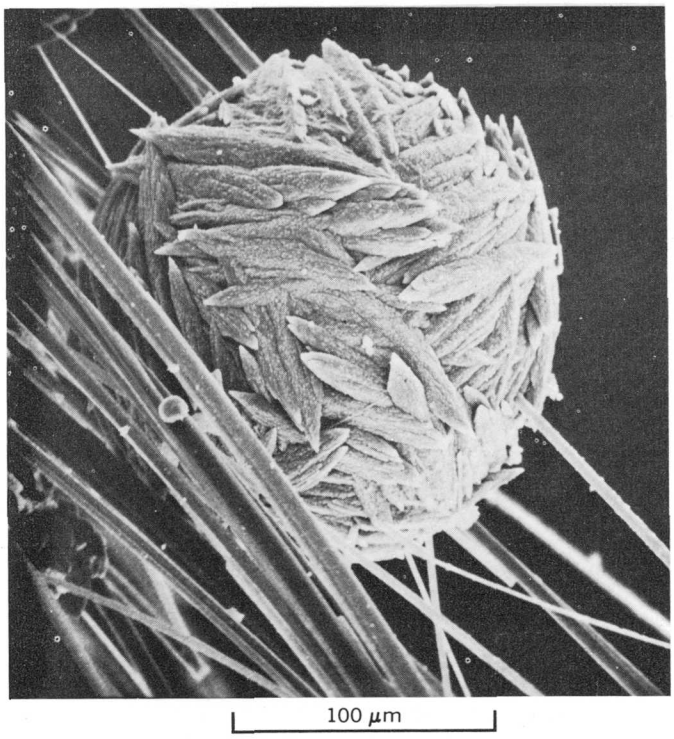

FIGURE. 1.—Scanning electron micrograph of ellipsoidal quartz crystals covering a chalcedony spherulite on mordenite fibers from a Chihuahua geode.

The material in the first geode seems identical to samples described by Ross and Shannon (1924) from a vesicular andesite from Idaho. They describe "geodal masses of fine cottony material which * * * consist usually of a thin shell of chalcedonic material filled with the light tufted fibers of the mordenite" (p. 3). The mordenite contains "minute spherulitic or spindle-

shaped grains of quartz with radial structure" (p. 4). Ross and Shannon noted that "the small quartz spherulites are pinned through by the mordenite fibers and have clearly developed subsequent to the mordenite. None of the fine cottony material was found to be free from quartz although the compact varieties are frequently free from any impurity" (p. 4).

The samples studied by Ross and Shannon are still available at the National Museum of Natural History (USNM 94512–94516). A reexamination of the samples verified the abundant spindle- or ellipsoidal-shaped quartz crystals perched on the mordenite fibers, but spherulitic forms are very rare. No quartz grains were observed in a sample of the compact variety. Observation of the mordenite and quartz grains with an SEM revealed that the ellipsoids in this sample are terminated by crystal faces (fig. 4) and are not identical to the ellipsoids from the Chihuahua geode. Five other samples of white, fibrous mordenite were also studied. All have quartz or chalcedony substrates and seem to have formed in cavities in igneous rocks. Three of these samples have quartz crystals perched on the mordenite fibers. A specimen from Westweld, British Columbia (USNM 115869), contains numerous clusters of radiating, elongated quartz crystals (fig. 5) and irregular to blocky rhombohedra of calcite (fig. 6). A specimen from Mossy Rock Dam, Wash. (USNM 120911), has abundant hexagonal dipyramids of quartz. The dipyramids occur individually (fig. 7) and in clusters and have very rough irregular surfaces, typical

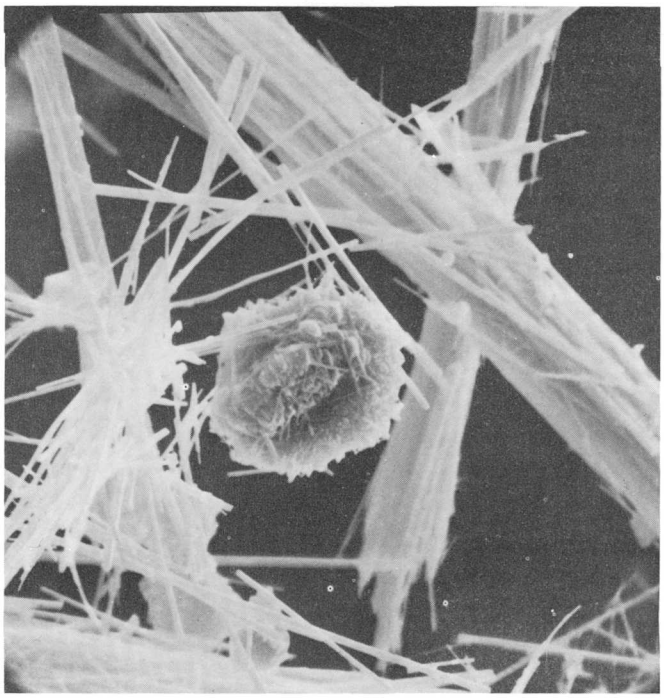

FIGURE 3.—Scanning electron micrograph of a hexagonal grain of quartz covered by mordenite fibers from a Chihuahua geode.

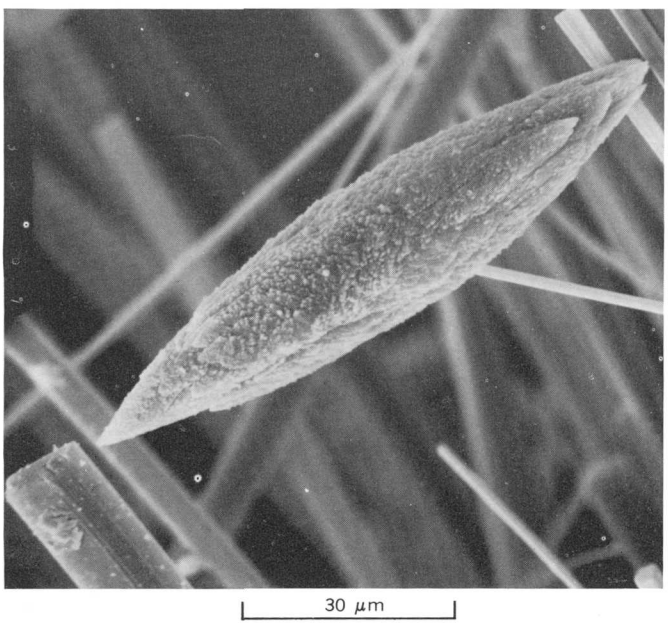

FIGURE 2.—Scanning electron micrograph of an ellipsoidal quartz crystal on a mordenite fiber from a Chihuahua geode.

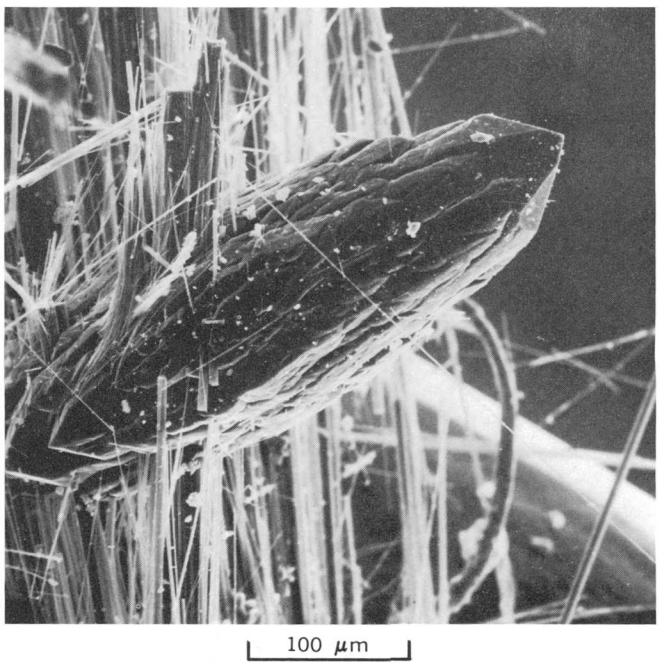

FIGURE 4.—Scanning electron micrograph of a quartz crystal in a stack of mordenite fibers. From the U.S. National Museum of Natural History (USNM) samples 94512–94516.

of quartz crystal growth (Krinsley and Doornkamp, 1973). Mordenite from Kaiser Quarry, Contra Costa County, Calif. (USNM R16494), has rare irregular clusters of silica minerals.

The only mordenite samples examined that do not contain perched crystals are from Poona, India (USNM R16837), and Green Mountain, Jefferson County, Colo. (USNM B17593). The mordenite from Poona resembles brittle ribbons (fig. 8) rather than the fine, flexible rods observed in all the other samples. The Green Mountain material contains numerous small calcite crystals and rare potassium-rich phases.

Perched crystals on zeolites are not rare. Staples (1946, p. 578) noted that "acicular zeolites often form mounts for calcite and other non-zeolite minerals." Coombs, Ellis, Fyfe, and Taylor (1959) noted that mordenite in cavities such as amygdules (and therefore geodes) is precipitated from solutions supersaturated with respect to quartz. Indeed, the association of silica minerals and mordenite is very common (R. A. Sheppard, oral commun., 1973). It is therefore somewhat surprising that, in addition to the observations reported here and those of Ross and Shannon (1924), only two other reports of perched silica crystals on mordenite fibers exist. Mason and Greenberg (1954) described crystals of quartz surmounting "cotton-like balls of mordenite in one cavity" of a vesicular basalt from southern Brazil. Van Valkenburg and Buie (1945) described vesicles in a basalt from the Deccan volcanics of India in which fibers of mor-

FIGURE 5.—Scanning electron micrograph of a cluster of radiating quartz crystals on mordenite fibers. From USNM sample 115869.

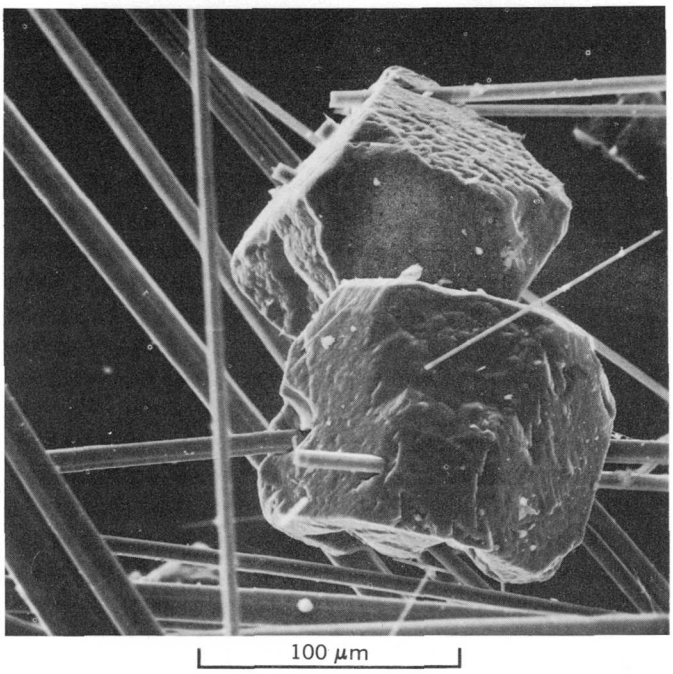

FIGURE 6.—Scanning electron micrograph of blocky calcite rhombohedra on mordenite fibers. From USNM sample 115869.

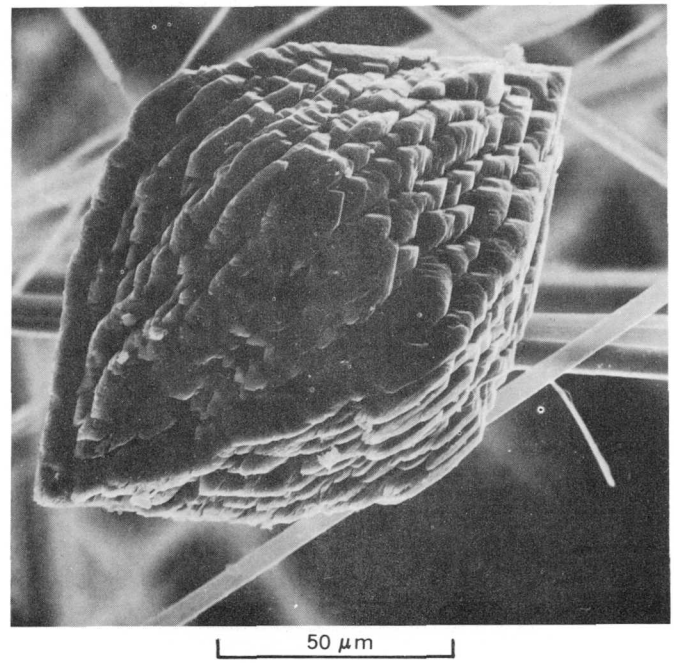

FIGURE 7.—Scanning electron micrograph of a quartz dipyramid on mordenite fibers. From USNM sample 120911.

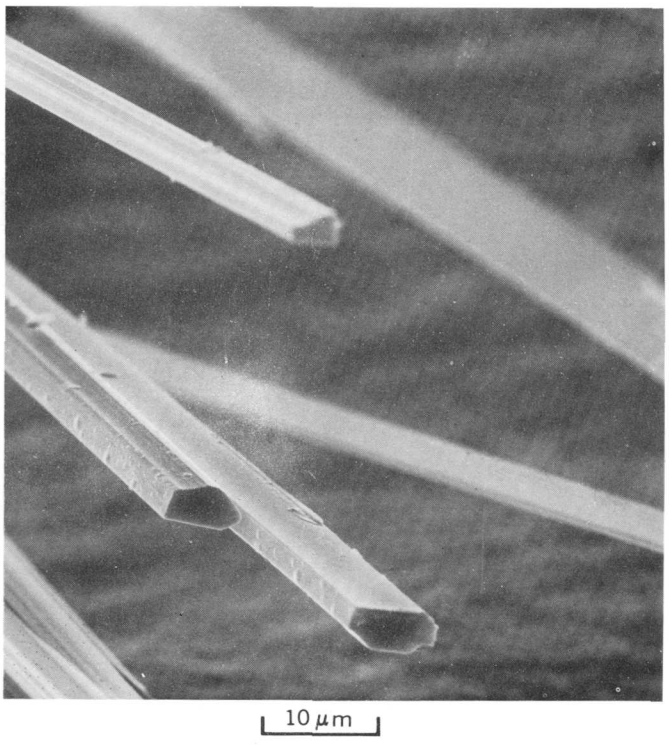

FIGURE 8.—Scanning electron micrograph of flat ribbonlike crystals of mordenite. From USNM sample R16837.

denite project through a quartz zone. Perched on the fibers are octahedra of cristobalite, some of which have inverted to quartz. However, their identification of the fibrous material as mordenite is uncertain. The X-ray powder pattern of this material differs considerably from the published patterns of mordenite or of the other zeolites, and the $SiO_2:Al_2O_3$ weight percent ratio (4.1) is lower than any other published analysis of mordenite (see below).

Semiquantitative energy dispersive analyses were obtained on mordenite fibers from each of the samples discussed above. The results are given in table 1. The values presented in the table are intensity ratios, which are not necessarily identical to (but are proportional to) the concentration ratios. The average $SiO_2:Al_2O_3$ weight percent ratio of 25 published analyses is 5.4 (range 4.4–6.2). Hay (1966) stated that the Si:Al ratio of of most mordenites is 4.4–5.0. Thus, the mordenites listed in table 1 seem to have typical $SiO_2:Al_2O_3$ weight percent ratios, except for the sample from Poona, India (USNM R16837). The mordenites with the highest $SiO_2:Al_2O_3$ ratios are the only samples examined that have no perched silica mineral. Although the data are less conclusive, due to the poor sensitivity for sodium, these samples also seem to have the lowest $CaO:Na_2O+K_2O+CaO$ ratio; this is corroborated by the relatively low refractive indices

TABLE 1.—Si:Al *intensity ratio and refractive index of mordenite fibers*

[See fig. 9]

Sample	Intensity ratio [1] (±0.5)	Refractive index
Compact mordenite from geode, Chihuahua, Mexico	[2 3] 5.7	1.470
Fibrous mordenite from geode, Chihuahua, Mexico	5.7	1.470
Ross and Shannon's fibrous samples, USNM 94512–94516, Idaho	[4] 5.3	1.471
Ross and Shannon's compact samples, USNM 94512–94516, Idaho	[3 5] 5.6	1.4705
USNM 115869, Westweld, British Columbia	5.7	1.472
USNM 120911, Mossy Rock Dam, Wash.	5.3	1.473
USNM R16837, Poona, India	6.5	1.467
USNM R16494, Kaiser Quarry, Calif.	5.7	1.471
USNM B17593, Green Mountain, Colo.	6.1	1.470

[1] Microprobe results, present study.
[2] Ratio of 4.8±0.4 obtained by D. Golightly using an argon plasma-jet emission spectrographic method.
[3] Sample difficult to analyze due to small grain size; in general, small clumps or clusters of fibers were analyzed.
[4] Analysis by Ross and Shannon (1924) gave 5.3 for the Si:Al ratio.
[5] Analysis by Ross and Shannon (1924) gave 5.2 for the Si:Al ratio.

(table 1 and fig. 9). Nakajima (1973) suggests that the variation of refractive index of mordenite is a linear function of the $CaO:Na_2O+CaO$ molar ratio, with the Na_2O-rich members having the lower index.

It should be noted that the lone exception to this rule reported by Nakajima is plotted incorrectly. In his figure 1, Nakajima plotted the refractive index of Ross and Shannon's mordenite at about 1.486. However, Ross and Shannon (1924) reported the indices to be 1.470–1.475 (see also table 1). This value, plotted correctly, is in excellent agreement with the other values. Nakajima's diagram is based on a series of synthetic compounds with Si:Al ratios of 5 and varying $CaO:Na_2O+CaO$ mole ratios. In figure 9 the Si:Al ratio of natural mordenites is plotted against

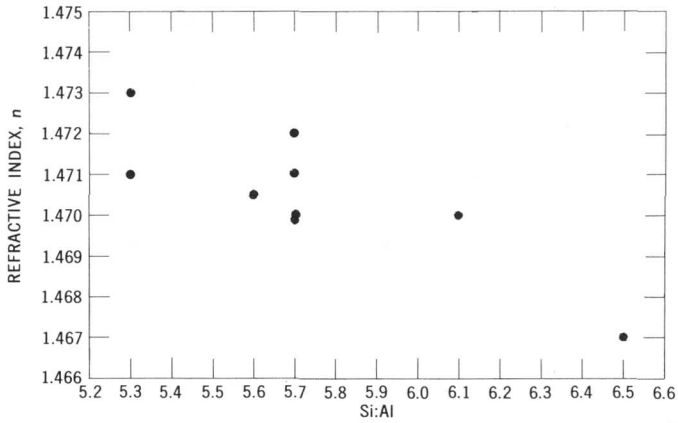

FIGURE 9.—Variation of Si:Al mole ratio of mordenites with refractive index. See table 1 for identification of samples.

the refractive index. A trend from low Si:Al, high-index mordenites to high Si:Al, low-index mordenites is apparent. This is what would be expected by extrapolating Nakajima's data to natural mordenites and also suggests that the presence of potassium does not greatly alter Nakajima's conclusions.

The relatively high Si:Al ratios of the samples from Poona, India, and Green Mountain, Colo., may be indicative of a mineralizing solution with very low pH. Hay (1966) noted that the silica content of zeolites may vary inversely with the pH of the solution from which they crystallize. This may also explain the absence of perched silica minerals because the hydroxyl ion can reduce the activity of silica by catalyzing the crystallization of amorphous silica to quartz (Hay, 1966).

Senderov (1963) noted that mordenite is unstable in the presence of quartz and that its formation is caused by the supersaturation of solutions with silica in the last stages of hydrothermal activity. He suggested that supersaturation of the mineralizing solutions can be created by decreasing the alkalinity or by bringing the solutions into contact with less stable modifications of silica.

The mordenites examined for this report appeared to form with equal facility on quartz and chalcedony. And, as has been described above, quartz formed both before and after the formation of mordenite. Intuitively it seems probable that these fluctuations in mineralogy are in response to changing pH rather than to changes in the crystallinity of silica in contact with the mineralizing solutions. Apparently the mordenites formed from solutions of relatively low pH (high silica activity); the character of the solutions changed with the pH increase, initiating the precipitation of the perched silica minerals. Environments with extremely low pH values would favor the formation of mordenites with high Si:Al ratios. The silica entering the mordenite structure may sufficiently reduce the silica activity of the solutions to the point where an increase in pH would not initiate the precipitation of quartz. This situation would substantiate the comments of Senderov (1963) and Hay (1966) that metastable equilibrium plays an important role in this system and may also explain the absence of transitional phases such as analcime ($NaAlSi_2O_6 \cdot H_2O$).

Several factors other than the pH and silica activity probably affect the presence of perched silica minerals on mordenite fibers. Among these are:

1. The compactness of the mordenite fibers. Far fewer silica crystals were observed in the denser (less porous) samples. The silica grains that were observed were considerably smaller and more irregular in shape than the perched crystals on the freely growing fibers.
2. The morphology of the mordenite fibers. All the silica crystals observed grew around one or more mordenite fibers, suggesting that the mordenite nucleated the growth. The flat, broad ribbon shape (USNM sample R16837 from Poona) may inhibit the nucleation effect.
3. Concentration of Al, Ca, Na, and K in the mineralizing solutions. Low concentrations of Al or Ca, or high concentrations of Na+K, would allow a high concentration of silica in the mordenites and thus decrease the likelihood of precipitating free silica.

In addition, the shape of the silica grains may be controlled by the rate of growth. Elongated crystals, as shown in figures 2, 4, and 5, suggest a period of relatively rapid growth. The crystal terminations on the grains in figures 4 and 5 suggest that the growth rate decreased markedly, reflecting either the depletion of silica or pH in the mineralizing solutions or a decrease in temperature. The presence of chalcedony, as in the spherulites from the geode, is also an indication of silica rapidly precipitating from solution. The well-formed dipyramids in figure 7 suggest a relatively uniform slow growth rate.

It is not understood why all the quartz crystals in USNM sample 115869 (Westweld, British Columbia) occur as clusters (fig. 5). The possibility of structural control by the mordenite cannot be ignored. In this context it is interesting to speculate on Van Valkenburg and Buie's (1945) sample. If the mordenite structure preferentially nucleates silica as quartz, then it is possible that the fibers in Van Valkenburg and Buie's sample were not mordenite but a mineral with a structure that preferentially nucleates silica in the form of cristobalite.

ACKNOWLEDGMENTS

The geode containing the spheroidal quartz crystals belongs to Mrs. H. Jennings of Houston, Tex., who brought the specimen to the attention of J. S. White, Jr., of the National Museum of Natural History, Washington, D.C. I thank Mr. White for allowing me to study the geode and for supplying me the other mordenite samples and an excellent polished thin section. I also thank Z. S. Altschuler, R. A. Sheppard, and E. Roedder, all of the U.S. Geological Survey, for their valuable suggestions and D. W. Golightly for the analysis of the compact mordenite from the Chihuahua geode. Dennis Kostic made the geode with the compact mordenite available to me. R. R. Larson took the scanning electron micrographs for figures 4–8.

REFERENCES CITED

Coombs, D. S., Ellis, A. J., Fyfe, W. S., and Taylor, A. M. 1959, The zeolite facies, with comments on the interpretation of hydrothermal syntheses: Geochim. et Cosmochim. Acta, v. 17, p. 53–107.

Hay, R. L., 1966, Zeolites and zeolitic reactions in sedimentary rocks: Geol. Soc. America Spec. Paper 85, 130 p.

Krinsley, D. H., and Doornkamp, J. C., 1973, Atlas of quartz sand surface textures: London, Cambridge Univ. Press, 91 p.

Mason, Brian, and Greenberg, S. S., 1954, Zeolites and associated minerals from southern Brazil: Arkiv Mineralogi och Geologi, v. 1, no. 5–6, nr. 18, p. 519–526.

Nakajima, Waitsu, 1973, Mordenite solid solution in the system $Na_2Al_2Si_{10}O_{24}$–$CaAl_2Si_{10}O_{24}$–H_2O: Japan, Kobe Univ. Bull. Fac. Education, v. 48, p. 91–98.

Ross, C. S., and Shannon, E. V., 1924, Mordenite and associated minerals from near Challis, Custer County, Idaho: U.S. Natl. Mus. Proc., v. 64, art. 19, p. 1–19.

Senderov, E. E., 1963, Crystallization of mordenite under hydrothermal conditions: Geochemistry (English translation), no. 9, p. 848–859.

Staples, L. W., 1946, Origin of spheroidal clusters of analcime from Benton County, Oregon: Am. Mineralogist, v. 31, p. 574–581.

Van Valkenburg, A., Jr., and Buie, B. F., 1945, Octahedral cristobalite with quartz paramorphs from Ellora caves, Hyderabad State, India: Am. Mineralogist, v. 30, nos. 7–8, p. 526–535.

Jour. Research U.S. Geol. Survey
Vol. 3, No. 2, Mar.-Apr. 1975, p. 203-212

EXPERIMENTAL ABRASION OF DETRITAL GOLD

By WARREN YEEND, Menlo Park, Calif.

Abstract.—The physical breakdown and abrasion rates of gold were studied using a tumbler to simulate natural high-energy environments. The gold fragments were tumbled for periods ranging from 30 to 240 h with different combinations of sand, cobbles, and water at velocities of 0.5 and 2.0 mi/h (0.85 and 3.22 km/h). With sand and gravel, the common bedload of the rivers that deposited the gold-bearing Tertiary sedimentary rocks of the Sierra Nevada, gold is abraded at rates of 0.015 to 0.007 percent (by weight) per hour of travel (at 0.5 mi/h or 0.845 km/h). Cobbles, rather than sand, are responsible for most of the physical changes and abrasion of the gold. Ten gold fragments tumbled for 120 h with cobbles and water (no sand) were broken down to 68 recoverable fragments and lost about 25 percent of their weight to particles smaller than could be recovered using conventional panning techniques. Gold tumbled for 120 h with sand and water lost less than 1 percent of its weight. Gold was abraded faster by wet sand than by dry sand. Velocity appears to be more important as a factor in abrasion of gold than travel distance—a fourfold increase in velocity produced a tenfold increase in hourly abrasion rates of gold. Scanning electron microscope examination of the gold fragments after the tumbling experiments revealed differences in surface texture between fragments tumbled with (1) sand, (2) sand and cobbles, and (3) cobbles only.

What happens to a sand-size particle of gold as it travels along the bed of a river? Does it lose appreciable weight or change shape through physical abrasion, or is gold so tenacious that any physical changes would scarcely be measurable? Answers to these questions were sought in a laboratory experiment subjecting gold particles to a simulated high-energy river environment in a tumbling mill.

PURPOSE AND PLAN

Information on the physical breakdown of detrital gold has practical application to the study of gold placers. In an earlier publication on the gold-bearing Tertiary gravels of the Sierra Nevada (Yeend, 1974), I raised the question whether substantial amounts of detrital gold could have been transported by the Tertiary rivers beyond the present position of the Sierras into the marine or deltaic environments near the river mouths. If so, a sizable gold resource might be present within the early Tertiary sedimentary rocks of the Great Valley. This possibility is based on the premise that, in order for substantial amounts of detrital gold to have been transported into the marine environment, a large quantity of gold must have been physically broken down into very fine particles, perhaps colloidal size, or have been very fine grained originally. Such fine gold could have been transported in the low-energy environment that probably existed in the lowest parts of the major river systems. Coarse gold would stay near the source in the upper and middle reaches of the rivers. In order to answer part of the question, therefore, it was necessary to determine the rate at which coarse detrital gold breaks down in the high-energy river streambed environment.

The entire study was conducted in the laboratory using placer gold particles and gravel derived from the ancestral Yuba River deposits of the Sierra Nevada. This paper discusses the laboratory methods used and the experimental results of seven separate samples run in the tumbler. Graphs show the change in weight of the gold fragments with duration of tumbling for each of the seven samples, and photographs show the characteristics of the gold particles before and after tumbling. Electron micrographs obtained from SEM (scanning electron microscope) examination reveal some significant differences in surface texture between gold fragments tumbled in different detrital environments.

PREVIOUS WORK

Numerous studies have been made of the effects of abrasion on the size and shape of rock and mineral fragments. Alling (1944), using a ball mill, noted the change in size with distance of travel of quartz, microcline, garnet, and tourmaline. Thiel (1940) reported on the relative resistance to abrasion of quartz, microcline, apatite, hornblende, garnet, and tourmaline. Others have studied the effects of tumbling pebbles, cobbles, and sand-size particles (Kuenen, 1956; Anderson, 1926; Krumbein, 1941; and Wentworth, 1919, 1931). More recently, Schumm and Stevens (1973) have studied the abrasion of coarse sediments in rivers compared with abrasion of coarse sediments in tumbling barrels and flumes. In this extensive literature

on experimental abrasion, however, almost no experiments have used gold fragments. The formation of colloidal gold particles by abrasion was studied by Goni, Guillemin, and Sarcia (1967), but this investigation emphasized the stability of gold colloids, their transport, flocculation, and the formation of gold nuggets. Most of the people who have studied gold in the laboratory, including alchemists, have been concerned primarily with its chemical properties, particularly solubility or insolubility, rather than its physical properties. Consequently, little background data exist on the physical abrasion of gold. This study of the physical abrasion of detrital gold is a direct outgrowth of my earlier work pertaining to gold placers of the ancestral Yuba River (Yeend, 1974).

EQUIPMENT AND PROCEDURES

The experiment required readily obtainable equipment and supplies and followed a rather simple but time-consuming procedure. A known weight of coarse gold fragments was tumbled at selected speeds with different combinations of sand, gravel, and water for time intervals ranging from 30 to 240 h. At intervals during a run, the tumbler was stopped, and the gold was separated from the sand or gravel and weighed. A plot showing change of weight of the gold fragments as a function of tumbling time was then constructed.

The tumbling apparatus consists of a jar mill powered by a small electric motor and a large, heavy polyethylene bottle commonly referred to as a "carboy" (fig. 1). The carboy is approximately 11 in (28 cm) in diameter (35 in or 89 cm in circumference) and 19.5 inches (49.5 cm) in height. The top opening is 2.5 in (6.35 cm) in diameter, large enough for the entry of medium-size cobbles. On opposite sides of the upper part of the bottle are two indented handles measuring 3 by 1 in (7.6 by 2.5 cm). These indentations fortuitously provided the irregularity or boulder obstruction in the simulated river-bed environment. As the bottle rotated, parts of the bedload were carried part way up the side on the leading edge of the indentation until they dropped back down into the bed of the rotating bottle. The plastic tumbler has certain advantages over the more conventional metal drums or ceramic jars often used. The plastic is soft enough that it does not abrade the contained material yet tough enough to take the scraping, grinding, and pounding that it is subjected to by many hours of use. It is also much quieter to operate.

Gold fragments used in the study were panned from churn-drill samples of Tertiary gravels obtained in 1968 near North Columbia, Calif. The gold ranged in size from 1 to 10 mm in diameter with the bulk of the fragments 1–3 mm.

FIGURE 1.—Tumbling apparatus used in this study. The plastic bottle is 11 in (28 cm) in diameter. During operation, a point on the circumference of the bottle could be made to rotate at the rate of 0.5 or 2.0 mi/h (0.85 or 3.22 km/h).

Sand, pebbles, and small cobbles used in the experiment were obtained from the same locality as the gold—the North Columbia hydraulic pit. The pebbles and cobbles were all subangular to well-rounded white vein quartz (fig. 2), the most common rock type within the Tertiary gravels of the ancestral Yuba River. The sand was composed primarily of quartz, phyllite, and slate. Distilled water was used to reduce the possibility of any chemical reaction that might have affected the solubility of the gold.

The gold used in the study was initially divided into five lots of 10 fragments each, and these were used in the first five experiments. Two lots of five fragments each were then selected from the initial lots for use in experiments 6 and 7. Photographs were taken of each of the initial lots before tumbling to show the size, shape, and general surface characteristics of the gold. The weight of each lot of gold was determined to the

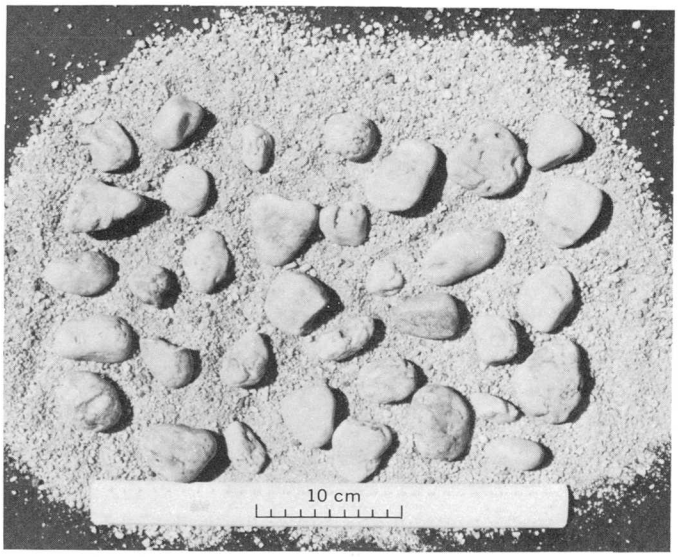

FIGURE 2.—Sand and cobbles used in experiment 2. The cobbles are white vein quartz. The scale is 12 in (30 cm) in length.

nearest 0.05 mg. The lots ranged in weight from 24.9 to 508.3 mg and only one weighed more than 100 mg.

In order to study the abrasive effects in different environments, each lot of gold was tumbled at selected velocities with the following combinations of sand, cobbles, and water: (1) sand, cobbles, and water; (2) sand and water; (3) cobbles and water; and (4) dry sand. In addition, the weight of the cobbles and sand used in each run was noted. In those runs that included water the plastic bottle was filled approximately one-fifth full of distilled water, which was always sufficient to cover the sand, cobbles, and gold during the tumbling operation. Each run included 120 h of tumbler travel except for experiment 5, which was stopped when the motor broke down after 105 h, and the final experiment in which the tumbler speed was increased by four times. The duration of this run was only 30 h, thus keeping the total distance traveled the same as in the other experiments. The tumbler was operated only during the 8-h workday; thus with the numerous interruptions for separating and accurately weighing the gold, it normally took 3–4 weeks to complete each of the seven separate experiments.

The rotation rates (of a point on the circumference of the tumbler) were established at 0.5 and 2.0 mi/h (0.85 and 3.22 km/h) by using a combination of different size pulleys on the motor and rolls. After 1, 3, 6, 15, 30, 60, and 120 h had elapsed, the tumbler was stopped, and the gold fragments separated from the sand and cobbles by panning. The gold fragments recovered were counted and weighed. The finely divided gold (product of abrasion) that could not be recovered by panning is assumed to be largely represented by the weight loss from the preceding weighing. This assumption was substantiated in experiments 6 and 7 in which the products of abrasion were collected, and analytical tests (fire assay and atomic absorption) detected the abraded gold. At the end of 120 h of tumbling, the gold, sand, and cobbles were separated and weighed (expts. 1–5). This time interval was selected as a convenient stopping point because by then the shape of the curve representing the weight loss of gold was well established. In order to facilitate comparison of the abrasive effects in the different environments, the weight loss was converted to an actual percentage of the original weight, since different weights of gold were used in each run. To facilitate further comparison of the separate experiments, the scales on the graphs are identical except for experiment 3. The losses by abrasion in experiment 3 were so large that the vertical scale was increased by a factor of 10. Finally, the recovered gold fragments were counted and photographed (expts. 1–5) for comparison with the original photographs.

EXPERIMENTAL RESULTS

Experiment 1

The gold fragments used in experiment 1 ranged in length from 0.8 to 2.7 mm (fig. 3*A*) and weighed 33.7 mg at the beginning of the experiment. This gold, as well as that used in experiments 2, 3, and 4, was thinly coated with iron oxide and silica.

Four pounds (1,814 g) each of white quartz cobbles and coarse sand were tumbled with the gold. The cobbles were subrounded, 1–2 in (2.5–5 cm) in diameter.

After 120 h of tumbling, the recovered gold fragments (fig. 3*B*) weighed 32.9 mg, a loss of 2.4 percent of initial weight; the cobbles lost 0.5 lb (227 g) or 12.5 percent, and the sand lost 2.25 lb (1,019 g) or 62 percent.

Because the gold lost only 2.4 percent of its weight, the fragments in figures 3*A* and *B* are very similar in size and shape.

Despite the obvious measurement errors, figure 3*C* shows that abrasion occurred quickly at first and then slowed to a more constant rate of approximately 0.015 percent (by weight) per hour. Reasons for this change in rate are presented later.

Experiment 2

Because of the problems involved in experiment 1, it seemed desirable to repeat the experiment again, tumbling sand, cobbles, and water with the gold fragments. Thus, experiment 2 could be used to check whether the low weight losses found in experiment 1 were real and reproducible under similar conditions.

The 10 gold fragments weighed 95.8 mg at the start of the experiment. Most of the gold fragments were thin flakes with rounded edges (fig. 4*A*).

Four pounds (1,814 g) of subrounded quartz cob-

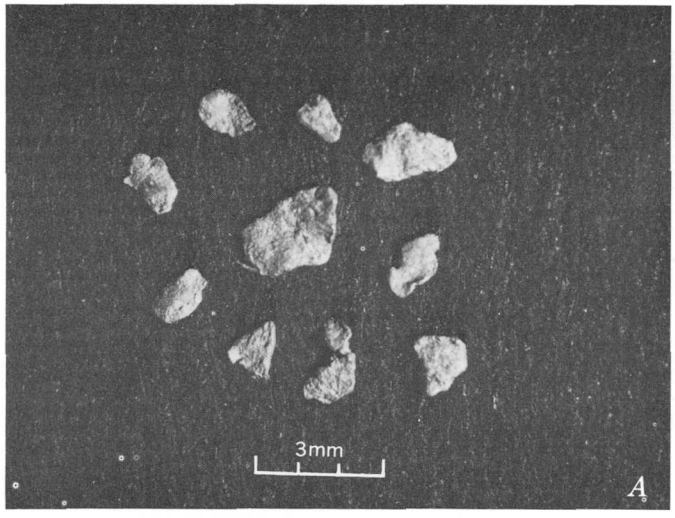

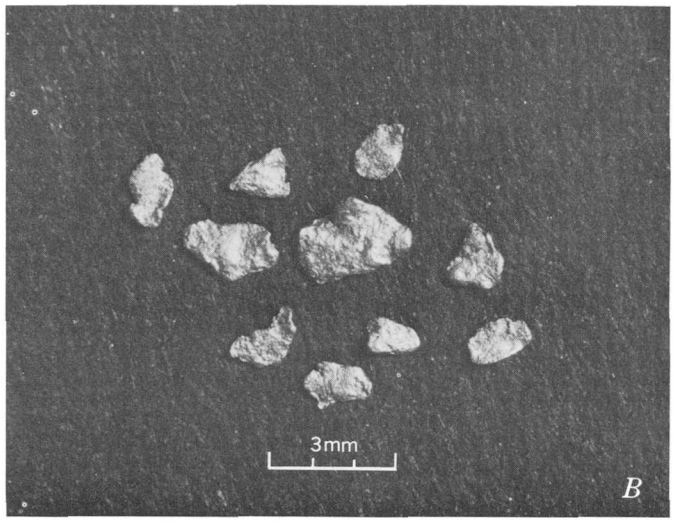

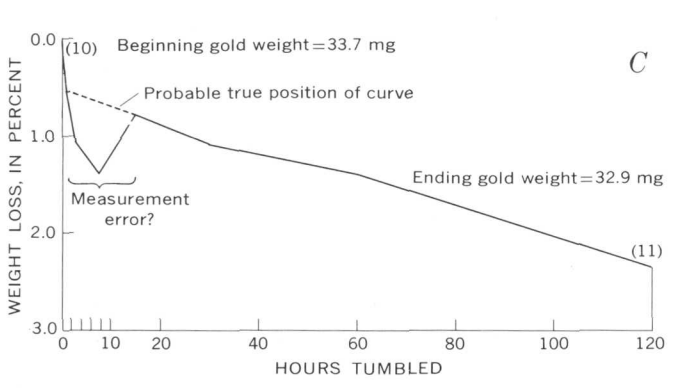

FIGURE 3.—Experiment 1: Abrasion of gold fragments by tumbling 120 h with sand, cobbles, and water. *A*, Gold fragments before tumbling. *B*, Gold fragments after tumbling. *C*, Weight loss of gold fragments during tumbling. Number of fragments before and after tumbling is shown in parentheses.

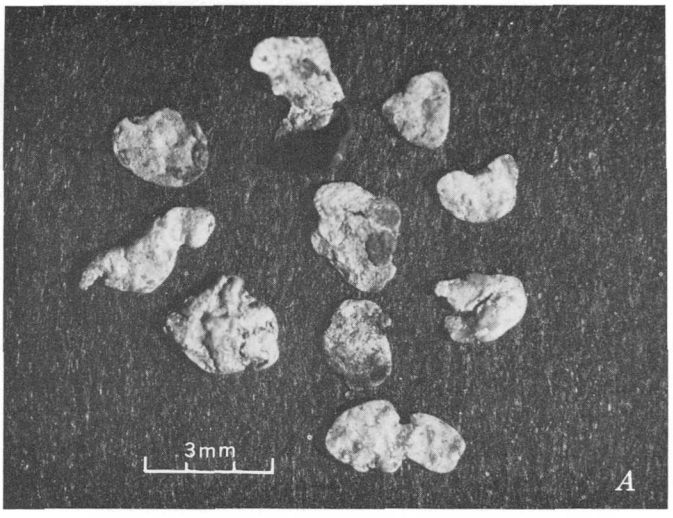

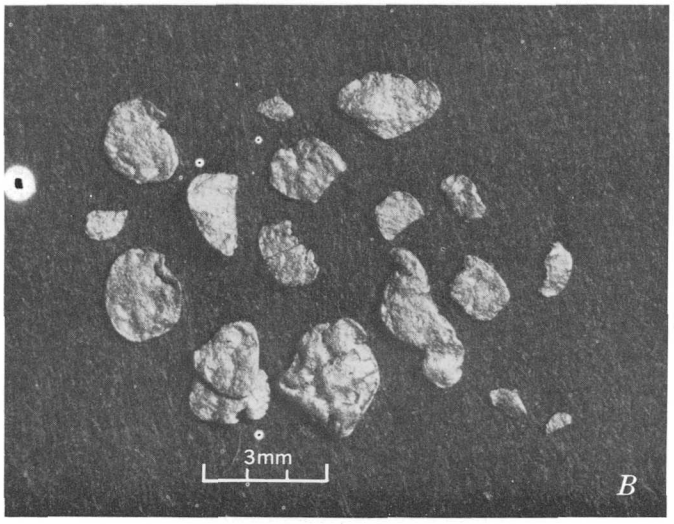

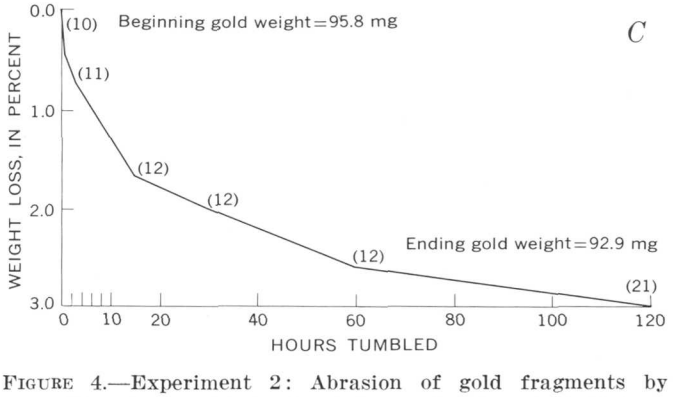

FIGURE 4.—Experiment 2: Abrasion of gold fragments by tumbling 120 h with sand, cobbles, and water. *A*, Gold fragments before tumbling. *B*, Gold fragments after tumbling. Of the 21 fragments recovered after tumbling, only 18 are shown. *C*, Weight loss of gold fragments during tumbling. Number of fragments recovered at various stages is shown in parentheses.

bles and 3.69 lb (1,673 g) of coarse sand were used in the experiment (fig. 2). Many of the grains in the coarse sand were composed of friable blue-gray phyllite and slate. This material broke down readily to clay and was lost during the panning stages; consequently little of the sand fraction survived the 120 h of tumbling.

At the end of the experiment, 21 gold fragments with a combined weight of 92.9 mg were recovered, representing a loss of 3 percent of the original weight. Of the original 10 fragments, five could be recognized (fig. 4*B*). With progressively longer travel, the rate of weight loss of the gold decreased. During the final 60 h of travel, the gold was abraded at a very low rate of 0.007 percent (by weight) per hour (fig. 4*C*). As with experiment 1, the greatest rate of weight loss, 0.5 percent per hour, occurred during the first 2 h of transport.

The cobbles lost 4 oz (113 g), or 6 percent of initial weight, and the sand lost 2.88 lb (1,308 g), or 78 percent.

Experiment 3

This experiment differed from the previous ones in including only cobbles and water and no sand in order to simulate a very high-energy environment that might occur in a pothole or at the base of a small rapid or riffle.

The gold fragments weighed 66.2 mg, were flattened with rounded edges, and measured as much as 3 mm long (fig. 5*A*). The same group of cobbles used in experiment 2 were used with the addition of three more to bring the starting weight to 4 lb (1,814 g).

After 120 h the original 10 gold particles had been broken down into many fragments; of these, 68 were large enough to recover with the gold pan. These 68 fragments weighed 49.2 mg; thus 26 percent of the weight of the original fragments had been lost or broken down to a size smaller than could be recovered by conventional panning techniques. Of the 68 gold fragments recovered, five can be recognized from the original 10 (fig. 5*B*). There were five large fragments (>1.0 mm diam.), 19 medium-size fragments (0.5–1.0 mm diam.), and 40 small fragments (<0.5 mm diam.). The 68 recovered gold fragments included five small spheres (four are shown in fig. 5*B*) that evidently resulted from tumbling with cobbles only.

The cobbles lost very little weight, however; the only derivative of the cobbles was 2 g of coarse sand.

As with the weight-loss curve for experiment 2 (fig. 4*C*), the rate of weight loss progressively decreased with increasing traveltime (fig. 5*C*). However, the rates of weight loss in experiment 3 are almost 10 times greater than in experiment 2. Between 30 and 120 h the rate of weight loss was nearly constant at 0.14 percent per hour (fig. 5*C*).

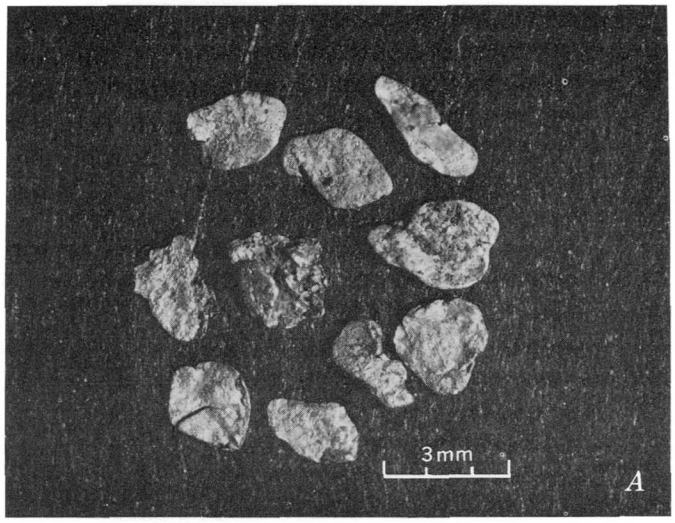

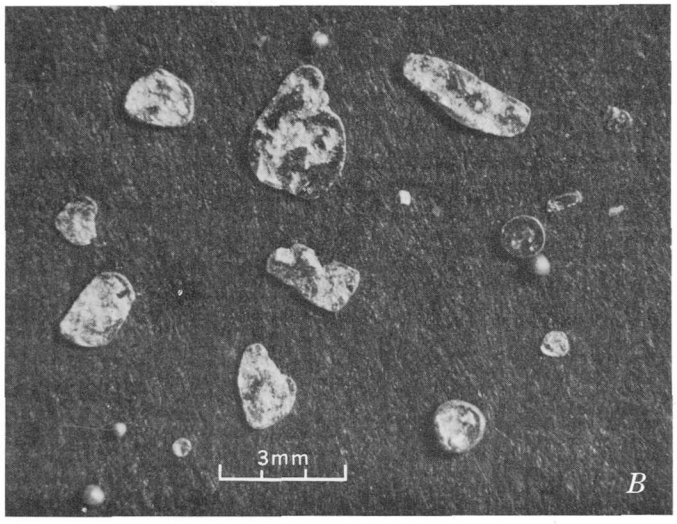

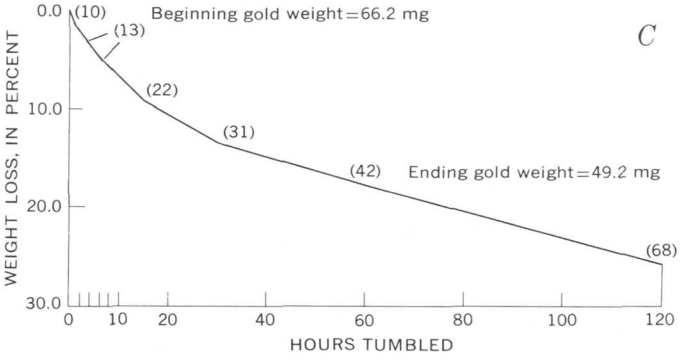

FIGURE 5.—Experiment 3: Abrasion of gold fragments by tumbling 120 h with cobbles and water. *A*, Gold fragments before tumbling. *B*, Gold fragments after tumbling. Of the 68 fragments recovered after tumbling, only 20 are shown. *C*, Weight loss of gold fragments during tumbling. Number of fragments recovered at various stages is shown in parentheses.

Experiment 4

Sand, water, and gold, but no cobbles, were the materials tumbled in experiment 4 to simulate the low-energy environment near a river mouth where gradients are low.

Believing that the abrasive losses would probably be low because of the lack of the hammering and pounding effect of cobbles, I selected the gold sample with the largest fragments, thinking that they would be most vulnerable to abrasion and would be most sensitive to small weight losses. The gold fragments weighed 508.3 mg and ranged in diameter from 2 to 10 mm at the beginning of the experiment (fig. 6*A*). Small bits of quartz adhered to some of the gold grains, and although the grains had rounded edges similar to the grains used in earlier experiments, they were more equidimensional and not flaky.

The coarse quartz-rich sand used in the experiment weighed 2.47 lb (1,120 g) and contained clasts as much as 5 mm in diameter; however, most were about 1 mm in diameter.

The original 10 gold fragments recovered at the end of the experiment show little observable change in size but were more lustrous (particularly the 10-mm-long fragment, fig. 6*B*). The gold weighed 504.0 mg at the end of the experiment, having lost only 0.84 percent. The rate of weight loss was slightly greater at the beginning of the experiment; however, beyond the 30-h mark, the rate of weight loss had become quite low and relatively constant at about 0.0045 percent per hour (fig. 6*C*). This rate is substantially lower than that determined in the earlier experiments—0.015 to 0.007 percent for gold tumbled with cobbles and sand, and 0.14 percent for gold tumbled with cobbles. The sand weighed 2.06 lb (935 g) at the end of 120 h of tumbling, having lost 17 percent of its original weight through abrasion.

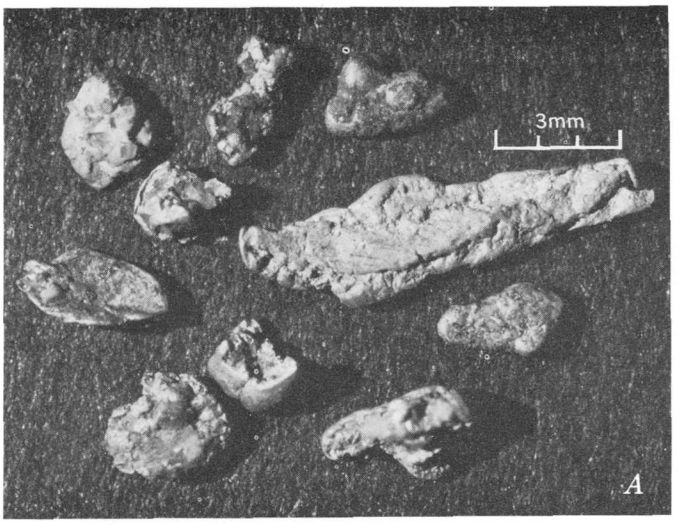

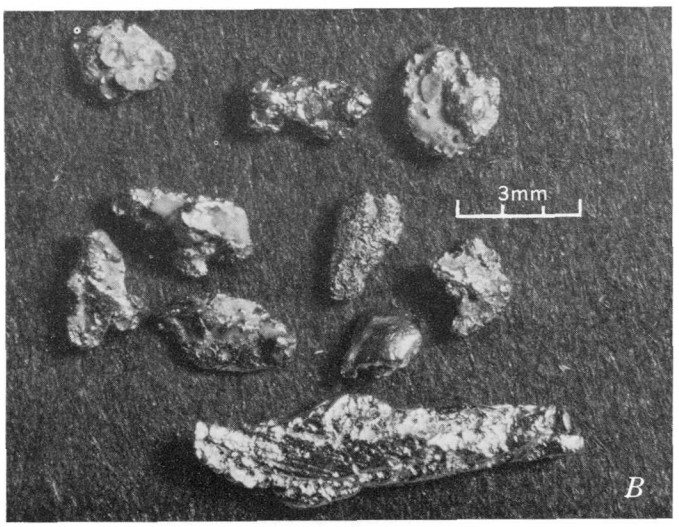

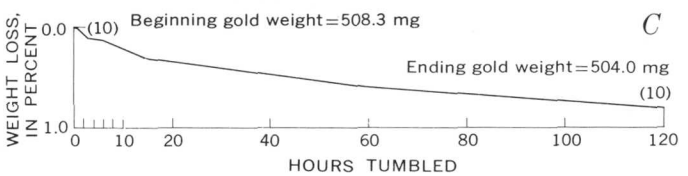

FIGURE 6.—Experiment 4: Abrasion of gold fragments by tumbling 120 h with sand and water. *A*, Gold fragments before tumbling. *B*, Gold fragments after tumbling. *C*, Weight loss of gold fragments during tumbling. Number of fragments before and after tumbling is shown in parentheses.

Experiment 5

The effect of the absence of water was studied in experiment 5. The 10 gold fragments were tumbled with dry sand for 105 h, at which point the electric motor broke down, and the experiment was concluded. I assumed that the absence of a water coating on the sand and gold fragments to act as a cushion would produce much higher abrasion rates than those found in the previous experiments. Thus a small sample of gold weighing 24.9 mg, with fragments ranging in diameter from 1 to 2.5 mm was used (fig. 7*A*).

The coarse, quartz-rich sand weighed 2.06 lb (935 g) at the beginning of the experiment. At the end of the experiment no change in the weight of sand was noted.

The 10 gold fragments showed little change after the 105 h of tumbling with the dry sand (fig. 7*B*); they were more lustrous, but changes in shape were impossible to detect with the naked eye. The gold lost 1.6 percent of its weight, however, in the first 30 h of travel. No measurable change in the weight of the gold was noted between the 30- and 105-h measurements

(fig. 7*C*); any weight loss that occurred was below the 0.05-mg sensitivity of the balance.

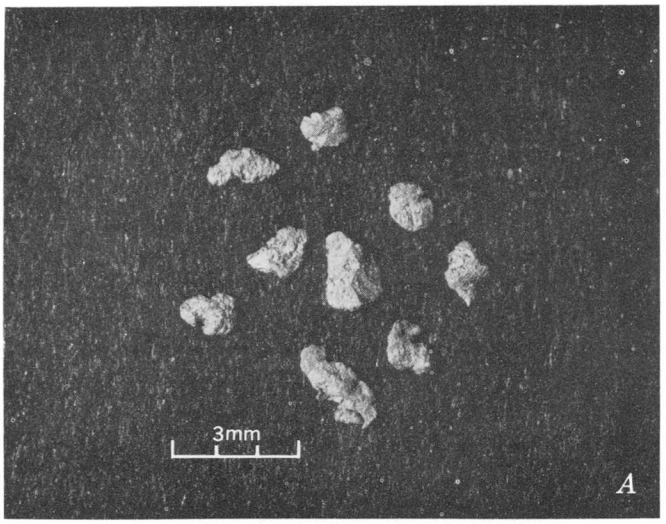

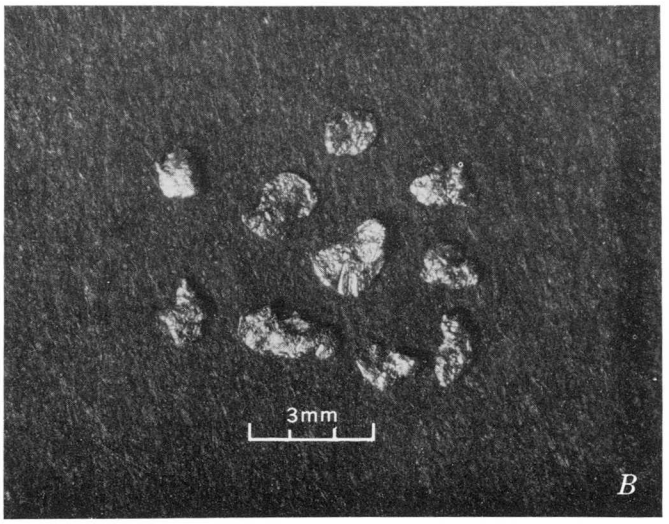

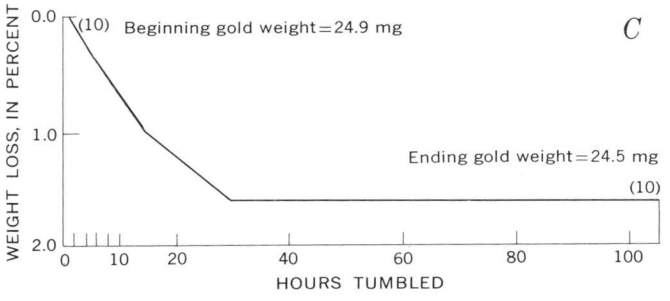

FIGURE 7.—Experiment 5: Abrasion of gold fragments by tumbling 105 h with dry sand. *A*, Gold fragments before tumbling. Only 9 of the original 10 fragments are shown. *B*, Gold fragments after tumbling. *C*, Weight loss of gold fragments during tumbling. Number of fragments before and after tumbling is shown in parentheses.

Experiments 6 and 7

A critical look at experiments 1 through 5 revealed some serious shortcomings; consequently, experiments 6 and 7 were conducted to establish firmer grounds for conclusions. Because it could be argued that 120 h was not sufficient time to establish the true abrasion rate of the gold particles, gold fragments that had already been tumbled for 120 h were tumbled for another 120 h in experiment 6. Likewise, because the products of abrasion had not been collected and analyzed for gold content, it could be argued that the loss in weight of the gold fragments resulted from the loss of impurities attached to the fragments rather than from a loss of elemental gold. The fines from experiments 6 and 7 were therefore analyzed for gold, and these results were compared with the calculated weight-loss figures. Furthermore, because the tumbler in experiments 1 through 5 had been run at the same speed, the effect of velocity on the abrasion of gold could not be determined. Experiments 6 and 7 were run under identical conditions except for velocity; in experiment 7 the tumbler was rotated approximately four times as fast as in experiment 6.

Experiment 6.—Five gold particles that had already been tumbled for 120 h were selected from those used in experiment 2 (fig. 4*B*). These fragments together with 4 lb (1,814 g) of coarse sand and 3.81 lb (1,742 g) of white quartz cobbles were tumbled together for 120 h at the same rate used in experiments 1 through 5 (0.5 mi/h or 0.85 km/h). The five gold particles, weighing 31.15 mg at the beginning of the experiment, broke down to six recoverable fragments after 120 h of tumbling and weighed 30.70 mg, a 1.44-percent weight loss (fig. 8). The cobbles showed a weight loss of 4.9 percent; the coarse sand, of 40 percent. All the fine-grained products of abrasion were saved for analytical tests for gold and combined with those produced in experiment 7.

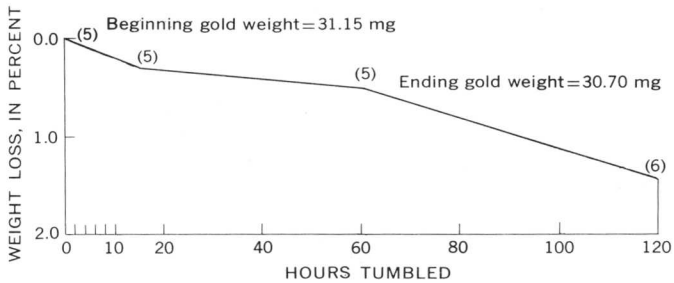

FIGURE 8.—Experiment 6. Abrasion of five gold fragments by tumbling 120 h with sand, cobbles, and water. Weight loss is shown; number of fragments recovered at various stages is shown in parentheses.

This experiment also indicated that 120 h of tumbling was, in fact, sufficient to establish the true abrasion rate of the gold particles. Although the values on the weight-loss curve for the second 120 h of tumbling (fig. 8) are not constant, they are within the same range as those obtained in the final 60 h of experiment 2 (fig. 4*C*). Thus the weight-loss values obtained near the end of the first 120 h of tumbling seem to be correct indicators of the abrasion rate of elemental gold and do not represent abrasion of impurities. This conclusion is supported by the detection of gold in the fine-grained products of abrasion.

Experiment 7.—Five gold fragments, similar in size and weight to those used in experiment 6 and previously tumbled for 120 h, were selected for experiment 7. These particles were tumbled for another 120 h with sand, cobbles, and water. The experiment differed from experiment 6 only in the tumbler speed, 2.0 mi/h (3.22 km/h) as compared with 0.5 mi/h (0.85 km/h) for experiment 6. The tumbling time was correspondingly reduced to 30 h (one-fourth of 120 h) to keep the total distance tumbled for the two experiments the same.

The gold weighed 31.65 mg at the beginning of the experiment and 30.35 mg at the end, a 3.65-percent loss. This is approximately two and a half times as great as the weight loss of the gold in experiment 6 (fig. 9).

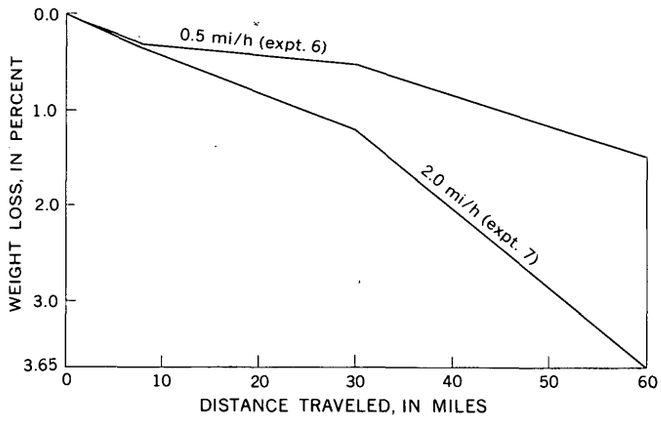

FIGURE 9.—Comparison of weight loss of gold fragments in experiments 6 and 7. In each experiment the fragments were tumbled with sand, cobbles, and water for the same distance but at different velocities; namely, 0.5 mi/h (0.85 km/h) in experiment 6 and 2.0 mi/h (3.22 km/h) in experiment 7.

The cobbles lost 6.5 percent of their weight as compared with 4.9 percent in experiment 6; the sand lost 89 percent as compared with 40 percent in experiment 6.

The total weight of the fines from experiments 6 and 7 was 2,190 g, 1.60 g of which should have been elemental gold on the basis of the weight-loss figures from the experiments. This is equivalent to about 0.73 ppm gold in the fines. The fines were analytically tested for gold by both atomic absorption and fire assay methods. Five runs, each on 15 g of sample, showed gold concentrations of 1.5 ppm by the fire assay method. Three runs, each using 10 g of sample, showed 0.8 ppm gold by the atomic absorption method, and two runs, each on 100 g of sample, showed 1.25 ppm gold by the atomic absorption method.

SEM EXAMINATION OF GOLD

In an attempt to determine the effects of abrasion on surface textures, representative gold fragments from each experiment were studied with the aid of a scanning electron microscope.

Significant differences in surface texture are apparent between fragments tumbled with (1) sand only, (2) sand and cobbles, and (3) cobbles only. The surface of the gold fragment tumbled with dry sand (expt. 5) is relatively smooth with few pits and no scratches (fig. 10*A*). Gold tumbled with cobbles and sand (expt. 2) shows a very irregular, pitted surface (fig. 10*B*), while gold tumbled with cobbles (expt. 3) shows, in addition to irregularities and pitting on the surface, many gouge or scratch marks (fig. 10*C*). The gold fragments tumbled only with cobbles lost the most weight in all the experiments. In other experiments the sand grains appear to have protected the gold from abrasion. When no sand was present, the cobbles scratched and gouged the gold fragments and caused the removal of minute gold particles.

INTERPRETATIONS AND CONCLUSIONS

In all seven experiments, the very slow rate of physical breakdown of the gold fragments is impressive, particularly when compared with the abrasion rate of the sand in the same experiments. Because gold is much more malleable than most of the common rock-forming minerals, these results are not surprising. Gold can absorb the impact and abrasive forces exerted by sand and gravel so that physical changes produced in the fragments are primarily changes in shape, unlike the common rock-forming minerals, which fracture and break when subject to impact and abrasion.

In experiments 1 through 5 the higher rates of weight loss occurred in the first 20 h of tumbling rather than the last 100 h (figs. 3*C*, 4*C*, 5*C*, 6*C*, 7*C*). Because all the gold fragments were originally coated to some degree with oxides that progressively disappeared with distance of travel, it seems clear that the high rates of weight loss in the early stages were produced by the attrition of the oxide coatings. Such a process probably occurs in nature as the individual

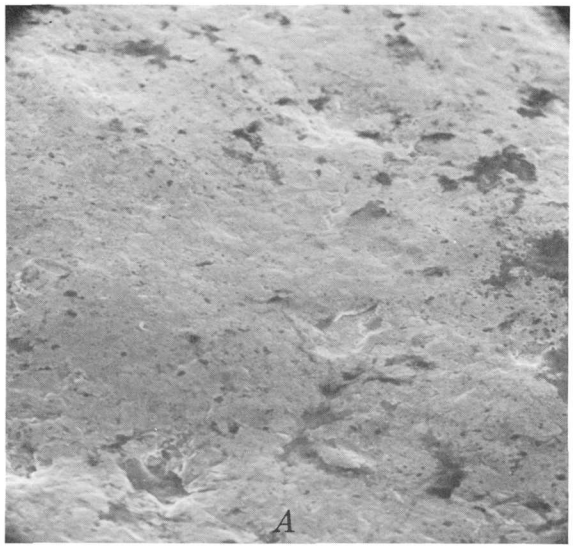

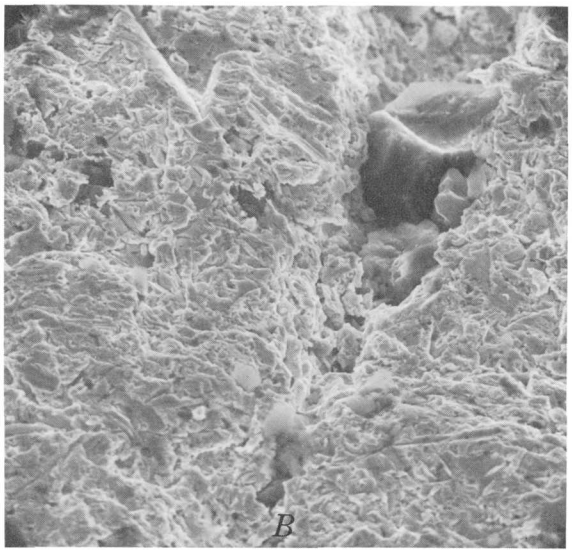

gold fragments are subjected to long periods of weathering and chemical action during the long process of their release from the mother lode, and they most likely arrive at the river or stream with substantial oxide coatings. Once the coatings are removed and the gold takes on the typical high luster, the abrasion curve flattens out and the rate of abrasion becomes fairly constant. The last 60–100 h of the curve is most important as it represents the rate of physical breakdown of the pure gold rather than the more easily abraded grain coatings.

It seems clear from experiments 1 through 5 that cobbles, rather than sand, are responsible for most of the abrasion and physical changes produced in the gold. In experiment 3 cobbles broke up the original 10 gold fragments into 68 (recovered) fragments with a corresponding weight loss of more than 25 percent. In experiment 4 the gold that was tumbled with sand rather than cobbles lost less than 1 percent of its weight with no observable change in shape of the gold fragments. These differing results probably were partly minimized by the fact that the fragments used in experiment 4 were much larger. If other factors were equal in the two experiments, the larger gold fragments would very likely undergo greater abrasion and weight loss. The larger gold sample was used in experiment 4 because it was expected that the weight losses would be low and a larger sample would produce larger weight losses that would be easier to measure.

Although experiments 1 and 2 were run under similar conditions with similar materials (gold, sand, cobbles, and water), the results differed (figs. 3 and 4). The gold in experiment 2 broke down into 21 recoverable fragments and lost about 3 percent of its weight, whereas the gold in experiment 1 broke down into 11 fragments and lost 2.4 percent of its weight. Several factors account for these differences. Experiment 2 utilized almost three times as much gold (by weight) as experiment 1, and therefore, the larger amount of gold lost a larger percentage of weight, particularly if correspondingly larger amounts of impurities were attached to the gold particles. Also, the sands used in the two experiments differed in composition. Sand with a high quartz content was used in experiment 1, whereas sand with a high percentage of friable rock fragments, slate, and phyllite was used in experiment 2. During the tumbling, the slate and phyllite clasts broke

FIGURE 10.—Electron micrographs of surfaces of gold fragments after experimental abrasion. *A*, Fragments tumbled with dry sand (expt. 5), × 1,600. *B*, Fragments tumbled with sand, cobbles, and water (expt. 2), × 1,600. *C*, Fragments tumbled with cobbles and water (expt. 3), × 1,360.

down to clay-size material and were removed during the panning stages; at the end of the experiment only 22 percent of the sand remained. In experiment 1, 38 percent of the sand survived the 120 h of tumbling. The gold in experiment 2, therefore, was subjected to more impact and abrasion from the cobbles because the gold fragments were not effectively protected by sand as they were in experiment 1. Evidently, the presence of even a small amount of sand greatly lessens the abrasive effects of pebbles and cobbles. Despite the small amount of sand present toward the end of experiment 2, the gold lost only 3 percent of its weight, but the gold in experiment 3 lost more than 25 percent of its weight merely because sand was absent.

Once the oxide coatings were abraded from the gold fragments being tumbled with dry sand in experiment 5, no measurable change in the size of the gold fragments occurred (fig. 7). Although the total percentage of weight loss of the gold is greater with the dry sand (expt. 5) than the wet (expt. 4), this may merely represent differing amounts of oxide coatings initially present on the gold. Thus pure gold may be abraded at a faster rate in an environment of wet rather than dry sand. From experiments on the rate of wear of sand grains, Anderson (1926) concluded that "sand submerged in water wears down more rapidly than dry sand transported over the same distance."

Because experiments 6 and 7 used gold fragments that had been previously tumbled for 120 h, the curves showing the percentage of weight loss versus time and length of travel (figs. 8 and 9) most likely represent actual weight loss of elemental gold and not loss of impurities. The average rate for experiment 6 is 0.012 percent per hour and for experiment 7 is 0.122 percent per hour. A fourfold increase in velocity produced a tenfold increase in abrasion rate on the basis of duration of travel. On the basis of equal travel distance, the fourfold increase in velocity increased abrasion two and a half times (fig. 9).

From these experiments it seems clear that velocity is a more important factor in abrasion of gold than travel distance. As with the silicate minerals, the vigorous, turbulent, high-energy environment is most critical in the mechanical breakdown of elemental gold. The presence of large cobbles and boulders with small amounts of fine-grained material in a high-velocity fluvial environment is the most effective situation for abrasion of native gold.

REFERENCES CITED

Alling, H. L., 1944, Grain analyses of minerals of sand size in ball mills: Jour. Sed. Petrology, v. 14, p. 103–114.

Anderson, G. E., 1926, Experiments on the rate of wear of sand grains: Jour. Geology, v. 34, p. 144–158.

Goni, J., Guillemin, C., and Sarcia, C., 1967, Geochimie de l'or exogéne: Mineralium Deposita, v. 1, p. 259–268.

Krumbein, W. C., 1941, The effects of abrasion on the size, shape, and roundness of rock fragments: Jour. Geology, v. 49, p. 482–520.

Kuenen, P. H., 1956, Rolling by current, pt. 2 *of* Experimental abrasion of pebbles: Jour. Geology, v. 64, no. 4, p. 336–368.

Schumm, S. A., and Stevens, M. A., 1973, Abrasion in place—A mechanism for rounding and size reduction of coarse sediments in rivers: Geology, v. 1, no. 1, p. 37–40.

Thiel, G. A., 1940, The relative resistance to abrasion of mineral grains of sand size: Jour. Sed. Petrology, v. 10, p. 102–124.

Wentworth, C. K., 1919, A laboratory and field study of cobble abrasion: Jour. Geology, v. 27, p. 507–522.

——— 1931, Pebble wear on the Jarvis Island Beach: Washington Univ. Studies, Sci. and Technology, no. 5, new ser., p. 11–37.

Yeend, W. E., 1974, Gold-bearing gravel of the ancestral Yuba River, Sierra Nevada, California: U.S. Geol. Survey Prof. Paper 772, 39 p.

Jour. Research U.S. Geol. Survey
Vol. 3, No. 2, Mar.–Apr. 1975, p. 213–221

CYLINDRICAL JOINTING IN MAFIC DIKES, CENTRAL BEARTOOTH MOUNTAINS, MONTANA

By THEODORE J. ARMBRUSTMACHER and FRANK S. SIMONS, Denver, Colo.

Abstract.—Cylindrical joints are well displayed in two Precambrian mafic dikes that cut granitic gneiss in the central Beartooth Mountains, Mont. The dikes are vertical and about 23 m (75 ft) and 23 to 46 m (75–150 ft) thick, respectively. The cylindrical joints are perpendicular to the dike walls, and the cylinders defined by the joints are as much as 5 m (16 ft) in diameter. No petrographic, textural, or other features related to or possibly responsible for the joints are recognized. The dikes are chemically and petrographically similar to quartz dolerite dikes found throughout the Beartooth Mountains. Some of these dikes show typical polygonal columnar joints; a few others have cylindrical jointing, but in most dikes neither kind of jointing was observed. The orientation of the cylindrical joints normal to the walls of the dikes indicates that they probably formed by thermal contraction during post-crystallization cooling of the dikes and are thus genetically related to the much more common polygonal jointing. However, the model proposed to explain the cylindrical joints suggests that their origin is partly dependent on the geometric relation between the orientation of the dikes and that of the predike fracture pattern in the host rock.

An exceptionally well exposed example of cylindrical jointing was observed at an altitude of approximately 3,570 m (11,700 ft) in a Precambrian mafic dike on the south flank of Mystic Mountain (fig. 1) in the central Beartooth Mountains. This dike is referred to as the Mystic Mountain dike. A second mafic dike that displays cylindrical jointing is in the Cloverleaf Lakes area on the southwest flank of the Beartooth Mountains about 10 km (6 mi) north of Beartooth Lake and was described by Prinz and Bentley (1964). We have extended their observations on this dike for several kilometres to the north and have recognized a probable extension of the dike to the south side of Beartooth Butte. This dike is referred to as the Whitetail Peak dike.

Cylindrical joints in mafic dikes have been described from the Bighorn Mountains, Wyo. (Heimlich, 1969); southern Beartooth Mountains, Mont. and Wyo. (Prinz and Bentley, 1964); Gowganda, Ontario (Eakins, 1961; Hester, 1967; Jambor, 1971); Mersey Bluff, Tasmania (Hill, 1965); and Olenegorsk, U.S.S.R. (Goryainov and Pesterev, 1970); but apparently they are rather rare.

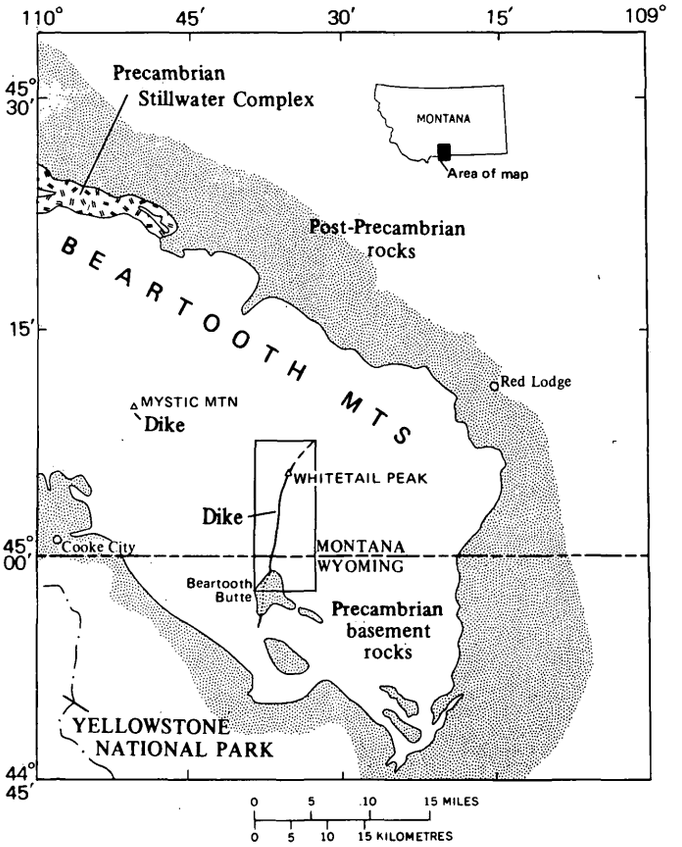

FIGURE 1.—Generalized geologic map of Beartooth Mountains vicinity, Montana and Wyoming, showing location of the Mystic Mountain dike and the Whitetail Peak dike. The dikes are dashed where approximately located and dotted where covered. Area of figure 3 is outlined.

FIELD RELATIONS

The Mystic Mountain dike is approximately 23 m (75 ft) thick, strikes about N. 45° W., dips about 90°, and crops out for less than a kilometre along strike. The dike is chilled against the fresh, pink granitic gneiss country rock but is holocrystalline less than a metre from the contact.

The dike displays abundant cylindrical joints at the only place in this rugged terrain where it is ac-

cessible to observation. The cylinders defined by jointing are circular to elliptical in cross section (figs. 2*A*, *B*, *C*) and as much as 3 m (10 ft) in diameter. They exhibit variable degrees of development (fig. 2*A*) and do not seem to interpenetrate. Axes of the cylinders are nearly horizontal, are perpendicular to the dike walls, and are not curved or deformed. In individual cylinders the joints are concentrated near the periphery and are sparse to nonexistent in the core. Radial fracturing is also better developed near the periphery of a cylinder and virtually absent from the center. The axial terminations observed in the Gowganda area, Ontario, by Eakins (1961) were not seen here. A strong set of planar joints is parallel to the dike walls, and so the cylinders break into large discoidal slabs as a result of frost wedging (fig. 2*D*). The distribution of these joints across the dike is generally uniform; at least they do not seem to be concentrated near either the northeast wall or the center; the southwest part of the dike is too poorly exposed to permit any generalization about distribution of planar joints. Some of these joints near the center

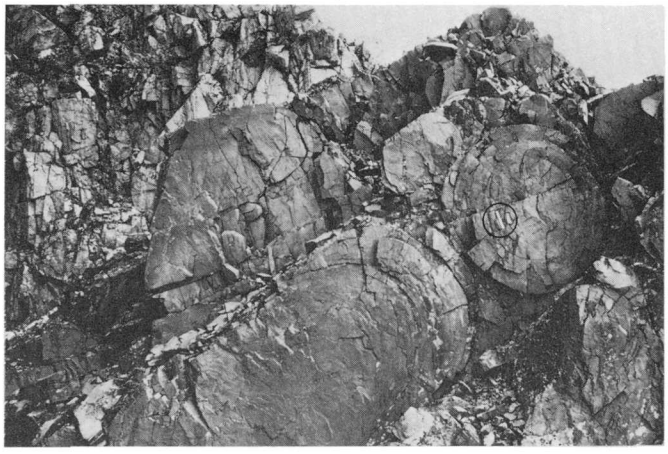

A

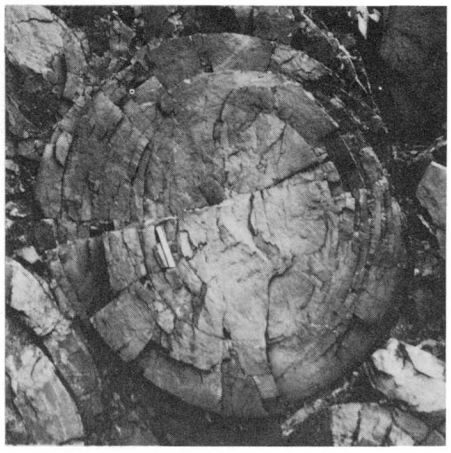

B

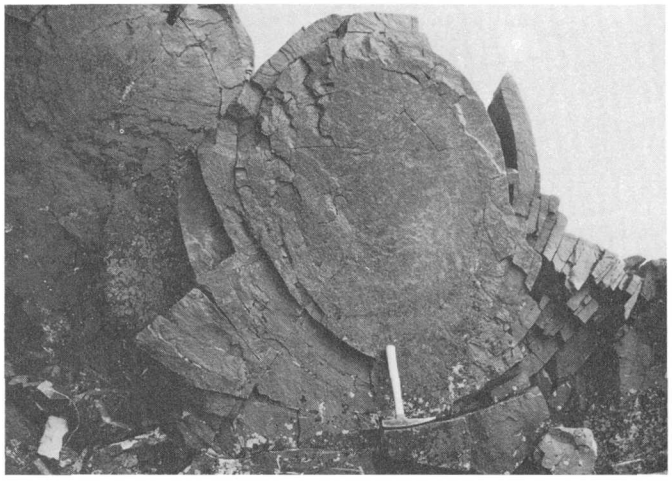

C

D

FIGURE 2.—Cross sections of several cylinders on Mystic Mountain. *A*, View northeast, about perpendicular to dike. Cylinder at lower center has elliptical cross section, but most cylinders are nearly circular. Handle of hammer (circled) is 33 cm (13 in.) long. *B*, Closeup of cylinder in upper right of *A*. Cylindrical joints are more closely spaced toward rim than in core. Radial joints are poorly developed and confined mainly to rim. Some crosscutting, nearly horizontal post-cylinder jointing can also be observed. (Illustration also appears on cover of Geotimes, v. 17, no. 4, April 1972.) *C*. Cylinder that has an ellipsoidal or egg-shaped cross section. Note partly detached curved slab (right center) and the unjointed nature of the core. Handle of hammer is 33 cm (13 in.) long. *D*, View approximately along the strike of dike, showing a broken discoidal slab bounded by cylindrical and planar joints. Note planar joints in the background and at right. Handle of hammer is 33 cm (13 in.) long.

of the dike appear in the background of figure 2*D*, in which the view is along the strike of the dike. A poorly developed, irregular, subhorizontal joint set passes between cylinders and rarely across cylinders (fig. 2*A*). The joint set between cylinders is interpreted to be inherited from the host rock and fundamental to the formation of cylindrical jointing (see "Discussion"). The joint set that crosses cylinders postdates formation of the cylinders. The absence of surface features on joint planes, such as plumose structures or concentric ridges, which may indicate shearing (Price, 1966, p. 121), suggests that movement was normal to joint planes (tension joints). Intracolumnar differentiation, observed by Lafeber (1956) in basalts of the Upper Tumut area, Australia, was not detected. In addition, deuteric alteration, weathering, and mineralization are not concentrated in or along joint surfaces.

The Whitetail Peak dike is exposed almost continuously from Native Lake, at the north end of Beartooth Butte, to the north flank of Whitetail Peak, a distance of 12 km (7.5 mi) (fig. 3). It is believed to extend southward beneath the younger rocks of Beartooth Butte and to reappear near the Beartooth Highway about 6.5 km (4 mi) south-southwest of Native Lake. It may also extend for about 5 km (3 mi) along the east wall of the canyon of West Fork Rock Creek, but exposures there are very limited. The dike thus is at least 12 km (7.5 mi) long, is probably 18.5 km (11 mi) long, and possibly is more than 23 km (14 mi) long.

The Whitetail Peak dike has a general trend of slightly east of north, which is unusual among mafic dikes of the Beartooth Mountains, and has a somewhat sinuous trace, as shown in figure 3. The dike is nearly vertical throughout its entire length and ranges in thickness from 23 to 46 m (75–150 ft). Wallrocks are mainly biotite gneiss typical of the Beartooth Precambrian terrane but also include several small masses of amphibolite. Dike borders are chilled against wallrocks, and the chill zone is as much as a metre thick.

It seems significant that the Whitetail Peak dike displays well-developed cylindrical joints over its entire observable length and through a vertical range of more than 750 m (2,500 ft), despite changes in strike of as much as 30° or 35° and considerable, but not unusual, variation in thickness. The cylinders are particularly well displayed just north of the crest of the mountains and west of Golden Lake. The cylinders are everywhere approximately perpendicular to the dike walls and resemble a stack of gigantic logs in outcrops along the steep slopes both north and south of the north branch of Lake Fork Rock Creek. The

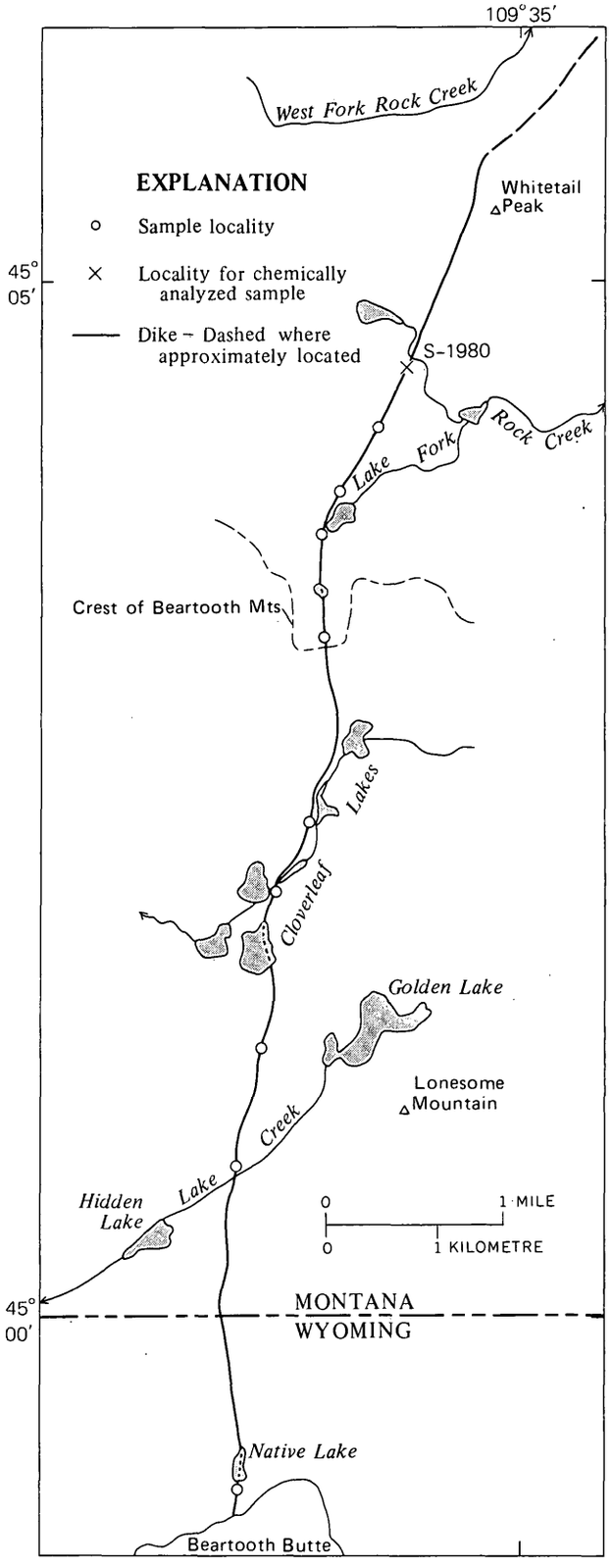

FIGURE 3.—Area between Native Lake and Whitetail Peak. Shown are trace of Whitetail Peak dike and localities of chemically analyzed sample S–1980 and of samples used in compilation of petrographic data in table 1.

dike is unmetamorphosed and does not seem to be structurally controlled by any metamorphic feature of the wallrocks. Its northerly trend is markedly different from the northeasterly, easterly, and southeasterly trends of the conspicuous lineaments of the region, and offsets of the dike by lineaments, faults, or other dikes are either small or nonexistent (Simons and others, 1973, pl. 1). Prinz and Bentley (1964) made a detailed study of jointing in both dike and wallrock gneiss in the Cloverleaf Lakes area and concluded that the fracture pattern in the dike was distinctly different from that in the wallrocks.

Most of the cylinders in the Whitetail Peak dike have diameters in the same size range as those of the Mystic Mountain dike, but some are thicker and attain diameters of 5 m (16 ft) or more (fig. 4*A*). In general the cylinders have the same features as seen in the Mystic Mountain dike; in particular, the cores of the cylinders are relatively unjointed and somewhat more resistant to weathering than the rims (fig. 4*B*). Radial fractures in cylinders from this dike, described by Prinz and Bentley (1964) as being best developed and more numerous near the center of cylinders, are actually better developed peripherally to unfractured cylinder cores. Cylindrical joints that extend through the entire dike, including the chilled border zone, are well exposed 1.6 km (1 mi) south of Whitetail Peak; the joints can be seen to end at the gneiss wallrocks.

PETROGRAPHY

Mafic rocks in the Mystic Mountain dike are petrographically similar to quartz dolerites in Precambrian terranes of the southern Beartooth Mountains (Prinz, 1964, p. 1227) and the southeastern Bighorn Mountains, Wyo. (Armbrustmacher, 1972). Modes of selected specimens are presented in table 1, columns 1–3.

At the knife-sharp contact with gneiss (fig. 5*A*), the dike rock is porphyritic and contains epidote-chlorite pseudomorphs after olivine(?), composite grains of slightly corroded augite, and laths of partly saussuritized plagioclase. These minerals have maximum sizes of 0.6–0.8 mm. Mineral grains in the groundmass cannot be resolved under the microscope.

About a metre from the contact the texture becomes subophitic (fig. 5*B*). Bimodal size distribution of clinopyroxenes (about 0.6 and 0.2 mm) gives the rocks a porphyritic aspect. Plagioclase laths average 0.4 mm long, are twinned according to Carlsbad and albite laws, and are slightly saussuritized. The clinopyroxene crystals consist of closely associated augite and pigeonite that can be readily distinguished only by optic angle ($2V$) and are therefore listed together in table 1. Hornblende and biotite are deuteric alteration

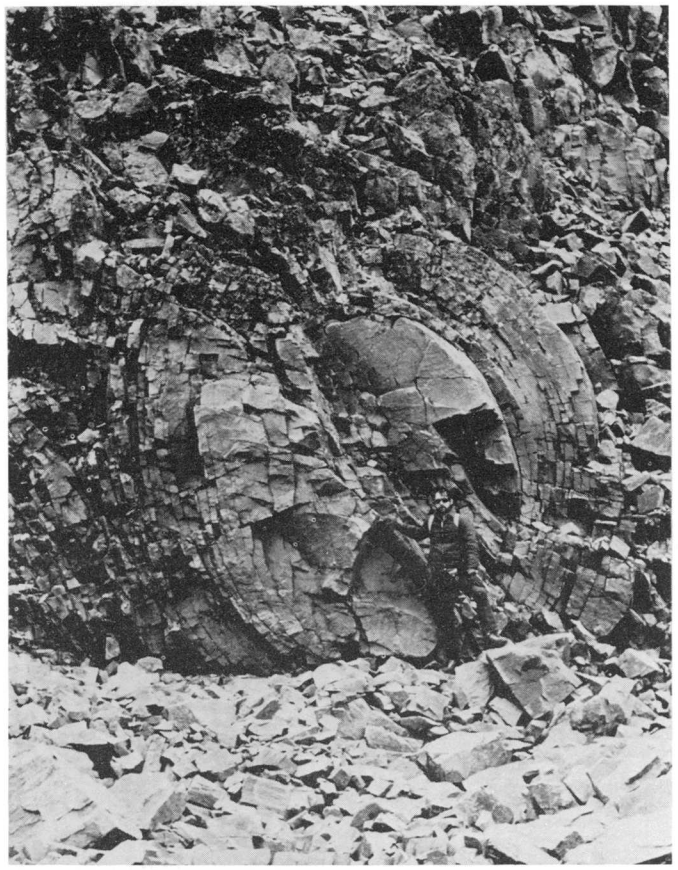

A

B

FIGURE 4.—Cylinders and cylindrical joints in Whitetail Peak dike. *A*, End view of large cylinder; view looking N. 70° W., about perpendicular to dike walls, from point 3 km (1.8 mi) south-southwest of Whitetail Peak. Cylinder is elliptical in cross section and has a maximum diameter of 5 m (16 ft); it consists of massive core 3–3.5 m (10–11.5 ft) in diameter and rim 1–1.5 m (3–4.5 ft) thick. Rim displays closely spaced conspicuous cylindrical and radial joints. *B*, Cylindrical joints exposed in cliff 12 m (40 ft) high, approximately parallel to dike walls. Note core (about 1-m diameter) of small cylinder (lower right center) protruding from cliff. Same area as *A*.

TABLE 1.—*Modes, in volume percent, of Mystic Mountain, Whitetail Peak, and quartz dolerite dikes*

[Tr, trace]

Mineral	1	2	3	4	5	6	7	8
Plagioclase	38.1	50.5	49.0	53.7	51.1–60.0	46.6	44.8	30.1–55.9
Clinopyroxene	50.9	37.1	36.4	34.7	32.7–37.4	46.2	34.5	24.6–49.3
Orthopyroxene	----	----	----	---	--------	---	3.0	0–10.2
Hornblende	3.9	3.5	4.5	5.0	3.4– 7.9	1.1	4.4	1.2–13.6
Quartz	.4	1.5	1.7	2.7	2.5– 4.2	1.6	1.3	0– 5.0
Biotite	1.4	.1	.4	.5	.1– 0.9	1.2	.6	0– 2.5
Chlorite	1.4	5.1	4.2	1.5	Tr.– 1.9	.7	1.1	0– 6.7
Opaque minerals	3.9	2.1	3.5	1.9	1.1– 2.6	2.6	6.5	3.1–16.8
Micropegmatite	----	----	----	---	---------	---	2.1	0– 7.9
Number of counts	1318	1556	1638	855–980	--------	820, 845	1500–2000	--------

1. Mystic Mountain dike; fine-grained border, 1 m from southwest contact.
2. Mystic Mountain dike; center of cylinder shown in figure 2*B*.
3. Mystic Mountain dike; periphery of cylinder shown in figure 2*B*.
4. Whitetail Peak dike; average of five modal analyses of coarse-grained parts of dike.
5. Whitetail Peak dike; range of percentages of each mineral of column 4.
6. Whitetail Peak dike; average of two modal analyses of chilled border. Plagioclase, 45.7 and 47.5 percent; clinopyroxene 45.9 and 46.5 percent.
7. Quartz dolerite dikes; average of 11 modal analyses of eight dikes (Prinz, 1964, p. 1224, table 2, cols. 1–11).
8. Quartz dolerite dikes; range of percentages of each mineral in column 7.

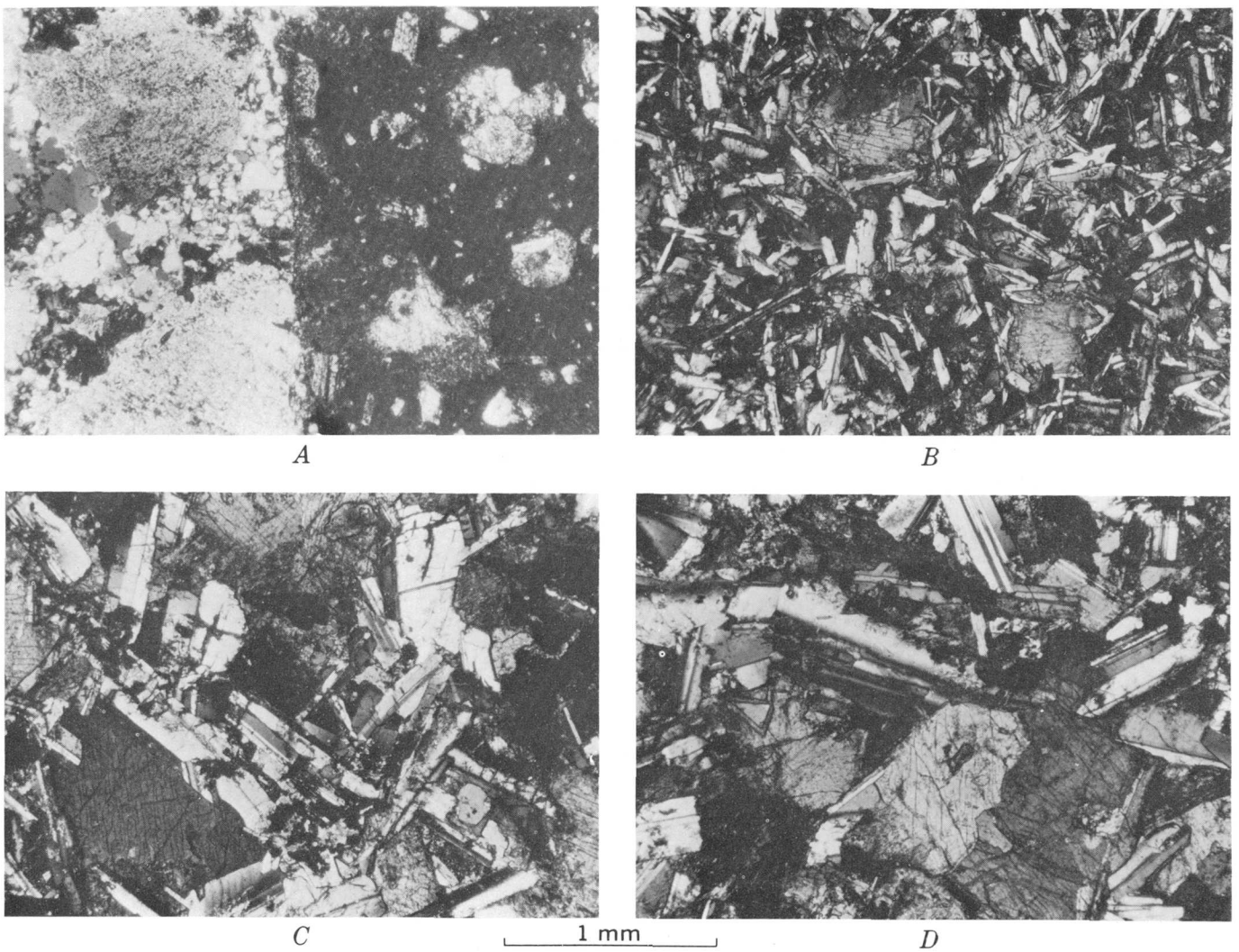

FIGURE 5.—Photomicrographs of Mystic Mountain dike. Crossed nicols. *A*, Contact of dike (dark) with granitic gneiss country rock (light). In dike rock, partly altered phenocrysts are enclosed in a microcrystalline groundmass. Contact metamorphism of gneiss is virtually absent. Specimen S–443E. *B*, Medium-grained porphyritic and subophitic diabase, near southwest wall of dike. Specimen S–443A. *C*, Diabase from center of cylinder shown in figure 2*B*, near middle of dike. Plagioclase is partly saussuritized. Specimen S–443B. *D*, Diabase from periphery of cylinder shown in figure 2*B*. Alteration similar to that in 5*C*. Specimen S–443C.

products of clinopyroxene, and chlorite occurs as pseudomorphs after olivine. Quartz is interstitial and probably crystallized late.

Specimens were collected from the center of a cylinder (table 1, analysis 2; fig. 5*C*), and from the periphery (table 1, analysis 3; fig. 5*D*), both approximately equidistant from the dike walls, in order to determine if cylinder development is related to any obvious lithologic variation. The textures of both these rocks are subophitic, and their modes are strikingly similar, especially if percentages of alteration minerals are added to primary minerals. The most abundant minerals are plagioclase and clinopyroxenes. The average grain size of plagioclase in both specimens is about 1 mm. Because petrographic studies across individual dikes have shown that the plagioclase-clinopyroxene ratio becomes larger away from dike contracts toward the dike center owing to fractionation (see Manzer and others, 1971; T. J. Armbrustmacher, unpub. data), the similarity of this ratio in specimens from center and core of a cylinder indicates that isotherms were probably parallel to dike walls during crystallization.

Specimens from 10 localities along the Whitetail Peak dike were studied microscopically, and modal analyses of five coarse-grained and two fine-grained specimens are summarized in table 1, columns 4–6. All specimens examined have a subophitic texture, and their modal analyses are similar, as shown by the narrow range of percentages of all minerals (table 1, col. 5). The specimens are all altered in a similar way. Plagioclase is approximately 75 percent turbid owing to development of epidote and clinozoisite as products of alteration; clinopyroxene (augite and pigeonite), however, is only slightly altered to hornblende, biotite, and chlorite. Sparse rounded areas of fine-grained secondary minerals, often surrounded by clinopyroxene, are interpreted as pseudomorphs after olivine.

TABLE 2.—*Chemical analyses and norms, in weight percent, of Mystic Mountain and Whitetail Peak dikes, quartz dolerite dikes, and continental tholeiites*

	1	2	3	4	5	6	7
Chemical analyses							
SiO_2	50.3	51.7	51.8	51.4	51.2	50.0	50.8
Al_2O_3	14.5	14.8	13.9	13.6	16.2	14.1	15.8
Fe_2O_3	2.1	1.8	[1]11.3	[1]11.4	[1]10.8	2.7	2.7
FeO	8.9	8.0	-----	-----	-----	9.9	8.6
MgO	6.9	7.6	8.7	9.3	6.9	6.3	6.5
CaO	11.1	10.9	11.6	11.3	11.4	9.0	9.8
Na_2O	2.0	1.8	2.1	2.2	1.8	2.5	2.5
K_2O	.54	.88	.62	.96	.58	1.2	.77
H_2O+	1.1	1.5	-----	-----	-----	1.8	-----
H_2O-	.22	.10	-----	-----	-----	.14	-----
TiO_2	.92	.65	.91	.68	.59	1.5	1.5
P_2O_5	.13	.02	-----	-----	-----	.12	.24
MnO	.22	.16	-----	-----	-----	.22	.16
CO_2	.84	<.05	-----	-----	-----	.16	-----
Sum	100	100	100.9	100.8	99.5	99.6	99.4
CIPW norms							
Q	3.6	2.6	-----	-----	-----	1.0	2.0
or	2.8	5.6	-----	-----	-----	7.2	4.5
ab	16.8	15.2	-----	-----	-----	21.0	21.0
an	29.2	29.5	-----	-----	-----	23.6	29.8
wo	8.2	10.3	-----	-----	-----	8.0	7.5
en	17.3	19.0	-----	-----	-----	15.6	16.2
fs	13.6	12.4	-----	-----	-----	13.9	11.2
il	1.7	1.4	-----	-----	-----	2.9	2.9
mt	3.0	2.6	-----	-----	-----	3.9	3.9
ap	.3	-----	-----	-----	-----	.3	.3
cc	1.9	-----	-----	-----	-----	.4	-----

[1] Total iron reported as Fe_2O_3.

1. Mystic Mountain dike, same as 1, in table 1. Field No. S–443A, Lab. No. W–176776. Analysts: P. D. Elmore, H. Smith, James Kelsey, and John Glenn.
2. Whitetail Peak dike, approximate mineral composition given in column 6, table 1. Field No. S–1980, Lab. No. W–178613. Analysts same as for 1. Lake Fork Rock Creek, 1.6 km S. 30° W. of Whitetail Peak; sample is from chilled border.
3. Whitetail Peak(?) dike (Mueller, 1971, app. D, sample MBT–35; 1.4 km west of Lonesome Mountain.
4. Whitetail Peak(?) dike (Mueller, 1971, app. D, sample MBT–91; Beartooth Highway about 4 km west-southwest of Beartooth Lake.
5. Whitetail Peak(?) dike (Condie and others, 1969, p. 1375, sample BT–39; same location as 4).
6. Precambrian quartz dolerite dikes, southern Beartooth Mountains; average of five analyses (Prinz, 1964, p. 1237, Nos. 18–22 inclusive)
7. Continental tholeiites, North America; average of 173 analyses (Manson, 1967, p. 223)

CHEMISTRY

Chemical analyses of the Mystic Mountain and Whitetail Peak dikes are given in table 2 along with the average of analyses of 5 quartz dolerites from the southern Beartooth Mountains (Prinz, 1964, p. 1237), and 173 North American continental tholeiites (Manson, 1967, p. 223). Spectrographic analyses of selected elements in specimens of the Mystic Mountain and Whitetail Peak dikes and quartz dolerite dikes from the northern Beartooth Mountains, the Bighorn Mountains, and in worldwide quartz-normative tholeiites (Prinz, 1967, p. 278) are given in table 3. The chemical analyses are similar, although the Mystic Mountain and Whitetail Peak dikes are somewhat higher in CaO and lower in TiO_2 than the average rocks shown in columns 6 and 7. The TiO_2 content of quartz dolerite in the southern Beartooth Mountains varies from about 0.74 to 3.2 percent (Mueller, 1970, p. 428); inasmuch as the TiO_2 contents reported for the Mystic Mountain dike and one analysis of the Whitetail Peak dike fall within that range and also within the range of Prinz's (1964, p. 1237) quartz dolerite analyses, they do not seem to represent unusually low concentrations. Contents of minor elements given in table 3 also are very similar, with minor variations reflecting minor mineralogical differences. Chemical analyses indicate that no readily apparent difference in composition occurs between dikes characterized by cylindrical joints and petrologically similar but apparently unjointed dikes.

TABLE 3.—*Selected elements determined by spectrographic analyses, in parts per million, in Mystic Mountain and Whitetail Peak dikes and mafic dikes of the Beartooth and Bighorn Mountains, and elsewhere*

Element	*1	*2	3	4	5	6
Ba	150	150	175	350	170	250
Co	50	20	40	60	50	38
Cr	100	300	240	230	390	153
Cu	150	30	105	100	85	141
Ni	150	70	90	80	175	77
Sc	50	30	35	40	20	34
Sr	300	150	120	170	135	471
V	300	200	200	280	145	266
Y	30	20	15	25	20	32
Zr	100	30	50	110	70	111

* Looked for but not detected: Ag, As, Au, B, Be, Bi, Cd, Ce, Eu, Ge, Hf, In, La, Li, Mo, Nb, Nd, Pb, Pd, Pr, Pt, Re, Sb, Sm, Sn, Ta, Te, Th, Tl, U, W, Zn.

1. Mystic Mountain dike, same as 1 in table 2. Semiquantitative analysis by J. L. Harris.
2. Whitetail Peak dike, same as 2 in table 2. Semiquantitative analysis by J. L. Harris.
3. Whitetail Peak dike; average of 10 analyses, including 2. Semiquantitative analyses by G. W. Day and W. D. Crim.
4. Quartz dolerite dikes, northern Beartooth Mountains; average of 110 analyses. Semiquantitative analyses by G. W. Day and others.
5. Quartz dolerite dikes, Cloud Peak Primitive Area, Bighorn Mountains, Wyo.; average of 20 analyses. (T. H. Kiilsgaard, written commun., 1971.)
6. Quartz-normative tholeiites, averages of variable numbers of analyses (Prinz, 1967, p. 278, table II, col. 1).

DISCUSSION

No large differences in petrography, chemistry, or texture are apparent between the cylindrically jointed Mystic Mountain and Whitetail Peak dikes and other quartz dolerite dikes of the Beartooth Mountains. Rocks from the center and periphery of cylinders in the Mystic Mountain dike are also nearly identical. The only petrographic variations observed are differences in grain size and texture related to distance from contacts, and these variations provide no clue to the origin of the cylinders, other than showing that formation of the cylinders occurred after crystallization because the cylindrical joints appear to be equally well developed in chilled borders and in more coarsely crystalline centers. Similarities in grain size, texture, and modal analyses of specimens from the center and periphery of a cylinder also indicate that cylindrical jointing occurred after crystallization.

The lack of distinctive characteristics in the cylindrically jointed dikes, other than the joints themselves, was noted by Prinz and Bentley (1964), Heimlich (1969), and Goryainov and Pesterev (1970). Hill (1965) noted that highly jointed dolerite at Mersey Bluff, Tasmania, contains abundant mesostasis (devitrified glass?), 5–15 percent, but concluded that joint formation was not controlled by this material; moreover, concentric cylindrical joints seem to be poorly developed in this rock as compared with those of the Beartooth dikes (Hill, 1965, pl. 1A, 2A, 3B; this report, fig. 2*D*). In mafic dikes from the Olenegorsk deposit (Goryainov and Pesterev, 1970), the dike material interstitial to the "ellipsoidal segregations" is finer grained and often "disintegrated and altered" relative to dike material within an ellipsoid, but this feature was not observed in the Beartooth dikes. Thus it seems clear that however the cylindrical joints were formed, their origin cannot be readily attributed to unique textural, lithologic, or chemical characteristics of the dikes; the explanation instead must be sought in the postcrystallization cooling history of the individual dikes themselves.

For a typical mafic dike, this history includes the development of tensional stresses within the dike owing to contraction, and relief of these stresses by formation of orthogonal joint sets within the dike (polygonal columnar joints plus planar joints parallel to the dike walls) and by shearing along the dike walls. Sheared walls and joint sets were observed in many dikes, and it is likely that even more of them would be recognized if all dikes were examined in detail.

In order for cylindrical joints to form, it appears that the usual subsolidus cooling history must be modified by some unusual feature or features of the geologic setting. One possible modifying influence for the Whitetail Peak dike is suggested by the north-northeasterly trend of the dike. This trend is nearly perpendicular to a conspicuous westerly to west-northwesterly trend of many joints, lineaments, and mafic dikes in the vicinity of the dike. These features together constitute a set of prismatic fractures that might provide a fairly regular pattern of channels along which heat flow from dike walls could be higher than in the intervening solid rock. Relatively rapid cooling along intersections of dike walls and fractures, aided perhaps by fluids circulating in the fractures, might then result in progagation of the fractures through the dike as the host rock took up movement owing to contraction of the dike rock. These newly formed fractures would then in turn become sites of more rapid cooling, or minimum-temperature isothermal surfaces. Within each roughly prismatic block (column) bounded by fractures, higher temperature isotherms would tend to assume elliptical or circular cross sections (see Carslaw and Jaeger, 1959, p. 174); cylindrical joints are reflections of these isotherms. The relatively rapid cooling around the periphery would cause a large volume reduction there, and radial fractures would open to compensate for the volume difference. As cooling progressed toward the core of a cylinder, the relatively slower volume reduction might result merely in closure of the radial fractures near the periphery rather than in their propagation to the center of a cylinder.

The proposed mechanism for the formation of cylindrical joints is therefore primarily dependent on the geometry of the dike with respect to fractures in the host rock. In the Beartooth Precambrian terrane, the most conspicuous fracture trends are approximately N. 45° W., N. 45° E., N. 65° W., and N. 15° W., and most mafic dikes are along these trends (Spencer, 1959; Prinz, 1965). The Whitetail Peak dike is unusual in that it cuts across the regional fracture pattern and is cylindrically jointed along its entire observable outcrop length. Limited observations by us and by Heimlich (1969) and Prinz and Bentley (1964) suggest that cylindrical jointing in other dikes is not generally as persistent as in the Whitetail Peak dike but typically tends to disappear along strike, a reflection perhaps of a change in the attitude of fractures in the host rock.

Although other modes of origin have been suggested, they do not seem to be pertinent to the Beartooth occurrences. For instance, Hester (1967, p. 1280–1282) ascribed a tectonic origin to groups of concentric curved joints associated with vein fractures in diabase at Gowganda, Ontario, but the features he discussed appear to differ appreciably, at least geometrically, from the cylindrical joints in the Beartooth dikes, and his explanation was not accepted by Jambor (1971, p. 37). Origin by what might be termed cylindroidal weathering (analogous to spheroidal weathering) along originally planar columnar joints seems unlikely for the Beartooth dikes because the cylinders as well as material interstitial to the cylinders show only slight weathering, although, as noted in the petrographic descriptions, they may be somewhat altered. Moreover, if weathering occurred along columnar joints, it also should have taken place along the equally well developed planar joints that are parallel to the dike walls, thus dividing the cylinders into ellipsoids or spheroids; in fact, weathering along planar joints has been negligible, as is shown by the many virtually continuous exposures of individual cylindrical joint surfaces several tens of metres long (fig. 6; Prinz and Bentley, 1964, pl. 2, fig. 2).

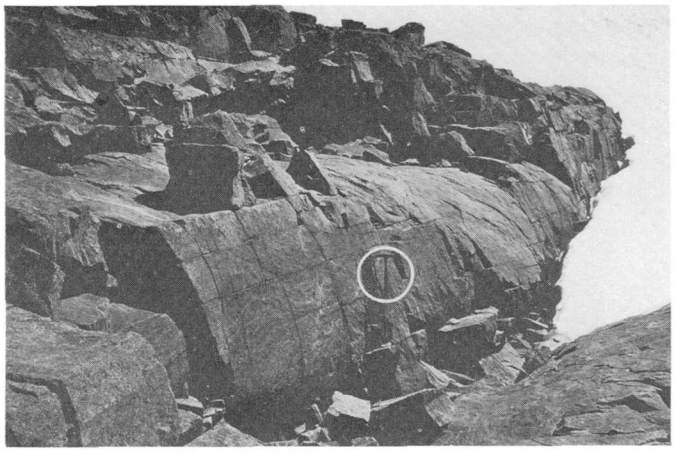

FIGURE 6.—Cylindrical joint surface on Whitetail Peak dike, 4 km (2.5 mi) south-southwest of Whitetail Peak. View to west. Note widely spaced orthogonal set of radial joints (trending from lower left to upper right) and joints normal to cylinders. Handle of hammer (circled) 33 cm (13 in.) long.

CONCLUSIONS

The model proposed for the development of cylindrical joints in quartz dolerite dikes suggests that the jointing is controlled by the geometric relation of the dikes to the fracture pattern in the host rock. Instead of a typical subsolidus cooling history during which isotherms are everywhere parallel to intrusive contacts and orthogonal fracturing of the dike and shearing along contacts take place as the dike rock contracts, the fractures in the host rock are transmitted through the dike, so prismatic cooling cells are formed. As cooling proceeds, the initially prismatic isotherms are quickly transformed into cylindrical isotherms, tensional stresses owing to cooling exceed the strength of the rock, and cylindrical joints are formed. Variation in the distance between fractures in wallrocks would cause a variation in the size and shape of the cylinders. (Compare the shape of the elongate form in the lower half of fig. 2*A* with fig. 23 of Carslaw and Jaeger, 1959, p. 174.) The change in the rate of subsolidus cooling from the periphery to the center of a cylinder suggests an explanation for the distribution of radial fractures. On the other hand, the addition of fluids along fractures might cause some local alteration, but none was observed. Finally, according to the proposed model, cylindrical joints might develop locally in other dikes at places where geometric requirements are satisfied; the fact that cylindrical joints have been recognized in only a few dikes may be due as much to vagaries of exposure and incomplete observation as to their apparent scarcity.

REFERENCES CITED

Armbrustmacher, T. J., 1972, Mafic dikes of the Clear Creek drainage area, southeastern Bighorn Mountains, Wyoming: Contr. Geology, v. 11, p. 31–40.

Carslaw, H. S., and Jaeger, J. C., 1959, Conduction of heat in solids: Oxford, Oxford Univ. Press, 510 p.

Condie, K. C., Barsky, C. K., and Mueller, P. A., 1969, Geochemistry of Precambrian diabase dikes from Wyoming: Geochim. et Cosmochim. Acta, v. 33, p. 1371–1388.

Eakins, P. R., 1961, Cylindroidal jointing in diabase at Gowganda, Ontario: Geol. Assoc. Canada Proc., v. 13, p. 85–93.

Goryainov, P. M., and Pesterev, F. V., 1970, Concentric spher-

ical cleavage in basic rock dikes of the Olenegorsk deposit [abs.]: Chem. Abs., v. 73, 6021m, p. 153.

Heimlich, R. A., 1969, Cylindrical columnar joints in Precambrian mafic dikes, Bighorn Mountains, Wyoming: Jour. Geology, v. 77, p. 371–374.

Hester, B. W., 1967, Geology of the silver deposits near Miller Lake, Gowganda: Canadian Mining and Metall. Bull., v. 60, no. 667, p. 1277–1286.

Hill, P. A., 1965, Curviplanar (radial, bow-tie, festoon) and concentric jointing in Jurassic dolerite, Mersey Bluff, Tasmania: Jour. Geology, v. 73, p. 255–270.

Jambor, J. J., 1971, The Nipissing diabase: Canadian Mineralogist, v. 11, pt. 1, p. 34–75.

Lafeber, David, 1956, Columnar differentiation in basaltic rocks: Koninkl. Nederlandsch Geol.-Mijnb. Genoot. Verh., Geol. Ser., pt. 16, p. 241–251.

Manson, Vincent, 1967, Geochemistry of basaltic rocks—Major elements, *in* Hess, H. H., and Poldervaart, Arie, eds., Basalts—The Poldervaart treatise on rocks of basaltic composition, v. 1: New York, Interscience Pubs., p. 215–270.

Manzer, G. K., Heimlich, R. A., and Ross, M. E., 1971, Mineralogic variations across Precambrian mafic dikes in the southern Bighorn Mountains, Wyoming: Compass, v. 48, p. 75–83.

Mueller, P. A., 1970, TiO_2 and K-Ar age—a covariation in the mafic rocks of the southern Beartooth Mountains of Montana and Wyoming: Earth and Planetary Sci. Letters, v. 9, p. 427–430.

——— 1971, Geochemistry and geochronology of the mafic rocks of the southern Beartooth Mountains, Montana and Wyoming: Houston, Tex., Rice Univ. Ph. D. thesis, 58 p.

Price, N. J., 1966, Fault and joint development in brittle and semi-brittle rock: Oxford, Pergamon Press, 176 p.

Prinz, Martin, 1964, Geologic evolution of the Beartooth Mountains, Montana and Wyoming—Pt. 5, Mafic dike swarms of the southern Beartooth Mountains: Geol. Soc. America Bull., v. 75, p. 1217–1248.

——— 1965, Structural relationships of mafic dikes in the Beartooth Mountains, Montana-Wyoming: Jour. Geology, v. 73, p. 165–174.

——— 1967, Geochemistry of basaltic rocks—Trace elements, *in* Hess, H. H., and Poldervaart, Arie, eds., Basalts—The Poldervaart treatise on rocks of basaltic composition, v. 1: New York, Interscience Pubs., p. 271–323.

Prinz, Martin, and Bentley, R. D., 1964, Cylindrical columnar jointing in dolerite dikes, Beartooth Mountains, Montana-Wyoming: Geol. Soc. America Bull., v. 75, p. 1165–1168.

Simons, F. S., Armbrustmacher, T. J., Van Noy, R. M., Zilka, N. T., Federspiel, F. E., and Ridenour, James, 1973, Mineral resources of the Beartooth Primitive Area and vicinity, Carbon, Park, Stillwater, and Sweet Grass Counties, Montana, and Park County, Wyoming: U.S. Geol. Survey open-file rept., 207 p.

Spencer, E. W., 1959, Geologic evolution of the Beartooth Mountains, Montana and Wyoming—Pt. 2, Fracture patterns: Geol. Soc. America Bull., v. 70, p. 467–508.

Jour. Research U.S. Geol. Survey
Vol. 3, No. 2, Mar.–Apr. 1975, p. 223–228

PRELIMINARY RESULTS OF A GRAVITY SURVEY OF THE HENRYS LAKE QUADRANGLE, IDAHO AND MONTANA

By DONALD L. PETERSON and IRVING J. WITKIND, Denver, Colo.

Abstract.—A gravity survey of the Henrys Lake quadrangle shows that a gravity low with about 10 milligals of closure coincides with the Henrys Lake basin. The low is interpreted to reflect a basin fill of 1,100 m or more of Cenozoic sediments and volcanic rock. The data indicate that on the east and probably on the west the basin is bounded by northwest- and north-trending faults, and near its waist by the east-trending Centennial fault. A model constructed across the Henrys Lake basin suggests a northwest-trending fault, located near the southeast corner of Henrys Lake and concealed beneath the basin fill. The sparse gravity data east of the Centennial Mountains are not sufficient to provide any evidence on the extension of the Centennial fault across the Henrys Lake basin.

The Henrys Lake quadrangle is about 19 km west of Yellowstone National Park and includes parts of southeastern Idaho and southwestern Montana (fig. 1). Henrys Lake, a broad shallow body of water, occupies the north end of an hourglass-shaped basin known as the Henrys Lake basin. This basin, about 26 km long and 3–8 km wide, covers an area of about 145 km^2. It is bounded on the northwest, north, and east by the Henrys Lake Mountains, and on the south by a densely forested plain. On the southwest the basin is constricted by the mass of Sawtell Peak, the very eastern tip of the eastward-trending Centennial Mountains.

Geologically, the eastern part of the Henrys Lake Mountains is an integral part of the southern end of the Madison Range. For clarity and purposes of discussion, therefore, this eastern part of the Henrys Lake Mountains is considered in this paper as the southern end of the Madison Range.

STRATIGRAPHY

The oldest rocks in the quadrangle are in the southern end of the Madison Range and in the Centennial Mountains. They consist chiefly of pre-Belt crystalline rocks which include dolomite, quartzite, gneiss, amphibolite, mica schist, and an orthogneiss—a metagranodiorite. The mica schist and dolomite are the most abundant. All these foliate crystalline rocks are intruded by minor bodies of nonfoliate diabase and gabbro.

The pre-Belt rocks are overlain in some places by extensive deposits of Mesozoic and Paleozoic rocks, and elsewhere by volcanic rocks. The pre-Tertiary sedimentary rocks recognized in the Henrys Lake quadrangle are summarized in table 1. These sedimentary rocks, mainly carbonates, total about 1,524 m in thickness, and range in age from Middle Cambrian (Flathead Sandstone) to Early Cretaceous (Thermopolis? Shale).

The volcanic rocks include mafic and felsic types. The mafic rocks, of Eocene(?) age, crop out on both sides of the southern end of the Henrys Lake basin. These rocks are dark-gray to black, dense pyroxene trachytes. The felsic volcanic rocks are widespread and are much more plentiful than the mafic rocks. They consist of three rhyolitic ash-flow tuffs, of Pleistocene age, that are remarkably alike in both mineral content and chemical composition. These rocks commonly have a fine-grained to aphanitic groundmass, but locally the large concentration of phenocrysts gives the rocks a coarse-grained appearance.

The mountains rise 450–920 m above the basin floor, which consists chiefly of unconsolidated sand and gravel. A broad sheet of one of the rhyolitic ash-flow tuffs forms a low apron around the basin's southern margin.

The eastern edge of the basin is clearly defined by a northwest-trending steep mountain front that reflects the Madison Range fault, a range-front fault which extends some 88 km to the northwest and ends near Ennis, Mont. The fault dips steeply southwestward and is normal; the basin has been depressed. The amount of stratigraphic throw is uncertain but is believed to be at least 600 m. North of the Henrys Lake basin a small scarplet 3–9 m high extends for many kilometres along the trace of the Madison Range fault, indicating that the fault is active. It probably has been active since the late Tertiary (Pardee, 1950, p. 373).

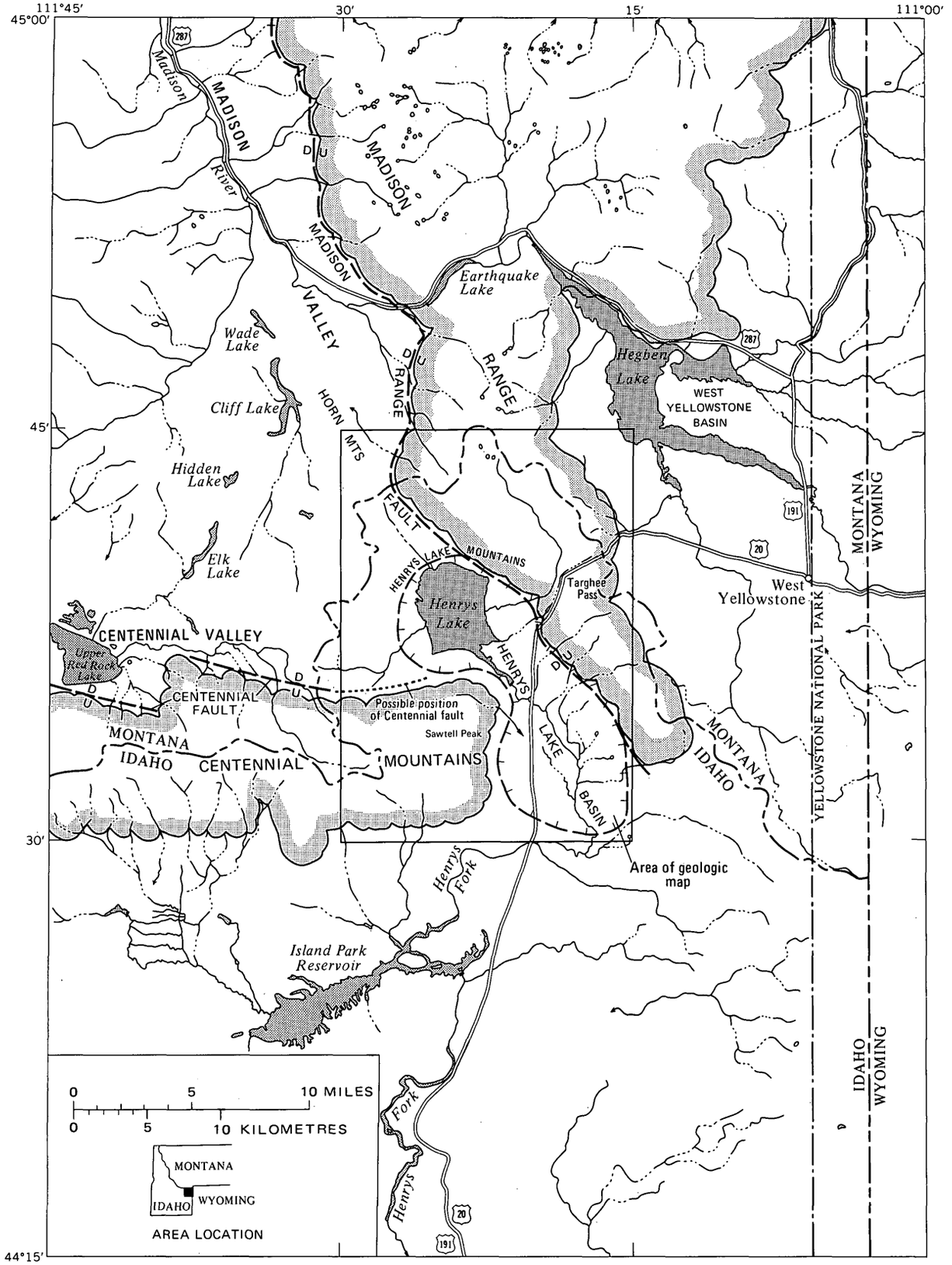

FIGURE 1.—Index map showing the topographic setting of the Henrys Lake quadrangle in southwestern Montana, southeastern Idaho, and northwestern Wyoming.

TABLE 1.—*Generalized section of pre-Tertiary sedimentary rocks exposed in Henrys Lake quadrangle, Idaho and Montana*

System	Series	Group and formation	Thickness (m)	Lithology
Cretaceous	Lower Cretaceous	Thermopolis(?) Shale. lower sandstone member	?	Sandstone, light brown, thin-bedded to massive, flaggy, fine-grained.
		Kootenai Formation	70	Chiefly claystone and siltstone, pale-red to variegated; basal unit is salt-and-pepper conglomerate.
		— Unconformity —		
Jurassic	Upper Jurassic	Morrison Formation	46	Chiefly sandstone, light-brown, thin-bedded to massive, lenticular, fine- to medium-grained.
	Middle Jurassic	Ellis Group	98	Chiefly calcareous claystone, light-gray; interbedded thin oolitic limestone. Upper unit is oolitic limestone rich in rounded chert grains.
		— Unconformity —		
Triassic	Lower Triassic	Woodside Sandstone	76	Sandstone and siltstone, reddish-brown, thin-bedded, fine-grained.
		Dinwoody Formation	92	Dolomite and calcareous siltstone, light-gray, thin- and even-bedded, platy.
		— Unconformity —		
Permian		Shedhorn Sandstone	38–125	Sandstone and cherty sandstone, grayish-brown, medium- to thick-bedded, fine-grained.
Pennsylvanian		Quadrant Sandstone	38–84	Sandstone, light-brown, thin-bedded, fine-grained.
		Amsden Formation — Upper part	5	Siltstone, shaly, reddish-brown, thin-bedded, platy.
Mississippian	Upper Mississippian	Amsden Formation — Lower part	240	Dolomite, light-gray, medium-bedded to massive; interbedded chert.
		— Unconformity —		
	Lower Mississippian	Madison Group	165–400	Limestone, bluish-gray, thin-bedded to massive; interbedded chert in lower part.
		— Unconformity —		
Devonian	Upper Devonian	Three Forks Formation	35	Siltstone, calcareous, light-brown, yellow, and pale-red, thin-bedded.
		— Unconformity —		
	Middle Devonian	Jefferson Formation	75	Dolomite, grayish-brown, thick-bedded to massive, vuggy.
		— Unconformity —		
Ordovician and Cambrian	Upper Ordovician and Upper Cambrian	Bighorn(?) Dolomite, Snowy Range(?) Formation, and Pilgrim(?) Limestone	110–160	Upper formation is dolomite, light-gray, thin- and even-bedded; middle and lower formations are chiefly limestone, light-gray, mottled, thin- and even-bedded, and contain much intraformational conglomerate and glauconite.
Cambrian	Middle Cambrian	Park Shale	52	Shale, greenish-gray, even-bedded, fissile; some oolitic limestone beds.
		Meagher Limestone	170	Limestone, light-gray, siltstone mottles, thin- and even-bedded.
		— Unconformity —		
		Flathead Sandstone	6–62	Sandstone, brown, medium- to thick-bedded, crossbedded, fine- to coarse-grained.
		— Unconformity —		
Precambrian		Pre-Belt metamorphic rocks		Foliate: Includes paragneiss types such as mica schist, quartzite, dolomite, and amphibolite, and orthogneiss metagranodiorite. Nonfoliate: Includes gabbro and diabase.

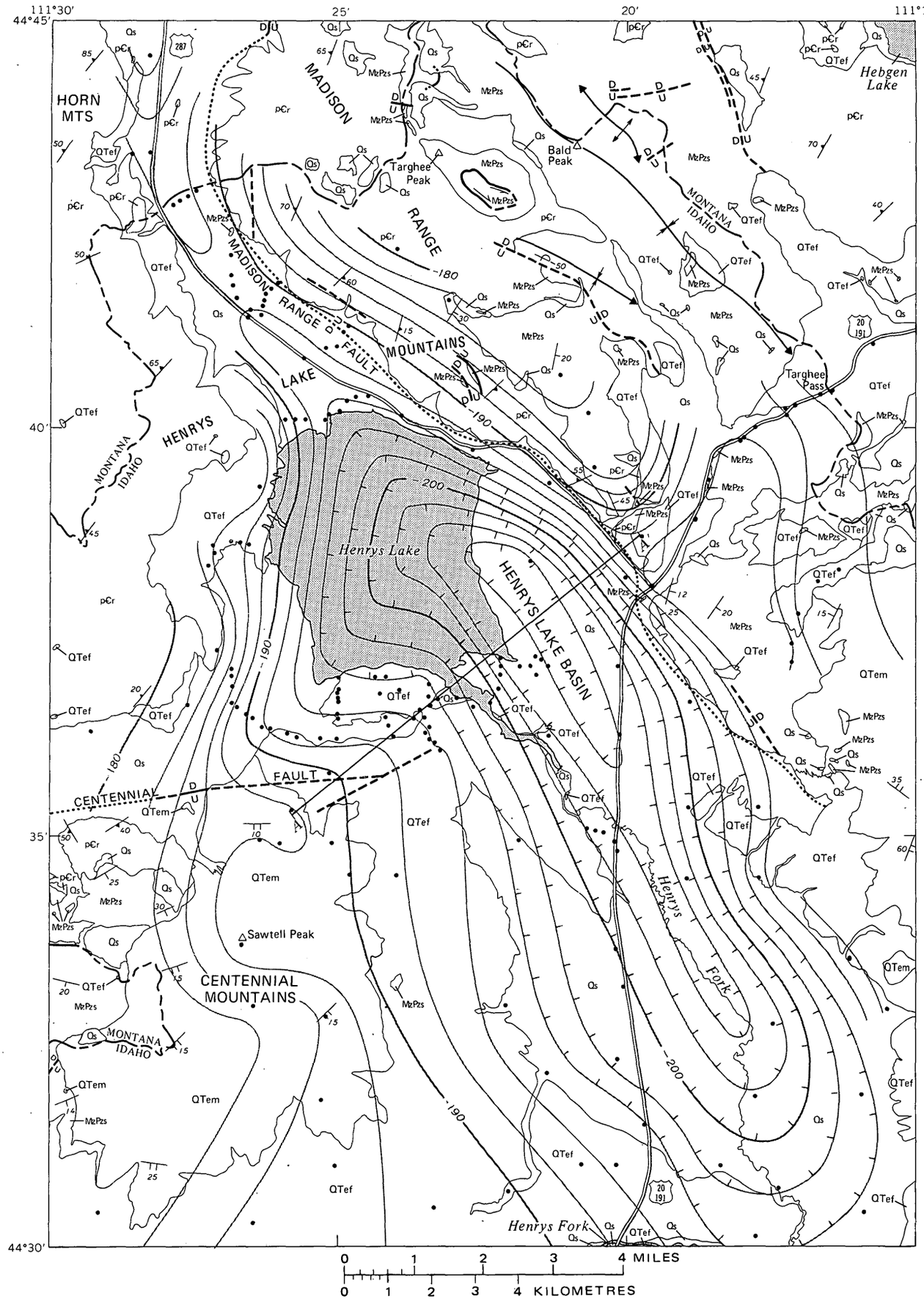
111°30'
25'
20'
111°15'
44°45'
40'
35'
44°30'
HORN MTS
MADISON RANGE
MADISON RANGE FAULT
HENRYS LAKE MOUNTAINS
Targhee Peak
Bald Peak
Hebgen Lake
Targhee Pass
Henrys Lake
HENRYS LAKE BASIN
CENTENNIAL FAULT
CENTENNIAL MOUNTAINS
Sawtell Peak
Henrys Fork
MONTANA
IDAHO
HENRYS
-180
-190
-200
0 1 2 3 4 MILES
0 1 2 3 4 KILOMETRES

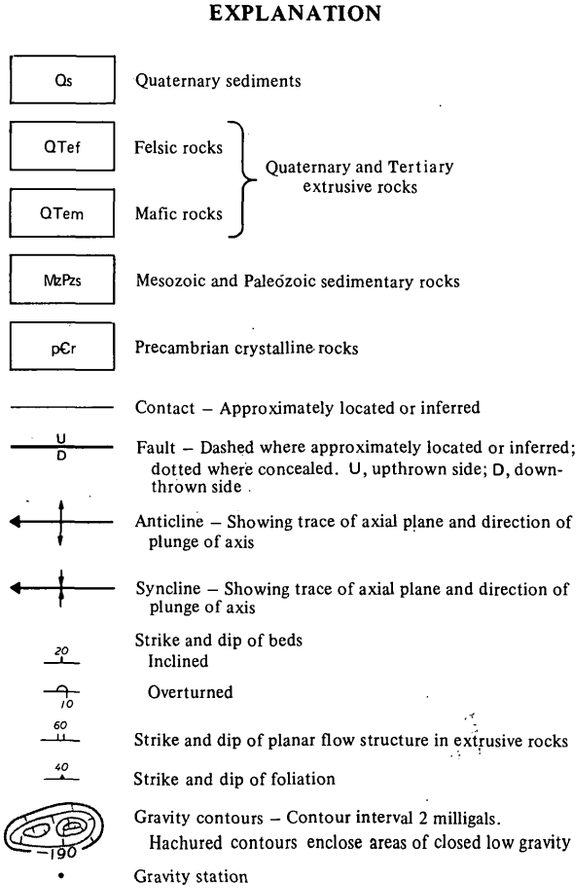

FIGURE 2.—Bouguer gravity and generalized geologic map of the Henrys Lake quadrangle, Idaho and Montana.

The steep north face of the eastward-trending Centennial Mountains is also bounded by a range-front fault, the Centennial fault; this fault, judging by small scarplets along part of its length, also has been active in recent time. It too probably dates from the late Tertiary. The Centennial fault is normal, is about 72 km long, dips steeply northward, and has a stratigraphic throw of 610–915 m (Pardee, 1950, p. 376). Centennial Valley, north of the fault, has been depressed. The Centennial fault reaches into the west end of the Henrys Lake basin; how far eastward it extends is uncertain.

In an attempt to determine how these two major faults are related structurally, geologic mapping was begun in the Henrys Lake quadrangle in 1967 and completed in 1971 (Witkind, 1972). The results are inconclusive.

In addition to the geologic mapping, a gravity survey in an area around Henrys Lake was completed in 1970. This paper is a preliminary statement presenting the results of that survey.

GRAVITY SURVEY

Fifty-seven gravity stations obtained by H. R. Blank, Jr., of the U.S. Geological Survey, and 122 stations obtained by the authors are shown on the Bouguer gravity map (fig. 2). Vertical and horizontal positions of most of the stations are from bench marks or spot elevations shown on U.S. Geological Survey quadrangle maps at scales of 1:24,000. Positions for about 80 stations were determined from planetable surveys.

Observed gravity values were referred to base station WU 29 in Salt Lake City, Utah (Behrendt and Woollard, 1961). In reducing the data to the complete Bouguer anomaly, a density of 2.67 g/cm^3 for the rock between sea level and station elevations was assumed. Terrain corrections were computed outward to a distance of 167 km for each station, by a method described by Plouff (1966). The corrections ranged from less than 1 mGal in the Henrys Lake basin to more than 20 mGal in the Madison Range and Centennial Mountains.

A northwest-trending gravity low with about 10 mGal of closure coincides with the Henrys Lake basin. At the north end of the basin, the low narrows and decreases in amplitude over a gravity saddle and increases again to the northwest. The gravity saddle is interpreted as reflecting a bedrock high of pre-Cenozoic rock. At the south end of the basin, the gravity low decreases in amplitude, implying either that the basin shallows or that volcanic rock thickens in the basin fill.

Most of the steeper gravity gradients reflect faults. The position and attitude of these faults, however, cannot be determined with any certainty from the gravity data because of lateral variations in the density of the basin fill, particularly along the margins of the basin. Also, the density of the gravity stations is not adequate to define the details of the faults.

The southwest-dipping gravity gradient alined along part of the southwestern front of the Madison Range reflects the Madison Range fault. Similarly, a north-trending gravity gradient along the west edge of Henrys Lake suggests another fault zone, but one concealed beneath a cover of unconsolidated sediments and volcanic rock. The westward bending of the gravity contours along the north side of the Centennial Mountains coincides approximately with the Centennial fault. The sparse gravity data east of the Centennial Mountains are not sufficient to provide any evidence on the extension of the Centennial fault across the Henrys Lake basin.

The variation of the Bouguer anomaly values over the ranges is produced mainly by density contrasts within or underlying the pre-Cenozoic bedrock. An abrupt change in the Bouguer anomaly values occurs in the Madison Range along U.S. Highway 20–191 near Targhee Pass. The values are about 12 mGal

higher northwest of the highway than they are to the southeast. This abrupt change coincides with exposures of Precambrian crystalline rocks that crop out in the mountains northwest of the highway but are buried beneath about 1,460 m of less dense sedimentary rocks southeast of the highway. The abrupt change in the anomaly values near the highway may be caused by a fault zone, but, if so, the gravity data are too few to substantiate this interpretation. A gravity gradient of about 6 mGal/km is located northwest of the highway and bends around and continues along the southwest edge of the Madison Range. This gradient is over Precambrian rocks and, therefore, is believed to reflect an increase in density of Precambrian rocks toward the core of the range rather than to reflect faulting.

In order to estimate the thickness of Cenozoic fill in the Henrys Lake basin, a two-dimensional model was prepared from gravity data along profile *A–A′* (fig. 3). The model assumes that the gravity low over the basin is produced by the density contrasts between three differing rock types: unconsolidated sediments, volcanic rocks, and pre-Cenozoic rocks.

Densities of the four different volcanic rocks which crop out near the basin were measured. All these volcanic rocks are probably represented in the basin fill, but it is not known in what proportions. Of the four, the three felsic rhyolitic tuffs of different flows have densities of 2.27, 2.30, and 2.37 g/cm³. The fourth, a mafic pyroxene trachyte which crops out both in the Madison Range and on Sawtell Peak in the Centennial Mountains, has a density of 2.76 g/cm³. The mean of these densities (2.4 g/cm³) was used for modeling.

The density of the unconsolidated sediments and the pre-Cenozoic rocks was not measured. A density of 2.1 g/cm³ for the sediments and 2.7 g/cm³ for the pre-Cenozoic rocks was taken from a table of rock densities prepared by Mabey and Oriel (1970) for an area about 210 km to the south.

Because of uncertainties relating to the densities chosen and their distribution and because of density variations from within or underlying the pre-Cenozoic rocks, the model is considered a gross representation of the actual thickness of basin fill across the Henrys Lake basin.

The model indicates that 1,100 m or more of Cenozoic sediments and volcanic rock fill the Henrys Lake basin. The steeply dipping slope near the right (northeast) edge of the model indicates the Madison Range fault. The steeper, northeast-dipping slope near the center of the model suggests a concealed northwest-trending fault, which probably has less vertical displacement than the Madison Range fault.

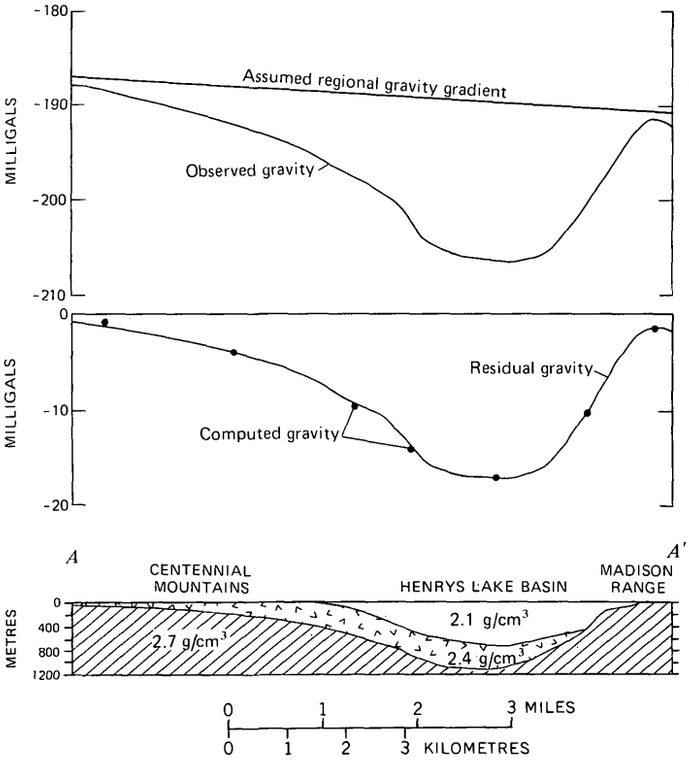

FIGURE 3.—Two-dimensional model computed along gravity profile *A–A′*. Line of profile is shown in figure 2. Solid dots indicate computed gravity.

CONCLUSIONS

Gravity data in the Henrys Lake quadrangle reveal a complex structure. The Henrys Lake basin is probably bounded by at least three major faults: a range-front fault along the southwestern edge of the Madison Range; another along the north edge of the Centennial Mountains; and a third, north-trending one, along the western edge of Henrys Lake. A northwest-trending fault is suggested beneath the Henrys Lake basin. The sparse gravity data east of the Centennial Mountains are not sufficient to provide evidence on the extension of the Centennial fault across the Henrys Lake basin.

REFERENCES CITED

Behrendt, J. C., and Woollard, G. P., 1961, An evaluation of the gravity control network in North America: Geophysics, v. 26, no. 1, p. 57–76.

Mabey, D. R., and Oriel, S. S., 1970, Gravity and magnetic anomalies in the Soda Springs region, southeastern Idaho: U.S. Geol. Survey Prof. Paper 646–E, 15 p.

Pardee, J. T., 1950, Late Cenozoic block faulting in western Montana: Geol. Soc. America Bull., v. 61, no. 4, p. 359–406.

Plouff, Donald, 1966, Digital terrain corrections based on geographic coordinates [abs.]: Soc. Explor. Geophysicists 36th Ann. Internat. Mtg., Houston, Tex., p. 109.

Witkind, I. J., 1972, Geologic map of the Henrys Lake quadrangle, Idaho and Montana: U.S. Geol. Survey Misc. Geol. Inv. Map I–781–A, scale 1:62,500.

Jour. Research U.S. Geol. Survey
Vol. 3, No. 2, Mar.–Apr. 1975, p. 229–231

COMPARISON OF FISSION-TRACK, K-Ar, AND Rb-Sr RADIOMETRIC AGE DETERMINATIONS FROM SOME GRANITE PLUTONS IN MAINE

By C. W. NAESER and D. G. BROOKINS,[1] Denver, Colo., Albuquerque, N. Mex.

Abstract.—Fission-track ages have been determined on eight apatite and four sphene concentrates separated from plutonic rocks in Maine. K-Ar and Rb-Sr ages for some of these rocks were previously published. In northeastern Maine the whole-rock Rb-Sr, biotite K-Ar, and apatite fission-track ages are concordant at 400–420 million years, whereas in south-central Maine the apatite fission-track age is 150 m.y. and the biotite K-Ar age is about 250 m.y. At intermediate positions along the traverse the whole-rock Rb-Sr, biotite K-Ar, and sphene fission-track ages agree fairly well in the range 390–325 m.y., but the apatite fission-track ages are all about 100 m.y. younger. This pattern is consistent with the hypothesis of burial metamorphism and uplift as proposed in 1970 by Zartman, Hurley, Krueger, and Giletti to explain the abundance of Permian K-Ar ages in central New England.

The granitic plutons of coastal and near-coastal Maine have been the subject of several geochronological investigations (Faul and others, 1963; Zartman and others, 1970). All these plutons are at least as old as Middle Devonian. K-Ar and Rb-Sr dates have been determined for several of these rocks. Various depths of formation for the plutons have been postulated, along with speculations about later burial and metamorphism of the terrane (see discussions in Zartman and others, 1970).

The K-Ar dates on biotite separated from these granites are progressively younger southwestward from Calais, Maine (Zartman and others, 1970). Zartman, Hurley, Krueger, and Giletti (1970, p. 3366) suggested four possible explanations for the decreased ages: "(1) contact metamorphism * * *, (2) alteration associated with major faulting, (3) regional metamorphism in late Paleozoic time, and (4) burial followed by uplift and erosion." These authors believed that each of these mechanisms may have contributed to reduced ages of some rocks in New England but that burial was probably the best explanation for the reduced ages in central Maine.

Fission tracks in apatite are affected by temperatures (Naeser and Faul, 1969) lower than those which affect argon diffusion in biotite. If burial and later uplift caused the reduced K-Ar ages, the fission-track ages of apatite should be even younger than the K-Ar ages.

No fission-track ages have heretofore been reported on minerals separated from these rocks. Therefore, we made a study of the fission-track ages of eight apatites separated from various granites of central and coastal Maine. Four sphene samples were dated by fission-track study. A total of nine plutons are represented. The sample localities are shown in figure 1, and the age data are in table 1. The K-Ar and Rb-Sr ages are in table 1. The fission-track methods used are similar to those described by Calk and Naeser (1973) and Naeser (1967).

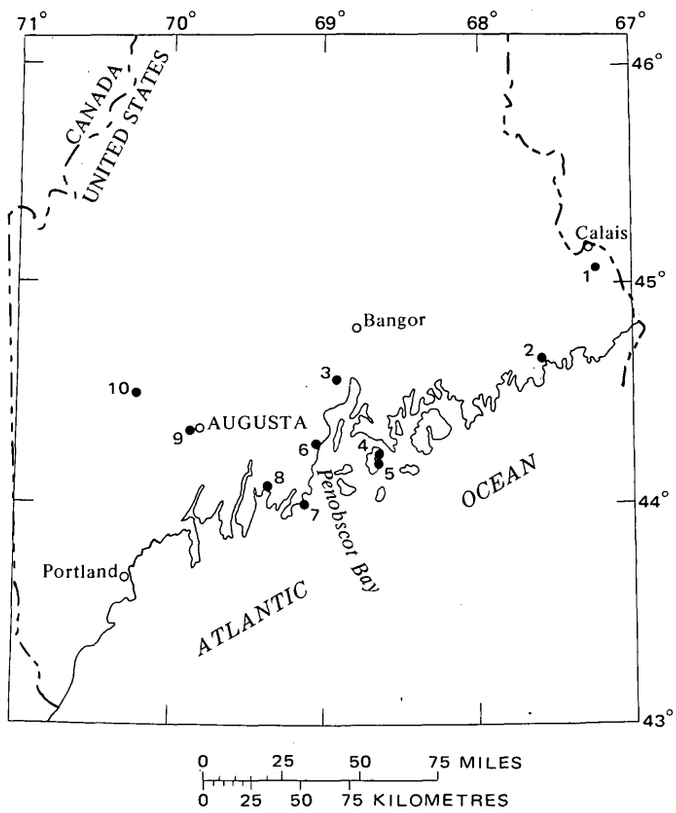

FIGURE 1.—Map of southern Maine showing sample localities.

[1] University of New Mexico.

TABLE 1.—*Sample localities, plutons represented, and comparative radiometric age determinations, in millions of years*

[Localities are listed from northeast to southwest and are shown in figure 1. References identified parenthetically are (1) Zartman and others, 1970, (2) Faul and others, 1963, D. G. Brookins, unpub. data, 1974, (4) Spooner and Fairbairn, 1970, and (5) Brookins and Spooner, 1970]

Locality	Sample	Granite pluton	Coordinates		Fission-track ages		K-Ar ages (biotite)		Rb-Sr ages (whole rock)	
			Lat. N.	Long. W.	Apatite	Sphene				
1	3079	Meddybemps	45°05′	67°14′	407±41	150±27	404	(2)	400	(4)
2	3078	Jonesboro	44°40′	67°35′	420±40	-------	-------		-------	
3	3060	Waldo	44°35′	68°55′	-------	-------	325±10	(1)	390±15	(3)
4	3085	Oak Point	44°12.9′	68°39.1′	223±22	366±18	354	(2)	357±1	(5)
5	Me153	Stonington	44°10.8′	68°39′	-------	357±24	355	(2)	341±21	(5)
6	3059	Lincolnville	44°16′	69°05′	222±22	-------	277±8	(1)	-------	
7	3058	Spruce Head Island	44°01′	69°06′	261±26	364±21	367±11	(1)	-------	
8	3057	Waldoboro	44°06′	69°22′	207±21	-------	*295±9	(1)	-------	
9	3055	Hallowell	44°18′	69°50′	219±22	-------	260±8	(1)	-------	
10	3056	North Jay	44°31′	70°14′	150±15	-------	247±8	(1)	-------	

* Determination on muscovite.

RESULTS AND DISCUSSION

The fission-track data are presented in table 2. The preliminary geological map of Maine (Hussey, 1967) shows the geological setting of the granites, and the map by Zartman, Hurley, Krueger, and Giletti (1970, fig. 1) shows the distribution of K-Ar ages in Maine and the other New England States.

TABLE 2.—*Fission-track data for samples from nine granite plutons*

[Sample localities are listed in the same sequence as in table 1. Number of tracks counted is shown parenthetically. ρ_s, spontaneous tracks per square centimetre; ρ_i, induced tracks per square centimetre (at the thermal neutron dose, ϕ, of 7.66×10^{15} for 1,439 tracks counted); and age based on decay constant λ_f of 6.85×10^{-17} yr^{-1}]

Locality	Mineral: Apatite	Mineral: Sphene	ρ_s	ρ_i	Age ($\times10^6$ yr)
1	×		5.95×10^5 (500)	6.64×10^5 (558)	407±41
	------	(1)	1.42×10^5 (264)	4.73×10^6 (399)	150±27
2	×	------	3.00×10^5 (311)	3.22×10^5 (572)	420±40
4	×	------	2.01×10^6 (461)	4.16×10^6 (953)	223±22
	------	×	1.16×10^7 (1,779)	1.44×10^7 (1,082)	366±18
5	------	×	5.86×10^6 (1,417)	2.53×10^6 (911)	357±24
6	×	------	2.39×10^6 (657)	4.98×10^6 (1,368)	222±22
7	×	------	6.55×10^5 (1,376)	11.6×10^5 (1,943)	261±26
	------	×	1.66×10^7 (1,809)	2.09×10^7 (1,145)	364±21
8	×	------	2.19×10^6 (2,044)	4.90×10^6 (1,831)	207±21
9	×	------	1.35×10^6 (1,264)	2.85×10^6 (2,666)	219±22
10	×	------	1.51×10^6 (1,408)	4.58×10^6 (1,714)	150±15

[1] Sphene date for sample 3079 from locality 1 is anomalously low.

The fission-track and K-Ar ages generally decrease southwestward. Apatite fission-track, biotite K-Ar, and whole-rock Rb-Sr ages are approximately identical for the Meddybemps granite pluton, the easternmost site. The sphene fission-track age for the Meddybemps pluton seems anomalously low, possibly owing to a high Th content. Southwestward, apatite fission-track ages are less than the sphene fission-track ages which are equal to biotite K-Ar ages. Near long 69° W. and farther west, biotite K-Ar ages decrease and the apatite fission-track ages are lower still. The decrease in mineral K-Ar ages in southwest Maine was already attributed to deep burial and subsequent uplift and erosion (Zartman and others, 1970). Our data now permit limited speculation on the rate of cooling associated with that uplift.

Annealing studies (Naeser and Faul, 1969) showed that a temperature of about 350°C removes tracks in sphene if the sphene is held at that temperature for longer than 10^6 yr, whereas a temperature of 150°C for 10^6 yr is sufficient to completely anneal apatite tracks. The fission-track ages therefore record the last time the sphene cooled below 300°–350°C and the apatite records the cooling of the rock below 100°–150°C. On the average there is about a 100-m.y. difference between the apatite and sphene fission-track ages in central and coastal Maine. The 100-m.y. difference between the apatite ages and the biotite and sphene ages represents a difference of about 200°–250°C. This suggests a cooling rate on the order of 2.5°C/m.y. for the plutonic rocks of central and coastal Maine. Further, if we assume that cooling resulted from uplift and the geothermal gradient was similar to the present value of about 20°C/km (Roy and others, 1968), in the 100 m.y. between the Permian and Jurassic these rocks moved up about 12.5 km at a rate of 0.125 km/m.y. During the Jurassic these rocks were about 5 km below the present surface. Five km of uplift thereafter during the last 150 m.y. gives an average uplift rate of 33 m/m.y.

If, alternatively, the geothermal gradient was much higher during the Paleozoic (perhaps 40°–50°C/km), the rock cover need only have been 5–6 km thick.

The concordant ages determined on the Meddybemps

pluton suggest that this granite was emplaced at a very shallow depth in the crust, on the order of 3 km or less. Only shallow emplacement would permit the rapid cooling necessary for the apatite fission-track age to be concordant. The plutons represented by sampling west of Penobscot Bay were either emplaced deeper in the crust or emplaced in a region where the thermal gradient was greater.

CONCLUSIONS

Our data, though limited, permit us the following conclusions:

1. The fission-track data support the statement by Zartman, Hurley, Krueger and Giletti (1970) that burial and uplift is a reasonable explanation for the lowered K-Ar ages in central Maine.
2. The plutonic rocks of northeastern Maine were emplaced at a shallow depth in the crust and (or) a region of lower thermal gradient.
3. The plutonic rocks in the region of Penobscot Bay and to the west were emplaced at a deeper level in the crust, where the thermal gradient was possibly greater than at present.

REFERENCES CITED

Brookins, D. G., and Spooner, C. M., 1970, The isotopic ages of the Oak Point and Stonington granites, eastern Penobscot Bay, Maine: Jour. Geology, v. 78, p. 570–576.

Calk, L. C., and Naeser, C. W., 1973, The thermal effect of a basalt intrusion on fission tracks in quartz monzonite: Jour. Geology, v. 81, p. 189–198.

Faul, H., Stern, T. W., Thomas, H. H., and Elmore, P. L. D., 1963, Ages of intrusion and metamorphism in the northern Appalachians: Am. Jour. Sci., v. 261, p. 1–19.

Hussey, A. M., ed., 1967, Preliminary State geological map of Maine: Augusta, Maine Geol. Survey, scale 1:500,000.

Naeser, C. W., 1967, The use of apatite and sphene for fission track age determinations: Geol. Soc. American Bull., v. 78, p. 1523–1526.

Naeser, C. W., and Faul, H., 1969, Fission track annealing in apatite and sphene: Jour. Geophys. Research, v. 74, p. 705–710.

Roy, R. F., Decker, E. R., Blackwell, D. D., and Birch, Francis, 1968, Heat flow in the United States: Jour. Geophys. Research, v. 73, p. 5207–5221.

Spooner, C. M., and Fairbairn, H. W., 1970, Relation of radiometric age of granitic rocks near Calais, Maine, to the time of Acadian Orogeny: Geol. Soc. America Bull., v. 81, p. 3663–3670.

Zartman, R. E., Hurley, P. M., Krueger, H. W., and Giletti, B. J., 1970, A Permian disturbance of K-Ar radiometric ages in New England—its occurrence and cause: Geol. Soc. America Bull., v. 81, p. 3359–3374.

Jour. Research U.S. Geol. Survey
Vol. 3, No. 2, Mar.–Apr. 1975, p. 233–236

K-Ar AGES OF PLUTONIC ROCKS IN THE LASSITER COAST AREA, ANTARCTICA

By HARALD H. MEHNERT, PETER D. ROWLEY, and DWIGHT L. SCHMIDT,
Denver, Colo.

Abstract.—Numerous middle Cretaceous stocks and small batholiths intruded Middle and Upper Jurassic sedimentary and volcanic rocks in the Lassiter Coast area of the southern Antarctic Peninsula. To establish the age of the quartz diorite and granodiorite plutonic events, five plutons were dated by the K-Ar method. The results indicate a timespan of about 20 m.y. for the emplacement of the plutons and a minimum age of 120 m.y. for the deformation of the sedimentary (Latady Formation) and volcanic rocks. Three of the more silicic plutons have concordant biotite and hornblende ages of 100 and 106 m.y.; two discordant ages of about 118 m.y. were obtained on the more mafic plutons. Petrographically, chemically, and geochronologically, the plutons of the southern to central Lassiter Coast are similar to the calc-alkaline suite of igneous rocks of the Andes of Patagonia, the Antarctic Peninsula, and eastern Ellsworth Land.

During the austral summer of 1969–70, a U.S. Geological Survey field party explored the mountain ranges of the southern to central Lassiter Coast, located along the Weddell Sea near the base of the Antarctic Peninsula, and mapped the Latady and Scaife Mountains and the RARE (acronym for Ronne Antarctic Research Expedition) Range on a reconnaissance basis. Five samples of the plutons in the region were collected for isotopic dating to support the geologic findings which have been described by Williams, Schmidt, Plummer, and Brown (1972). A general summary of the geology including the location of the dated plutonic rocks is illustrated in figure 1.

The region is underlain by Middle and Upper Jurassic (R. W. Imlay, written commun., 1970; E. G. Kauffman, written commun., 1974) sedimentary (Latady Formation) and volcanic rocks that were tightly folded along gently plunging north-northeast axes and later intruded by plutons of middle Cretaceous age that are analyzed in this study. Crosscutting relationships show that the granodiorite plutons were emplaced after the quartz diorites. Copper and molybdenum are associated with some of the plutons (Rowley and others, 1974). Mapping north of the RARE Range during subsequent U.S. Geological Survey expeditions demonstrated that the geology there is similar to that of the central and southern Lassiter Coast, although plutons increase in size and number toward the north (Williams and Rowley, 1971; Rowley, 1973). The Lassiter Coast area is geologically, petrographically, and geochronologically similar to eastern Ellsworth Land (Laudon, 1972; Laudon and others, 1969), which is less than 200 km west-southwest of the area of figure 1, and shares the same suite of igneous rocks with the rest of the Antarctic Peninsula (Adie, 1972) and with the Andes of Patagonia (Halpern, 1968).

Acknowledgments.—This work is part of a U.S. Geological Survey geologic study of the Lassiter Coast area done under the auspices of and financed by the NSF (National Science Foundation), grant AG–187. The U.S. Antarctic Research Program of NSF and the U.S. Navy Operation Deep Freeze provided logistic support in Antarctica. We are indebted to the other geologists of the 1969–70 field party, to P. L. Williams, party leader, L. E. Brown, and C. C. Plummer. For the critical review of the manuscript we are thankful to P. L. Williams and J. D. Obradovich.

AGE DETERMINATIONS AND PETROGRAPHY

Analytical K-Ar data for five dated samples, considered to be representative of other plutons in the Lassiter Coast, are summarized in table 1. Samples

TABLE 1.—*Analytical data for K-Ar ages for plutons in the Lassiter Coast*

[Decay constants for ^{40}K: $\lambda_\beta = 4.72 \times 10^{-10} yr^{-1}$, $\lambda_\epsilon = 0.584 \times 10^{-10} yr^{-1}$; atomic abundance: $^{40}K/K = 1.19 \times 10^{-4}$; $^{40}Ar^*$ = radiogenic argon]

Name of pluton	Sample	Mineral analyzed	K_2O (percent)	$^{40}Ar^* \times 10^{-10}$ (mol/g)	$^{40}Ar^*$ (percent)	Age $\pm 2\sigma$ (m.y.)
North RARE	S54a	Biotite	7.356	12.69	96.0	113.4 ± 2.3
		Hornblende	.857	1.558	91.3	119.4 ± 2.5
Crowell	W56	Biotite	7.102	10.76	92.6	100.0 ± 2.1
		Hornblende	.782	1.179	85.0	98.7 ± 2.1
North Latady	S10a	Biotite	7.494	12.36	91.0	108.6 ± 2.3
		Hornblende	1.172	2.087	90.3	117.0 ± 2.4
McLaughlin	S16x	Biotite	8.560	13.76	94.9	105.9 ± 2.2
		Hornblende	.943	1.535	87.8	107.1 ± 2.3
Terwilleger	S47e	Biotite	8.322	12.54	94.7	99.4 ± 2.1
		Hornblende	.789	1.219	86.9	102.8 ± 2.2

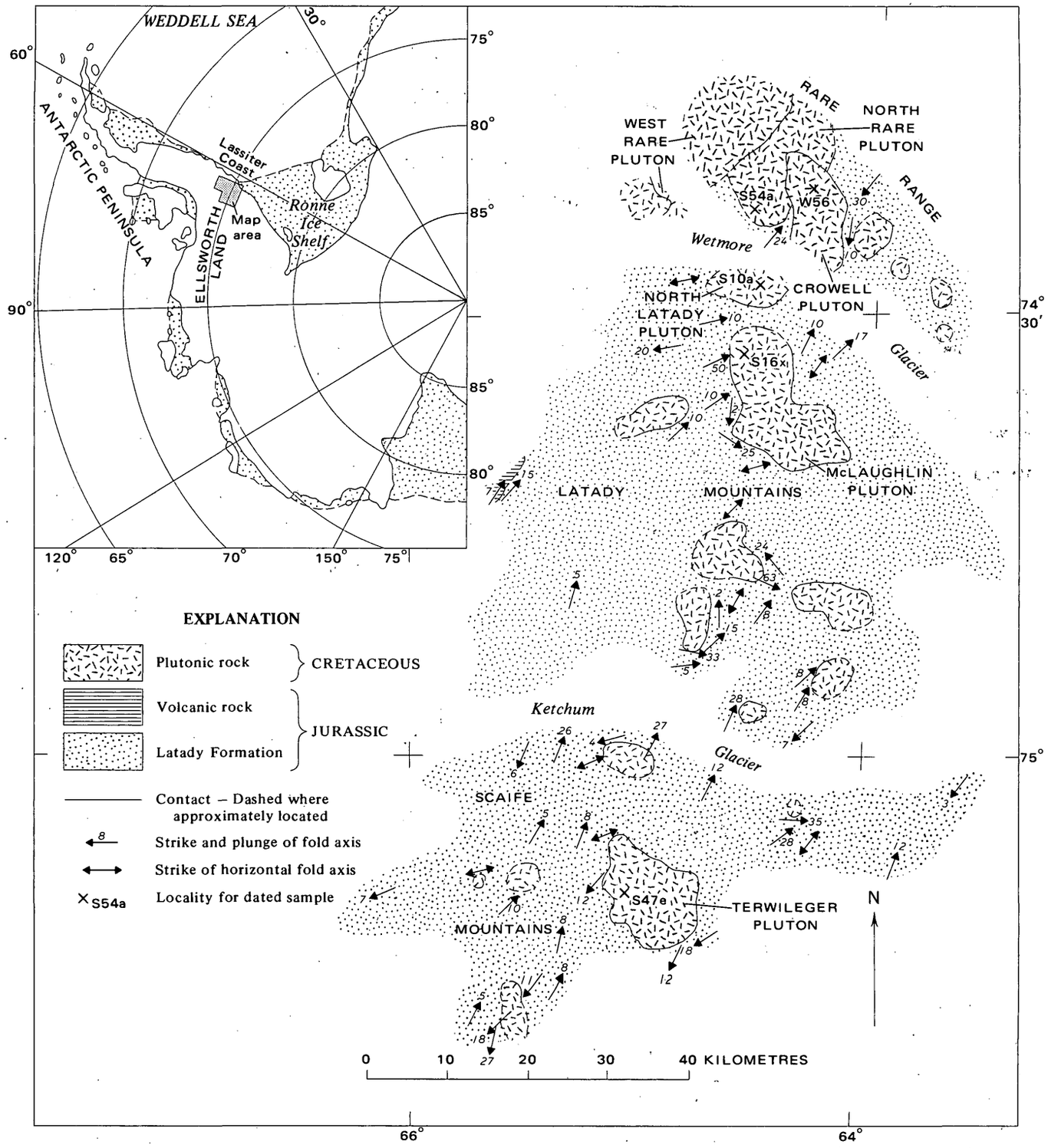

FIGURE 1.—Geologic sketch map of the RARE Range, Latady Mountains, and Scaife Mountains, southern and central Lassiter Coast, showing localities for samples analyzed in this study. From Williams, Schmidt, Plummer, and Brown (1972, fig. 2).

TABLE 2.—*Modal data and collection localities of dated specimens*

[Five hundred points counted on thin sections and stained rock slabs. Locations from 1:500,000 scale U.S. Geol. Survey Antarctic sketch map of Ellsworth Land (east part)–Palmer Land (south part)]

Mineral	Modes (volume percent)				
	[1]S10a	[2]S16x	[3]S47e	[4]S54a	[5]W56
Plagioclase	58.6	42.5	41.2	49.8	41.4
Quartz	8.5	21.6	28.2	20.0	22.1
K-feldspar	8.3	18.3	19.2	15.2	26.9
Biotite	2.0	8.6	6.2	2.4	5.6
Hornblende	20.0	7.2	3.2	11.2	2.6
Chlorite	.4	Trace	1.0	Trace	.2
Opaque minerals	.8	.8	.4	1.0	.4
Sphene	1.0	1.0	.6	.2	.8
Apatite	Trace	Trace	Trace	Trace	Trace
Epidote	.4	Trace	Trace	.2	Trace

[1] Mafic granodiorite of North Latady pluton. Fine- to medium-grained rock with a noticeable flow foliation; texture is hypidiomorphic-granular, except for scattered, somewhat larger (as much as 5 mm) light-gray poikilitic K-feldspar crystals that lack grid twinning. Plagioclase is commonly zoned, with rims that average An 29 and cores that average An 57. Specimen locality: 74°28′ S. 64°28′ W., northern Latady Mountains; about 12.7 km S. 54° E. of Mount Aaron.

[2] Granodiorite of McLaughlin pluton. Medium-grained rock; texture is hypidiomorphic-granular, except for scattered large (as much as 1 cm) light-gray poikilitic K-feldspar crystals that lack grid twinning. Plagioclase is commonly zoned with rims that average An 26 and cores that average An 42. Specimen locality. 73°33′ S. 64°33′ W., northern Latady Mountains; about 7.6 km N 61° W. of McLaughlin Peak.

[3] Silicic granodiorite of Terwileger pluton. Medium-grained rock; texture is hypidiomorphic-granular, except for widely scattered, larger poikilitic K-feldspar crystals that lack grid twinning. Plagioclase is commonly zoned with rims that average An 23 and cores that average An 35. Specimen locality: 75°09′ S., 65°02′ W., Scaife Mountains; about 10.8 km N. 54° W. of Mount Terwileger.

[4] Mafic granodiorite of North RARE pluton. Medium-grained rock; texture is hypidiomorphic-granular, except for scattered large (as much as about 1 cm) light-gray poikilitic K-feldspar crystals that lack grid twinning. Plagioclase is commonly zoned, with rims that average An 31 and cores that average An 45. Specimen locality: 74°22′ S. 64°28′ W., northern RARE Range; about 10.6 km S. 75° W. of Mount Crowell; specimen is about 3 km from the contact of the younger Crowell pluton, which thermal event conceivably could have reset the age.

[5] Quartz mónzonite of Crowell pluton. Medium- to coarse-grained rock; texture is hypidiomorphic-granular, except for scattered large (as much as 1 cm) light-gray poikilitic K-feldspar crystals that lack grid twinning. Plagioclase is commonly zoned, with rims that average An 21 and cores that average An 39. Specimen locality: 74°21′ S., 64°16′ W., central RARE Range; about 4.8 km S. 69° W. of Mount Crowell.

range in age from 99 to 119 m.y. and thus determine the minimum age for the deformation of the Latady Formation and provide an age for the copper and molybdenum mineralization that accompanied some of the intrusions. Petrographic data on the analyzed samples are given in table 2. Volume ratios of normative and modal quartz and feldspars are shown on a triangular diagram (fig. 2), based on data from the samples in table 2 and from other samples from the five plutons for which both modes and chemical analyses exist (Rowley, unpub. data, 1974). This diagram illustrates that petrographically and chemically the plutons occupy discrete to overlapping compositional fields but overall are of the same calc-alkaline plutonic suite described by Adie (1955, 1964), Halpern (1968), and Laudon (1972).

The northernmost dated intrusion is the North RARE pluton (S54a) for which ages of 119.4 m.y. on hornblende and 113.4 m.y. on biotite were obtained (table 1). These data suggest a slight resetting of the biotite during later intrusive events. This pluton is

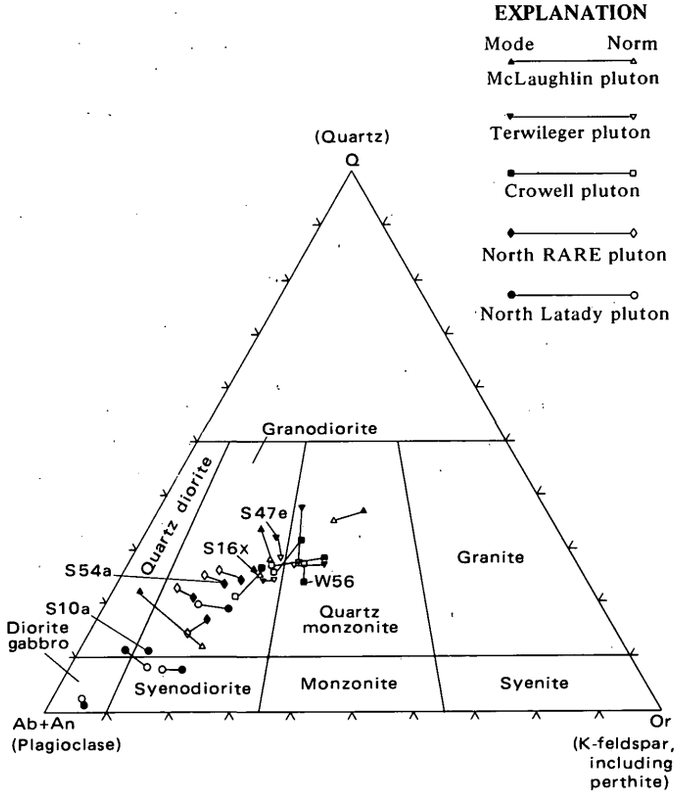

FIGURE 2.—Comparison of modal and normative quartz-orthoclase-plagioclase (Ab+An) ratios for selected rocks of the five dated plutons Lassiter Coast, Antarctica. Dated specimens are numbered. Modal plutonic rock classification is shown in diagram.

homogeneous in composition and texture and consists of a fine- to medium-grained granodiorite. Although contact relations are obscured, a less mafic composition and a K-Ar biotite age determination of 104.8 m.y. by Rowley, Williams, Schmidt, and others (1975) on the adjacent West RARE batholith suggest that the North RARE pluton is intruded by the West RARE batholith. The Crowell pluton (W56), which also intrudes the North RARE pluton, yielded ages of 98.7 and 100.0 m.y. for hornblende and biotite, respectively (table 1). It is a compositionally and texturally homogeneous, coarse-grained silicic stock with a general composition of quartz monzonite, but has a narrow contact zone of granodiorite.

Farther south, discordant hornblende and biotite ages of 117.0 and 108.6 m.y. were obtained on the North Latady pluton (table 1, S10a). Again, the biotite age seems to be reset by younger intrusions. This irregularly zoned stock has a general composition near the quartz diorite–granodiorite boundary, but ranges in composition from quartz monzonite to pyroxene–hornblende gabbro. The rock contains abun-

dant hornblende; it is medium grained and exhibits flow foliation. The hornblende and biotite ages on the McLaughlin pluton are 107.1 and 105.9 m.y. respectively (table 1, S16x) and are geochronologically correlated with the age of the West RARE pluton. This small, irregularly zoned batholith has a compositional range from quartz monzonite to quartz diorite and typical composition along the granodiorite–quartz monzonite boundary; the rocks in the contact zone tend to be more mafic. The rocks are medium to coarse grained, except in the contact zone, where they are fine to medium grained.

The Terwileger pluton, the southernmost dated pluton, yielded ages of 102.8 m.y. on the hornblende and 99.4 m.y. on the biotite (table 1, S47e). It is a large stock that appears to be concentrically zoned by composition, with a somewhat more felsic interior. The central part is quartz monzonite and the borders, which are mostly granodiorite, may be as mafic as quartz diorite in some places; average composition is granodiorite, near the quartz monzonite boundary. Most rock is medium to coarse grained, but contact phases are fine to medium grained.

CONCLUSIONS

These data indicate that the Jurassic sedimentary and volcanic rocks of the Lassiter Coast area were deformed between Late Jurassic and middle Cretaceous time. After their deformation, quartz diorite plutons were emplaced at about 119 m.y., followed by the intrusion of granodiorite and quartz monzonite plutons between 99 and 107 m.y. The data agree well with Rb-Sr ages on plutonic and hypabyssal rocks from eastern Ellsworth Land, which have been found to range from 102 to 109 m.y. (Halpern, 1967). The Lassiter Coast dates of 99 to 119 m.y. also fall within the range of widespread middle Cretaceous plutonism in the Andean province of the Antarctic Peninsula and Patagonia (Adie, 1972; Halpern, 1971; Krylov, 1972).

REFERENCES CITED

Adie, R. J., 1955, The petrology of Graham Land—II. The Andean granite-gabbro intrusive suite: Falkland Islands Dependencies Survey (British Antarctic Survey), Sci. Rept. 12, 39 p.

——— 1964, The geochemistry of Graham Land, *in* Adie, R. J., ed., Antarctic geology: Internat. Symposium on Antarctic geology, 1st, Capetown 1963, Proc. (North-Holland Pub Co., Amsterdam), p. 541–547.

——— 1972, Recent advances in the geology of the Antarctic Peninsula, *in* Adie, R. J., ed., Antarctic geology and geophysics: Internat. Union Geol. Sci. Symposium on Antarctic geology and solid earth geophysics, Oslo 1970, Ser. B, no. 1 (Universitetsforlaget, Oslo), p. 121–124.

Halpern, Martin, 1967, Rubidium-strontium isotopic age measurements of plutonic igneous rocks in eastern Ellsworth Land and northern Antarctic Peninsula, Antarctica: Jour. Geophys. Research, v. 72, no. 20, p. 5133–5142.

——— 1968, Ages of Antarctic and Argentine rocks bearing on continental drift: Earth and Planetary Sci. Letters, v. 5, p. 159–167.

——— 1971, Evidence for Gondwanaland from a review of west Antarctic radiometric ages, *in* Quam., L. O., ed., Research in the Antarctic: Am. Assoc. Adv. Sci. Pub. 93, p. 717–730.

Krylov, A. Ya, 1972, Antarctic geochronology, *in* Adie, R. J., ed., Antarctic geology and geophysics: Internat. Union Geol. Sci. Symposium on Antarctic geology and solid earth geophysics, Oslo 1970, Ser. B, no. 1, (Universitetsforlaget, Oslo), p. 491–494.

Laudon, T. S., 1972, Stratigraphy of eastern Ellsworth Land, *in* Adie, R. J., ed., Antarctic geology and geophysics: Internat. Union Geol. Sci. Symposium on Antarctic geology and solid earth geophysics, Oslo 1970, Ser. B, no. 1 (Universitetsforlaget, Oslo), p. 215–223.

Laudon, T. S., Lackey, L. L., Quilty, P. G., and Otway, P. M., 1969, Geology of eastern Ellsworth Land, *in* Craddock, Campbell, and others, Geologic maps of Antarctica, Folio 12: Am. Geog. Sci., pl. 3.

Rowley, P. D., 1973, Geologic observations on the northern Lassiter Coast and southern Black Coast: Antarctic Jour. U.S., v. 8, no. 4, p. 154–155.

Rowley, P. D., Williams, P. L., Schmidt, D. L., Reynolds, R. L., Ford, A. B., Clark, A. H., Farrar, E., and McBride, S. L., 1975, Copper mineralization along the Lassiter Coast of the Antarctic Peninsula: Econ. Geology. (In press.)

Williams, P. L., and Rowley, P. D., 1971, Geologic studies of the Lassiter Coast: Antarctic Jour. U.S., v. 6, no. 4, p. 120.

Williams, P. L., Schmidt, D. L., Plummer, C. C., and Brown, L. E., 1972, Geology of the Lassiter Coast area, Antarctic Peninsula—preliminary report, *in* Adie, R. J., ed., Antarctic geology and geophysics: Internat. Union Geol. Sci. Symposium on Antarctic geology and solid earth geophysics, Oslo 1970, Ser. B, no. 1, (Universitetsforlaget, Oslo) p. 143–148.

Jour. Research U.S. Geol. Survey
Vol. 3, No. 2, Mar.–Apr. 1975, p. 237–251

FLOWS OF IMPACT MELT AT LUNAR CRATERS

By K. A. HOWARD and H. G. WILSHIRE, Menlo Park, Calif.

Abstract.—Lavalike materials that were emplaced in a fluid state occur in and around lunar impact craters whose diameters range from 3 km to more than 200 km and whose ages span a time interval of at least 3.5 b.y. Evidence of fluid emplacement includes flow lobes and leveed channels, a veneer mantling rough crater topography, level-surfaced pools, and complex contraction fissuring. The distribution of the lavalike deposits conforms to asymmetries of other ejecta from the same craters, and the material is concentrated downrange to distances as great as a crater radius. The character and distribution of the lavalike materials support the idea that they formed by impact melting rather than by volcanism. Returned samples indicate that materials with appropriate physical characteristics are generated by partial melting of feldspathic rocks by impact. The geologic evidence at lunar craters suggests that there is more melt rock in and near the craters than is predicted by experiment and theory.

Evidence of fluid materials that ponded or flowed downhill is found in photographs of the textures and structures of material on floors, walls, and rims of many large lunar craters. The flow features are seen most clearly at the young craters Tycho, Aristarchus, and King where they have attracted considerable attention (Shoemaker and others, 1968; Gault, Adams, and others, 1968; Crittenden, 1968; Lowman, 1969; Strom and Fielder, 1968, 1970, 1971; Moore, 1968, 1971; Cruikshank and Wood, 1972; Howard, 1971, 1972; Strom and Whitaker, 1971; El-Baz, 1971, 1972; Young and others, 1972; Guest, 1973). Commonly these lavalike materials have been ascribed to volcanic eruptions, but Shoemaker and others (1968) and Guest (1973) offered reasons to support the idea that some of these materials at Tycho and Aristarchus are partly molten impact debris. This report shows that similar materials can be recognized in consistent patterns at probable impact craters with an age range of more than three and a half billion years and that these patterns strongly support the impact-melt interpretation.

Acknowledgments.—This work was done in cooperation with the National Aeronautics and Space Administration under contracts W13,130 and T–4738a. We thank N. J. Trask, E. C. T. Chao, and D. E. Gault for reviewing the manuscript.

MORPHOLOGY OF FLOW DEPOSITS

Distinctive morphologic features of the lavalike deposits include (1) superposition as a veneer over irregular surfaces, (2) flow lobes and channels, (3) complexly fractured pools on crater floors, and (4) smaller ponds on crater walls and rims. Craters at which these features are well developed, including Copernicus, Tycho, and King, are among those for

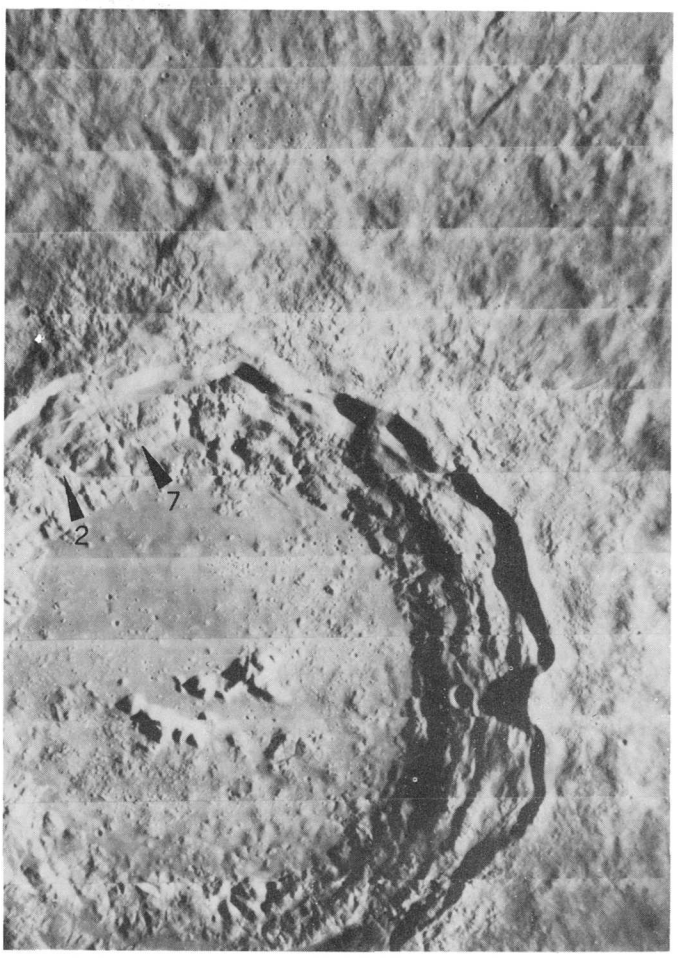

FIGURE 1.—The crater Copernicus, 95 km wide and 3 km deep, typifies many lunar craters of presumed impact origin. Lavalike materials flood the floor and veneer much of the terraced walls and the adjacent rim. Pointers show locations of figures 2 and 7. (Lunar Orbiter IV photograph 121H.)

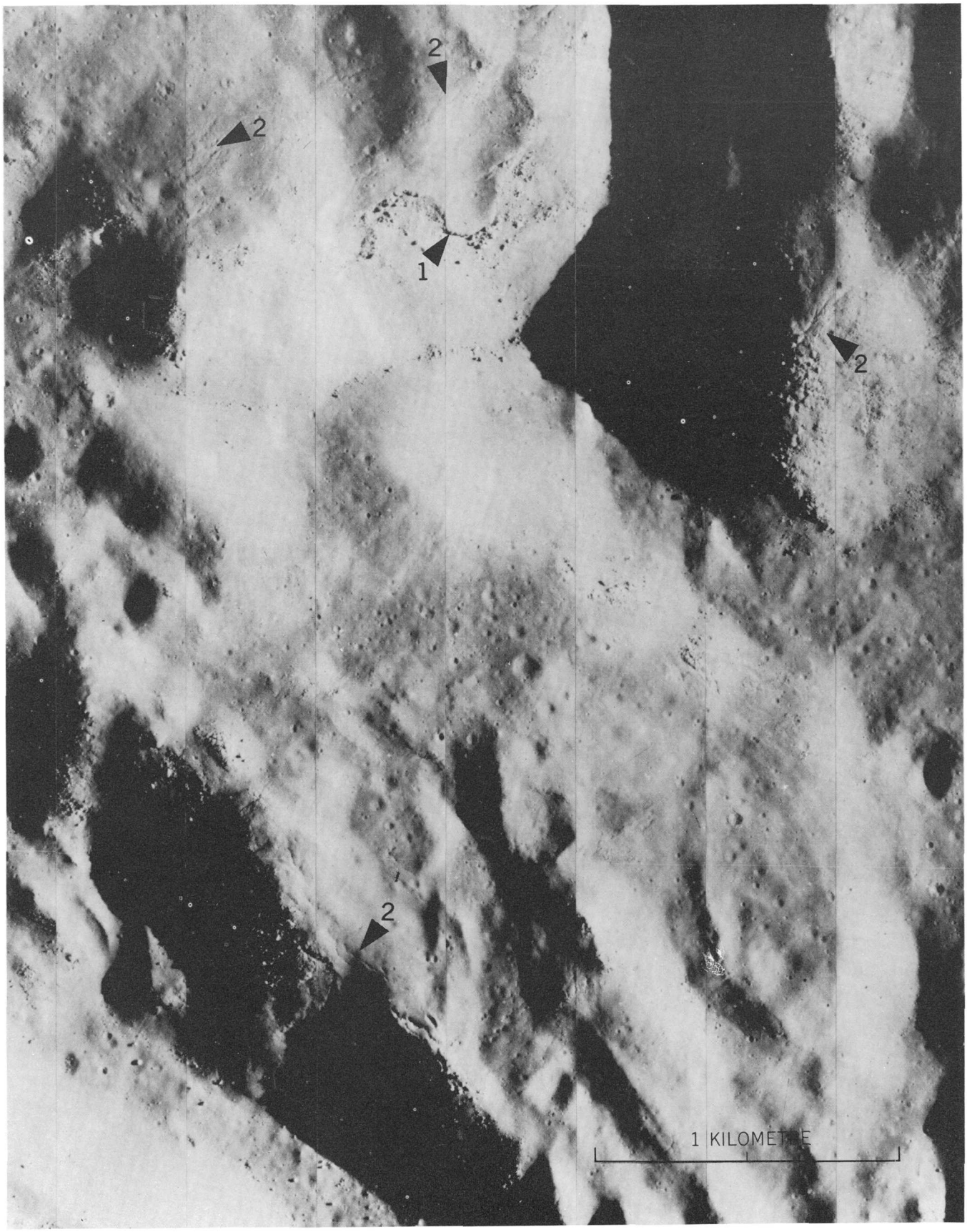

FIGURE 2.—Veneer of hard rock on the walls of Copernicus. Sunlight is from the east (right). Numbers show (1) edge of veneer, and (2) cracks in veneer. (Lunar Orbiter V photograph 155H.)

which morphologic evidence of impact origin is clearest (Gilbert, 1893; Baldwin, 1949; Shoemaker, 1962; Wilhelms and McCauley, 1971; Pike, 1972). Copernicus (fig. 1), a rayed crater 95 km across, is the classic example (Shoemaker, 1962; Schmitt and others, 1967; Howard, 1974). Copernicus is surrounded by hummocky ejecta with radial and locally concentric lineations ascribed to radial outward flow from the crater. Clusters of secondary craters lie beyond the continuous ejecta. The crater walls are series of slump terraces that descend to the floor; a cluster of peaks occupies the center of the crater floor. The lavalike materials are superposed on this basic physiography.

Veneer.—A veneer of the lavalike material remains draped over the crater wall terraces of Copernicus and the inner part of the crater rims of Copernicus, Tycho, King, and Mösting C. Blocky outcrop ledges (fig. 2) and blocky ejecta from superposed craterlets indicate that the veneer solidified to hard rock. Cracks occur where the veneer is draped over hills (fig. 2). Many of the cracks are at topographic inflections and evidently resulted from stretching by downhill creep of the material while it was still plastic. Locally the veneer is exposed as a thin outcrop ledge at the very top of the main crater wall or on other steep, mass-wasted scarps on the wall. The cracked veneer on the main crater rim of Copernicus contrasts with blocky areas where no cracks occur; similar features appear at Tycho crater (fig. 3). The blocky areas suggest unmelted residues left behind when more fluid parts drained away. A

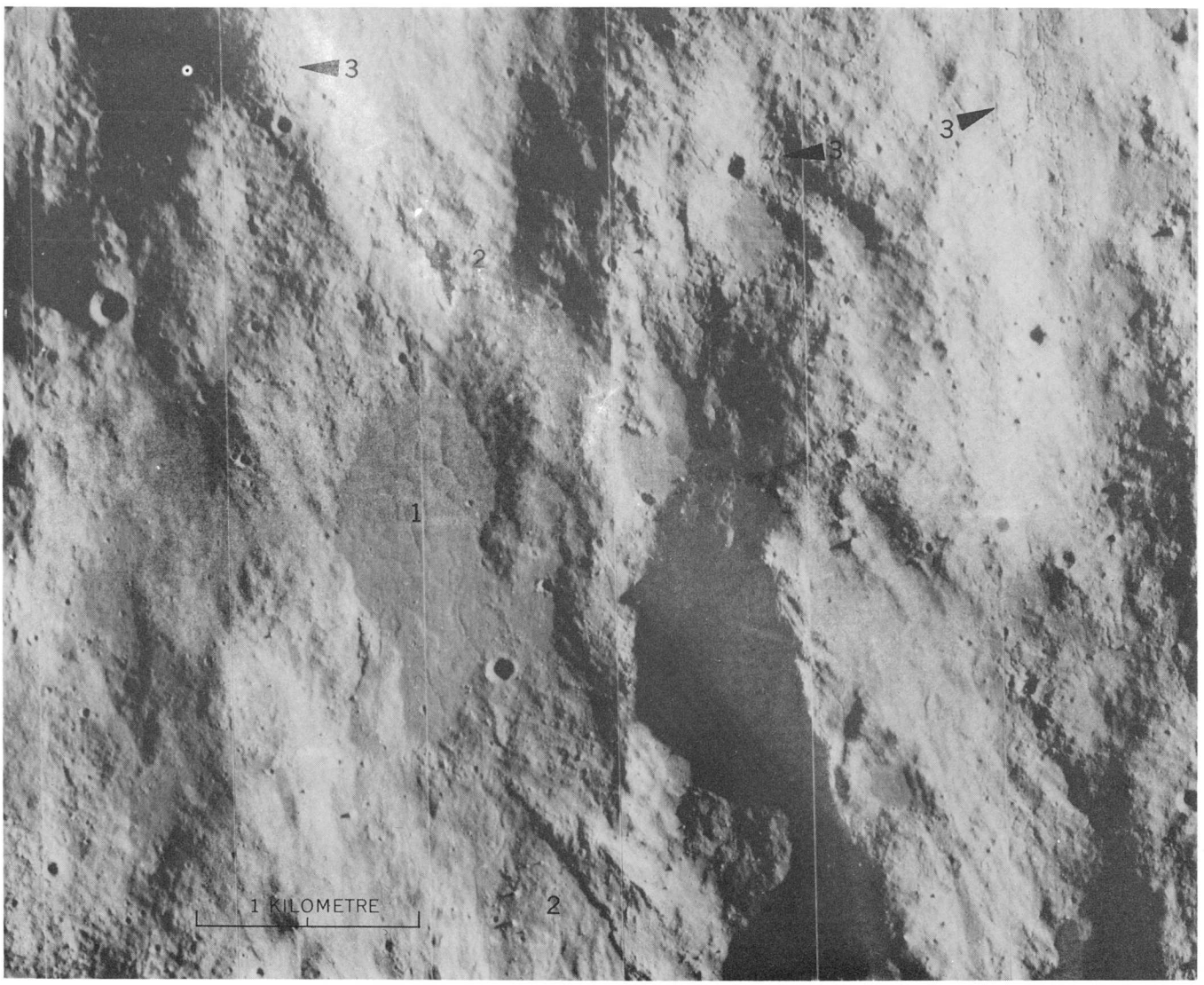

FIGURE 3.—Veneer, pools, and blocky areas on the north rim of Tycho crater. Large pool (1) has polygonal cracks. Blocky residues (2) are present in some areas where more fluid material apparently drained toward pools; elsewhere a cracked veneer (3) still drapes the landscape. (Lunar Orbiter V photograph 127 H.)

large area of the north rim of King crater (fig. 4) is coated by cracked veneer that partly obscures underlying radially textured ejecta (figs. 5, 14; Howard, 1972). Here the veneer clearly merges with flow channels and with large pooled accumulations of similarly fissured material. Downhill creep and flow apparently occurred after the radial flow of ejecta from the crater had ceased. In one place the veneer terminates abruptly high on a slope facing the crater, suggesting that a surge of fluid material from the crater failed to top the hill (fig. 5*A*).

Flows.—Leveed flow channels and lobes demonstrate that lavalike materials flowed downhill both outside on crater rims and inside on crater walls (figs. 5, 6, 7). Detailed study of such features near the Surveyor 7 site at Tycho showed flows with a variety of surface textures and apparent viscosities (Shoemaker and others, 1968; Strom and Fielder, 1968, 1970; Gault, Adams, and others, 1968). A large flow on the wall of Copernicus apparently drained a pond high on the wall (fig. 7); the flow merges at the bottom with cracked material on the crater floor and merges laterally with cracked veneer that coats adjacent parts of the wall. This example, like the large leveed channel on the rim of King crater (fig. 5*B*), shows that veneer, flows, and pond material are at least locally continuous.

Floor material.—Thicker accumulations of fluid material, characterized by complex patterns of blocky cracks and wrinklelike corrugations and by a somewhat knobby but generally level surface (fig. 8), flood the crater floors. In smaller craters this material may flood only part of the floor (fig. 9). The cracks in the material (fig. 8) commonly continue over hummocks in the floor, indicating that the fluid material mantled these hummocks. In Tycho some hummocks are surrounded part way up by concentric shells implying that the tops of the hummocks are not coated (Kosofsky and El-Baz, 1970, p. 83). The fissured lavalike material forms isolated terraces along the edges of some crater floors, for example, Copernicus (Howard, 1974), Tycho, and Aristarchus (Strom and Fielder, 1970). Partly coated hummocks and terraces indicate that the level of the fluid was originally higher and has subsided (Strom and Fielder, 1970; Guest, 1973). The amount of subsidence in the floor of Copernicus may be as much as about 200 m, the height of the largest coated hummocks. Isolated hummocks imply that the underlying hummocky ground is only shallowly flooded so that the present thickness of the fissured floor material is no more than 100–200 m. Subsidence may result partly from compression of voids, as in a welded tuff. Rimless pit craters in the floor material (Hart-

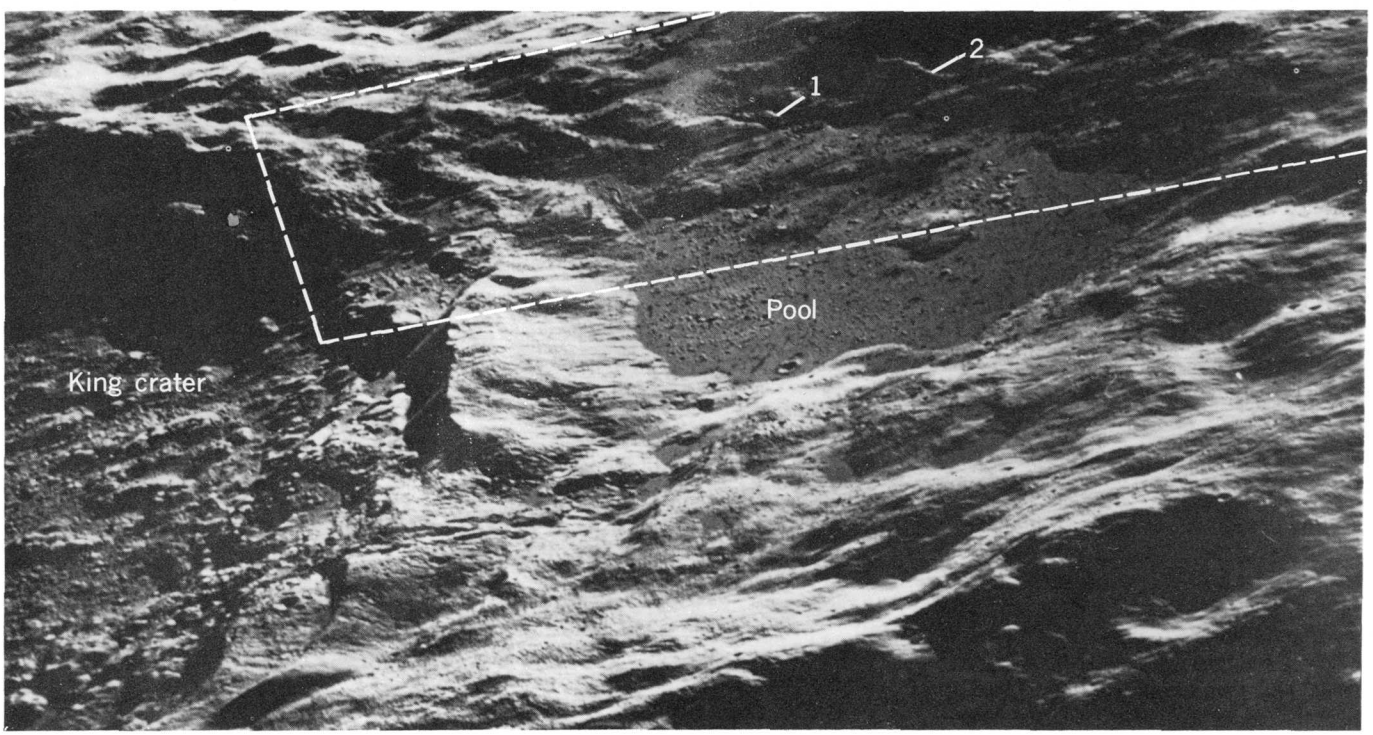

FIGURE 4.—Oblique westward view of large pool of lavalike material on the north rim of King crater (7°N., 121°E.). Area shown is about 40 km across. (Apollo 16 photograph 12–19266.) Outlined area is shown in figure 5*A*; numbers refer to features in figure 5*A*.

mann, 1968) suggest that some of the fluid may have drained downward, possibly into underlying breccia. Crater counts at Copernicus suggest that small collapse pits may be present also in some of the ponds (Greeley and Gault, 1971). Extensive cracks in the floor material indicate that the fluids also contracted. Some cratered hummocks on the floor of Copernicus have been compared with cinder cones (Hartmann, 1968; Lowman, 1969; Kosofsky and El-Baz, 1970; Green, 1971). However, no compelling evidence has been put forward that these features are not random impact craters on hummocks.

Ponds.—Fluid material that ponded to a level surface occupies numerous small depressions on crater walls and rims. At Tycho, where these ponds (also called pools, lakes, and playas) appear very fresh, they have been compared with solidified lava lakes because of a network of branching cracks on the pond surface (fig. 3; Shoemaker and others, 1968; Strom and Fielder, 1970). Most ponds have no apparent source other than local slopes and may be ponded runoff from local catchments. Others have meniscuslike flow fronts on one side and are fed by channels from higher ponds (Strom and Fielder, 1970; El-Baz, 1972). A few have meniscuslike fronts on all sides, suggesting a source from below (Strom and Fielder, 1970). Most ponds are several hundred metres to several kilometres across, but some are much larger. Near Weiner, a large pooled

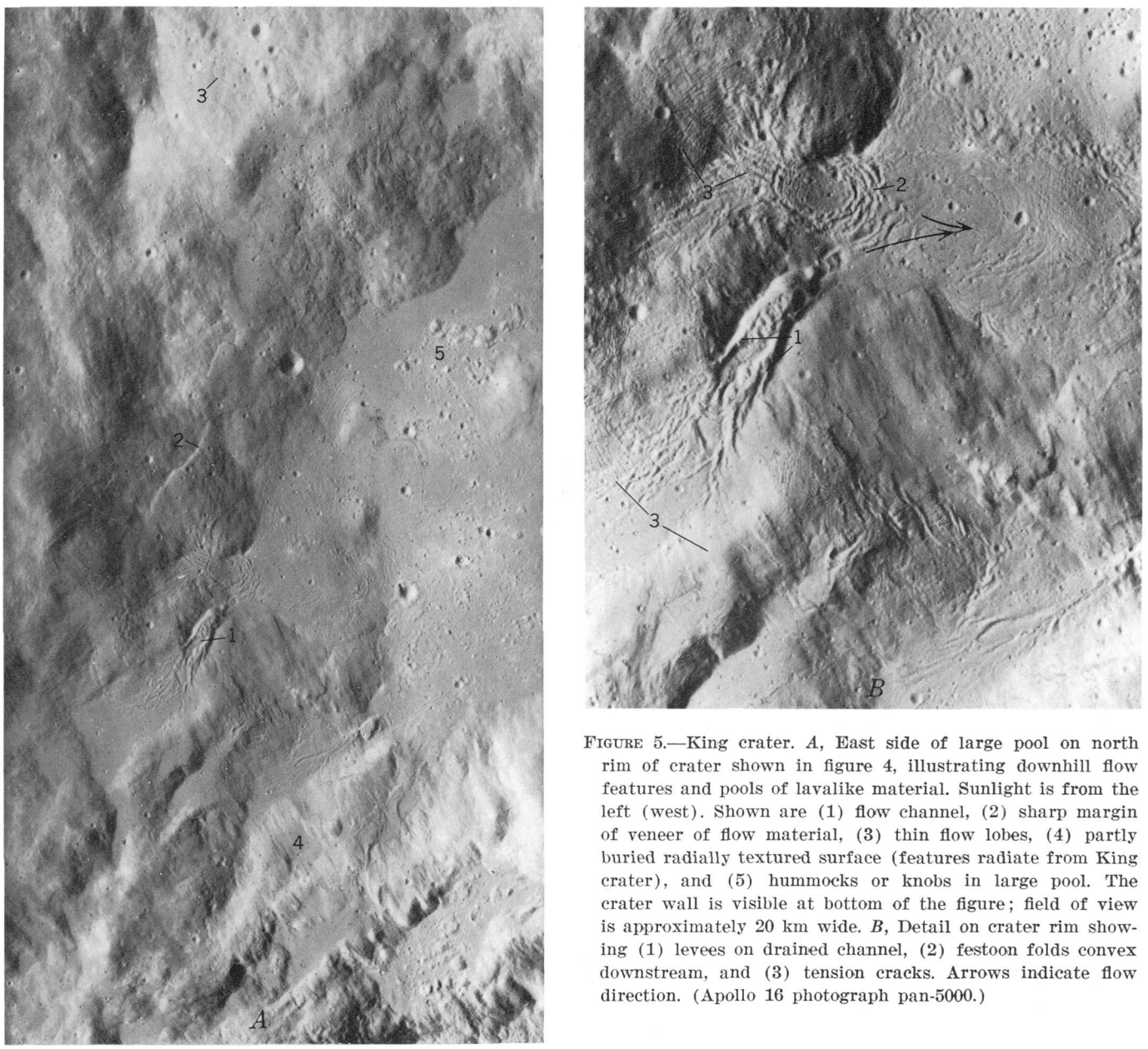

FIGURE 5.—King crater. *A*, East side of large pool on north rim of crater shown in figure 4, illustrating downhill flow features and pools of lavalike material. Sunlight is from the left (west). Shown are (1) flow channel, (2) sharp margin of veneer of flow material, (3) thin flow lobes, (4) partly buried radially textured surface (features radiate from King crater), and (5) hummocks or knobs in large pool. The crater wall is visible at bottom of the figure; field of view is approximately 20 km wide. *B*, Detail on crater rim showing (1) levees on drained channel, (2) festoon folds convex downstream, and (3) tension cracks. Arrows indicate flow direction. (Apollo 16 photograph pan-5000.)

flow of lavalike material is concentrated in a natural moat on the rim of a crater (fig. 10). Even larger is the 20-km-wide pond on the north rim of King crater (figs. 4, 5). An old crater in which this pond occurs apparently served to collect drainage from a large area. The floor of the large pond (fig. 5) contains numerous cracks and closely resembles the pooled material on crater floors (fig. 8). Some rim pools also have corrugations like those of crater floor pools, and the rim pool of King crater encloses several sharp knobs or hummocks (fig. 5*A*). It is uncertain whether similar small knobs on crater floors are related to underlying structure, to fallback, or to the lavalike floor filling. The knobs shown in figure 5*A* are clearly much sharper than the general terrain mantled by the pond materials and thus must be in some way related to the pond material. Inasmuch as the pond material seems to have drained mostly from the surrounding hills, the knobs are not likely to be rooted volcanoes. Possibly they are rootless spatter mounds or floating unmelted blocks.

ALBEDO AND CRATER DENSITY

Albedo.—Ponds and thin fluid veneer on crater rims are typically darker than the rest of the ejecta; examples are the north rim of King (Strom and Whitaker, 1971) and dark halos around Tycho and Aristarchus (Strom and Fielder, 1970). Thick flows, thick deeply fissured pools on crater floors, and blocky areas are commonly bright. None of the lavalike materials considered in this paper are as dark as mare, except for part of a pond on the southeast rim of Tsiolkovsky crater. This pond, the rest of which has a typically

FIGURE 6.—Flow lobes and channels on the rim of a crater (in shadow at left) about 15 km across near Mandel'shtam on the lunar far side (5°N., 167°E). This is the smallest crater recognized with such flows on the rim (Moore, 1972). (Apollo 16 photograph pan–4136.)

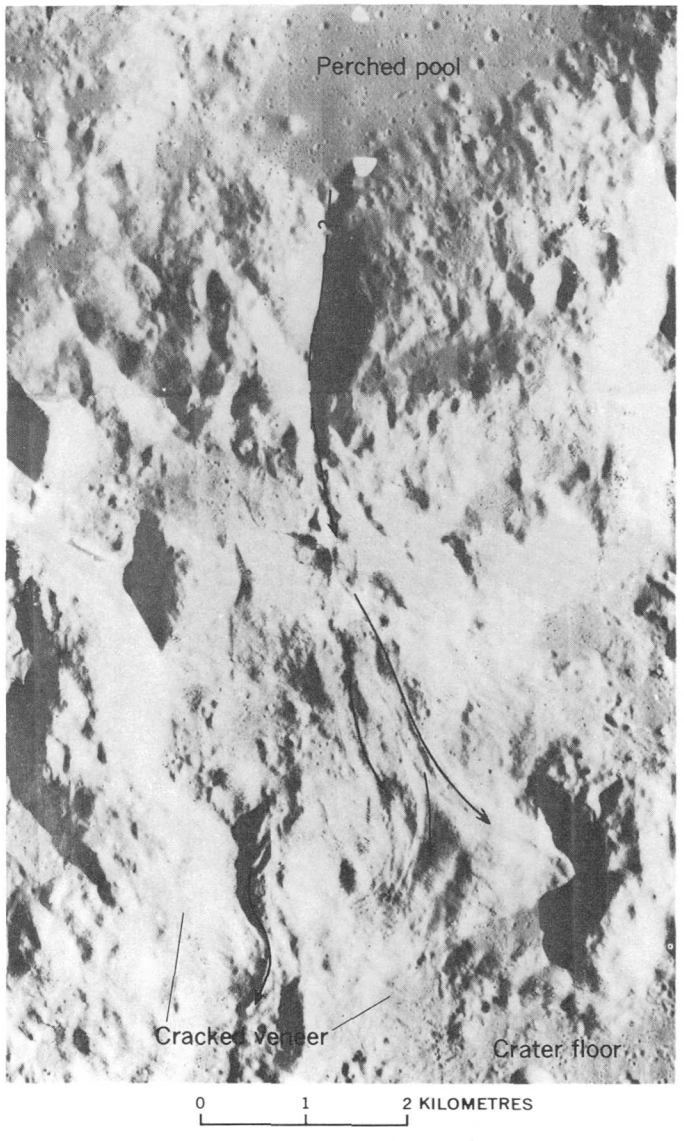

FIGURE 7.—Flows on the north wall of Copernicus. The large flow, which may be a drainage channel from the perched pool, merges with veneer and with lavalike material on the crater floor. Arrows indicate flow direction (Lunar Orbiter V photographs 155H and 156H.)

light tone, is further anomalous in that it is segmented into differentially subsided platforms and basins. On the south rim of Tsiolkovsky dark marelike materials coat the floor of Waterman crater and also are differentially subsided. Waterman is nearly as low as the mare floor of Tsiolkovsky, which suggests that the dark materials here may be basaltic lavas of internal origin. Basaltic volcanism at Tsiolkovsky may have been triggered by the impact (French, 1970).

Crater density.—Detailed study of the flows on the rim of Tycho indicated a complex succession and showed that the youngest flows and the pooled material in ponds and on the crater floor are less cratered than older flows (Shoemaker and others, 1968; Strom and Fielder, 1970; Hartmann, 1968). The age differences implied by crater frequencies at Tycho and also at Aristarchus suggested to Strom and Fielder (1970) that multiphase volcanic eruptions occurred over a long time. If, however, the excess craters on older flows are the result of late-falling secondary impacts, then the older flows formed during or immediately after the cratering event, and solidified within a few minutes (Shoemaker and others, 1968). Less cratered flows then

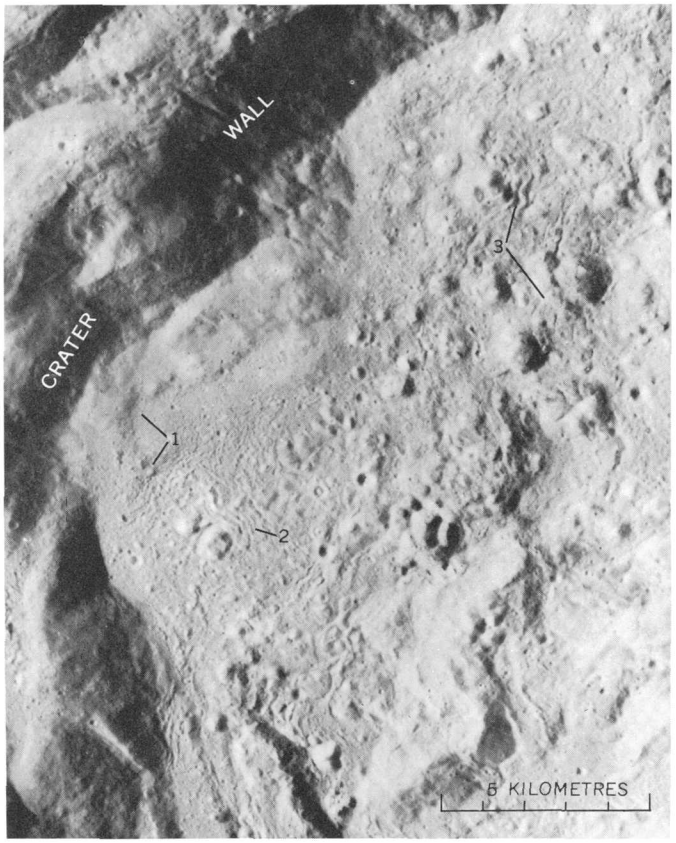

FIGURE 8.—Floor material in King crater. Cracks (1) and corrugations (2) indicate that the material is like lava. Some cracks extend over hummocks (3), which shows that the hummocks are draped by the same material.

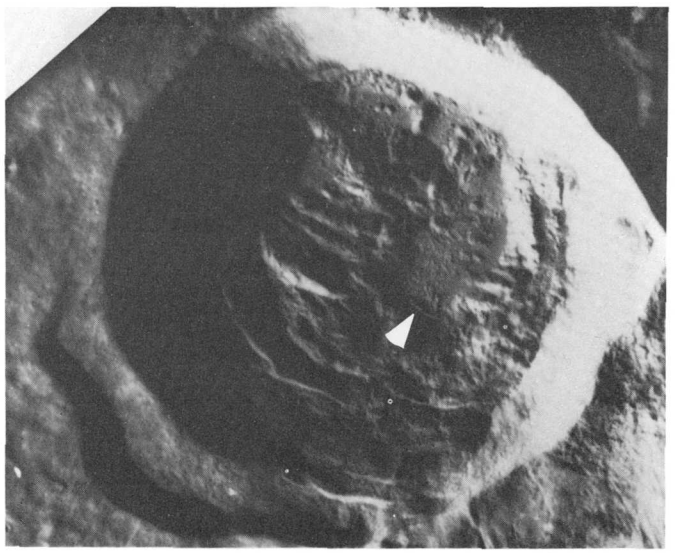

A

B

FIGURE 9.—Fresh crater 35 km across near Bečvář on the lunar far side (5°S., 123°E.). *A*, Parts of the floor are flooded by lavalike materials (pointer). *B*, Detail from floor showing (1) flow front, and (2) typical corrugations on lavalike materials; blocky areas (3) are not flooded. (Apollo 14 photographs 70–9671 and 72–9975.) Fractures and flow directions within the lavalike materials were mapped by El-Baz and Roosa (1972).

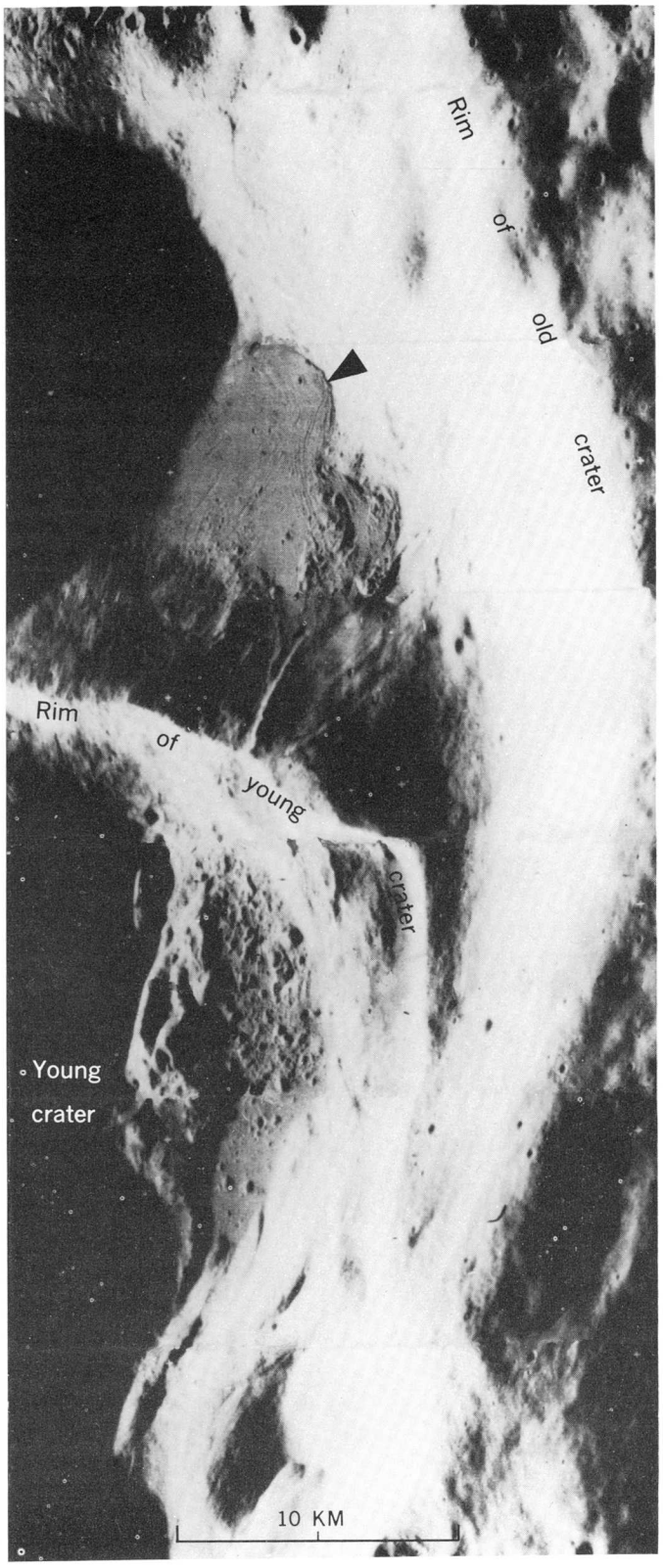

FIGURE 10.—Young crater nested in an old larger crater near Weiner on the far side (149°E., 41°N.). Pointer shows a large pooled flow of lavalike material confined in the moat. (Lunar Orbiter V photograph H 103.)

may have remained fluid after all ballistic ejecta had fallen. (All ballistic fallback impacts the Moon within about 50 min after being ejected (Saunders, 1968)). The thickest and most fluid accumulations of lavalike materials, in ponds and on the crater floor, probably remained fluid for months, years, or decades.

DISTRIBUTION, VOLUME, AND AGE

The lavalike materials are more extensive at large craters than at smaller ones. Most craters wider than 20–30 km contain lavalike materials on their floors (fig. 9). Some craters 1–5 km across have ponded floor material but no cracks are visible (fig. 11). This may be because the material is not similar to that in larger craters or because it is thinner. Cracked veneer occurs on the rim of at least one crater in this size range, 3.5-km-wide Mösting C. Lavalike flows are generally absent from the rims of craters smaller than about 30 km, with some exceptions at craters as small as 15 km across (fig. 6; Moore, 1972). Lavalike ponds are recognizable on the rims of most fresh craters wider than 40–50 km for which good photographs are available. Rim flows are more conspicuous than ponds for craters in the size range of Aristarchus (45 km across). Ponds

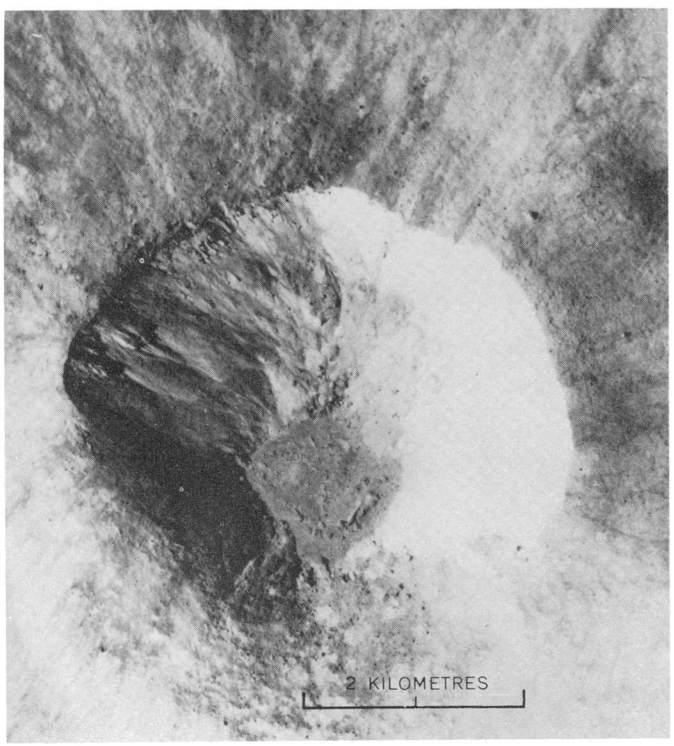

FIGURE 11.—Small fresh crater 4 km across (on the rim of Gibbs) with pooled material on the floor. This material does not exhibit contraction cracks and may not be the same as lavalike materials in larger craters. (Apollo 15 photograph pan-0018.)

on the rims of larger craters represent the greatest concentrations and the most fluid lavalike materials and are the most easily recognizable feature on poor photographs or at old, degraded craters (fig. 12). Using ponds as the main criterion for recognition of lavalike materials, we find that at many craters larger than 50 km across the materials extend to a maximum distance of between one-half and one crater radius beyond the crater. This maximum stays constant, relative to crater size, for craters as large as 200 km and possibly 300 km across. Table 1 and figure 13 show this maximum distance for selected craters for which good photographs are available.

TABLE 1.—*Asymmetry of fresh craters with lavalike deposits*

Crater	Diameter (km)	Direction (from crater) of most extensive deposits		Maximum distance of rim ponds from crater (crater radii)
		Ejecta blanket or rays	Rim ponds	
Schrödinger	300	NE?	E	0.70?
Humboldt	201	SSE	SE	.96
Tsiolkovsky	190	SSE	SE	.49
Petavius	177	SSE	S	.68
Hausen	170	?	SW	>.41
Langrenus	132	SE?	SSE	.68
Pythagorus	128	---	NE	.72
Theophilus	100	NE	NE	.94
Copernicus	95	NW?	NW?	.66
Aristotoles	87	N?	S?	.50
Tycho	85	E	E	.88
King	71	NNW	NNW	.83
Philolaus	70	NE?	NE	1.00
Anaxagorus	51	ESE	ESE	.31
Crookes	50	---	---	0
Near Steno (162°E. 35°N.)	45	?	SSE	1.20
Aristarchus	45	---	---	.65
Near Bečvář (fig. 9)	35	N	---	0
Near Weiner (fig. 10)	30	---	N	.85
Near Mandel'shtam (fig. 6)	15	NW?	W	[1].26

[1] Flows used instead of ponds.

The distribution of lavalike materials at the fresh multi-ring Orientale basin (900 km across) differs from that of the smaller craters in at least one important respect: ponded lavalike material is rare or absent on the ejecta blanket near the basin rim. There is, however, a crackled blanket in the inner basin of Orientale that appears to be equivalent to lavalike materials on crater floors (J. F. McCauley in Saunders, 1968, p. 32–33), and some areas of the Hevelius Formation (textured ejecta) are cracked like lavalike materials (H. J. Moore, oral commun., 1974). The apparent absence of ponded material is discussed later.

A generous estimate of the volume of lavalike material at Copernicus (95 km diam) is 400 km^3 inside the crater and 160 km^3 on the rim outside the crater.

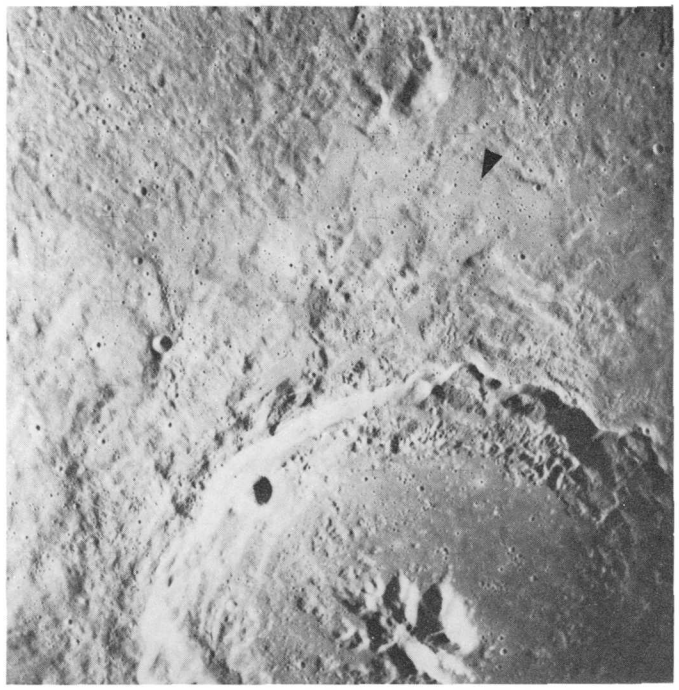

FIGURE 12.—Numerous ponds (degraded because of age) on the north rim of Theophilus crater (110 km in diameter) are indicated by pointer. These materials, part of the Theophilus Formation, are mainly on the northeast rim, the direction in which the Theophilus ejecta blanket is also most extensive (Milton, 1968). (Apollo 16 photograph met–0164.)

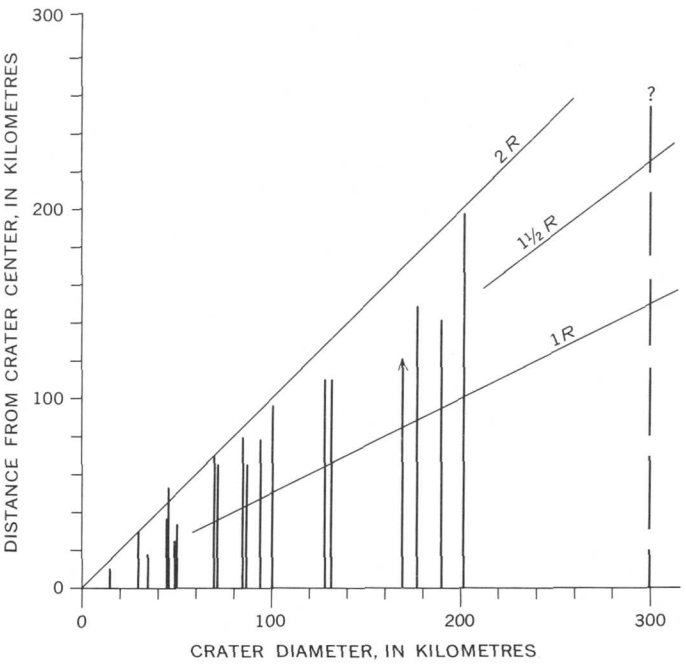

FIGURE 13.—Graph showing maximum distance of lavalike materials from the centers of fresh lunar craters. For craters larger than about 50 km the relative distance stays constant at ½ to 1 R (radius) beyond the crater lip (which is at 1 R). Arrow indicates a minimum value; query denotes uncertain association of pond materials with crater.

This assumes average thicknesses of 100–200 m for the floor, 25 m for the wall and the rim out to 0.3 radius beyond the crater, and 10 m for the rim beyond out to the distance of the farthest recognized ponds (0.66 radius). An additional 200 km^3 may be represented by subsidence of the floor materials. An estimate of lava-like material at King crater (71 km diam) is 225 km^3. For Tycho crater (85 km diam), Shoemaker and others (1968) estimated 120 km^3 of such materials on the rim and suggested that a comparable amount may be present on the floor.

The largest rim pools are concentrated on the east side of Tycho where the ray pattern is most extensive. This suggested to Shoemaker and others (1968) that the impact was oblique. We find the same type of asymmetry at other craters (table 1 and fig. 14). Where oblique impact is suggested by asymmetry of rays, secondary crater field, or ejecta blanket, the rim pools tend to be concentrated on the inferred downrange side. The crater floor also commonly is most deeply flooded and therefore flatter on the inferred downrange side, probably because the crater was deeper on that side. Asymmetries of lavalike materials on the floors and rims of craters possibly will prove to be reasonable criteria of oblique impact even where other indications of asymmetry are obscure.

The craters (table 1) that show the rim ponds range in age from upper Copernican to middle Imbrian or older. Tycho, for example, is young—on the order of 10^8 yr old (Hartmann, 1968; Baldwin, 1972). Humboldt, Petavius, and Tsiolkovsky are middle Imbrian craters that predate some mare basalts and are therefore about $3.5–3.8\times10^9$ yr old. The largest craters listed are the oldest because there are no younger craters of comparable size. Lavalike deposits are difficult to recognize on small old craters because they are too degraded. The oldest and largest crater listed in table 1, Schrödinger (actually a small double-ringed basin), is degraded enough that ponds on the rim cannot be associated with the crater with complete confidence. The deposits generally appear to be about the same age as their crater, but they are superposed on the crater ejecta; they may be less cratered than the ejecta blanket, as at Tycho and Copernicus.

It appears, therefore, that since at least the time of mare flooding three and a half billion years ago, lava-like materials have consistently formed on the rims and floors of craters during or shortly after their excavation.

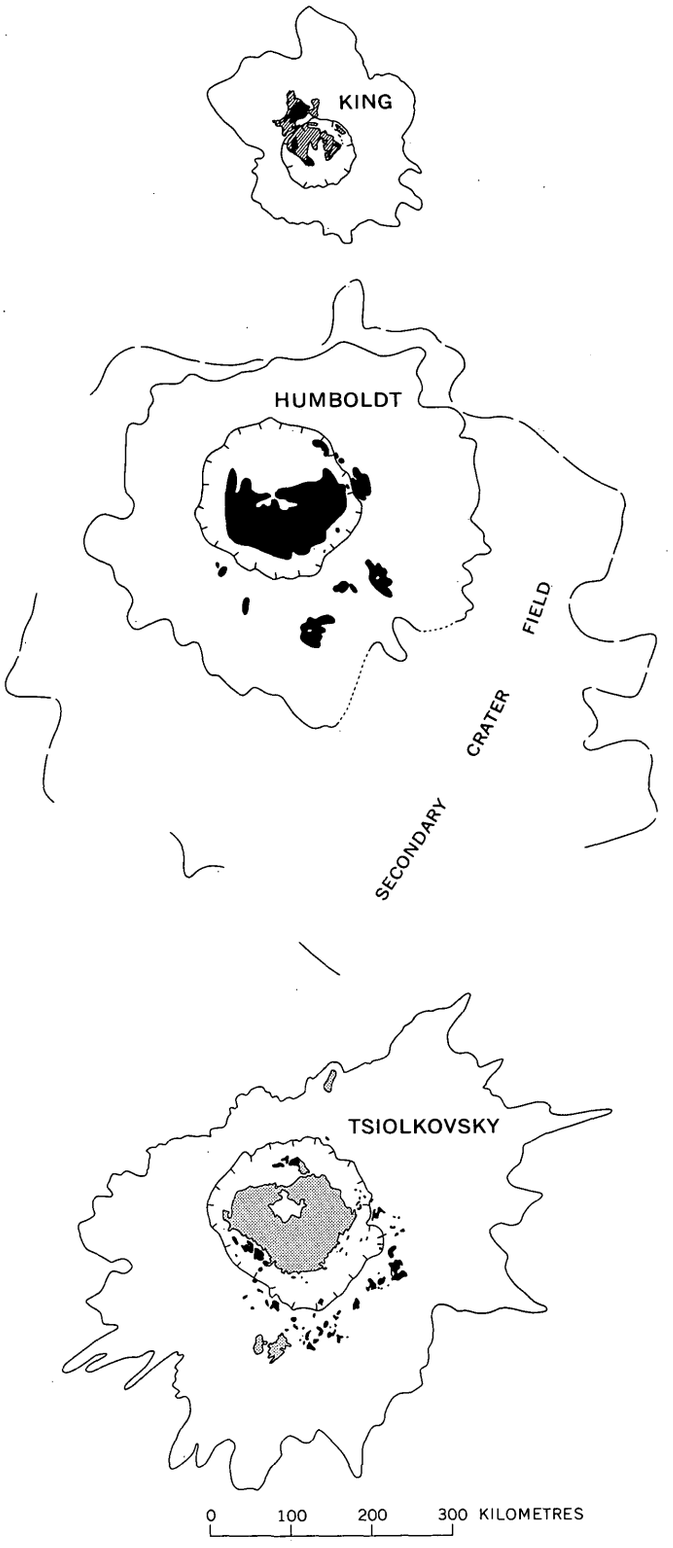

FIGURE 14.—Sketch maps showing asymmetric distribution of ponded lavalike materials (black) and ejecta blankets at King, Humboldt, and Tsiolkovsky craters. Lined pattern at King indicates veneered area. Stippled pattern at Tsiolkovsky indicates dark mare and other dark materials. Ejecta blanket of Tsiolkovsky from Guest and Murray (1969).

INTERPRETATION AS IMPACT MELT

The materials described clearly behaved like liquids. Characteristics such as festoons and tension cracks in

the materials indicate that they generally flowed sluggishly, like lava flows or wet debris flows as opposed to gas-fluidized flows such as avalanches or ash flows. Water is unlikely to be the liquifying agent because returned lunar samples are anhydrous. A much more probable liquid component, which would account for solidification to hard rocks, is rock melt.

A volcanic origin for this melt seems unlikely. It would be remarkable if similar patterns of volcanic eruptions occurred at every large impact crater over at least the last three and a half billion years, a time interval in which the thermal regime of the Moon has changed markedly. The lavalike materials appear to mantle large areas and to have drained from the topographic highs, but clear-cut volcanic vents are lacking. The materials do show local sequences of emplacement and a variety of apparent viscosities, as carefully documented for Tycho by Strom and Fielder (1970) and Shoemaker and others (1968). Shoemaker and others cited evidence at Tycho, however, as we have cited evidence at King and Copernicus, that the various types of fluid materials are gradational and interrelated. The most fluid parts ponded in depressions, less fluid parts flowed in channels and lobes of various apparent viscosities, and the veneer over intervening ground stretched plastically. The variety of viscosities could be a function of melt content, gas content, composition of melt, or temperature at time of flow.

The characteristics of the materials, the lack of apparent sources, and the distribution patterns are most easily explained if the materials are impact melts with variable proportions of unmelted inclusions. Several criticisms can be leveled at this interpretation: (1) The crater counts surprisingly suggest that some secondary projectiles fell after part of the melt had flowed and solidified, (2) the amount of melt in or near the crater is higher than predicted by current theory or experiments, and (3) the melted material had to coalesce as a fluid even though it had opportunity to cool in flight. These problems, however, seem outweighed by the extent to which the impact-melt interpretation can explain most characteristics and distribution patterns of the lavalike materials.

According to this interpretation, rock melt (with inclusions) coated the crater and part of its ejecta blanket late in the cratering event and flowed into its present shape mainly after the crater walls slumped and after radial flow away from the crater had ceased. Lunar photographic evidence suggests that the melt may have been deposited at the top of the ejecta blanket in several ways:

1. It may have been mixed with the rest of the blanket and then sweated out. That the entire upper part of the blanket was partly fluid is suggested by flows that appear to head at collapsed hills of debris. Blocks present in flows, in the veneer, and in places from which the veneer appears to have drained away, suggest that some of the fluid was partitioned from blocky parts of the ejecta by coalescence of the fluid.
2. The melt may have splashed out as a mass at the end of the cratering event. The uphill-facing front of fluid veneer at King crater (fig. 5) and the flows at the right-hand pointer in figure 6 give the impression that these materials were propelled away from the craters. These features are rare, however, suggesting that such splashing is not a dominant process.
3. The melt may have fallen as a rain of hot clots that coalesced and ran together as they settled. This could account for the thinness of the hard, cracked veneer (figs. 2, 3) and might be analogous to lava spatter erupted from high fire fountains; when the lava clots fall back to earth, they commonly coalesce as agglutinate veneers or as liquid flows (Richter and others, 1970).
4. The melt may have been locally erupted from dikes, similar to those at some terrestrial craters (French and others, 1970; Dence, 1971). This subsurface origin could explain the few ponds that have a meniscus on all sides; it could also explain the anomalous pattern of differential subsidence of ponds on the rim of Tsiolkovsky crater, if part of the melt drained back downward.

Comparison with terrestrial analogs suggests that most of the melt rock at lunar craters was only partly molten. Most impact melts that have survived erosion at terrestrial craters are on the crater floor or in lenticular masses beneath the floor (Dence, 1971). Most of these materials contain unmelted debris. Such materials range from breccias with small amounts of interstitial glass to mainly rock melt with a few unmelted inclusions. The lavalike material on the floors of many lunar craters is presumably similar (Masursky, 1968). Large sheets of igneous rock without inclusions occur in the large Manicouagan (60 km diam) and West Clearwater Lake (32 km diam) craters in Quebec, Canada (Dence, 1971). By analogy, completely molten material may occupy some of the larger lunar craters. The largest known terrestrial crater, Sudbury, in Ontario, Canada, is filled by the Onaping Tuff, a breccia containing mostly clasts and only 10–20 percent melt (French, 1970). Whether a breccia as rich as this in unmelted clasts could account for the lavalike fillings of some large craters is uncertain. Evidence that

Sudbury crater filled immediately with water suggests that its crater fill may be chilled and therefore atypical for larger craters (French, 1970). The subsided floor material of lunar craters suggests that drainage from the crater floor into underlying cavities and spall zones could account for some sill-like bodies of rock melt beneath terrestrial craters.

Impact melts are preserved on the rim of a terrestrial crater in significant quantity only at the 23-km-wide Ries crater in Germany. At other crater rims, melt rocks have been eroded, or the crater was too small to produce much melt. The impact-melt deposit (suevite) on the rim of the Ries lies at the top of the ejecta blanket, and patches extend to nearly one crater radius beyond the crater (Hörz, 1965; Dennis, 1971; Chao, 1973); the deposit may have been more extensive because it has been significantly eroded. The suevite is a breccia of glass bombs and particles and lesser amounts of highly shocked unmelted debris in a fine matrix. The suevite on the rim is typically 5–10 m thick (a maximum of 20 m) and overlies buntebreccia ejecta that is little shocked (Chao, 1973). It is inferred that this melt rock on the rim was produced in the last stage of cratering, was ejected at steep angles, and was the last ejecta to settle (Chao, 1973). Cooling histories of the glassy masses suggest that they cooled largely in the air before settling (Hörz, 1965; von Englehardt, 1967) but remained hot enough that the suevite deposit formed chill zones at the top and bottom and tended to crystallize in the center (Dennis, 1971). It is not likely that Ries suevite flowed to assume lavalike landforms. Complete melting and flow may have occurred, however, in a crystalline vesicular melt-rock deposit on the rim of of the Ries locally, near Polsingen (von Englehardt and others, 1969; Dennis, 1971; Dence, 1971). A precise comparison between lunar craters and the Ries crater is difficult because of different gravities and the absence of an atmosphere on the Moon. The Ries is near the lower size limit for lunar craters on which flow effects are found on the rim. At larger craters, melt rocks probably are thicker on the rim than at the Ries and may be mixed with less unmelted material. Thus the deposits they form may stay hot enough and fluid enough to form the flow features that we have described.

The quantities of melt rock at lunar craters are compatible with those of terrestrial craters. French (1970) has summarized estimates and extrapolations of impact-melt volumes at terrestrial craters. According to these data, a crater the size of Copernicus could be expected to produce about 10^3 km^3 of impact melt. If we assume that the 500–600 km^3 of lavalike material at Copernicus is completely melted and then compute the impact energy for Copernicus according to Baldwin's (1963, p. 176) formula, it becomes apparent that the melting represents only about 2 percent of the impact energy. Of course, some melt was probably distributed beyond the crater environs and so was unaccounted for, but on the other hand the recognized lavalike materials almost certainly include a major fraction of unmelted material. Theoretical conclusions with some experimental support (Gault and others, 1972) indicate that for impact velocities between 10 and 20 km/s, melting accounts for about 2 percent of the impact energy.

Theoretical and experimental data suggest that impact melt should be concentrated not in the crater but dispersed far beyond (Chapman, 1972; Short, 1965; Shoemaker and others, 1968; Gault, Quaide, and Oberbeck, 1968). This prediction, however, relies on gross extrapolations up to the large craters under consideration. The geologic evidence at large terrestrial and lunar craters indicates that the thickest concentration of melt rock is inside the crater. A large fraction, however, is outside the crater. Furthermore, there may be significant volumes of melt rock well beyond the crater that are too thin or too mixed with unmelted material to pool or behave as flows. Copernicus may be used as an example to estimate how much unseen melt rock might be on the outer rim. At Copernicus the estimated volume of melt rock distributed for each radial kilometre falls off from an average of 14 km^3/km within the crater to 8 km^3/km on the adjacent rim and to 4 km^3/km out to the farthest pools. If this falloff rate is extrapolated outward beyond the farthest pools to a distance of one crater diameter beyond the rim, then melt rock would average 3 m thick at this distance and an additional volume of 200 km^3 would be added to the 500–600 km^3 visible in and near the crater. Distant ejecta may also contain much melt rock, as suggested by the presence of glassy particles thought to be Copernicus ray material at the Apollo 12 site (Anderson and Smith, 1971; Morgan and others, 1973).

The impact model that the evidence at lunar craters suggests to us is as follows. During crater excavation, the bulk of the ejecta is propelled radially outward at or near the ground surface. The crater walls begin slumping during the closing stages. The last material to be ejected may be hotter and may contain higher proportions of melt. Some of this melt may be propelled outward in flowlike sheets at or near the ground surface. Much of the melt remains inside or falls back into the crater or on the adjacent rim. Where the accumulation of melt splashes is thick enough, the material coalesces and tends to drain downhill like lava, carrying some unmelted inclusions with it. Unknown amouts of melt may be extruded from fissures.

While the materials are flowing, they are continually bombarded by fallback particles that have been propelled to great heights at high angles. Deep pools of melt that accumulate in depressions crust over and may stay fluid in the interior for years. Part of the material in the crater floor may drain downward into underlying cavities and fractures.

LUNAR SAMPLES

The textures of returned lunar samples bear on the impact-melt hypothesis, even though none of the Apollo landings was within the recognized melt zone of a large crater. Abundant impact glass is produced at small cratering events as indicated by glass splashes in secondary craters (Schaber and others, 1972), by glass-coated ejecta blocks (Wilshire and Moore, 1974), and by the abundance of glassy particles and agglutinates in the lunar regolith (Apollo Soil Survey, 1971). Thermal welding of soil breccias from the Apollo 11 site suggests that impact ejecta stays hot during transport (McKay and Morrison, 1971). Glassy particles in probable Copernicus ray material at the Apollo 12 site confirm that some ejecta from large impacts was completely melted. Large clast-rich blocks televised by Surveyor 7 in the lavalike materials on the rim of Tycho suggest that some of the proposed melt rock contains abundant unmelted material (Shoemaker and others, 1968).

The Surveyor 7 materials at Tycho are rich in alumina (Patterson and others, 1970), and textures of rocks in the vicinity now appear, in the light of returned samples, most likely to be breccias. Their similarity, both in occurrence of light clasts in a dark matrix and composition of the soils, to Apollo 16 and Luna 20 materials is striking. The comparable Apollo 16 breccias—the B_2 and B_4 breccias of Wilshire, Stuart-Alexander, and Jackson (1973)—show signs of extensive fusion (Warner and others, 1973), especially those samples that are inferred to represent the Cayley Formation (Ulrich, 1973), which has long been considered a deposit of fluid material (Wilhelms and McCauley, 1971).

In general, the pulverized, finely recrystallized, and partly melted materials derived from anorthositic highland rocks are much darker than their source rocks, or their more coarsely annealed equivalents, though still lighter than mare basalts. Thus the generally lower albedo of impact-melt pools and veneer, a clear example of which is the dark halo around Tycho, is readily explained as a consequence of impact melting of light-colored feldspathic rocks. Lighter toned areas of melt rock, such as viscous flows on the rim of Tycho (Strom and Fielder, 1970), may include abundant unmelted shock-crushed inclusions. Light-toned deposits in crater floors may be coarsely crystalline as a result of slow cooling in thick accumulations.

Because the maximum range of ponded melt rock is between one-half and one crater radius beyond large craters, extrapolation of this distribution to large multi-ring basins would indicate that impact melt might be expected around the Imbrium basin as far as the Apollo 14 site, in the Fra Mauro Formation three-quarters of a basin radius (550 km) beyond the Apennine ring. This is a greater range than Dence and Plant (1972) suggested, and as pointed out earlier, the distribution of lavalike features at basins differs from that at craters. No certain lavalike features are known on the Fra Mauro ejecta blanket. In agreement with this observation, the Apollo 14 breccias show evidence of variable temperature; some small parts were molten, but the amounts were probably insufficient to allow lavalike flow. Although ponds are lacking on the Orientale ejecta blanket near the basin rim, a planar facies of ejecta at the distal edge of the blanket has a pondlike morphology, lobate forms, and a leveed channel suggestive of emplacement as a fluid moving away from the basin (Hodges and others, 1973). This material is generally indistinguishable from more widely distributed ponded material termed the Cayley Formation (Hodges and others, 1973). The Cayley Formation at the Apollo 16 site may represent distant ejecta from the Imbrium or Orientale basins (Eggleton and Schaber, 1972; Muehlberger and others, 1972; Chao and others, 1973; Hodges and others, 1973). The pondlike morphology of the Cayley, the predominance of impact breccias in Cayley samples from the Apollo 16 site, and the evidence of partial fusion noted above, all are consistent with the emplacement of the Cayley as a fluidal component of basin ejecta. We do not suggest that the Cayley Formation is the exact equivalent of ponded lavalike materials at craters, because the distribution patterns are different and the Cayley is largely beyond any local source of runoff in the textured ejecta blanket. If, however, the Cayley is a basin-related analog of the ponded lavalike material around craters, then impact melt is not distributed in the same way for large basins as it is for craters. Rather it may be that in basin ejecta, the hot material is segregated from and largely dispersed beyond the continuous ejecta blanket (Eggleton and Schaber, 1972). Alternatively, the Cayley may not be basin ejecta (Head, 1974; Oberbeck and others, 1973). If not, then the impact melt from large basins may be restricted mainly to the basin or else thoroughly mixed with the rest of the ejecta.

REFERENCES CITED

Anderson, A. T., Jr., and Smith, J. V., 1971, Nature, occurrence, and exotic origin of "gray mottled" (Luny Rock) basalts in Apollo 12 soils and breccias, *in* Proceedings of Second Lunar Science Conference: Geochim. et Cosmochim, Acta Supp. 2, v. 1, p. 431–438.

Apollo Soil Survey, 1971, Apollo 14: Nature and origin of rock types in soil from the Fra Mauro Formation: Earth and Planetary Sci. Letters, v. 12, p. 49–54.

Baldwin, R. B., 1949, The face of the Moon: Chicago, Ill., Univ. Chicago Press, 239 p.

——— 1963, The measure of the Moon: Chicago, Ill., Univ. Chicago Press, 488 p.

——— 1972, Comments on paper by Dean R. Chapman, "Australasian tektite geographic pattern, crater and ray of origin, and theory of tektite events": Jour. Geophys. Research, v. 77, no. 14, p. 2616–2617.

Chao, E. C. T., 1973, Geologic implications of the Apollo 14 Fra Mauro breccias and comparison with ejecta from the Ries crater, Germany: U.S. Geol. Survey Jour. Research, v. 1, no. 1, p. 1–18.

Chao, E. C. T., Soderblom, L. A., Boyce, J. M., Wilhelms, D. E., and Hodges, C. A., 1973, Lunar light plains deposits (Cayley Formation)—a reinterpretation of origin [abs.], *in* Lunar Science IV: Houston, Tex., Lunar Science Inst., p. 127–128.

Chapman, D. R., 1972, Reply to comments on paper by Dean R. Chapman, "Australasian Tektite geographic pattern, crater and ray of origin, and theory of tektite events": Jour. Geophys. Research, v. 77, p. 2618–2619.

Crittenden, M. D., 1968, Lunar "mudflows" in Orbiter V imagery, *in* Lunar Orbiter Photo Data Screening Group, A preliminary geologic evaluation of areas photographed by Lunar Orbiter V: Natl. Aeronautics Space Adm., Langley Working Paper LWP–506, p. 158–163.

Cruikshank, D. P., and Wood, C. A., 1972, Lunar rilles and Hawaiian volcanic features: Possible analogues: The Moon [Dordrecht, Holland], v. 3, p. 412–447.

Dence, M. R., 1971, Impact melts: Jour. Geophys. Research, v. 76, no. 23, p. 5552–5565.

Dence, M. R., and Plant, A. G., 1972, Analysis of Fra Mauro samples and the origin of the Imbrium basin, *in* Proceedings Third Lunar Science Conference: Geochim. et Cosmochim. Acta Supp. 3, v. 1, p. 379–399.

Dennis, J. G., 1971, Ries structure, southern Germany, a review: Jour. Geophys. Research, v. 76, p. 5394–5406.

Eggleton, R. E., and Schaber, G. G., 1972, Cayley Formation interpreted as basin ejecta, *in* Apollo 16 preliminary science report: Natl. Aeronautics Space Adm., SP–315, p. 29–7—29–16.

El-Baz, Farouk, 1971, Lunar igneous intrusions: Science, v. 167, p. 49–50.

——— 1972, King crater and its environs, *in* Apollo 16 preliminary science report: Natl. Aeronautics Space Adm., SP–315, p. 29–62—29–70.

El-Baz, Farouk, and Roosa, S. A., 1972, Significant results from Apollo 14 orbital photography, *in* Proceedings of Third Lunar Science Conference: Geochim. et Cosmochim. Acta Supp. 3, v. 1, 63–83.

Englehardt, Wolf von, 1967, Chemical composition of Ries glass bombs: Geochim. et Cosmochim. Acta, v. 31, p. 1677–1689.

Engelhardt, Wolf von, Stöffler, D., and Schneider, W., 1969, Petrologische Untersuchungen im Ries, Das Ries: Geol. Bavarica, v. 61, p. 229–295.

French, B. M., 1970, Possible relations between meteorite impact and igneous petrogenesis, as indicated by the Sudbury structure, Ontario, Canada: Bull. Volcanol., v. 34, p. 466–517.

French, B. M., Hartung, J. B., Short, N. M., and Dietz, R. S., 1970, Tenoumer crater, Mauritania: Age and petrologic evidence for origin by meteorite impact: Jour Geophys. Research, v. 75, no. 23, p. 4396–4406.

Gault, D. E., Adams, J. B., Collins, R. J., Kuiper, G. P., Masursky, H., O'Keefe, J. A, Phinney, R. A., and Shoemaker, E. M., 1968, Lunar theory and processes, *in* Surveyor VII Mission report, Part II, Science results: Natl. Aeronautics Space Adm. Tech. Rept. 32–1265, p. 267–313.

Gault, D. E., Hörz, Friedrich, and Hartung, J. B., 1972, Effects of microcratering on the lunar surface, *in* Proceedings of Third Lunar Science Conference: Geochim. et Cosmochim. Acta Supp. 3, v. 3, p. 2713–2734.

Gault, D. E., Quaide, W. I., and Oberbeck, V. R., 1968, Impact cratering mechanics and structures, *in* French, B. M., and Short, N. M., eds., Shock metamorphism of natural materials: Baltimore, Mono Book Corp., p. 87–100.

Gilbert, G. K., 1893, The Moon's face, a study of the origin of its features: Philos. Soc. Washington Bull., v. 12, p. 241–292.

Greeley, Ronald, and Gault, D. E., 1971, Endogenetic craters interpreted from crater counts on the inner wall of Copernicus: Science, v. 171, p. 477–479.

Green, Jack, 1971, Copernicus as a lunar caldera: Jour. Geophys. Research, v. 76, no. 23, p. 5719–5731.

Guest, J. E., 1973, Stratigraphy of ejecta from the lunar crater Aristarchus: Geol. Soc. America Bull., v. 84, no. 9, p. 2873–2894.

Guest, J. E., and Murray, J. B., 1969, Nature and origin of Tsiolkovsky crater, lunar farside: Planetary and Space Sci., v. 17, p. 121–141.

Hartmann, W. K., 1968, Lunar crater counts VI: The young craters Tycho, Aristarchus, and Copernicus: Arizona Univ. Lunar Planetary Lab. Commun., v. 7, pt. 3, p. 145–156.

Head, J. W., 1974, Stratigraphy of the Descartes region, Apollo 16: Implications for the origin of samples: The Moon [Dordrecht, Holland], v. 9.

Hodges, C. A., Muehlberger, W. R., and Ulrich, G. E., 1973, Geologic setting of Apollo 16, *in* Proceedings of Fourth Lunar Science Conference: Geochim. et Cosmochim. Acta Supp. 4, v. 1, p. 1–25.

Hörz, Friedrich, 1965, Untersuchungen an Riesgläsern: Beitr. Mineralogie u. Petrologie, v. 11, p. 621–661.

Howard, K. A., 1971, The Apollo 10 lunar highlands, *in* Analysis of Apollo 10 photography and visual observations: Natl. Aeronautics Space Adm., SP–232, p. 12–14.

——— 1972, Ejecta blankets of large craters exemplified by King crater, *in* Apollo 16 preliminary science report: Natl. Aeronautics Space Adm., SP–315, p. 29-70—29-77.

——— 1974, Geologic map of the crater Copernicus: U.S. Geol. Survey Misc. Geol. Inv. Map I–840.

Kosofsky, L. J., and El-Baz, Farouk, 1970, The Moon as viewed by Lunar Orbiter: Natl. Aeronautics Space Adm., SP–200, 152 p.

Lowman, P. D., 1969, Lunar Panorama: Zurich, Switzerland, Weltflugbild Reinhold A. Müller, 101 p.

McKay, D. S., and Morrison, D. A., 1971, Lunar breccias: Jour. Geophys. Research, v. 76, p. 5658–5669.

Masursky, Harold, 1968, Preliminary geologic interpretations of Lunar Orbiter photography, *in* Hearings before the U.S. House of Representatives Subcommittee in Space Science and Applications of the Committee on Science and Astronautics: U.S. 90th Cong. 2d sess., H.R. 15086, p. 665–691.

Milton, D. J., 1968 Geologic map of the Theophilus quadrangle of the Moon: U.S. Geol. Survey Misc. Geol. Inv. Map I–546.

Moore, H. J., 1968, Site V–48, Aristarchus, *in* Lunar Orbiter Photo Data Screening Group, A preliminary geologic evaluation of areas photographed by Lunar Orbiter V: Natl. Aeronautics Space Adm., Langley Working Paper LWP–506, p. 129–132.

——— 1971, Geologic interpretation of lunar data: Earth-Sci. Rev., v. 7, p. 5–33.

——— 1972, Ranger and other impact craters photographed by Apollo 16, *in* Apollo 16 preliminary science report: Natl. Aeronautics Space Adm., SP–315, p. 29–45—29–51.

Morgan, J. W., Ganapathy, R., Laul, J. C., and Anders, Edward, 1973, Lunar crater Copernicus: Search for debris of impacting body at Apollo 12 site: Geochim. et Cosmochim. Acta, v. 37, p. 141–154.

Muehlberger, W. R., Batson, R. M., Boudette, E. L., Duke, C. M., Eggleton, R. E., and others, 1972, Preliminary geologic investigation of the Apollo 16 landing site, *in* Apollo 16 preliminary science report: Natl. Aeronautics Space Adm., SP–315, p. 6–1—6–81.

Oberbeck, V. R., Hörz, Friedrich, Morrison, R. H., and Quaide, W. L., 1973, Emplacement of the Cayley Formation: Natl. Aeronautics Space Adm. Tech. Memo. TM X–62, 302, 38 p.

Patterson, J. H., Turkevich, A. L., Franzgote, E. J., Economou, E. J., Sowinski, K. P., 1970, Chemical composition of the lunar surface in a terra region near the crater Tycho: Science, v. 168, no. 3933, p. 825–828.

Pike, R. J., 1972, Geometric similitude of lunar and terrestrial craters: Internat. Geol. Cong., 24th, Montreal, Canada, 1972, Comptes rendus, sec. 15, p. 41–47.

Richter, D. H., Eaton, J. P., Murata, K. J., Ault, W. U., and Krivoy, H. L., 1970, Chronological narrative of the 1958–60 eruption of Kilauea Volcano, Hawaii: U.S. Geol. Survey Prof. Paper 537–E, 73 p.

Saunders, R. S., 1968, Problems for geologic investigations of the Orientale region of the Moon, *in* Ulrich, G. E., Advanced systems traverse research project report: U.S. Geol. Survey Interagency Rept., Astrogeology 7, p. 30–59.

Schaber, G. G., Scott, D. R., and Irwin, J. B., 1972, Glass in the bottom of small lunar craters: An observation from Apollo 15: Geol. Soc. America Bull., v. 83, p. 1573–1578.

Schmitt, H. H., Trask, N. J., and Shoemaker, E. M., 1967, Geologic map of the Copernicus quadrangle of the Moon: U.S. Geol. Survey Misc. Geol. Inv. Map I–515.

Shoemaker, E. M., 1962, Interpretation of lunar craters, *in* Kopal Zdeněk, ed., Physics and astronomy of the Moon: New York, Academic Press, p. 283–359.

Shoemaker, E. M., Batson, R. M., Holt, H E., Morris, E. C., Rennilson, J. J., and Whitaker, E. A., 1968, Television observations from Surveyor VII, *in* Surveyor VII Mission report, Part II, Science results: Natl. Aeronautics Space Adm. Tech. Rept. 32–126A, p. 9–76.

Short, N. M., 1965, A comparison of features characteristic of nuclear explosion craters and astroblemes, *in* Geological problems in lunar research: New York Acad. Sci. Annals, v. 123, art. 2, p. 573–616.

Strom, R. G., and Fielder, Gilbert, 1968, The multiphase development of the lunar crater Tycho: Nature, v. 217, p. 611.

——— 1970, Multiphase eruptions associated with Tycho and Aristarchus: Arizona Univ. Lunar Planetary Lab. Commun., v. 8, pt. 4, no. 150, p. 235–288.

——— 1971, Multiphase eruptions associated with the craters Tycho and Aristarchus, *in* Fielder, Gilbert, ed., Geology and physics of the Moon: New York, Elsevier, p. 55–92.

Strom, R. G., and Whitaker, E. A., 1971, An unusual far-side crater, *in* Analysis of Apollo 10 photography and visual observations: Natl. Aeronautics Space Adm., SP–323, p. 20–24.

Ulrich, G. E., 1973, A geologic model for North Ray crater and stratigraphic implications for the Descartes region, *in* Proceedings of Fourth Lunar Science Conference, Houston, Tex.: Geochim. et Cosmochim. Acta supp. 4, v. 1, p. 27–39.

Warner, J. L., Simonds, C. H, and Phinney, W. C., 1973, Apollo 16 rocks: Classification and petrogenetic model, *in* Proceedings of Fourth Lunar Science Conference, Houston, Tex: Geochim. et Cosmochim. Acta supp. 4, v. 1, p. 481–504.

Wilhelms, D. E., and McCauley, J. F., 1971, Geologic map of the near side of the Moon: U.S. Geol. Survey Misc. Geol. Inv. Map I–703, scale 1:5,000,000.

Wilshire, H. G., and Moore, H. J., 1974, Glass-coated lunar rock fragments: Jour. Geology, v. 82, no. 4, p. 403–417.

Wilshire, H. G., Stuart-Alexander, D. E., and Jackson, E. D., 1973, Apollo 16 rocks: Petrology and classification: Jour. Geophys. Research, v. 78, no. 14, p. 2379–2392.

Young, R. A., Brennan, W. J., and Wolfe, R. W, 1972, Selected volcanic and surficial features, *in* Apollo 16 preliminary science report: Natl. Aeronautics Space Adm., SP–315, p. 29-78—29-79.

☆ U.S. Government Printing Office 1975: 585-405/4

RECENT PUBLICATIONS OF THE U.S. GEOLOGICAL SURVEY

(The following books may be ordered from the Superintendent of Documents, Government Printing Office, Washington, DC 20402, to whom remittances should be sent by check or money order. Give series number, title, stock number shown in parentheses in this list, and catalog number shown in brackets. Prices of Government publications are subject to change. Increases in costs make it necessary for the Superintendent of Documents to increase the selling prices of many publications offered. As it is not feasible for the Superintendent of Documents to correct the prices manually in all the publications stocked, the prices charged on your order may differ from the prices printed in the publications and in this list.)

Professional Papers

716–B. Stratigraphy of the Bannu and Dera Ismail Khan areas, Pakistan, by W. R. Hemphill and A. H. Kidwai. 1973 (1974). p. B1–B36; plates in pocket, $3.35. (2401–02448) [I 19:16:716–B]

782. Geology of the San Francisco North quadrangle, California, by Julius Schlocker. 1974. 109 p.; plates in pocket. $4.80. (2401–02490) [I 19:16:782]

788. Geology of the Negaunee quadrangle, Marquette County, Mich., by W. P. Puffett. 1974. 53 p.; plates in pocket. $4.05. (2401–02494) [I 19:16:788]

805. Lower and lower Middle Devonian rugose corals of the central Great Basin, by C. W. Merriam. 1974. 83 p.; 25 plates showing fossils. $2.85. (2401–02488) [I 19:16:805]

816. Geology of the Betterton quadrangle, Kent County, Md., and a discussion of the regional stratigraphy, by J. P. Minard. 1974. 27 p.; plate in pocket. $1.20. (2401–02558) [I 19:16:816]

826. Geomorphology and Quaternary geology of the glaciated Ohio River valley—A reconnaissance study, by L. L. Ray. 1974. 77 p.; plates in pocket. $2.65. (2401–02556) [I 19:16:826]

845. Ammonites from the Navesink Formation at Atlantic Highlands, N.J., by W. A. Cobban. 1974. 21 p.; 11 plates showing fossils. $1.35. (2401–02501) [I 19:16:845]

866. Tectonic features of the Precambrian Belt basin and their influence on post-Belt structures, by J. E. Harrison, A. B. Griggs, and J. D. Wells. 1974. 15 p. 65¢ (2401–02554) [I 19:16:866]

Bulletins

1302. Progressive metamorphism of iron-formation and associated rocks in the Wologizi Range, Liberia, by R. W. White. 1973 (1974). 50 p.; plate in pocket. $1.95. (2401–02454) [I 19:3:1302]

1327. The geologic story of Canyonlands National Park, by S. W. Lohman. 1974. 126 p. $2.65. (2401–02498) [I 19:3:1327]

1380. Some suggested stratigraphic relations in part of southwestern New England, by N. L. Hatch, Jr., and R. S. Stanley. 1973 (1974). 83 p.; plates in pocket. $2.20. (2401–02451) [I 19:3:1380]

1395–E. Changes in nomenclature of upper Precambrian to lower Paleozoic(?) formations in the Natick quadrangle, eastern Massachusetts, and their tentative correlations with rocks in Rhode Island and Connecticut, by A. E. Nelson. 1974. p. E1–E14. 35¢. (2401–02549) [I 19:3:1395–E]

Water-Supply Papers

1532–H. Sediment transport by streams draining into the Delaware estuary, by L. J. Mansue and A. B. Commings. 1974. p. H1–H18. 40¢. (2401–02548) [I 19:13:1532–H]

1987. Subsurface geology and ground-water resources of the Jackson Purchase region, Kentucky, by R. W. Davis, T. Wm. Lambert, and A. J. Hansen, Jr. 1973 (1974). 66 p.; text and plates in case. $9.10. (2401–02443) [I 19:13:1987]

2029–D. Geologic and hydrologic control of chloride contamination in aquifers at Brunswick, Glynn County, Ga., by D. O. Gregg and E. A. Zimmerman. 1974. p. D1–D44; plates in pocket. $2.80. (2401–02506) [I 19:13:2029–D]

2141. Quality of surface waters of the United States, 1969—Part 1, North Atlantic slope basins. 1974. 449 p. $3.30. (2401–02511) [I 19:13:2141]

2144. Quality of surface waters of the United States, 1969—Parts 4 and 5, St. Lawrence River basin and Hudson Bay and Upper Mississippi River basins. 1974. 367 p. $2.80. (2401–02525) [I 19:13:2144]

2149. Quality of surface waters of the United States, 1969—Part 11, Pacific slope basins in California. 1974. 349 p. $2.70. (2401–02517) [I 19:13:2149]

2150. Quality of surface waters of the United States, 1969—Parts 12–16, North Pacific slope basins, Alaksa, Hawaii, and other Pacific areas. 1974. 480 p. $3.50. (2401–02524) [I 19:13:2150]